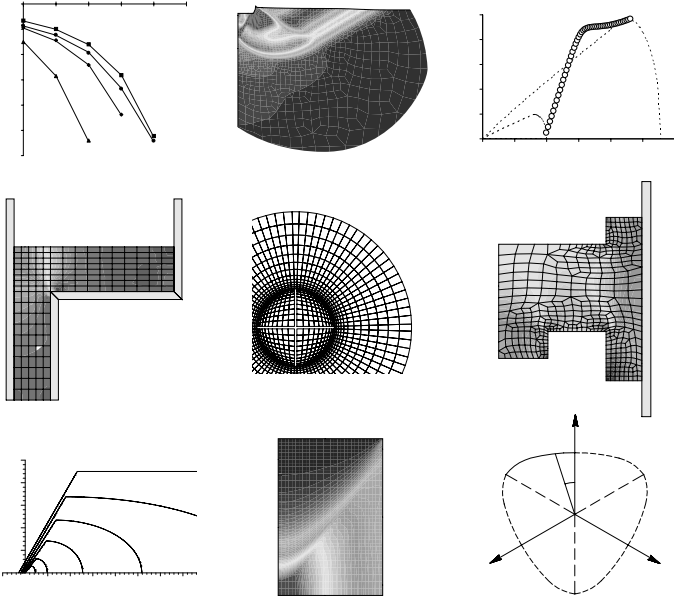


# Key issues in computational geomechanics

A. Pérez-Foguet  
A. Rodríguez-Ferran  
A. Huerta





# Contents

<b>List of Tables</b>	<b>iii</b>
<b>List of Figures</b>	<b>v</b>
<b>1 Introduction</b>	<b>1</b>
1.1 Kinematic formulation . . . . .	1
1.2 Nonlinear solvers . . . . .	2
1.3 Constitutive modelling . . . . .	3
<b>2 Arbitrary Lagrangian–Eulerian formulations</b>	<b>5</b>
2.1 Analysis of the vane test considering size and time effects . . . . .	5
2.1.1 Introduction . . . . .	6
2.1.2 Main features of field vane test . . . . .	7
2.1.3 Constitutive laws . . . . .	12
2.1.4 Basic equations and ALE formulation . . . . .	14
2.1.5 Analyses using theoretical constitutive laws . . . . .	17
2.1.6 Application to real materials . . . . .	20
2.1.7 Size and time effects . . . . .	24
2.1.8 Concluding remarks . . . . .	26
2.2 Arbitrary Lagrangian–Eulerian formulation for hyperelastoplasticity . . . . .	27
2.2.1 Introduction . . . . .	27
2.2.2 Multiplicative finite–strain plasticity in a Lagrangian setting . . . . .	28
2.2.3 Multiplicative finite–strain plasticity in an ALE setting . . . . .	29
2.2.4 Numerical examples . . . . .	33
2.2.5 Concluding remarks . . . . .	43
<b>3 Non-standard consistent tangent operators</b>	<b>45</b>
3.1 Numerical differentiation for local and global tangent operators in computational plasticity . . . . .	45
3.1.1 Introduction . . . . .	45
3.1.2 Problem statement . . . . .	46
3.1.3 Numerical differentiation . . . . .	48
3.1.4 Examples . . . . .	51
3.1.5 Concluding remarks . . . . .	62
3.2 Consistent tangent matrices for substepping schemes . . . . .	62
3.2.1 Introduction . . . . .	63
3.2.2 Problem statement . . . . .	64
3.2.3 The consistent tangent matrix for the substepping technique . . . . .	66
3.2.4 Examples . . . . .	67
3.2.5 Concluding remarks . . . . .	77
3.2.6 Appendix: Consistent tangent moduli for substepping with the generalized midpoint rule . . . . .	77
3.2.7 Appendix: Computationally efficient expression of the consistent tangent moduli for substepping with the backward Euler method . . . . .	79

<b>4</b>	<b>Elastoplastic models for granular materials</b>	<b>81</b>
4.1	Plastic flow potential for the cone region of the MRS–Lade model . . . . .	81
4.1.1	Introduction . . . . .	81
4.1.2	MRS–Lade model . . . . .	82
4.1.3	Modified plastic flow potential . . . . .	83
4.1.4	Corrected plastic flow potential . . . . .	84
4.1.5	Concluding remarks . . . . .	85
4.2	Numerical differentiation for non-trivial consistent tangent matrices: an application to the MRS–Lade model . . . . .	85
4.2.1	Introduction . . . . .	86
4.2.2	Problem statement . . . . .	87
4.2.3	Proposed approach . . . . .	89
4.2.4	Numerical differentiation . . . . .	90
4.2.5	Examples . . . . .	91
4.2.6	Concluding remarks . . . . .	103
4.2.7	Appendix: MRS–Lade model definition . . . . .	104
4.3	The MRS–Lade model for cohesive materials . . . . .	106
4.3.1	Introduction . . . . .	106
4.3.2	The original MRS–Lade model for cohesionless materials . . . . .	106
4.3.3	The proposed MRS–Lade model for cohesive materials . . . . .	107
4.3.4	Recovering the meaning of cap parameters . . . . .	109
4.3.5	Yield function . . . . .	110
4.3.6	Concluding remarks . . . . .	111
4.4	Consistent tangent matrices for density–dependent finite plasticity models . . . . .	111
4.4.1	Introduction . . . . .	111
4.4.2	Problem statement . . . . .	112
4.4.3	Consistent tangent moduli for density–dependent finite plasticity models . . . . .	115
4.4.4	Examples . . . . .	118
4.4.5	Concluding remarks . . . . .	129
4.4.6	Appendix: Density–dependent finite plasticity models . . . . .	130
<b>5</b>	<b>An application to powder compaction processes</b>	<b>135</b>
5.1	Introduction . . . . .	135
5.2	Problem statement . . . . .	136
5.2.1	Kinematics . . . . .	136
5.2.2	Constitutive model . . . . .	137
5.2.3	Numerical time–integration . . . . .	139
5.3	Numerical simulations . . . . .	140
5.3.1	Homogeneous tests . . . . .	140
5.3.2	A plain bush component . . . . .	141
5.3.3	A rotational flanged component . . . . .	143
5.3.4	A multi–level component . . . . .	150
5.4	Concluding remarks . . . . .	151
<b>6</b>	<b>Summary and future developments</b>	<b>153</b>
	<b>Bibliography</b>	<b>155</b>
	<b>Index</b>	<b>164</b>

# List of Tables

2.1	Some generalized Newtonian fluid models defined in terms of viscosity. A simplified 1D representation of the models is included. (After Huerta and Liu 1988). . . . .	14
2.2	Numerical values of $N_1$ and $N_2$ for different materials, vane sizes and angular velocities. . . . .	15
2.3	Numerical values of the analyses of the vane test using theoretical constitutive laws. . . . .	19
2.4	Numerical values of the analyses of the vane test applied to Red Mud. . . . .	20
2.5	Numerical values of the analyses of the vane test applied to soft clay. . . . .	24
2.6	The proposed ALE approach for hyperelastoplasticity . . . . .	32
2.7	Material parameters for the necking test. . . . .	34
3.1	Numerical approximations to the derivatives of the flow vector. . . . .	49
3.2	Relative stepsizes that give the same convergence results as analytical derivatives, for the von Mises perfect plasticity global problem. . . . .	58
3.3	Relative stepsizes that give the same convergence results as analytical derivatives, for the von Mises exponential hardening global problem. . . . .	58
3.4	The convergence results for sixth load step of the pile problem: (a) 1ND-O( $h$ ), (b) 2ND-O( $h^2$ ). . . . .	59
3.5	Relative stepsizes that give the same convergence results as analytical derivatives, for the pile problem. . . . .	60
3.6	Relative stepsizes that give the same convergence results as analytical derivatives, for the rigid footing problem. . . . .	61
3.7	Time overheads of the numerical approximations, for the rigid footing problem. . . . .	62
3.8	Rigid footing problem. Relationship between number of global load increments and relative CPU time. . . . .	72
3.9	Triaxial test problem. Relationship between number of global load increments and relative CPU time. . . . .	73
4.1	Numerical approximations to first derivatives. . . . .	91
4.2	Sets of material parameters. S1 is a Sacramento River sand (Macari et al. 1997). S2 is a modification of S1. . . . .	91
4.3	Definition of the three stress paths for the local problems. . . . .	92
4.4	Evolution of the Lode angle $\theta$ (in degrees) during the three stress paths defined in table 4.3. . . . .	92
4.5	Range of relative stepsizes $h_r$ that give quadratic convergence in the local problem, stress paths A and B. . . . .	92
4.6	Range of relative stepsizes $h_r$ that give quadratic convergence in the local problem, stress path C. . . . .	94
4.7	Range of relative stepsizes $h_r$ that give quadratic convergence up to a tolerance of $10^{-10}$ in the pile problem. . . . .	98
4.8	Relative CPU time of the three numerical differentiation techniques with several relative stepsizes $h_r$ in the pile problem. . . . .	98
4.9	Range of relative stepsizes $h_r$ that give quadratic convergence in the homogeneous triaxial problem up to a tolerance of $10^{-8}$ (1ND-O( $h$ ) approximation) or $10^{-10}$ (the other two). . . . .	99
4.10	Number of accumulated iterations for the non-homogeneous triaxial problem: (a) with a tolerance of $10^{-8}$ ; (b) with a tolerance of $10^{-10}$ . . . . .	103

4.11	Relative CPU time of the three numerical differentiation techniques with several relative stepsizes $h_r$ in the non-homogeneous triaxial problem up to a tolerance of $10^{-10}$ . . . . .	103
4.12	Sets of material parameters for the elliptic and the cone-cap models. . . . .	119
5.1	The overall ALE scheme. . . . .	139
5.2	Material parameters. . . . .	140

# List of Figures

2.1	Typical dimensions of the field vane (after Chandler 1988). . . . .	7
2.2	Measured stress distributions at vane blades (after Menzies and Merrifield 1980). . . . .	8
2.3	Shear stress distributions on sides and top of vane obtained from numerical simulations. a) Elastic model (after Donald et al. 1977) b) Using an elastoplastic model and a strain softening model including anisotropy (after Griffiths and Lane 1990). . . . .	9
2.4	Shear stress–angular rotation obtained using different testing rates on Bäckebol clay, Sweden (after Torstensson 1977). . . . .	10
2.5	Rheological state of soil in accordance with water content for some Japanese clays (after Komamura and Huang 1974). . . . .	11
2.6	Effect of strain rate on undrained shear stress obtained using torsional hollow cylinder (after Cheng 1981). . . . .	12
2.7	Shear stress–shear strain rate obtained from viscosimeter experiments. St. Alban–1 marine clay with a salt content of 0.2 g/l. $\tau_y$ is yield stress, $I_L$ is liquidity index and $\mu$ is viscosity (after Locat and Demers 1988). . . . .	13
2.8	Finite element mesh used in the analyses of the vane test, with a dimensionless vane radius of 1. . . . .	16
2.9	Dimensionless shear stress versus dimensionless shear strain rate for the theoretical constitutive laws. . . . .	17
2.10	Shear strain rate and shear stress distributions using: (a–c) the theoretical constitutive laws: (a) Bingham–1, (b) Bingham–2 and (c) Carreau–2; and (d–e) the soft clay constitutive laws: (d) Bingham and (e) Logarithmic. . . . .	18
2.11	Dimensionless velocity and shear strain rate between blades using theoretical constitutive laws. . . . .	19
2.12	Dimensionless torque versus dimensionless time for the theoretical laws. . . . .	20
2.13	Shear stress [Pa] versus shear strain rate [ $s^{-1}$ ] for the Red Mud constitutive laws. . . . .	21
2.14	Summary of undrained rate effects in isotropically consolidated soils of different composition (after Lacasse 1979). Continuous line corresponds to the case analyzed in numerical simulations. . . . .	21
2.15	Dimensionless shear stress versus dimensionless shear strain rate for the soft clay constitutive laws. . . . .	22
2.16	Dimensionless velocity and shear strain rate between blades using soft clay constitutive laws. . . . .	22
2.17	Dimensionless torque versus dimensionless time for the soft clay constitutive laws. . . . .	23
2.18	Dimensionless shear stress versus shear strain rate (1/s) for the soft clay constitutive laws. . . . .	23
2.19	Simulation results and potential interpolation of relationship between dimensionless torque and angular velocity ( $^\circ/\text{min}$ ) for different soft clay constitutive laws. . . . .	25
2.20	Dimensionless torque versus dimensionless time for different inertial forces, using Bingham–1 model. . . . .	25
2.21	Domains, mappings and deformation gradients in the ALE description . . . . .	30
2.22	Necking of a cylindrical bar. Problem definition and computational mesh. . . . .	34
2.23	Necking test with the von Mises model. Mesh configurations for different top displacements d: (a–c) Lagrangian formulation and (d–f) ALE formulation. . . . .	35

2.24	Necking test with the von Mises model. Lagrangian and ALE formulations. Global response: (a) vertical edge reaction and (b) dimensionless radius in the necking zone versus vertical edge displacement. . . . .	35
2.25	Necking test with the von Mises model. Distribution of the von Mises stress in the necking zone. Hyperelastic–plastic model: (a) Lagrangian formulation, (b) ALE formulation. Hypoelastic–plastic model (after Rodriguez–Ferran et al. 1998): (c) Lagrangian formulation, (d) ALE formulation. . . . .	36
2.26	Necking test with the Tresca–type model. Distribution of the von Mises stress in the necking zone: (a) Lagrangian and (b) ALE formulations. . . . .	36
2.27	Necking test with the Tresca–type model. Lagrangian and ALE formulations. Global response: (a) vertical edge reaction and (b) dimensionless radius in the necking zone versus vertical edge displacement. . . . .	37
2.28	Necking test with the Tresca–type model. Mesh configurations for different top displacements, d: (a–c) Lagrangian formulation and (d–f) ALE formulation. . . . .	37
2.29	Coining test. Problem definition and computational mesh. . . . .	37
2.30	Coining test with the von Mises model. Mesh configurations and distribution of the von Mises stress for different height reductions. Lagrangian and ALE formulations. . . . .	38
2.31	Coining test with the von Mises model. Lagrangian and ALE formulations. Representative results: (a–b) point C displacements, (c–d) point D displacements, and (e–f) punch reactions. . . . .	39
2.32	Flanged component. Problem definition and computational mesh, after Lewis and Khoei 1998. . . . .	40
2.33	Top punch compaction of the flanged component. Mesh configurations for different punch displacements $d_t$ : (a–d) Lagrangian formulation and (e–h) ALE formulation. . . . .	41
2.34	Bottom punch compaction of the flanged component. Mesh configurations for different punch displacements $d_b$ : (a–d) Lagrangian formulation and (e–h) ALE formulation. . . . .	41
2.35	(a–b) Top and (c–d) bottom punch compactions of the flanged component. Final relative density distribution, Lagrangian and ALE formulations. . . . .	42
3.1	Relation between the relative error of the numerical approximations to the flow vector derivatives versus the relative stepsize, von Mises model. . . . .	52
3.2	Main features of the Rounded Hyperbolic Mohr–Coulomb yield surface: trace on the deviatoric and meridian planes (after Abbo 1997). . . . .	53
3.3	Relation between the relative error of the numerical approximations to the flow vector derivatives versus the relative stepsize, RHMC model. . . . .	53
3.4	Convergence results of the local problem with RHMC model. . . . .	54
3.5	Perforated strip under traction (after Simo 1985). Due to symmetry, only one quarter is considered. . . . .	55
3.6	Convergence results for the fourth and the eighth load steps. Von Mises perfect plasticity. . . . .	56
3.7	Convergence results for the fourth and the eighth load steps. Von Mises exponential hardening plasticity. . . . .	57
3.8	Pile problem (after Potts and Gens 1985). . . . .	59
3.9	Rigid footing: (a) problem definition, (b) mesh and final plastic strains. Due to symmetry, only one half is considered. . . . .	60
3.10	Convergence results for the load steps fifteen and twenty. Rigid footing with RHMC model. . . . .	61
3.11	Rounded Hyperbolic Mohr–Coulomb model. Number of iterations of the local problem for trial stresses in the deviatoric plane ( $\theta$ – $J_2$ ) at various levels of confinement ( $I_1/3$ ). . . . .	68
3.12	Rigid footing: (a) problem definition, (b) mesh. . . . .	69
3.13	Rigid footing problem. Dimensionless force versus vertical displacement. . . . .	69
3.14	Rigid footing problem. Equivalent plastic strain for different load levels. . . . .	70
3.15	Rigid footing problem. Evolution of the number of Gauss points with substepping activated (top), the sum of substeps over the domain (center) and the maximum number of substeps for all the Gauss points (bottom). . . . .	71
3.16	Rigid footing problem. Convergence results for different load levels. . . . .	72



3.17 Rigid footing problem. Relationship between accumulated iterations and load level.	73
3.18 Triaxial test problem. Force versus relative vertical displacement. . . . .	73
3.19 Triaxial test problem. Distribution of the cone internal variable for different values of the relative vertical displacement. . . . .	74
3.20 Triaxial test problem. Distribution of the number of substeps required for different values of the relative vertical displacement. Problem solved with (a) 20 l.i., and (b) with 50 l.i. . . . .	74
3.21 Triaxial test problem. Evolution of the number of Gauss points with substepping activated (top), the sum of substeps over the domain (center) and the maximum number of substeps for all the Gauss points (bottom). . . . .	75
3.22 Triaxial test problem. Convergence results for different values of the relative vertical displacement. . . . .	76
4.1 Trace of the simplified MRS–Lade yield function and characteristic flow vectors on the $p - q$ plane. Original formulation (a), modified flow potential (b) and corrected flow potential (c). . . . .	83
4.2 $p$ -component of modified flow vector as function of $p$ . . . . .	84
4.3 $p$ -component of corrected flow vector as function of $p$ . . . . .	85
4.4 MRS–Lade model. Trace of the yield criterion: (a) on the meridian plane; (b) on the deviatoric plane. . . . .	88
4.5 MRS–Lade model. Hardening–softening function $\eta_{\text{con}}(\kappa_{\text{con}})$ . (a) Soil S1 and (b) soil S2; see table 4.2. . . . .	88
4.6 Trace of the three paths and of their initial and final yield criteria on the meridian plane. . . . .	93
4.7 Convergence results for various steps of paths A, B and C . . . . .	94
4.8 Convergence of the different unknowns of the local problem for step 31 of path A. . . . .	95
4.9 Evolution of the stress invariants and the yield criterion during the iterations of step 11 of path A and step 3 of path B. . . . .	95
4.10 Convergence results for step 31 of path A using the approximations defined in table 4.1 with several relative stepsizes $h_r$ . . . . .	96
4.11 Convergence results for path A with only 10 steps . . . . .	97
4.12 Load versus displacement curve for the pile problem. . . . .	97
4.13 Convergence results for various load steps of the pile problem . . . . .	98
4.14 Triaxial test. Problem statement. . . . .	99
4.15 Invariant $q$ versus axial strain curves for the homogeneous triaxial problem with various precompressions. . . . .	100
4.16 Accumulated iterations versus load level for the homogeneous triaxial problem with three nonlinear solvers. . . . .	100
4.17 Convergence results for step 2 of the homogeneous triaxial problem with various relative stepsizes $h_r$ . . . . .	101
4.18 Second invariant of the deviatoric part of the strain tensor for different values of the axial strain (vertical displacement/initial height) in the non-homogeneous triaxial problem. . . . .	102
4.19 Non-homogeneous triaxial problem. Evolution of (a) load and (b) number of Gauss points with plastic loading versus displacement. . . . .	102
4.20 Convergence results for various load steps of the non-homogeneous triaxial problem. . . . .	103
4.21 Accumulated iterations versus load level for the non-homogeneous triaxial problem with various nonlinear solvers. . . . .	104
4.22 MRS–Lade model for cohesionless materials. Trace of the simplified yield criterion on the meridian plane. . . . .	106
4.23 MRS–Lade model for cohesive materials. Trace of the yield criterion on the meridian plane: (a) incorrect open surface; (b) correct closed surface . . . . .	108
4.24 MRS–Lade model for cohesive materials. Relationships between $\hat{p}_{\text{cap}}$ , $\hat{\alpha}$ , $p_{\text{cap}}$ and $\alpha$ . . . . .	110
4.25 Load–displacement results of the uniaxial compression test. Cauchy–based and Kirchhoff–based Drucker–Prager models with different friction angles, $\phi$ . (a) Load divided by deformed area and (b) load divided by undeformed area. . . . .	119

4.26	Uniaxial compression test. Left (a,c,e) Kirchhoff-based and right (b,d,f) Cauchy-based Drucker-Prager models with different friction angles, $\phi$ . Convergence results for different vertical displacements. . . . .	120
4.27	Convergence results for different vertical displacements obtained with the standard (density-independent) consistent tangent moduli. . . . .	121
4.28	Traces of the elliptic yield function on the meridian plane $q_{\tau}-p_{\tau}$ for different relative densities, $\eta$ . Powder-A material parameters, see table 4.12. . . . .	121
4.29	Results of (a) isostatic and (b) triaxial tests with powder-A material, see table 4.12. Experimental data from Doremus et al. (1994). . . . .	122
4.30	Powder-A isostatic test. Convergence results for different load levels. . . . .	123
4.31	Powder-A triaxial test (150 MPa initial isostatic compaction). Convergence results for different load levels and with (a,c) unsymmetric and (b,d) symmetric linear solvers, left and right respectively. . . . .	124
4.32	Results of isostatic and uniaxial tests with powder-B material, see table 4.12. Experimental data from Ernst and Barnekov (1994). . . . .	124
4.33	Powder-B isostatic test. Convergence results for different load levels. . . . .	125
4.34	Frictionless compaction of the flanged component with (a) the elliptic model (b) the cone-cap model. Final relative density, $\eta$ , distribution after a top displacement of 6.06 mm. . . . .	125
4.35	Frictionless compaction of the flanged component with the elliptic model. Final distribution of Cauchy stresses at Gauss-point level on the meridian plane $q_{\sigma}-p_{\sigma}$ . Blue marks indicate plastic steps and green marks indicate elastic steps. . . . .	125
4.36	Frictionless compaction of the flanged component with the elliptic model. Convergence results for different load levels. . . . .	126
4.37	Traces of the cone-cap yield function on the meridian plane $q_{\tau}-p_{\tau}$ for different relative densities, $\eta$ . Powder-A material parameters, see table 4.12. . . . .	127
4.38	Frictionless compaction of the flanged component with the cone-cap model. Distribution of Cauchy stresses at Gauss-point level on the meridian plane $q_{\sigma}-p_{\sigma}$ for different load levels. Blue marks indicate plastic steps on the cap region, red marks plastic steps on the cone region and green marks elastic steps. . . . .	128
4.39	Frictionless compaction of the flanged component with the cone-cap model. Convergence results for different load levels. . . . .	129
5.1	Dependence of parameters $a_1(\eta)$ and $a_2(\eta)$ on the relative density, $\eta$ . Parameters of Powder-C material, see table 5.2. . . . .	138
5.2	Trace of the elliptic yield function on the meridian plane $q_{\tau}-p_{\tau}$ for different relative densities, $\eta$ . Parameters of Powder-C material, see table 5.2. . . . .	138
5.3	Plain bush component. Problem definition (after Lewis and Khoei 1998) and computational mesh. . . . .	141
5.4	Plain bush component. Relative density profile at radius equal to 10.5 mm. . . . .	142
5.5	Plain bush component. Relationship between top punch vertical reaction and its vertical displacement. . . . .	142
5.6	Plain bush component. Relative density distribution for different top punch movements. Note that two different scales are used. . . . .	144
5.7	Flanged component. Relationships between the vertical reactions of the punches and their vertical movements: top reaction for top punch compaction, bottom reaction for bottom punch compaction, and top and bottom reactions for double-punch compaction. . . . .	145
5.8	Relative mass variation during the three compaction processes of the flanged component. The load levels are referred to the punch displacements imposed at the end of each test. . . . .	145
5.9	Top punch compaction. (a-d) Relative density distribution for different top punch movements and (e) relative density profile at 1.88 mm from line $\overline{GD}$ (section 1-1'). . . . .	146
5.10	Bottom punch compaction. (a-d) Relative density distribution for different bottom punch movements and (e) relative density profile at 3.9 mm from line $\overline{GD}$ (section 1-1'). . . . .	147

---

5.11	Double-punch compaction. Relative density distribution for different movements of the top and bottom punches. . . . .	148
5.12	Multi-level component. Relative density distribution for three different compaction processes. . . . .	148
5.13	Double-punch compaction. Relative density profiles at 3.47 mm (section 1-1') and 1.3 mm (section 2-2') from the line $\overline{GD}$ , and at radii equal to 9.37 mm (section 3-3') and 8.77 mm (section 4-4'). . . . .	149
5.14	Multi-level component. Problem definition (after Khoei and Lewis 1999) and computational mesh. . . . .	150
5.15	Multi-level component. Relative density profile at radius equal to 30 mm for the three different compaction processes. . . . .	151



# Chapter 1

## Introduction

Numerical modelling of problems involving geomaterials (i.e. soils, rocks, concrete and ceramics) has been an area of active research over the past few decades. This fact is probably due to three main causes: the increasing interest of predicting the material behaviour in practical engineering situations, the great change of computer capabilities and resources, and the growing interaction between computational mechanics, applied mathematics and different engineering fields (concrete, soil mechanics ...). This report fits within this last multidisciplinary approach. Based on constitutive modelling and applied mathematics and using both languages the numerical simulation of some complex geomechanical problems has been studied.

The state of the art regarding experiments, constitutive modelling, and numerical simulations involving geomaterials is very extensive. The report focuses in three of the most important and actual ongoing research topics within this framework:

1. The treatment of large boundary displacements by means of Arbitrary Lagrangian–Eulerian (ALE) formulations.
2. The numerical solution of highly nonlinear systems of equations in solid mechanics.
3. The constitutive modelling of the nonlinear mechanical behaviour of granular materials.

The three topics have been analyzed and different contributions for each one of them have been developed. The new developments are presented in chapters 2 to 4, which are related, respectively, to the three topics outlined above. Several applications have been included in these chapters in order to show the main features of each contribution.

After that, in chapter 5, some of the new developments have been applied to the numerical modelling of cold compaction processes of powders. These processes consist in the vertical compaction through the movement of a set of punches of a fine powder material at room temperature. The process transforms the loose powder into a compacted sample through a large volume reduction. This problem has been chosen as a reference application of the report because it involves large boundary displacements, finite deformations and highly nonlinear material behaviour. Therefore, it is a challenging geomechanical problem from a numerical modelling point of view. Finally, in chapter 6, a brief summary of the report is presented, together with an overview of the possible future developments.

In the following, a general description of the three main research topics is presented.

### 1.1 Kinematic formulation

In many geomechanical problems, the domain of interest is subjected to large boundary displacements. Moreover, these problems usually lead to non-uniform large-strain solutions. An adaptive strategy for space discretization can help to handle these problems. Several alternatives are available (Huerta, Rodríguez-Ferran, Díez and Sarrate 1999). Two common approaches in finite element simulations are  $h$ -remeshing techniques and ALE schemes. The  $h$ -remeshing techniques imply, usually, a high computational effort and the loss of accuracy due to interpolations from the

old mesh to the new mesh. For these reasons the report focuses in the formulation of different ALE schemes.

ALE formulations reduce the drawbacks of purely Lagrangian or Eulerian formulations. In a Lagrangian formulation, mesh points coincide with material particles. Each element contains always the same amount of material and no convective effects are generated. In this case the resulting governing equations are simple, but it is difficult to deal with large deformations. On the other hand, an Eulerian formulation takes a fixed mesh, and the particles move through it. Now important convective effects appear due to the relative motion between the grid and the particles, but it is possible to simulate large strains. In ALE formulations, the mesh and material deformations are uncoupled, and a computationally efficient compromise between Lagrangian and Eulerian formulations is achieved.

The ALE approach was first proposed for fluid problems with moving boundaries (Donéa, Fasoli-Stella and Giuliani 1977, Donea 1983, Hughes, Liu and Zimmermann 1981, Huerta and Liu 1988). Nowadays, in some fields of solid mechanics, such as the modelling of forming processes, ALE fluid-based formulations are widely used. In the report, an ALE fluid-based formulation has been applied to quasistatic and dynamic simulations of the vane test for soft materials, see section 2.1 (Pérez-Foguet, Ledesma and Huerta 1999). This particular application is an example of how an ALE formulation allows to manage the movement of the boundary in a straightforward manner. Several detailed analyses related with the test are included in section 2.1.

On the other hand, the ALE approach has been extended and successfully employed in nonlinear solid mechanics (Liu, Belytschko and Chang 1986, Benson 1986, Huétink, Vreede and van der Lugt 1990, Ghosh and Kikuchi 1991, Rodríguez-Ferran, Casadei and Huerta 1998) and structural mechanics (Askes, Rodríguez-Ferran and Huerta 1998, Huerta et al. 1999). However, this is still an important research area. Recently, a specific ALE scheme for hyperelastoplasticity has been presented (Armero and Love 2000). This approach, as a previous formulation for hyperelasticity (Yamada and Kikuchi 1993), is based on a total Lagrangian formulation of the problem. In both cases, the distortion on both the material mesh and the spatial mesh have must be kept under control. Here, in section 2.2, a new ALE scheme for hyperelastoplasticity based on an updated Lagrangian approach is presented (Rodríguez-Ferran, Pérez-Foguet and Huerta 2000). The deformed configuration at the beginning of the time-step is chosen as the reference configuration; consequently, only the quality of the spatial mesh must be ensured by the ALE remeshing strategy. Several applications of the proposed approach are presented in sections 2.2, 4.4 and in chapter 5. Most of them correspond to powder compaction problems, a field where the ALE approach shows to be crucial for an accurate numerical simulation.

## 1.2 Nonlinear solvers

Numerical simulation in solid mechanics usually leads to highly (geometrically and materially) nonlinear problems. The report focuses in quasistatic problems. Two kinds of methods can be applied to solve them: implicit and explicit. Implicit methods are preferred, because they are unconditionally stable. Nevertheless, for large scale problems explicit methods are widely used, because the computational effort is lower. The adequacy of explicit solutions for simulations in solid mechanics is still a subject of debate (Owen, Perić, de Souza Neto, Yu and Dutko 1995). It is expected that implicit methods will become the standard approach for large scale problems (like during the later eighties they became for 2-D elastoplastic problems).

The report focuses on implicit methods. Although various nonlinear solvers may be used, see for instance the recent works of Alfano, Rosati and Valoroso (1999) and Sloan, Sheng and Abbo (2000), a common choice is the full Newton-Raphson method. In the context of solid mechanics, the consistent tangent operators ensure quadratic convergence of the Newton-Raphson method. The concept of consistent tangent operator was introduced for simple elastoplastic models (Simo and Taylor 1985, Runesson, Samuelsson and Bernspang 1986). Since then, it has been systematically applied to a broad class of constitutive models of inelastic behaviour (Simo, Kennedy and Govindjee 1988, Ramm and Matzenmiller 1988, Simo 1992, Hofstetter, Simo and Taylor 1993, de Souza Neto, Perić and Owen 1994, Li 1995, Crisfield 1997, Simo 1998, Armero 1999, Belytschko, Liu and Moran 2000). In section 4.4, the expression for finite strain density-dependent plastic models is developed (Pérez-Foguet, Rodríguez-Ferran and Huerta 2000*b*). Several applications of these

models to powder compaction processes are shown in sections 2.2, 4.4 and in chapter 5.

Consistent tangent operators depend on the numerical scheme used for the time-integration of the constitutive equations. The expressions of the consistent tangent operators for the most usual time-integration schemes (such as the backward Euler method or the midpoint rule) are available elsewhere. Other time-integration schemes are those based on substepping techniques (Sloan 1987, Sloan and Booker 1992, Potts and Ganendra 1994). They are less common because, among other things, they lack of the corresponding consistent tangent operators. For this reason, in section 3.2, the consistent operators for different substepping techniques are presented. Moreover, one of them is applied together with an adaptive time-integration strategy. This approach can result in a large reduction of the computational cost for some complex geomechanical problems. This fact is illustrated with the simulation of the rigid footing problem on a frictional material in section 3.2.

Independently of the time-integration scheme, there are some difficulties in the analytical definition and the computation of consistent operators for non-trivial constitutive laws. Because of this, in some cases the full Newton-Raphson method is abandoned and specific nonlinear solvers are devised to integrate the constitutive model (Pramono and Willam 1989*b*, Etse and Willam 1994, Jeremić and Sture 1997, Macari, Weihe and Arduino 1997). However, quadratic convergence is not achieved with these methods, because they are not based on a consistent linearization of all the equations with respect to all the unknowns. Here, numerical differentiation has been applied to compute consistent tangent operators with the goal of precluding these difficulties. The proposed approach (Pérez-Foguet, Rodríguez-Ferran and Huerta 2000*d*) is presented in section 3.1. Several applications are shown in different parts of the report: in section 4.2 it is applied to a work hardening cone-cap model for sands, in sections 2.2, 4.4 and in chapter 5 to density-dependent plastic models for powder compaction simulations, and in section 3.2 to several problems solved with the substepping scheme.

### 1.3 Constitutive modelling

Two different approaches are usually followed to model the mechanical behaviour of granular materials: micromechanical and macroscopic. The micromechanical approach consists in modelling each particle separately and computing the behaviour at macroscopic level through the relative interaction between many particles (Borja and Wren 1995, Wren and Borja 1997). The macroscopic approach is based on model the material as a continuous medium. Several continuous constitutive laws have been used for granular materials (typically elastoplastic and viscoplastic models). Elastoplastic models are the most used for isothermal modelling. In fact, nowadays, elastoplastic models are widely used to model many different geomaterials in small-strain problems, ranging from virgin noncohesive sand (Sture, Runesson and Macari-Pasqualino 1989, di Prisco, Nova and Lanier 1993) to hard rocks and concrete (Pramono and Willam 1989*a*). Recently, several finite strain hyperelastic-plastic models specific for geomaterials have also been developed (Simo and Meschke 1993, Meschke, Liu and Mang 1996, Oliver, Oller and Cante 1996, Borja and Tamagnini 1998, Callari, Auricchio and Sacco 1998). Moreover, an important issue related with the numerical modelling of granular materials is the mathematical notion of well-posedness. This requires the use of regularized constitutive laws to model properly failure situations, see for instance Askes (2000) and references therein. This is an actual important area of research.

The report focuses in classical elastoplastic modelling. Two different approaches are followed: a work hardening-softening cap model for small-strain problems and density-dependent hyperelastic-plastic models for finite strain simulations. Two issues are common to both approaches: the treatment of non-smooth plastic equations and the proper computation of tangent operators.

In many elastoplastic models (such as Tresca, Mohr Coulomb and cone-cap models) the yield function is defined by parts, leading to a non-smooth transition of the flow equations at the intersection. The problem is solved, typically, by means of corner return-mapping algorithms based on the Koiter's rule, see for instance Simo et al. (1988) and references therein. However, in order to reduce the computational effort of the time-integration algorithm, smoothing approaches are preferred in some cases. Two alternatives can be devised: smoothing the yield function (and as a result the flow equations) or smoothing only the flow equations. In both cases corner return-

mapping algorithms are not needed. The von Mises–Tresca model (Miehe 1996, Pérez-Foguet and Armero 2000) and the Rounded Hyperbolic Mohr Coulomb model (Sloan and Booker 1986, Abbo and Sloan 1995) are examples of the first alternative. Here, both models are used in several applications in section 2.2 and in chapter 3. The second alternative, to smooth only the flow equations, is more recent (Macari, Runesson and Sture 1994, Macari et al. 1997). In sections 4.1 (Pérez-Foguet and Huerta 1999) and 4.3 (Pérez-Foguet and Rodríguez-Ferran 1999) the second alternative has been applied to work hardening–softening cap models and in section 4.4 to a density–dependent hyperelastic–plastic model.

On the other hand, especial attention has been dedicated to the computation of tangent operators for both types of models in sections 4.2 and 4.4. Both cases are examples of non-trivial elastoplastic models with coupled dependence between the plastic strain flow and the hardening–softening laws (which are based on the plastic work and the relative density respectively). As a result of the use of full tangent operators together with the new developments presented in chapters 2 and 3 (ALE formulations, numerical differentiation and consistent operators for substepping techniques) it has been possible to simulate numerically and analyze three complex geomechanical problems involving granular materials: the triaxial response of homogeneous and non-homogeneous sand samples in sections 3.2 and 4.2, the failure of a frictional material under a rigid footing in section 3.2, and several compaction processes of powder materials in chapter 5.



## Chapter 2

# Arbitrary Lagrangian–Eulerian formulations

This chapter has two different parts. In the first part, section 2.1, a fluid–based Arbitrary Lagrangian–Eulerian (ALE) formulation is applied to quasistatic and dynamic simulations of the vane test for viscous materials. In the second part, section 2.2, a new ALE formulation for finite strain hyperelastoplasticity is presented.

The fluid–based ALE formulation (Huerta and Liu 1988) is used to perform a detailed analysis of the vane test. This test is used to measure the ‘in situ’ undrained shear strength of soft materials, as some clays and slurried mineral wastes, and to characterize the viscosity of plastic fluids in laboratory tests. The ALE finite element simulation of this test has enabled the study of the influence of the constitutive law on the shear band width, the position of the failure surface and the shear stress distributions on the failure surface. The influence of the vane size has also been analyzed, by means of a dimensionless analysis of the constitutive equations, and, finally, an experimental relation between the undrained shear strength and the vane angular velocity has been reproduced.

The new formulation for finite strain hyperelastoplasticity is based on the same approach presented previously for hypoelastic–plastic models (Rodríguez-Ferran et al. 1998). The numerical time–integration is performed with a fractional–step method, with a Lagrangian phase and a convection phase. In contrast to previous ALE formulations of hyperelasticity or hyperelastoplasticity, the deformed configuration at the beginning of the time–step, not the initial undeformed configuration, is chosen as the reference configuration. The proposed ALE approach has a major advantage: only the quality of the mesh in the spatial domain must be ensured by the ALE remeshing strategy; thus, the full potential of the ALE description as an adaptive technique can be exploited. These aspects are illustrated in detail with three numerical examples: a necking test, a coining test and a frictionless powder compaction test.

### 2.1 Analysis of the vane test considering size and time effects

An analysis of the vane test using an Arbitrary Lagrangian–Eulerian formulation within a finite element framework is presented. This is suitable for soft clays for which the test is commonly used to measure ‘in situ’ undrained shear strength. Constitutive laws are expressed in terms of shear stress–shear strain rates, and that permits the study of time effects in a natural manner. An analysis of the shear stress distributions on the failure surface according to the material model is presented. The effect of the constitutive law on the shear band amplitude and on the position of the failure surface is shown. In general, the failure surface is found at 1. to 1.01 times the vane radius, which is consistent with some experimental results. The problem depends on two dimensionless parameters that represent inertial and viscous forces. For usual vane tests, viscous forces are predominant, and the measured shear strength depends mainly on the angular velocity applied. That can explain some of the comparisons reported when using different vane sizes. Finally, the

range of the shear strain rate applied to the soil is shown to be fundamental when comparing experimental results from vane, triaxial and viscosimeter tests. Apart from that, an experimental relation between undrained shear strength and vane angular velocity has been reproduced by this simulation.

### 2.1.1 Introduction

The vane shear test has been used extensively from the 50's to measure the 'in situ' shear strength of soft clays, due to the simplicity of the test and to the difficulties in obtaining undisturbed samples in these materials. In fact most site investigation manuals and codes of practice in geotechnical engineering include a description of the vane equipment and some recommendations for its use (ASTM-D2573-72 1993, Weltman and Head 1983). Also, the vane test has been useful in characterizing the 'in situ' behaviour of very soft materials like slurried mineral wastes and in the determination of the viscosity of plastic fluids in laboratory tests (Nguyen and Boger 1983, Keentok, Milthorpe and O'Donovan 1985). However, in spite of its common use, the interpretation of the vane test has been quite often a controversial issue. The work presented by Donald, Jordan, Parker and Toh (1977) summarizes the main drawbacks of the test and the usual sources of error in the estimation of the undrained strength: soil anisotropy effects, strain rate effects, and progressive failure. Classical interpretation of vane results did not take into account those effects. To overcome these difficulties, some research has been devoted to the experimental analysis of the vane test in the laboratory or in the field: Menzies and Merrifield (1980) measured shear stresses in the vane blades, and Matsui and Abe (1981) measured normal stresses and pore pressures in the failure surface. Also Kimura and Saitoh (1983) obtained pore water pressure distributions from transducers located in the vane blades.

On the other hand, numerical simulations of the vane test are scarce, due to its mathematical complexity. Donald et al. (1977) presented a three-dimensional (3D) finite element analysis of the vane using a linear elastic constitutive model. Matsui and Abe (1981) also compared their experimental results with a coupled 2D finite element simulation using a strain-hardening model. More recently, de Alencar, Chan and Morgenstern (1988) and Griffiths and Lane (1990) have presented 2D finite element simulations of the vane with a strain-softening constitutive law. The latter also showed stress distributions in a quasi 3D analysis. These experimental and numerical reports have improved the knowledge of the stress distributions around the failure surface and therefore have contributed to an improvement on the interpretation of the vane test. Nevertheless, there is still some concern about the validity of the undrained strength  $(s_u)_{vane}$  obtained in this way. Bjerrum (1973) proposed a correction factor for the vane undrained strength which decreased with plasticity index. Also Bjerrum proposed to extend the procedure considering two correction factors in order to take into account anisotropy and time effects. That correction has been improved using information from case histories of embankment failures (Azzouz, Baligh and Ladd 1983). Despite this correction factor, important differences between corrected  $(s_u)_{vane}$  and undrained shear strength measured with independent tests have been reported for some clays (Ladd and Foott 1974, Kirkpatrick and Khan 1981, Tanaka 1994). The contradictory results presented by different authors show that conceptual analyses of the vane test are still required to establish the validity of the test. As there are several factors influencing the result, it is difficult to deal with all of them simultaneously. Even some probabilistic approaches have been presented elsewhere to deal with the uncertainties involving the 'in situ' measurement of the mobilized undrained shear strength (Kirkpatrick and Khan 1984). Recently, a new model to estimate a theoretical torque based on critical state concepts have been presented (Morris and Williams, 1993, 1994). Comparing theoretical and measured torques from a literature survey, they have defined a correction factor similar to that proposed by Bjerrum, although more elaborated.

In this section, a particular approach to the vane test that allows one to study size and time effects in a natural way is presented. Also some results concerning the failure mechanism are presented and compared with the ones obtained from classical solid mechanics simulations. One of the difficulties associated to the numerical analysis of the vane test is dealing with large deformations and the strain localized zone produced in the failure area. Even some of the large-strain finite element models have disadvantages when large local deformations are involved. The problems derived from the distortion of elements can be avoided if an Arbitrary Lagrangian-Eulerian formulation (ALE) coupled to the Finite Element Method is used. In a Lagrangian formulation mesh points

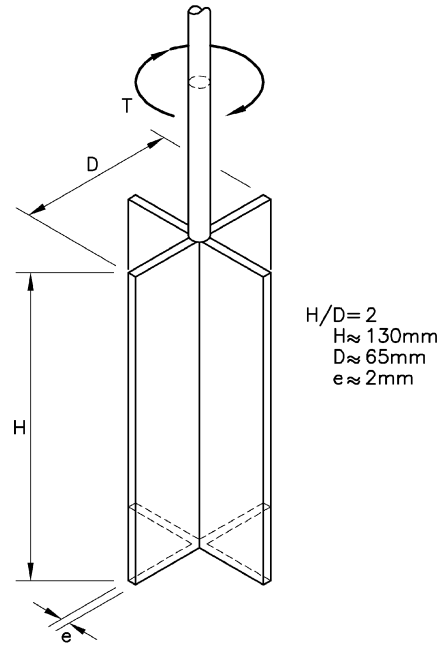


Figure 2.1: Typical dimensions of the field vane (after Chandler 1988).

coincide with material particles. Each element contains always the same amount of material and no convective effects are generated. In this case the resulting expressions are simple, but it is difficult to deal with large deformations. On the other hand, a Eulerian formulation considers the mesh as fixed and the particles just move through it. Now convective effects appear due to the relative movement between the grid and the particles, but it is possible to simulate large distortions. An ALE formulation reduces the drawbacks of the purely Lagrangian or Eulerian formulations, and it is appropriate when large deformations are expected. For this reason the method was first proposed for fluid problems with moving boundaries (Donéa et al. 1977, Huerta and Liu 1988) and has been used in this section to analyze the vane test. Following that approach, the material involved in the vane test has been simulated as a plastic incompressible fluid. That would take into account the large strains involved in the test. Also, the rate of rotation may be easily considered as velocities instead of displacements are the main variables. The fact that the vane test is more appropriate for very soft materials makes reasonable the analysis using a constitutive law for a plastic fluid. Applications of ALE to Geomechanics using classical elastoplastic constitutive laws for solids have been published elsewhere (van der Berg, Teunissen and Huetink 1994, Pijaudier-Cabot, Bodé and Huerta 1995, Rodríguez-Ferran et al. 1998).

In next subsection, the main characteristics of vane test are outlined, pointing out some of the drawbacks of the test that complicate its interpretation. Then a basic description of the theoretical constitutive laws used in this section is presented. Also the equations involved in the problem, taking into account the ALE formulation, are shown. A dimensionless formulation allows the definition of some combination of parameters that control the mathematical problem. These dimensionless numbers can explain the variability of vane results reported in some previous works. Then some applications to theoretical fluids and to real materials (soft clay and slurry red mud) are presented. These examples show a close dependency between amplitude of the strain localized zone, type of failure during the test, and constitutive models considered and are useful to clarify the interpretation of the vane test.

### 2.1.2 Main features of field vane test

There is a general agreement concerning the essential geometry of the vane. Figure 2.1 shows the main elements of the equipment and its usual dimensions (Chandler 1988). Although there are other configurations with different shapes and number of blades (Silvestri, Aubertin and

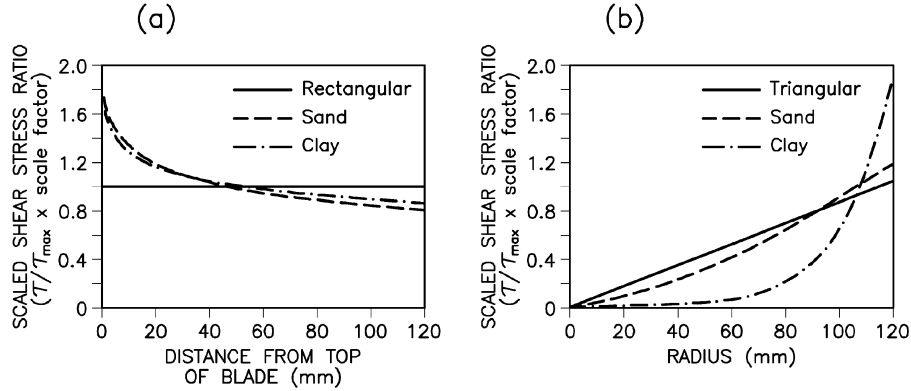


Figure 2.2: Measured stress distributions at vane blades (after Menzies and Merrifield 1980).

Chapuis 1993), the most popular one consists of four rectangular blades with a ratio  $H/D$  of 2:1. The test is performed by rotating the central rod (usually by hand) and measuring the torque applied. This produces a cylindrical shear surface on the soil, and therefore the maximum torque measured is related to the undrained shear strength of the material,  $s_u$ . Despite its simple use, the interpretation of the test is not always straightforward. A few shortcomings of the test have been reported during the last thirty years, mainly related to the stress distributions on the failure surfaces and to the influence of time on the results.

### Stress distributions

The distribution of stresses around the failure surface is not always uniform, although the usual expressions presented in the codes of practice to compute  $s_u$  from the torque assume that uniformity. Two causes have been reported as main origin of non-uniformity: soil anisotropy and progressive failure.

The total torque,  $T$ , is employed in creating a vertical cylindrical failure surface and, also, two horizontal failure surfaces in the top and the bottom of the material involved in the test. Thus  $T = T_v + T_h$ , where each term corresponds to the contribution of the torque from each failure surface. If the stress distribution is assumed constant in all surfaces then, by limit equilibrium, it is possible to evaluate

$$T_v = \frac{1}{2}\pi D^2 H s_u \quad \text{and} \quad T_h = \frac{1}{6}\pi D^3 s_u \quad (2.1.1)$$

where  $D$  and  $H$  are the diameter and the height of the vane respectively. If the maximum torque during the test,  $T$ , is measured, then, from (2.1.1)

$$s_u = \frac{T}{\pi \left[ \left( \frac{D^2 H}{2} \right) + \left( \frac{D^3}{6} \right) \right]}, \quad (2.1.2)$$

or for a vane of height equal to twice its diameter

$$s_u = \frac{T}{3.66 D^3} \quad \text{and} \quad \frac{T_h}{T_v} = \frac{1}{6}. \quad (2.1.3)$$

The stress distributions obtained from experiments or from numerical analyses are partly different from the assumptions above considered. For instance, figure 2.2 shows the stress distributions on the failure surfaces measured in the blades of an instrumented vane (Menzies and Merrifield 1980), and it may be seen that the distribution of shear stresses on the top is very different from the uniform assumption. Numerical results using an elastic constitutive law (Donald et al. 1977) already suggested a nonlinear distribution of stresses in the top of the vane (figure 2.3a). From these results Worth (1984) proposed a polynomial function to represent the shear stress distribution  $\tau = \tau(r)$  at the top and bottom surfaces, and therefore

$$\tau = s_u \left( \frac{r}{D/2} \right)^n \quad \text{and} \quad T_h = \frac{\pi D^3 s_u}{2(n+3)} \quad (2.1.4)$$

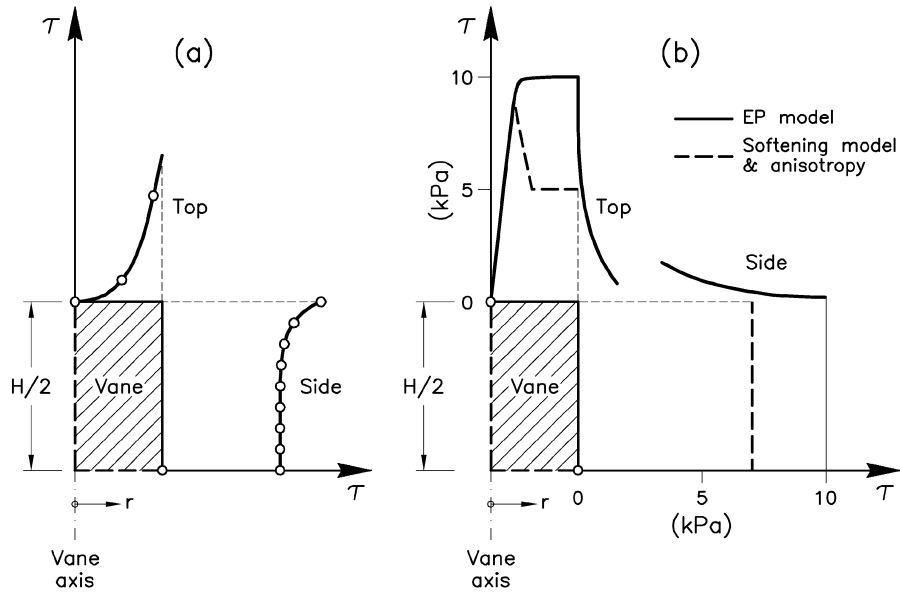


Figure 2.3: Shear stress distributions on sides and top of vane obtained from numerical simulations. a) Elastic model (after Donald et al. 1977) b) Using an elastoplastic model and a strain softening model including anisotropy (after Griffiths and Lane 1990).

where  $r$  is indicated in figure 2.3a. Worth suggested a value of  $n = 5$  for London clay, based on the results from Menzies and Merrifield (1980). For this value, the torque ratio becomes smaller:  $T_h/T_v = 1/16$ . Hence, the contribution of the horizontal failure surfaces to the total torque seems to be less significant in practice. That is, almost 94% of the resistance to torque is provided by the vertical failure surface. As a consequence of that, classical expressions to obtain  $s_u$  would underestimate the actual value of shear strength and that has been reported by some authors (Worth 1984, Eden and Law 1980).

Equation (2.1.4) is quite general as according to the value of  $n$  different stress distributions for the top and bottom of the vane can be considered. From that results it seems that a value about  $n = 5$  could be appropriate. However, some authors have confirmed recently values close to  $n = 0$  for different soils (Silvestri et al. 1993), which corresponds again to a uniform stress distribution. A finite element analysis presented by Griffiths and Lane (1990) confirms that for elastoplastic materials the shear stress can be close to a constant value on the top of the vane (figure 2.3b). They also showed an elastic analysis which is consistent with that presented by Donald et al. (1977). Therefore, the value of  $n$  will depend on the stress state reached on the top and bottom of the vane, and that is difficult to predict in advance. This conclusion assumes that soil is isotropic, which is not always the case. When the soil is anisotropic, the interpretation of the test becomes more difficult, as, for instance, maximum shear stress can be reached in the vertical surface whereas the situation on the top is still elastic. As the result used from the test is the peak of the curve torque–rotated angle, which is in fact an integral of all these stresses, it is difficult to distinguish all these effects from just one measured value. As the vane includes vertical and horizontal failure surfaces, some attempts have been made to identify anisotropy by means of vanes with different dimensions and shapes in order to estimate  $T_h$  and  $T_v$  separately (Aas 1965, Wiesel 1973, Donald et al. 1977). Bjerrum (1973) proposed a correction factor to account for the anisotropy that has been criticized in some cases (Garga and Khan 1994, Tanaka 1994).

When the soil is isotropic and is not strain softening, as the maximum shear strains are produced at  $r = R_v$ , where  $R_v$  is the vane radius, it is expected to reach the maximum shear stress at the vertical surface failure. If this value is kept constant, then plastification of the top and bottom vane will occur and the peak measured torque will correspond to a uniform distribution of shear stresses in all surfaces. However, if the soil has a strain softening constitutive law, the shear stress on the vertical failure will decrease and the peak torque will correspond to an intermediate situation and  $n > 0$ . Moreover, when strain softening occurs, the shear stress is not constant,

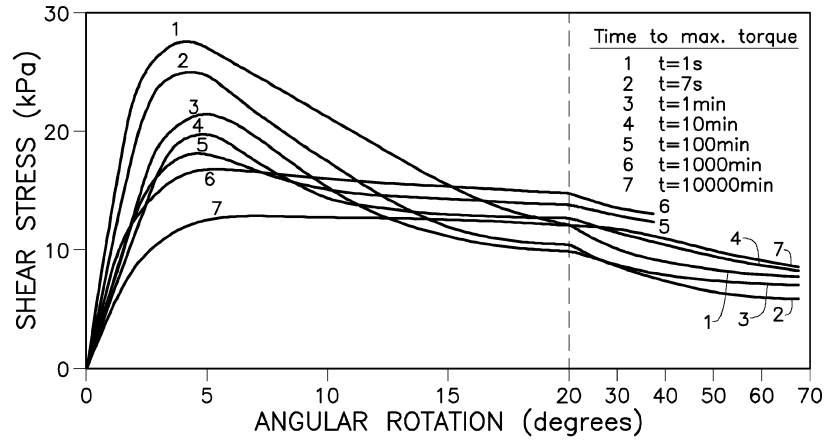


Figure 2.4: Shear stress–angular rotation obtained using different testing rates on Bäckebol clay, Sweden (after Torstensson 1977).

which makes the result of the vane test insufficient to estimate  $s_u$ . These arguments are consistent with the conclusions obtained by de Alencar et al. (1988) in a 2D numerical analysis. They simulated the vane using different strain softening constitutive laws (but all of them with the same peak shear strength). The torque–rotation curve was totally dependent on the constitutive law employed. Numerical simulations presented by Griffiths and Lane (1990) (figure 2.3b) present the same dependence. All those results showed the influence of progressive failure on the final interpretation of the test.

A consequence of all the works involved in the study of the interpretation of the vane is that the complete stress–strain curve of the material and its anisotropy must be known in advance in order to explain correctly the results of the test. However, for isotropic soft materials it seems to be an appropriate test, and the vertical failure surface would be predominant in that case.

### Time effects

The influence of time on the results of the test has two different aspects: the delay between insertion and rotation of vane, and the rate of vane rotation. The disturbance originated by the vane insertion and the consolidation following that insertion are difficult to predict in general. There are a few experimental studies about these effects. They suggest that in order to reduce the vane insertion effects, blade thickness related to vane size must be as small as possible (Rochelle, Roy and Tavenas 1973, Torstensson 1977). On the other hand, the delay on carrying out the test after vane insertion increases the measured shear strength, due to the dissipation of pore water pressures originated by the insertion and also due to thixotropic effects. This effect is usually not considered in vane analyses, but there is experimental evidence on the high pore pressure developed by vane insertion (Kimura and Saitoh 1983) and on the microstructural changes due to thixotropic phenomena (Osipov, Nikolaeva and Sokolov 1984). Results from Torstensson (1977) show that within five minutes after insertion measured shear strength does not change. It must be pointed out that both effects depend on the type of clay involved in the test (sensitivity, consolidation coefficient  $c_v$ , etc.). Fabric disturbance due to insertion reduces the true undrained strength in about 10%, but if consolidation after insertion is permitted a 20% increase on strength is produced (Chandler 1988). The standard vane test is usually performed 1 minute after the insertion of the blades, which is the maximum delay value suggested by Roy and Leblanc (1988). In that case, no consolidation is allowed.

The effect of the rate of vane rotation on the interpretation of the test is also important. The standard rate is 6 — 12°/minute. That produces failure in about 30 — 60 seconds, a shorter time than in classical triaxial tests or shear tests. Due to this difference, undrained strengths from vane tests are overestimated if compared with that obtained from classical laboratory tests. This effect can be compensated with the underestimation of  $s_u$  provided by other effects (fabric disturbance, stress uniformity,...), but their magnitude is difficult to estimate. As the vane is an undrained test,

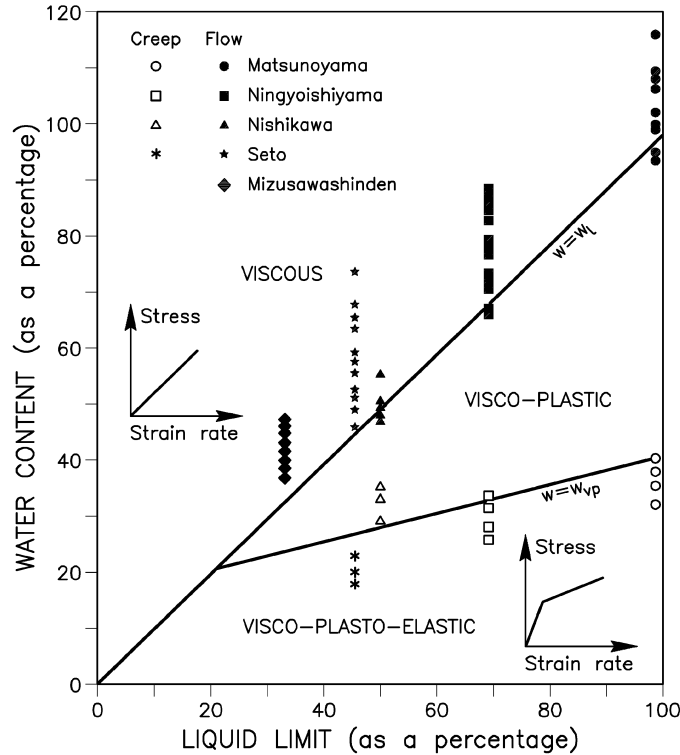


Figure 2.5: Rheological state of soil in accordance with water content for some Japanese clays (after Komamura and Huang 1974).

some recommendations regarding a minimum angular velocity are defined in the codes of practice. Assuming a time to failure of one minute, undrained conditions can be assured if the consolidation coefficient of the material is :  $c_v \leq 3.5 \cdot 10^{-2} \text{cm}^2/\text{s}$  (Chandler 1988), which is usually the case when soft clays are tested. However, as in other undrained tests, measured strength increases with the velocity of the load application and this effect leads to difficulties in the interpretation of results. To consider that, Bjerrum (1973) proposed a reduction of the shear strength measured with the vane according to the plasticity index of the clay, as the usual values of shear strength obtained in the laboratory correspond to slower experiments than field vane. Measurements of vane shear strength for different velocities of rotation have been published by Wiesel (1973) and Torstensson (1977). Both presented a potential expression between shear strength,  $s_u$ , and angular velocity,  $\omega$ , (or time to failure) from interpolation of their results

$$(s_u)_{vane} = k_1 \omega^{k_2} \quad (2.1.5)$$

where  $k_1$  and  $k_2$  are constants. The value of  $k_2$  ranged from 0.02 to 0.07. Figure 2.4 presents shear strength versus rotation angle for different durations of the test (Torstensson 1977).

The comparison of results from vanes of different shapes and different strain rates has been difficult as these effects are only related to the shear strength on the basis of empirical relations which may depend on the soil considered. A reference shear velocity:  $v = \omega R_v$  as a variable to compare results from different vanes was proposed by Perlow and Richards (1977). They obtained an almost linear relationship between vane shear strength and shear velocity  $v$  for two marine sediments, but they did not have enough experimental data to propose a definite relationship. In fact some results reported by other authors (Tanaka 1994), show no influence of the vane radius on the measured shear strength. These differences may be due to side effects as sampling disturbance or stress relief for soils used in laboratory vane tests, which would reduce the apparent shear strength (Kirkpatrick and Khan 1984). However, in general, that is taken into account when estimating  $s_u$ . This is still a controversial issue, and it will be considered later using the formulation presented in following sections.

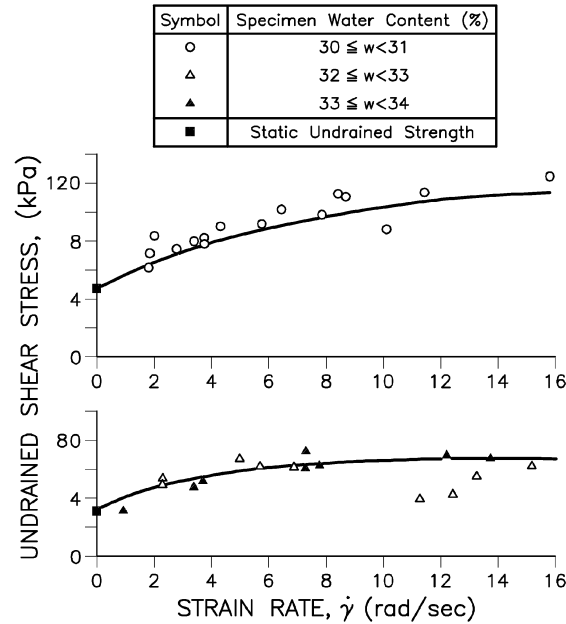


Figure 2.6: Effect of strain rate on undrained shear stress obtained using torsional hollow cylinder (after Cheng 1981).

The shortcomings presented have been extensively studied by many authors, but still there are contradictions on results and on interpretations of vane measurements. This is due to the fact that vane test is a model test rather than an element test (Morris and Williams 1993). Apart from that, other effects on vane strength have been rarely studied: for instance, influence of the stress state and  $K_0$  (coefficient of lateral earth pressure at rest) on the result (Law 1979, Garga and Khan 1994). As a consequence of the drawbacks above mentioned, the vane test seems indicated for very soft isotropic materials. Also the dominant failure surface is the vertical one. Therefore, it is reasonable to perform numerical simulations by means of two-dimensional analyses, in order to study rate effects and stress distributions. Hence the use of plastic fluid constitutive laws and fluid mechanics equations may be appropriate to analyze time effects and to deal with this soft isotropic materials. The disturbance due to vane insertion and the 3D effects of the test are not considered within this approach.

### 2.1.3 Constitutive laws

Soft materials have been successfully modelled by means of fluid constitutive laws to simulate classical geomechanics problems like landslides or debris flows (Vulliet and Hutter 1988, Rickenmann 1991, Gili, Huerta and Corominas 1993). The model is defined in terms of a shear stress–shear strain rate relationship, instead of a stress–strain one. The study of strain rate effects on soil behaviour has been considered in many works (Berre and Bjerrum 1973, Komamura and Huang 1974, Cheng 1981, Mesri, Febres-Cordero, Shields and Castro 1981, Leroueil, Kabbaj, Tavenas and Bouchard 1985). Some of them have proposed constitutive laws relating stresses with strains and strain rates to account for time influence, based on a visco–elasto–plastic theory. Bjerrum (1973) indicates that time effects in soft clays are associated with the cohesive component of the shear strength which is of a viscous nature; the frictional component of the shear strength would be further mobilized. Therefore it is not absurd to study the vane test assuming that the material involved is a plastic fluid, particularly at the beginning of the test, when viscous effects are definite. These effects depend on the type of clay considered, and plasticity index has been used historically to distinguish between different behaviours of normally consolidated clays. However, Tavenas and Leroueil (1980) propose to use the limit liquid instead, because it requires only a single test and in fact the resulting correlations are essentially the same.

Let us assume that the clay involved in the test is saturated and normally consolidated. When



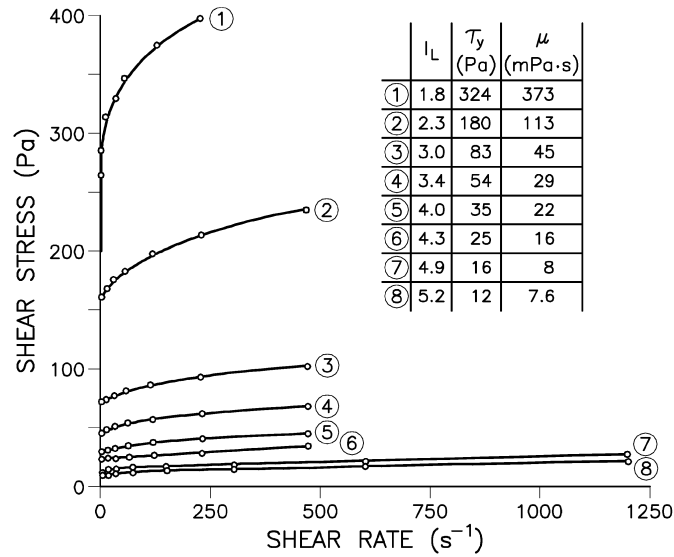


Figure 2.7: Shear stress–shear strain rate obtained from viscosimeter experiments. St. Alban–1 marine clay with a salt content of 0.2 g/l.  $\tau_y$  is yield stress,  $l_L$  is liquidity index and  $\mu$  is viscosity (after Locat and Demers 1988).

viscous effects are studied in detail, it is found that for a particular soil (that is for a particular liquid limit  $w_l$ ), the soil behaviour depends on the water content  $w$ , as shown in figure 2.5, from Komamura and Huang (1974). According to them, when  $w > w_l$  the behaviour is viscous, that is, close to a newtonian fluid; whereas when  $w < w_{vp}$  the behaviour is visco–elasto–plastic. The value  $w_{vp}$  was defined as viscoplastic limit, between plastic and liquid limits.

Results obtained in a torsional hollow cylinder are reproduced in figure 2.6, from Cheng (1981). The material was a Mississippi Buckshot clay with a water content close to its plastic limit. It may be seen that its behaviour is consistent with the trends established by Komamura and Huang (1974). However, further works have shown that some clays may have a visco–elasto–plastic behaviour with water content above their liquid limit (Bentley 1979, Torrance 1987, Locat and Demers 1988). Curves obtained by Locat and Demers (1988) using a viscosimeter device are presented in figure 2.7. Note, nevertheless, that the shear rate range is different for the results reproduced in figure 2.6 and for those indicated in figure 2.7. Some consequences of this difference will be treated later. The works indicated show that fluid constitutive laws for modelling the soil behaviour have been successfully employed to account for the time effects which are supposed to be important when water content is high, but it is difficult to establish a particular behaviour for each soil state in advance.

The general constitutive equation to be used in this work is a general relationship between stresses and strain rates:

$$\sigma_{ij} = f(d_{ij}) \quad (2.1.6)$$

where  $\sigma_{ij}$  is Cauchy's stress tensor and the strain rate tensor is defined as

$$d_{ij} = \frac{1}{2} \left( \frac{\partial v_i}{\partial x_j} + \frac{\partial v_j}{\partial x_i} \right) \quad (2.1.7)$$

where  $x_i$  and  $v_i$  are position and velocity vectors respectively. A common expression for equation (2.1.6) is:

$$\sigma_{ij} = -p\delta_{ij} + 2\mu d_{ij} \quad (2.1.8)$$

where  $p$  is the hydrostatic pressure (tension positive) and  $\mu$  is the dynamic viscosity. Equation (2.1.8) can be rewritten as

$$\sigma_{ij}^d = 2\mu d_{ij} \quad (2.1.9)$$

where  $\sigma_{ij}^d$  is the deviatoric stress tensor. When viscosity is assumed constant, the fluid is called newtonian. A generalized newtonian fluid is defined by a viscosity which depends on the strain

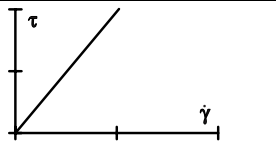
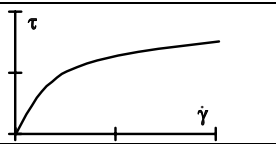
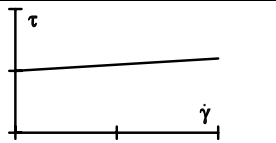
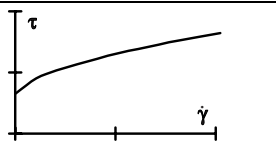
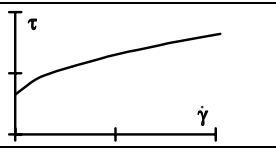
Newtonian	$\mu = \mu_0$	
Carreau	$\mu = (\mu_0 - \mu_\infty)(1 + (\lambda\dot{\gamma})^2)^{(n-1)/2} + \mu_\infty$	
Bingham	$\mu = \infty$ if $\tau \leq \tau_0$ $\mu = \mu_p + \tau_0/\dot{\gamma}$ if $\tau > \tau_0$	
Herschel–Bulkley	$\mu = \infty$ if $\tau \leq \tau_0$ $\mu = \mu_p \dot{\gamma}^{n-1} + \tau_0/\dot{\gamma}$ if $\tau > \tau_0$	
Casson	$\mu = \infty$ if $\tau \leq \tau_0$ $\sqrt{\mu} = \sqrt{\mu_p} + \sqrt{\tau_0/\dot{\gamma}}$ if $\tau > \tau_0$	

Table 2.1: Some generalized Newtonian fluid models defined in terms of viscosity.  $\tau = \sqrt{\sigma_{ij}^d \sigma_{ij}^d}/2$  and  $\dot{\gamma} = \sqrt{2d_{ij}d_{ij}}$ . A simplified 1D representation of the models is included. (After Huerta and Liu 1988).

rate tensor. Also, some plastic fluids show a “yield stress”, that is, below that value no flow is observed, which is equivalent to an infinite viscosity in terms of equation (2.1.9). However, some authors (Barnes and Walters 1985) indicate that the yield stress does not exist, provided that accurate measurements are performed. That is, “yield stress” is just an idealization of the actual behaviour.

Table 2.1 shows a list of constitutive laws available for fluids (Huerta and Liu 1988). From that list, the models by Bingham, Casson and Herschel and Bulkley seem to be most appropriate for soft materials. Those models simulate a “yield stress” value up to which no velocities or displacements occur. According to the yield stress magnitude, it is possible to reproduce effects observed in the actual behaviour of soft materials. For instance, the amplitude of the strain localized zone, the influence of the progressive failure or the brittleness of the material are supposed to be determined by the constitutive law used and specially by the existence of the “yield stress”. The fluid models indicated above are consistent with experimental results like the ones depicted in figures 2.6 and 2.7, and they will be used as constitutive laws in this simulation. However, any relation between stresses and strain rates could be implemented in the formulation.

## 2.1.4 Basic equations and ALE formulation

### Basic equations

Fluid movement is described by two basic equations: mass conservation equation and equilibrium equation. These equations are, respectively:

$$\frac{\partial \rho}{\partial t} + \rho \frac{\partial v_i}{\partial x_i} = 0 \quad \text{in } \Omega, \quad (2.1.10a)$$

$$\rho \frac{\partial v_i}{\partial t} + \rho c_j \frac{\partial v_i}{\partial x_j} = \rho b_i + \frac{\partial \sigma_{ji}}{\partial x_j} \quad \text{in } \Omega, \quad (2.1.10b)$$

	$\rho$ Kg/m <sup>3</sup>	$R^*$ m	$\tau^*$ Pa	$\omega^*$ s <sup>-1</sup>	$N_1$	$\min(N_2)$
Red Mud	1200	0.013	126	0.01	1.6E-7	2.E-2
	1200	0.013	126	0.21	7.1E-5	2.E-2
Soft Clay	1400	0.0325	2000	0.0017	2.1E-9	4.E-2
	1400	0.0325	2000	0.0035	9.1E-9	4.E-2
	1400	0.0325	2000	0.0070	3.6E-8	4.E-2

Table 2.2: Numerical values of  $N_1$  and  $N_2$  for different materials, vane sizes and angular velocities.

where  $\rho$  is the density of the material,  $t$  is time,  $c_j = \hat{v}_j - v_j$  where  $\hat{v}_j$  is the velocity of the reference system,  $b_i$  is the mass forces vector and  $\Omega$  is the domain of study. Also, repeated index means summation.

As incompressible flow is assumed, density is constant and expression (2.1.10a) leads to  $\text{div} v = 0$  which is equivalent to the undrained condition assumed in the standard field vane test. Introducing this result and the constitutive law presented above in (2.1.10b) gives

$$\rho \frac{\partial v_i}{\partial t} + \rho c_j \frac{\partial v_i}{\partial x_j} = \rho b_i - \frac{\partial p}{\partial x_i} + \frac{\partial}{\partial x_j} \left( \mu[\dot{\gamma}] \left( \frac{\partial v_i}{\partial x_j} + \frac{\partial v_j}{\partial x_i} \right) \right) \quad \text{in } \Omega \quad (2.1.11)$$

where  $\mu[\dot{\gamma}]$  is the dynamic viscosity, function of the shear strain rate,  $\dot{\gamma} = \sqrt{2d_{ij}d_{ij}}$ .

The boundary conditions applied are  $v_x = v_y = 0$  at the outer boundary and  $v_x = \omega r \sin(\theta_o + \omega t)$  and  $v_y = -\omega r \cos(\theta_o + \omega t)$  at the blade contours, with  $\omega$  the angular velocity of the vane and  $(r, \theta_o)$  the polar coordinates of the blade nodes at  $t = 0$ . The initial stresses and velocities are considered zero in all the points and in the boundaries.

In order to find out the parameters that govern the problem, a set of dimensionless variables

$$\bar{x} = x/R^*, \quad \bar{p} = p/\tau^*, \quad \bar{v} = v/R^*\omega^* \quad \text{and} \quad \bar{t} = t\omega^* \quad (2.1.12)$$

is substituted in equation (2.1.11), where  $R^*$ ,  $\tau^*$ ,  $\omega^*$  are characteristic length, stress and angular velocity of the test respectively. Usually, the vane radius,  $R_v$ , is adopted for  $R^*$ , the angular velocity of the test for  $\omega^*$ , and the material yield stress for  $\tau^*$ . Then equation (2.1.11) is transformed into a dimensionless expression:

$$\frac{1}{Ne} \left( \frac{\partial \bar{v}_i}{\partial \bar{t}} + \bar{c}_j \frac{\partial \bar{v}_i}{\partial \bar{x}_j} \right) = - \frac{\partial \bar{p}}{\partial \bar{x}_i} + \frac{\partial}{\partial \bar{x}_j} \left( \frac{1}{NeRe} [\dot{\gamma}] \left( \frac{\partial \bar{v}_i}{\partial \bar{x}_j} + \frac{\partial \bar{v}_j}{\partial \bar{x}_i} \right) \right) \quad \text{in } \Omega \quad (2.1.13)$$

with  $Re$  and  $Ne$  equal to Reynolds and Newton numbers. The Reynolds number is related to viscous forces and the Newton one to inertial forces. They are defined as

$$Ne = \frac{\tau^*}{\rho(R^*\omega^*)^2} \quad \text{and} \quad Re = \frac{\rho\omega^*(R^*)^2}{\mu}. \quad (2.1.14)$$

The influence of  $Re$  and  $Ne$  in equation (2.1.13) is in the form of

$$N_1 = \frac{1}{Ne} = \rho \frac{(R^*\omega^*)^2}{\tau^*} \quad \text{and} \quad N_2[\dot{\gamma}] = \frac{1}{NeRe} [\dot{\gamma}] = \mu[\dot{\gamma}] \frac{\omega^*}{\tau^*}, \quad (2.1.15)$$

and their characteristic values for some typical vane tests are shown in table 2.2. As  $N_1$  is much less than  $N_2$  and accelerations usually are not large enough to compensate this difference, the inertial terms can be neglected and the problem becomes quasistatic. In these cases the problem depends just on  $N_2$ , and therefore the test will be independent of the vane radius or the fluid density. The use of those dimensionless numbers may be useful when comparing different vanes, and they will be considered later to account for size and time effects.

### Computational aspects

The finite element mesh employed in the analyses is shown in figure 2.8. The mesh has 1492 elements and 1576 nodes, it is composed of 4 node-elements and increases the density of elements

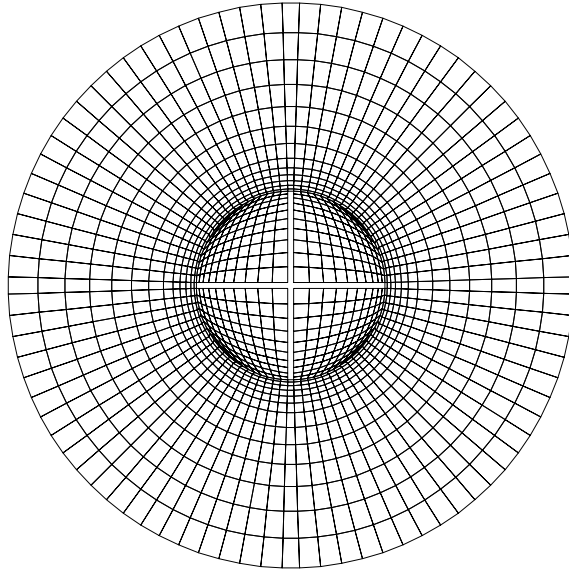


Figure 2.8: Finite element mesh used in the analyses of the vane test, with a dimensionless vane radius of 1.

in the expected failure zone. Note that elements inside the vane failure circle have basically a rigid solid movement so a coarse mesh can be adopted there. Plane strain conditions were adopted in the simulations.

An Arbitrary Lagrangian–Eulerian (ALE) description was used for the resolution of the problem. ALE formulation has been employed to avoid the disadvantages of pure Eulerian or pure Lagrangian descriptions. If an Eulerian description is used, the mesh is fixed. That is easy to formulate, but makes difficult imposing the boundary conditions at the vane blades. On the other hand if a Lagrangian description is adopted, the nodes will follow the particle movements and mesh distortions will arise. ALE formulation can be interpreted as a combination of both descriptions: the mesh is rotated at the same velocity as the vane blades, so the soil particles have an Eulerian description; whereas the boundary is defined in Lagrangian terms, as the mesh follows the boundaries during the test. Therefore the velocities of any node of the mesh are

$$\hat{v}_x = \omega r \sin(\theta_o + \omega t) \quad \text{and} \quad \hat{v}_y = -\omega r \cos(\theta_o + \omega t) \quad (2.1.16)$$

where the symbol  $\hat{\cdot}$  stands for mesh prescriptions. Mesh displacements are found by integrating mesh velocities.

As a predictor–corrector algorithm is used in the numerical formulation, unknowns for time  $t$  are computed from values at time  $t - \Delta t$  simulating the transient problem. Similarly to any transient problem starting from rest, boundary conditions (in this case the angular velocity of the blade) can not be discontinuous, i.e. a finite jump from zero to an imposed angular velocity which would induce an unphysical infinite angular acceleration. Therefore, a smooth variation of the angular velocity has been used. Thus, angular acceleration is always finite and becomes zero after a few time increments. As the problem is quasistatic, the acceleration is not important for the final torque, which depends mainly on the steady state value of the angular velocity reached.

As the simulation is performed by applying an angular velocity, the torque must be computed as a result of the analysis. One possibility is to estimate the torque from pressures acting on the vane blades, but in a mixed pressure–velocity formulation, the accuracy for the pressure is one order lower than the velocity. Thus, it is preferable to use an approach based on the evaluation of the power input; as the Finite Element Method is an energy based formulation. The power input,  $P_{\text{input}}$ , is the sum of two domain integrals; the first is the material time derivative of the kinetic energy of the system, while the second takes into account the variation of the internal energy:

$$P_{\text{input}} = \frac{d}{dt} \int_{\Omega} \frac{1}{2} \rho v_i v_i d\Omega + \int_{\Omega} \sigma_{ij} d_{ij} d\Omega . \quad (2.1.17)$$

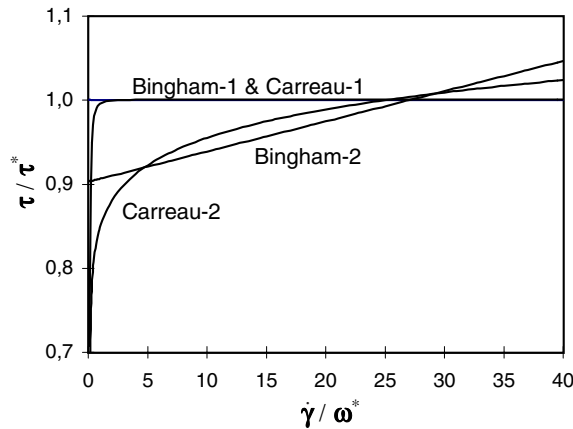


Figure 2.9: Dimensionless shear stress versus dimensionless shear strain rate for the theoretical constitutive laws.

The first term can be neglected because the vane test is quasistatic and the second one is obtained by summation of the element contributions:

$$P_{\text{input}} = T\omega \approx \sum_{i=1}^{n_{\text{elem}}} \tau_i \dot{\gamma}_i S_i \quad (2.1.18)$$

where  $n_{\text{elem}}$  is the number of elements and  $S_i$  the corresponding area for each element of the mesh. Note that in (2.1.18) only shear strain rates are used, as the problem has been considered incompressible. Finally, the torque applied,  $T$ , is directly obtained from that expression.

### 2.1.5 Analyses using theoretical constitutive laws

Simulations using dimensionless Bingham and Carreau models are presented in order to analyze the influence of “yield stress” in strain rate distribution. The four dimensionless constitutive laws depicted in figure 2.9 have been considered. These models are similar within the range considered. However, there are two main differences between them: models–1 have mainly a horizontal relation between shear stress and shear strain rate and models–2 do not, and Bingham models have a well defined “yield stress”, whereas Carreau models do not. The distribution of shear strain rates and shear stresses obtained in the simulations are represented in figure 2.10(a–c) (Bingham–1, Bingham–2 and Carreau–2). The shear strain rate and the particle velocity distribution over a line at  $45^\circ$  between blades, are depicted in figure 2.11. The torque actually applied while performing the test is presented, in dimensionless form, in figure 2.12. Also, table 2.3 presents some numerical values corresponding to these examples.

Note that models–1 give almost the same results, and so do models–2. The main difference between both is the more definite failure surface produced by models–1. Indeed, figure 2.10(a) shows a well defined failure surface and close to a circle of unit radius, which corresponds to the vane radius in dimensionless form. Also the amplitude of the shear strain rate localization zone is very small, and the material between blades has almost a rigid solid movement, evident in figure 2.11 where the velocity distribution in the material in a intermediate plane ( $\theta = 45^\circ$ ) is almost  $v = \omega r$ , as in the blades. On the other hand models–2 have a wider shear strain rate localization zone, although it still could be considered a circular failure surface. It has been verified that models with a plateau in the  $\tau$  vs.  $\dot{\gamma}$  constitutive law have a more definite and narrower localization zone. The differences between Bingham and Carreau models are similar but less important than between models–1 and models–2. Apart from that, Carreau models tend to present a wider shear strain rate localization zone and a less homogeneous distribution of velocities around failure surface than Bingham models.

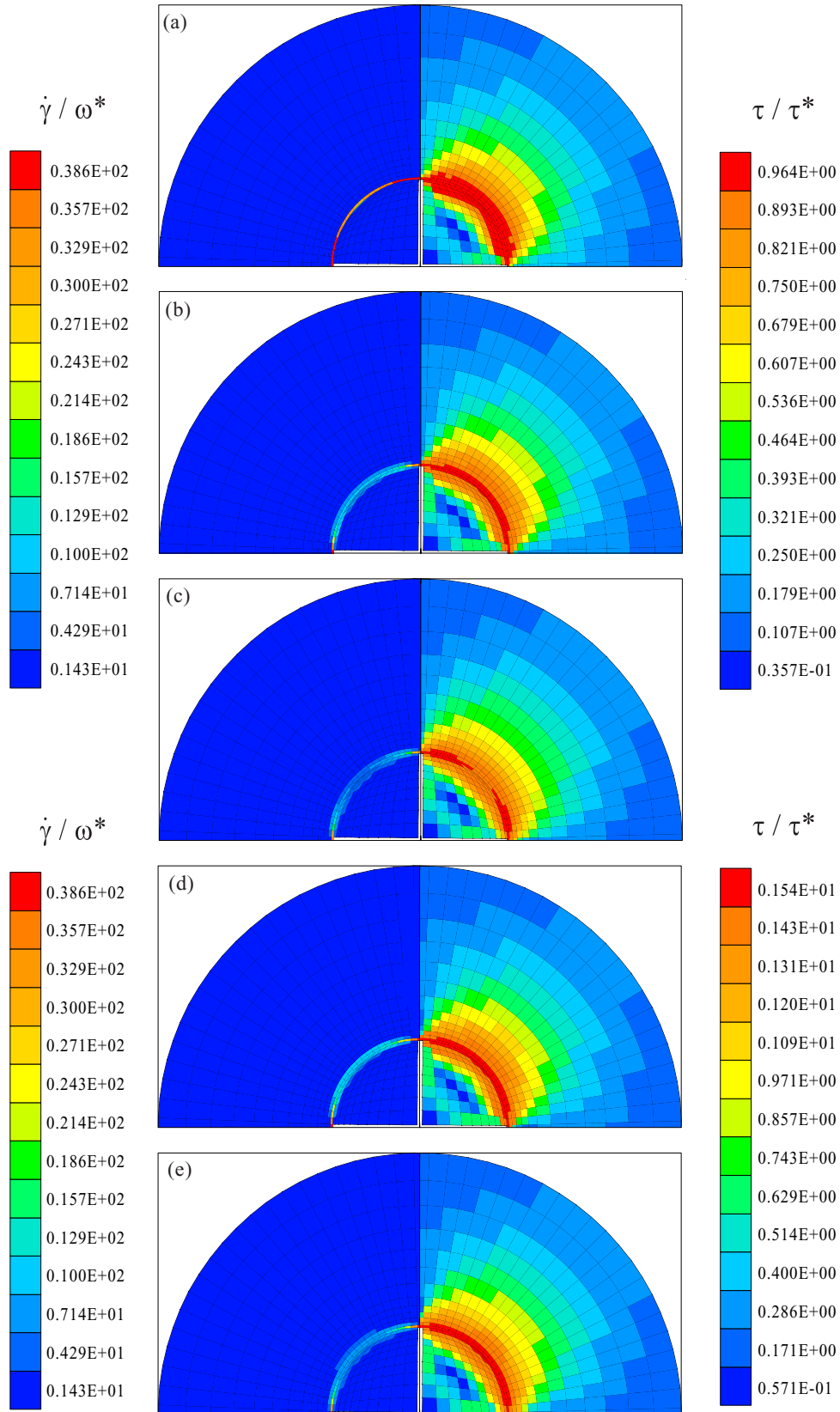


Figure 2.10: Shear strain rate and shear stress distributions using: (a–c) the theoretical constitutive laws: (a) Bingham–1, (b) Bingham–2 and (c) Carreau–2; and (d–e) the soft clay constitutive laws: (d) Bingham and (e) Logarithmic.

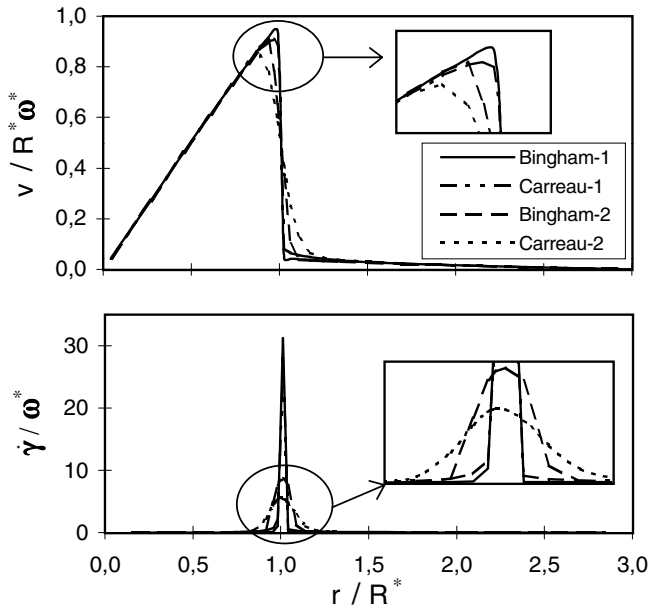


Figure 2.11: Dimensionless velocity and shear strain rate between blades using theoretical constitutive laws.

	Bingham-1	Carreau-1	Bingham-2	Carreau-2
$\max_{\theta=0^\circ}(v/R^*\omega^*)$	1.00	1.00	1.00	1.00
$\max_{\theta=45^\circ}(v/R^*\omega^*)$	0.95	0.91	0.91	0.78
$r/R^* \mid \max_{\theta=45^\circ}(v/R^*\omega^*)$	0.97	0.97	0.94	0.94
$\max_{\theta=0^\circ}(\dot{\gamma}/\omega^*)$	39.39	38.74	37.90	35.38
$\max_{\theta=45^\circ}(\dot{\gamma}/\omega^*)$	31.25	28.04	8.58	5.53
$r/R^* \mid \max_{\theta=45^\circ}(\dot{\gamma}/\omega^*)$	1.01	1.01	1.01	1.00
$\max_{\theta=0^\circ}(\tau/\tau^*)$	1.00	1.00	1.04	1.02
$\max_{\theta=45^\circ}(\tau/\tau^*)$	1.00	1.00	0.93	0.93
$r/R^* \mid \max_{\theta=45^\circ}(\tau/\tau^*)$	0.95 — 1.01	1.00 — 1.01	1.01	1.00
$T/\tau^*(R^*)^2$	6.44	6.44	6.15	6.11

Table 2.3: Numerical values of the analyses of the vane test using theoretical constitutive laws.

It should be pointed out that the radius where the maximum shear stress is produced in a intermediate plane ( $\theta = 45^\circ$ ) is almost the same in all the examples (table 2.3). At the blade planes, the maximum value of shear stress is obviously produced at  $r = 1$ . Therefore the value adopted in classical formulations that consider the failure surface constant at  $r = 1$  seems reasonable. However some authors have reported failure surfaces at  $r = 1.05 R_v$  based on experimental observations (in Arvida clay—sensitive and overconsolidated, Roy and Leblanc (1988)), and even higher values (but in fibrous peat whose fibers extend the failure zone, Landva (1980)). That should be dependent on the material involved in the test so the result obtained in this simulation could only apply for soft clays.

On the other hand, the shear strain rate is not constant on the failure surface, even if the Bingham-1 model is used, where dimensionless  $\dot{\gamma}$  varies from 31.3 at  $\theta = 45^\circ$  to 39.4 at  $\theta = 0^\circ$ . This pattern is more pronounced when a wider shear strain rate localization zone is formed: when the Carreau-2 model is used dimensionless  $\dot{\gamma}$  varies from 5.5 to 35.4 at the failure surface. Nevertheless the usual assumption that shear strength is constant on the failure surface is quite correct because usually a wide range of  $\dot{\gamma}$  has a narrow range of  $\tau$ . Models-2 simulations have a maximum difference of 10% in  $\tau$  at the failure surface (table 2.3).

Note that in figure 2.9, constitutive laws are expressed in a dimensionless form, by means of angular velocity  $\omega^*$ . Thus for different values of  $\omega^*$ , different responses of shear strength are

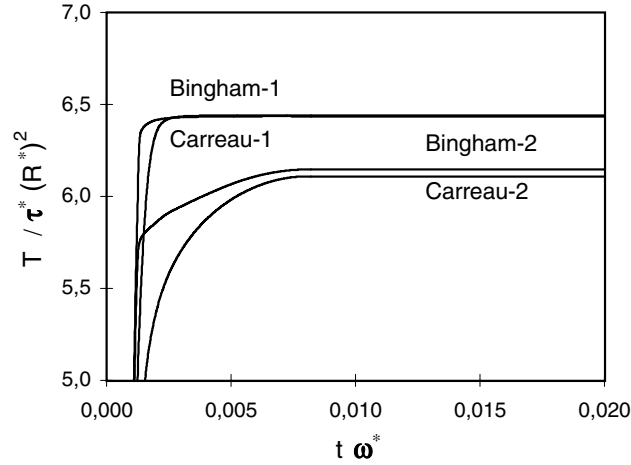


Figure 2.12: Dimensionless torque versus dimensionless time for the theoretical laws.

	Bingham	Casson	H-B
$\max_{\theta=0^\circ} (v/R^* \omega^*)$	1.00	1.00	1.00
$\max_{\theta=45^\circ} (v/R^* \omega^*)$	0.95	0.92	0.88
$r/R^* \mid \max_{\theta=45^\circ} (v/R^* \omega^*)$	0.97	0.94	0.89
$\max_{\theta=0^\circ} (\dot{\gamma}/\omega^*)$	39.33	38.67	37.32
$\max_{\theta=45^\circ} (\dot{\gamma}/\omega^*)$	26.84	11.09	6.63
$r/R^* \mid \max_{\theta=45^\circ} (\dot{\gamma}/\omega^*)$	1.01	1.01	1.01
$\max_{\theta=0^\circ} (\tau/\tau^*)$	1.01	1.17	0.84
$\max_{\theta=45^\circ} (\tau/\tau^*)$	1.01	1.13	0.75
$r/R^* \mid \max_{\theta=45^\circ} (\tau/\tau^*)$	1.01	1.01	1.01
$T/\tau^* (R^*)^2$	6.51	7.37	4.96

Table 2.4: Numerical values of the analyses of the vane test applied to Red Mud.

obtained, unless the type-1 model is used. If material behaviour depends on  $\omega^*$ , a type-2 model constitutive law should be expected, whereas a behaviour independent of  $\omega^*$  is typical of type-1 models. That is, independence of  $s_u$  from  $\omega$  indicates that shear stress is constant in the range of shear strain rate applied. Note that this behaviour could change for other strain rate ranges, as in triaxial or viscosimeters tests.

### 2.1.6 Application to real materials

Numerical simulation of vane test using constitutive laws estimated for actual materials has also been performed. Two materials have been considered: a slurry waste material called red mud and a soft clay. Both require the definition of a relationship between shear stress and shear strain rate, in order to use the above formulation.

#### Red mud

This material has been extensively studied by Nguyen and Boger (1985). It is a material produced in the extraction process of aluminium from bauxite. It consists of a mixture of oxides dissolved in a plastic liquid which shows some special characteristics like tixotropy (links between particles broken due to the flow), yield stress and non constant viscosity. A particular red mud formed by a concentration of 37.3% of titanium oxide is simulated. Vane result and viscosimeter experimental values corresponding to that red mud are reported by Nguyen and Boger (1985). Vane tests performed with vane radius equal to 1.3 cm and angular velocity equal to 0.1 cycles/min gave  $(s_u)_{vane}$  of 126 Pa. Viscosimeter experimental data and least square approximation by means of three different constitutive models are presented in figure 2.13. The models used are Bingham, Casson and Herschel-Bulkley.



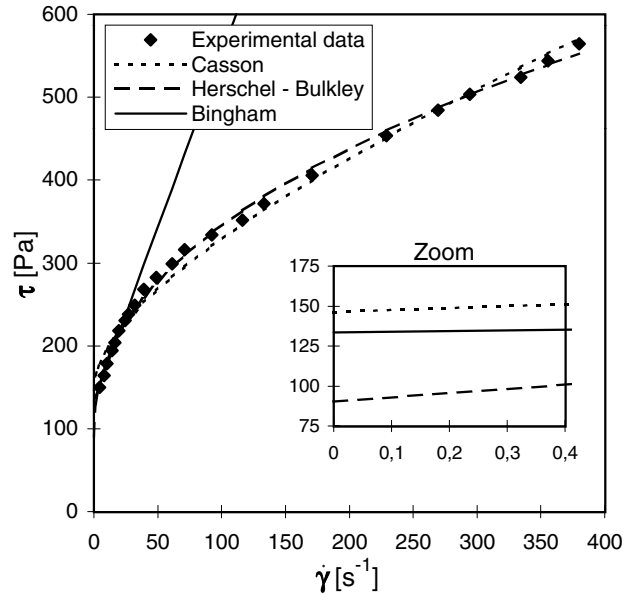


Figure 2.13: Shear stress [Pa] versus shear strain rate [ $\text{s}^{-1}$ ] for the Red Mud constitutive laws.

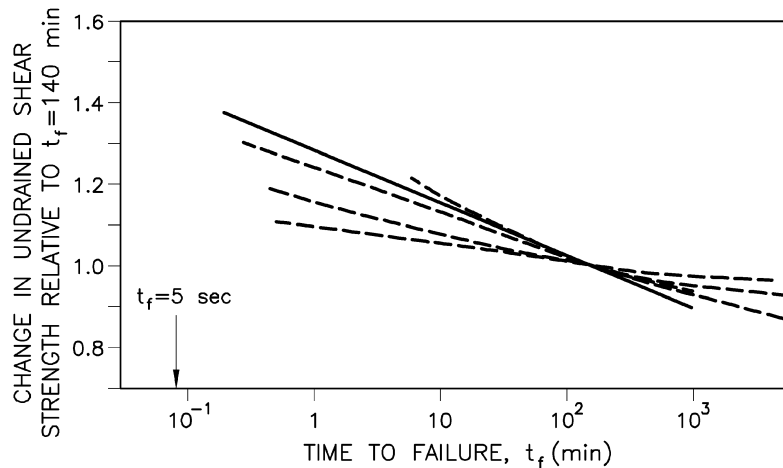


Figure 2.14: Summary of undrained rate effects in isotropically consolidated soils of different composition (after Lacasse 1979). Continuous line corresponds to the case analyzed in numerical simulations.

Table 2.4 shows some numerical results of the analyses in order to compare the models employed (with  $R^* = 1.3$  cm,  $\omega^* = 0.1$  cycles/min and  $\tau^* = 133.5$  Pa). Note that again  $r = 1.01$  is the radius at which the maximum shear strain rate and shear strength is produced irrespective of the model used. The applied torque values are very different. The reason for that is the range of shear strain rate mobilized during the test: 0 to 40 (dimensionless values) which correspond to  $\dot{\gamma} = 0$  to  $0.42$   $\text{s}^{-1}$ . In the zoom of figure 2.13, the different stress level for this range of  $\dot{\gamma}$  is clearly highlighted. That zoom shows that a correct interpolation must be used to perform a correct analysis.

The value of  $(s_u)_{vane}$  calculated with Bingham model simulations, 136 Pa, is quite similar to  $(s_u)_{vane}$  measured by Nguyen and Boger (1985), 126 Pa. Note that Bingham model has been approximated from experimental viscosimeter data at low shear strain rate, but still 10 times larger than the shear strain rate mobilized in the vane test. In general, extrapolation of experimental values from viscosimeters must be used carefully because the range applied in a vane test is very small when compared to that of a viscosimeter.

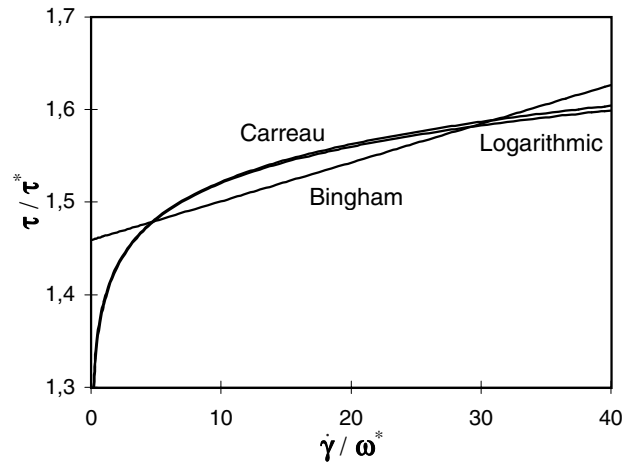


Figure 2.15: Dimensionless shear stress versus dimensionless shear strain rate for the soft clay constitutive laws.

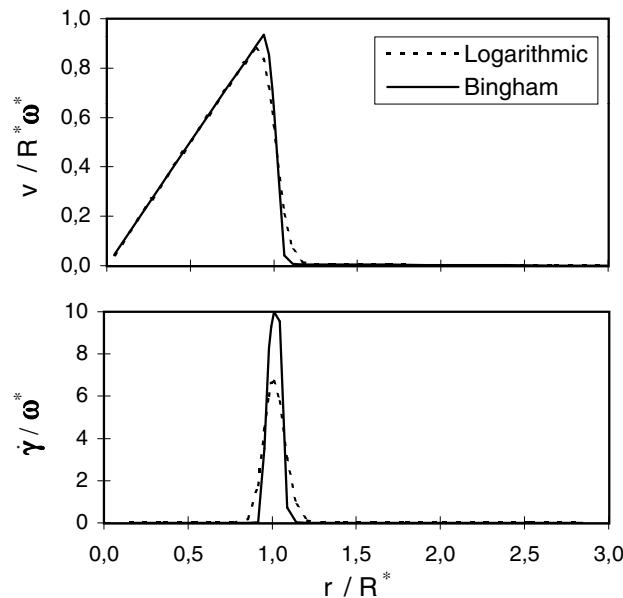


Figure 2.16: Dimensionless velocity and shear strain rate between blades using soft clay constitutive laws.

### Soft Clay

Soft clays have been extensively studied also by many researchers, but usually a soil mechanics point of view has been employed to define their behaviour. As a consequence of that, constitutive laws suggested for soft clays are presented usually in terms of a stress–strain relationship instead of a stress–strain rate one, even for clays with a high liquidity index. Most of the studies have been carried out using the conventional triaxial test, which can take from a few minutes to one or two hours. Hence rate effects are expected to be less important than in the vane test, where failure is reached in about one minute. Nevertheless, experimental results obtained in viscosimeters have also been published (figures 2.5 and 2.7), although its shear strain range is different from that used in the vane.

In order to obtain a general form of a shear stress–strain rate relationship, information about duration of triaxial tests and rate effects has been used (Torstensson 1977, Lacasse 1979, Hight, Jardine and Gens 1987). A logarithmic relation between shear stress and time to failure has been proposed by many researchers. Typical curves from Lacasse (1979) are presented in figure 2.14.

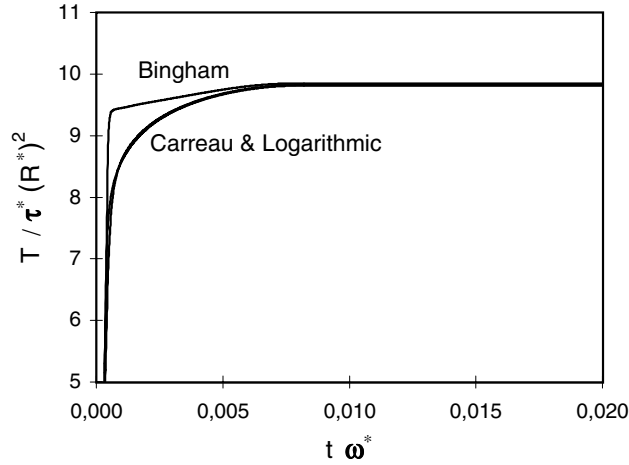


Figure 2.17: Dimensionless torque versus dimensionless time for the soft clay constitutive laws.

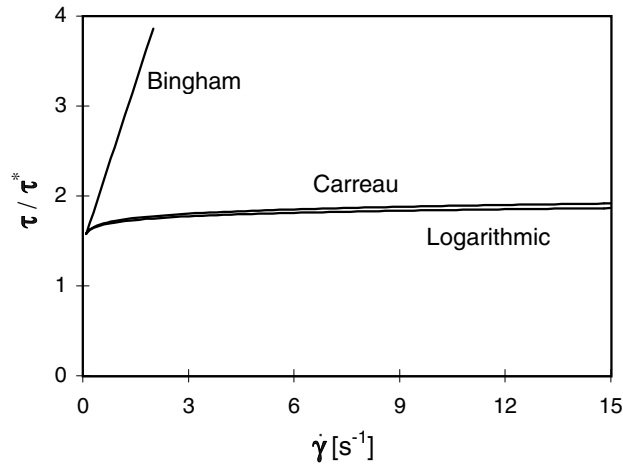


Figure 2.18: Dimensionless shear stress versus shear strain rate (1/s) for the soft clay constitutive laws.

Using strain rate as main variable, this relationship may be expressed as

$$\tau / \tau_r = a \log(\dot{\gamma} / \dot{\gamma}_r) + b, \quad (2.1.19)$$

where  $\tau_r$  is the failure shear strength at reference time,  $\dot{\gamma}_r$  is the failure strain rate at same reference time and  $a, b$  are constants. If the test is performed at a constant strain rate,  $\dot{\gamma}_r$  can be computed from the ratio shear deformation at failure vs. time to failure. Equation (2.1.19) shows the effect of increase in shear strength when the test is faster, which is a known behaviour for soft clays.

From the curves of figure 2.14, a clay with the following constitutive law has been considered (assuming the reference time equal to 140 min and a 3% of the failure shear deformation at that time):

$$\text{Logarithmic model : } \tau / \tau^* = 0.13 \log(\dot{\gamma} / \omega^*) + 1.39, \quad (2.1.20a)$$

where  $\tau^*$  is a shear strength reference value and  $\omega^*$  the rotation velocity that has been fixed to  $12^\circ/\text{min}$ . Also a Bingham and a Carreau models have been considered interpolating the Logarithmic one in the interval  $\dot{\gamma} / \omega^* \in [0.1, 40]$ :

$$\text{Bingham model : } \tau / \tau^* = 1.46 + 0.0042 \dot{\gamma} / \omega^*, \quad (2.1.20b)$$

$$\text{Carreau model : } \mu \omega^* / \tau^* = 100 \left( 1 + 7200 (\dot{\gamma} / \omega^*)^2 \right)^{-0.48}. \quad (2.1.20c)$$

	Logarithmic	Carreau	Bingham
$\max_{\theta=0^\circ}(v/R^*\omega^*)$	1.00	1.00	1.00
$\max_{\theta=45^\circ}(v/R^*\omega^*)$	0.88	0.88	0.94
$r/R^* \mid \max_{\theta=45^\circ}(v/R^*\omega^*)$	0.89	0.89	0.94
$\max_{\theta=0^\circ}(\dot{\gamma}/\omega^*)$	38.39	38.34	39.84
$\max_{\theta=45^\circ}(\dot{\gamma}/\omega^*)$	6.70	6.73	10.00
$r/R^* \mid \max_{\theta=45^\circ}(\dot{\gamma}/\omega^*)$	1.01	1.01	1.01
$\max_{\theta=0^\circ}(\tau/\tau^*)$	1.60	1.60	1.63
$\max_{\theta=45^\circ}(\tau/\tau^*)$	1.50	1.50	1.50
$r/R^* \mid \max_{\theta=45^\circ}(\tau/\tau^*)$	1.01	1.01	1.01
$T/\tau^*(R^*)^2$	9.81	9.82	9.85

Table 2.5: Numerical values of the analyses of the vane test applied to soft clay.

As in previous sections, Bingham and Logarithmic models have been approximated with a initial dimensionless viscosity of 100, to avoid infinite viscosity values. Figure 2.15 shows the shear strain–strain rate curves corresponding to these models. Note that the Carreau model interpolates so well the Logarithmic model that no difference can be observed over the interesting interval.

The results obtained with these models are represented in figures 2.10(d–e), 2.16 and 2.17, and they are compared in table 2.5. As could be expected, Logarithmic and Carreau results are exactly the same, and the shear strain localized zone originated using the Logarithmic and Carreau models is slightly wider than the one obtained with the Bingham model. However, the value of the radius at which maximum shear strain rate occurs in an intermediate plane is again 1.01 for all the models. Calculated torques are the same for the three models, so the  $(s_u)_{vane}$  associated to the simulations will be also the same. Nevertheless if these laws are extrapolated to other strain rate ranges, the predicted behaviour could be very different, as shown in figure 2.16.

After comparing experimental results (figures 2.6 and 2.7) with figure 2.18, it must be pointed out that Bingham models must be used with caution. It is very important to choose the correct range of applicability when one desires to approximate the actual behaviour of soft clays by Bingham models. However Carreau and Logarithmic models seem to capture better the changing scale between the results of vane test and viscosimeter ones. Therefore, Carreau and Logarithmic models seem to give continuity from the results of the triaxial undrained tests to that obtained from viscometers.

### 2.1.7 Size and time effects

The dimensionless numbers defined in (2.1.15) are very useful to analyze the factors that influence the results of the test. For instance, size effects that have traditionally been considered from an empirical point of view, can be studied in a more objective manner with this approach. A relationship between vane shear strength and shear velocity computed as  $v = \omega R_v$  was depicted from experimental results by Perlow and Richards (1977). However, that result was based on just few data, and it was not definite. In fact, other authors (Tanaka 1994) have reported completely different results. Based on many laboratory small vane tests and field vane tests on Japanese clays, they did not find any substantial difference between vane sizes, when the same angular velocity,  $\omega$ , was used.

In fact, according to (2.1.15) the mathematical problem is controlled by  $N_2 = \mu\omega^*/\tau^*$ , as  $N_1$  is usually very small. Thus the problem does not depend on the vane size, but on the rotation velocity, the yield stress and the viscosity. For a particular soil,  $\omega$  is the fundamental parameter. That applies for soft materials for which the constitutive laws used are reasonable. And it is confirmed by experimental evidence, as the results presented by Tanaka (1994). An attempt has also been made to use the formulation presented above to reproduce the effect of vane rotation (and therefore the time to failure) on the shear strength provided by the vane.

If different rotation velocities are used in the simulation, a relationship similar to equation (2.1.5) is expected to be found. Figure 2.19 presents the results obtained using two models employed previously (Bingham and Logarithmic). If the computed torque is expressed as

$$(s_u)_{vane}/\tau^* = k_1\omega^{k_2}, \quad (2.1.21)$$

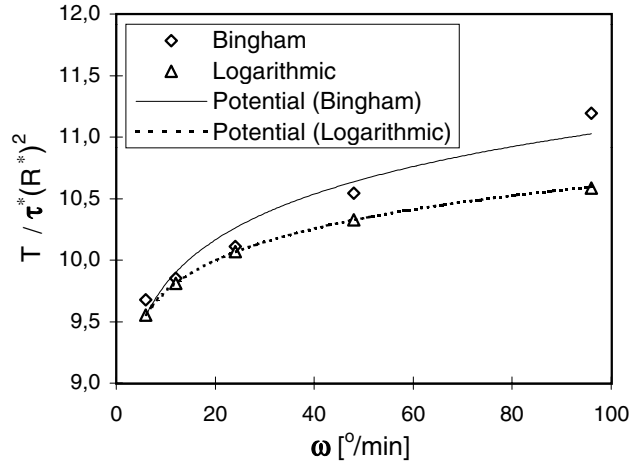


Figure 2.19: Simulation results and potential interpolation of relationship between dimensionless torque and angular velocity ( $^\circ/\text{min}$ ) for different soft clay constitutive laws.

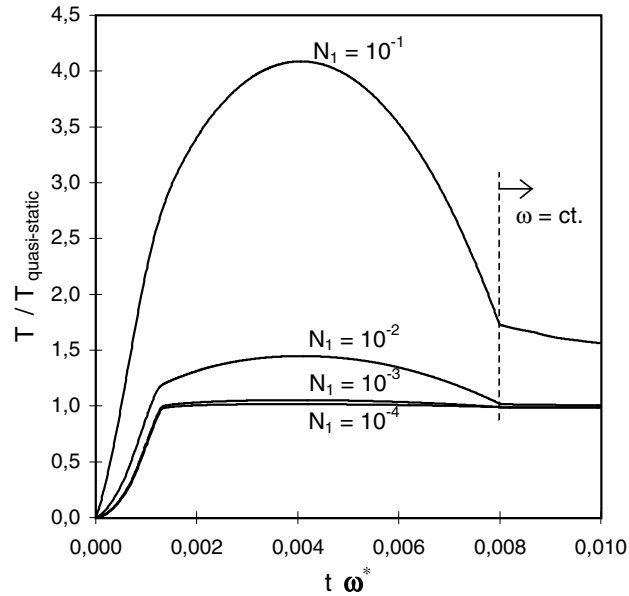


Figure 2.20: Dimensionless torque versus dimensionless time for different inertial forces, using Bingham-1 model.

the values obtained for Bingham model are

$$(k_1)_{\text{Bin}} = 1.358 \quad \text{and} \quad (k_2)_{\text{Bin}} = 0.052, \quad \text{with} \quad r^2 = 0.95, \quad (2.1.22a)$$

where  $r^2$  is the correlation coefficient, and for Logarithmic model are

$$(k_1)_{\text{Log}} = 1.395 \quad \text{and} \quad (k_2)_{\text{Log}} = 0.037, \quad \text{with} \quad r^2 = 0.99. \quad (2.1.22b)$$

These values are consistent with the experimental ones provided Wiesel (1973) and Torstensson (1977) indicated in equation (2.1.5). In particular, Logarithmic model seems to be specially designed to approximate experimental relationships expressed as equation (2.1.21). Therefore, time effects seem to be simulated correctly by means of this model based on fluid mechanics principles. This was expected as those effects were measured on soft clays where viscous phenomena are supposed to be important.

In conventional vane tests, viscous forces dominate inertial ones, and the problem depends on  $N_2$  (equation 2.1.15). When a fluid constitutive law is used, the torque increases with time up to a

limit value, as in figure 2.17. It is not possible to reproduce a peak in the torque–time curve in this way, unless inertial forces become important. For usual vane velocities, this is not the case, but some measurements at high velocities have also been reported in the literature (Torstensson 1977). Figure 2.20 shows the effect of inertial forces on the shape of the torque–time curve, in terms of  $N_1$  dimensionless value, using the Bingham–1 model from figure 2.9. Thus, even for that model, at high rotation velocities, inertial effects produce a peak on that curve. This is consistent with the measurements presented in figure 2.4 (Torstensson 1977), where the peak of the curve torque–rotation (or time) is more pronounced when the test is faster, as inertial forces become more important. For the normal velocity range however, a Bingham model can not produce such a peak, and an explanation in terms of softening of the material could be appropriate.

### 2.1.8 Concluding remarks

A simulation of the vane test using an Arbitrary Lagrangian–Eulerian formulation and appropriate for soft clays has been presented. As the dominant failure surface is the vertical one, a 2D analysis has been useful enough to study stress distributions. Also, the use of fluid mechanics principles and fluid mechanics constitutive laws have permitted the characterization of time effects in a natural manner, as velocities instead of displacements are the main variables.

The mathematical problem is governed by two dimensionless numbers. They are related to inertial forces (Newton number) and to viscous forces (Reynolds number). Two tests performed with vanes of different sizes and different rotation velocities, can only be compared by means of these numbers. In most cases, at a typical angular velocity and with usual vane dimensions, the problem becomes quasistatic and independent from inertial forces. Thus in this case, the problem is independent from vane radius and density, and it is controlled by the value of  $N_2 = \mu\omega^*/\tau^*$  ( $\mu$ : viscosity,  $\omega^*$ : rotation velocity,  $\tau^*$ : characteristic yield stress). Therefore, rotation velocity should be used as main variable to compare different vanes tested on the same soil, provided that the assumptions considered apply (i.e. when 2D conditions are predominant and soft materials are tested).

For soft clays and usual vane conditions, the simulated torque is always increasing with time. Thus a peak in the curve torque–time should be related to other effects as strain softening of the material tested. However, if rotation velocity is increased, inertial effects become more important, and a peak in that curve is always obtained.

Stress and strain rate distributions on the failure surface depend on the constitutive laws adopted for the material, as stated in previous works. However, the position of the failure surface (where maximum shear stresses are developed) has been found to be always at 1. to 1.01 times the vane radius.

Differences around 10% have been found in the shear stress distribution along the failure surface, depending on the material model. Also, amplitude of the shear band is related to that: Bingham models tend to produce more definite shear bands. On the other hand, a yield stress is clearly obtained when results of the vane test are independent of its rotation velocity. That is, when shear stress is constant irrespective of the shear strain rate reached in the test.

To compare triaxial, vane and viscosimeters results, it is necessary to take into account the different shear strain rate mobilized in each test. The same model will give different strengths in each case. Carreau and Logarithmic models seem to reproduce well that change of scale.

Also, the effect of rotation velocity in shear strength has been simulated using this approach. In fact, shear strength increase associated to rotation velocity increase is directly related to the increment of shear strength due to shear strain increments. The experimental relation between these variables that has been reported in the literature, has been reproduced by means of this approach. Thus time effects, defined in terms of rotation velocity (or time to failure), have been studied in this manner.

Finally, it can be concluded that the use of a fluid mechanics approach has proved to be appropriate for the interpretation of this test when soft materials are involved.

## 2.2 Arbitrary Lagrangian–Eulerian formulation for hyperelastoplasticity

The Arbitrary Lagrangian–Eulerian (ALE) description in nonlinear solid mechanics is nowadays standard for hypoelastic–plastic models. An extension to hyperelastic–plastic models is presented here. A fractional–step method—a common choice in ALE analysis—is employed for time–marching: every time–step is split into a Lagrangian phase, which accounts for material effects, and a convection phase, where the relative motion between the material and the finite element mesh is considered. In contrast to previous ALE formulations of hyperelasticity or hyperelastoplasticity, the deformed configuration at the beginning of the time–step, not the initial undeformed configuration, is chosen as the reference configuration. As a consequence, convecting variables is required in the description of the elastic response. This is not the case in previous formulations, where only the plastic response contains convection terms. In exchange for the extra convective terms, however, the proposed ALE approach has a major advantage: only the quality of the mesh in the spatial domain must be ensured by the ALE remeshing strategy; in previous formulations, it is also necessary to keep the distortion of the mesh in the material domain under control. Thus the full potential of the ALE description as an adaptive technique can be exploited here. These aspects are illustrated in detail by means of three numerical examples: a necking test, a coining test and a powder compaction test.

### 2.2.1 Introduction

The Arbitrary Lagrangian–Eulerian (ALE) formulation is a standard approach in large–strain solid mechanics to keep mesh distortion and element entanglement under control (Liu et al. 1986, Benson 1986, Huétink et al. 1990, Ghosh and Kikuchi 1991, Huerta and Casadei 1994, Rodríguez-Ferran et al. 1998). The basic idea of the ALE formulation is the use of a referential domain for the description of motion, different from the material domain (Lagrangian description) and the spatial domain (Eulerian description). When compared to fluid dynamics, where the ALE formulation originated (see Donea 1983 and references therein), the main difficulty of ALE solid mechanics is the path–dependent behaviour of plasticity models. The relative motion between the mesh and the material must be accounted for in the treatment of the constitutive equation.

Two approaches may be used to describe large (elastic and inelastic) strains. In hypoelastic–plastic models (Bonet and Wood 1997, Simo and Hughes 1998, Belytschko et al. 2000), the evolution of stresses is expressed in rate format, relating an objective stress rate with a rate of deformation. In hyperelastic–plastic models (Bonet and Wood 1997, Simo and Hughes 1998, Simo 1998, Belytschko et al. 2000), on the contrary, there is no rate equation for stresses: they can be computed from the deformation gradient via direct functional evaluation of the free energy function. However, the plastic response is still described in rate form, involving the Lie derivative.

Various formulations for large–strain solid mechanics which combine an ALE kinematic description and hypoelastic–plastic models can be found in the literature (Liu et al. 1986, Benson 1986, Huétink et al. 1990, Ghosh and Kikuchi 1991, Huerta and Casadei 1994, Rodríguez-Ferran et al. 1998). In all of them, a key issue is the ALE convective term in the rate equation for stresses, which reflects the relative motion between the mesh and the material. The most popular approach to deal with this convective term is the use of a split or fractional–step method. Each time–step is divided into a material phase and a convection phase. Convection is neglected in the material phase, which is thus identical to a time–step in a standard Lagrangian analysis. After that, stresses and plastic internal variables are transported to account for the relative mesh–material motion in the convection phase.

On the other hand, ALE formulations for hyperelastoplasticity are not standard. In the context of incompressible hyperelasticity (i.e. no plastic strains), Yamada and Kikuchi (1993) propose an ALE finite element method with no need of convecting variables. The basic idea is that the referential, material and spatial domains are linked by appropriate mappings, so the deformation gradient that relates the spatial and material domains (and hence the stresses) can be computed from the referential domain simply by applying the chain rule. However, as discussed later, the price to pay for this coupled, convection–free approach is high: the distortion must be controlled in *two* mappings (referential to material and referential to spatial), rather than only one.

If large plastic strains are also considered, convection of the internal plastic variables is needed, because a convective term appears in the rate equations describing the plastic response (Armero and Love 2000).

To summarize: using the total deformation gradient (from the current deformed configuration to the initial undeformed configuration) to describe the hyperelastic response (Yamada and Kikuchi 1993, Armero and Love 2000) leads to an algorithm with the attractive property that no variables must be convected. It has, however, two major shortcomings: (1) it forces ALE remeshing to prevent distortion in two mappings, instead of only one, and (2) it cannot be extended into a convection-free algorithm for ALE hyperelastoplasticity, because convection of plastic variables is still needed for the plastic response.

For this reason, a different ALE formulation for hyperelastoplasticity is proposed here. It is very similar to the split ALE formulations for hypoelastoplasticity discussed above. The hyperelastic response is described by means of the incremental deformation gradient (relating the deformed configurations before and after the time-step) rather than the total deformation gradient. In fact, the last converged deformed configuration, rather than the initial undeformed configuration, is used as a reference. As a consequence, elastic strains must be transported during the convection step. In exchange for this, ALE remeshing must prevent distortion in only one mapping (from the referential to the spatial domains). Thus, the full potential of the ALE formulation as an  $r$ -adaptive technique (Huerta et al. 1999) can be exploited.

The general case of non-isochoric plasticity is considered in this section. This means that the volume change (i.e. the determinant of the deformation gradient) cannot be computed solely from the elastic strains, so it must also be convected. Thus, the following information must be transported: elastic strains, plastic internal variables and volume change.

An outline of paper follows. Finite-strain multiplicative plasticity in a standard ALE setting is briefly reviewed in subsection 2.2.2. The proposed extension to an ALE setting is presented in subsection 2.2.3, and illustrated by means of some representative numerical examples in subsection 2.2.4. Finally, subsection 2.2.5 contains some concluding remarks.

## 2.2.2 Multiplicative finite-strain plasticity in a Lagrangian setting

This subsection contains a very brief review of multiplicative finite-strain plasticity with a Lagrangian description. Only the basic ingredients which are later needed in subsection 2.2.3 are discussed. Detailed presentations of  $\mathbf{F}^e \mathbf{F}^p$  plasticity can be found in the textbooks of Simo and Hughes (1998), Simo (1998) and Belytschko et al. (2000).

Let  $R_X \subset \mathbb{R}^{n_{\text{dim}}}$  ( $n_{\text{dim}} = 2, 3$ ) be the material configuration of a continuum body with particles labelled by their initial position vector  $\mathbf{X} \in R_X$ . The motion of the body is described by the one-parameter family of mappings  $\varphi_t : R_X \mapsto \mathbb{R}^{n_{\text{dim}}}$  with  $t \in [0, T]$ .  $R_x = \varphi_t(R_X)$  is the spatial configuration of the body at time  $t$ , and  $\mathbf{x} = \varphi_t(\mathbf{X}) = \varphi(\mathbf{X}, t) \in R_x$  is the current position of the material particle  $\mathbf{X}$ . In a Lagrangian setting,  $\mathbf{X}$  are used as the independent variables in the description of motion. The fundamental unknown is the field of particle displacements  $\mathbf{u}$ :

$$\mathbf{u}(\mathbf{X}, t) = \mathbf{x}(\mathbf{X}, t) - \mathbf{X}. \quad (2.2.1)$$

The deformation gradient is defined as

$$\mathbf{F}(\mathbf{X}, t) = \frac{\partial \varphi}{\partial \mathbf{X}}(\mathbf{X}, t) \quad (2.2.2)$$

and it is locally decomposed into elastic and plastic parts as

$$\mathbf{F} = \mathbf{F}^e \mathbf{F}^p. \quad (2.2.3)$$

Uncoupled isotropic hyperelastic behaviour is assumed, with the local thermodynamic state defined by means of the elastic left Cauchy–Green tensor

$$\mathbf{b}^e = \mathbf{F}^e \mathbf{F}^{eT} \quad (2.2.4)$$

and a set of strain-like scalar internal variables  $\mathbf{p} \in \mathbb{R}^{n_p}$  (the superscript  $T$  means transpose). In this situation, the Kirchhoff stress tensor,  $\boldsymbol{\tau}$ , and the stress-like internal variables,  $\mathbf{q}$ , conjugate to



$\mathbf{p}$ , are given by

$$\boldsymbol{\tau} = 2 \frac{dW^e}{d\mathbf{b}^e} \mathbf{b}^e \quad \text{and} \quad \mathbf{q} = - \frac{dW^p}{d\mathbf{p}}, \quad (2.2.5)$$

where  $W^e$  and  $W^p$  are the elastic and plastic parts of the free energy function

$$W(\mathbf{b}^e, \mathbf{p}) = W^e(\mathbf{b}^e) + W^p(\mathbf{p}). \quad (2.2.6)$$

The Cauchy stress tensor  $\boldsymbol{\sigma}$  is given by

$$\boldsymbol{\sigma} = \frac{\boldsymbol{\tau}}{\det(\mathbf{F})} \quad (2.2.7)$$

In equation (2.2.7),  $\det(\mathbf{F})$  accounts for the volume change. For isochoric plasticity (i.e. no plastic volume change),  $\det(\mathbf{F}^p) = 1$  together with equations (2.2.3) and (2.2.4) result in  $\det(\mathbf{F}) = \sqrt{\det(\mathbf{b}^e)}$ . For the general case of non-isochoric plasticity considered here, on the contrary, this equation does not hold.

The material time derivative of  $\det(\mathbf{F})$  is given by the general relationship

$$\frac{\partial |\mathbf{F}|}{\partial t} \Big|_{\mathbf{X}} = |\mathbf{F}| \nabla_{\mathbf{x}} \cdot \mathbf{v}, \quad (2.2.8)$$

where, following standard notation,  $|\cdot|_{\mathbf{X}}$  means ‘‘holding the material particle  $\mathbf{X}$  fixed’’,  $\nabla_{\mathbf{x}} \cdot \mathbf{v}$  is the divergence of the particle velocity  $\mathbf{v}$  and  $|\cdot|$  denotes the determinant.

*Remark 2.2.1.* In a standard Lagrangian analysis,  $\det(\mathbf{F})$  is typically *not* updated via direct numerical time-integration of equation (2.2.8). This rate equation will be useful in the next section to discuss the treatment of volume change in an ALE setting.  $\square$

The plastic response of the material is assumed isotropic and defined by a yield function  $f$ ,

$$f(\boldsymbol{\tau}, \mathbf{q}) = 0 \quad (2.2.9)$$

and the generic flow rule

$$\mathcal{L}_{\mathbf{v}} \mathbf{b}^e = -2\dot{\gamma} \mathbf{m}_{\boldsymbol{\tau}}(\boldsymbol{\tau}, \mathbf{q}) \mathbf{b}^e \quad \text{and} \quad \dot{\mathbf{p}} = \dot{\gamma} \mathbf{m}_{\mathbf{q}}(\boldsymbol{\tau}, \mathbf{q}), \quad (2.2.10)$$

where  $\mathcal{L}_{\mathbf{v}}$  is the Lie derivative with respect to the particle velocity  $\mathbf{v}$ , which involves the velocity gradient  $\mathbf{l}$ ,

$$\mathcal{L}_{\mathbf{v}} \mathbf{b}^e = \dot{\mathbf{b}}^e - \mathbf{l} \mathbf{b}^e - \mathbf{b}^e \mathbf{l}^T, \quad (2.2.11)$$

$\mathbf{m}_{\boldsymbol{\tau}}$  and  $\mathbf{m}_{\mathbf{q}}$  are the flow directions and  $\dot{\gamma}$  is the plastic multiplier, determined with the classical Kuhn–Tucker conditions. The superposed dot denotes material time derivative (that is, holding fixed the material particle  $\mathbf{X}$ ). Associated plasticity is defined by the choice

$$\mathbf{m}_{\boldsymbol{\tau}} = \frac{\partial f}{\partial \boldsymbol{\tau}} \quad \text{and} \quad \mathbf{m}_{\mathbf{q}} = \frac{\partial f}{\partial \mathbf{q}}. \quad (2.2.12)$$

### 2.2.3 Multiplicative finite-strain plasticity in an ALE setting

The hyperelastic–plastic model of the previous section is reformulated here in an ALE setting. First, some preliminaries on ALE kinematics are briefly reviewed and after that, the proposed ALE approach for hyperelastoplasticity is presented.

#### ALE kinematics

The key ingredient of the ALE formulation is the referential configuration  $R_{\chi}$ , with grid (or reference) points  $\chi$  used as independent variables to describe body motion. This referential configuration  $R_{\chi}$  is mapped into the material and spatial configurations by  $\boldsymbol{\Psi}$  and  $\boldsymbol{\Phi}$  respectively, see figure 2.21:

$$\mathbf{X} = \boldsymbol{\Psi}(\chi, t) \quad (2.2.13)$$

and

$$\mathbf{x} = \boldsymbol{\Phi}(\chi, t) \quad (2.2.14)$$

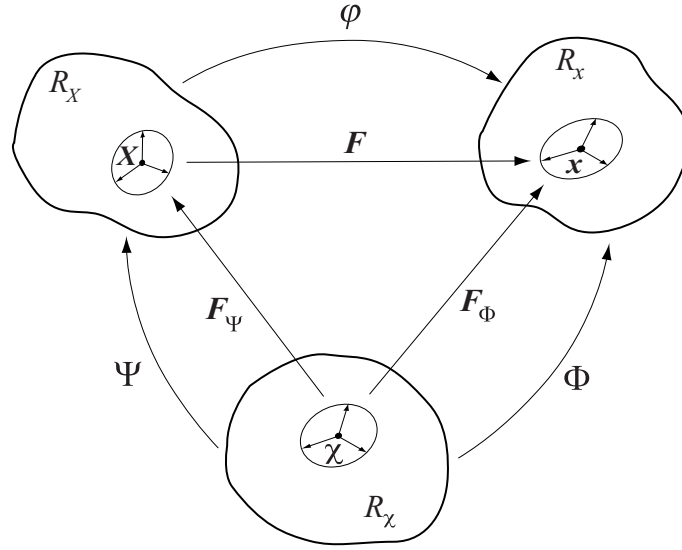


Figure 2.21: Domains, mappings and deformation gradients in the ALE description

with the corresponding deformation gradients

$$\mathbf{F}_\Psi(\chi, t) = \frac{\partial \Psi}{\partial \chi}(\chi, t) \quad \text{and} \quad \mathbf{F}_\Phi(\chi, t) = \frac{\partial \Phi}{\partial \chi}(\chi, t) \quad (2.2.15)$$

The three mappings  $\varphi$ ,  $\Phi$  and  $\Psi$  are related by

$$\varphi = \Phi \circ \Psi^{-1}. \quad (2.2.16)$$

Direct application of the chain rule to equation (2.2.16) leads to the relation between the three deformation gradients defined in equations (2.2.2) and (2.2.15):

$$\mathbf{F} = \mathbf{F}_\Phi \mathbf{F}_\Psi^{-1} \quad (2.2.17)$$

In an ALE setting, two displacement fields can be defined on the referential configuration: the material displacement  $\mathbf{u}_\Psi$

$$\mathbf{u}_\Psi(\chi, t) = \mathbf{X}(\chi, t) - \chi \quad (2.2.18)$$

and the spatial displacement  $\mathbf{u}_\Phi$

$$\mathbf{u}_\Phi(\chi, t) = \mathbf{x}(\chi, t) - \chi \quad (2.2.19)$$

These two displacement fields describe how the material particles and the spatial points respectively move with respect to the grid points.

*Remark 2.2.2.* In general, the three displacement fields ( $\mathbf{u}$ ,  $\mathbf{u}_\Psi$  and  $\mathbf{u}_\Phi$ ) are different. Note that *material* displacements are defined according to equation (2.2.18), so the notation *particle* displacements is used to refer to the “real” (i.e. physically meaningful) displacements, equation (2.2.1).  $\square$

### The proposed ALE approach

For expository purposes, the proposed ALE approach is first presented for hyperelasticity and later extended to hyperelastoplasticity.

**Hyperelasticity** As discussed in the introduction, large elastic strains can be handled in an ALE context with no need of convecting variables (Yamada and Kikuchi 1993, Armero and Love 2000). In every time-step  $[^n t, {}^{n+1} t]$ , the fundamental unknowns are the increment of material

displacements  ${}^{n+1}\Delta\mathbf{u}_\Psi$  and the increment of spatial displacements  ${}^{n+1}\Delta\mathbf{u}_\Phi$ . Material and spatial coordinates,  $\mathbf{X}$  and  $\mathbf{x}$ , are updated according to

$${}^{n+1}\mathbf{X}(\boldsymbol{\chi}) = {}^n\mathbf{X}(\boldsymbol{\chi}) + {}^{n+1}\Delta\mathbf{u}_\Psi(\boldsymbol{\chi}) \quad (2.2.20)$$

and

$${}^{n+1}\mathbf{x}(\boldsymbol{\chi}) = {}^n\mathbf{x}(\boldsymbol{\chi}) + {}^{n+1}\Delta\mathbf{u}_\Phi(\boldsymbol{\chi}). \quad (2.2.21)$$

After that, the deformation gradients  ${}^{n+1}\mathbf{F}_\Psi$  and  ${}^{n+1}\mathbf{F}_\Phi$  can be computed, equations (2.2.13) and (2.2.14), and used to compute the total deformation gradient  ${}^{n+1}\mathbf{F}$ , equation (2.2.17), which is the basic ingredient to compute the stresses, equations (2.2.3)–(2.2.5).

The main advantage of this approach is that it leads naturally to a coupled ALE formulation with no need for convection algorithms. The spatial and material configurations,  $R_x$  and  $R_X$ , are linked via the referential configuration  $R_\chi$ , and this allows the computation of  $\mathbf{F}$ .

However, there is also a major drawback: it is essential to avoid element distortion or entanglement in *two* mappings:  $\Psi$  and  $\Phi$ . If not, gradients  $\mathbf{F}_\Psi$  and/or  $\mathbf{F}_\Phi$  cannot be properly computed. This is rather cumbersome and limits the potential of the ALE approach as an *r*-adaptive technique.

For this reason, a different approach is proposed here: the two fundamental unknowns in every time–step are the increment of spatial (or mesh) displacements  ${}^{n+1}\Delta\mathbf{u}_\Phi$ , equation (2.2.21), and the increment of particle displacements  ${}^{n+1}\Delta\mathbf{u}$ ,

$${}^{n+1}\Delta\mathbf{u}({}^n\mathbf{X}(\boldsymbol{\chi})) = {}^{n+1}\mathbf{x}({}^n\mathbf{X}(\boldsymbol{\chi})) - {}^n\mathbf{x}({}^n\mathbf{X}(\boldsymbol{\chi})) \quad (2.2.22)$$

which is referred to the particles  ${}^n\mathbf{X}$  associated to grid points  $\boldsymbol{\chi}$  at the beginning of the time–step,  ${}^n\mathbf{X} = \mathbf{X}(\boldsymbol{\chi}, {}^nt)$ . The difference between these two increments is the so–called increment of convective displacements  ${}^{n+1}\Delta\mathbf{u}_{\text{conv}}$ ,

$${}^{n+1}\Delta\mathbf{u}_{\text{conv}}(\boldsymbol{\chi}) = {}^{n+1}\Delta\mathbf{u}(\boldsymbol{\chi}) - {}^{n+1}\Delta\mathbf{u}_\Phi(\boldsymbol{\chi}), \quad (2.2.23)$$

which represents the relative motion between particles and grid points during the time–step.

In contrast to the previous approach, the increment of material displacements  ${}^{n+1}\Delta\mathbf{u}_\Psi$  is not computed. In fact, the mapping  $\Psi$  is not tracked at all. This means, of course, that the material deformation gradient  ${}^{n+1}\mathbf{F}_\Psi$  is not available, so the total deformation gradient  ${}^{n+1}\mathbf{F}$  cannot be computed according to equation (2.2.17), like before. Instead, the deformation is expressed by means of the so–called incremental deformation gradient  ${}^{n+1}\mathbf{f}$ . The combination of equations (2.2.22) and (2.2.2) yields

$${}^{n+1}\mathbf{f}({}^n\mathbf{X}) = \frac{\partial {}^{n+1}\mathbf{x}({}^n\mathbf{X})}{\partial {}^n\mathbf{x}({}^n\mathbf{X})} = \mathbf{I} + \frac{\partial {}^{n+1}\Delta\mathbf{u}({}^n\mathbf{X})}{\partial {}^n\mathbf{x}({}^n\mathbf{X})}, \quad (2.2.24)$$

which relates the total deformation gradients at  ${}^nt$  and  ${}^{n+1}t$  according to

$${}^{n+1}\mathbf{F}({}^n\mathbf{X}) = {}^{n+1}\mathbf{f}({}^n\mathbf{X}) {}^n\mathbf{F}({}^n\mathbf{X}). \quad (2.2.25)$$

Numerical time–integration of the elastic response consists then of a simple push–forward of the elastic left Green–Cauchy tensor:

$${}^{n+1}\mathbf{b}^e({}^n\mathbf{X}) = {}^{n+1}\mathbf{f}({}^n\mathbf{X}) {}^n\mathbf{b}^e({}^n\mathbf{X}) {}^{n+1}\mathbf{f}({}^n\mathbf{X})^T. \quad (2.2.26)$$

*Remark 2.2.3.* Note that this approach is of an *updated* nature, in the sense that the deformed configuration at the beginning of the time–step is used as a reference. The approach of Yamada and Kikuchi (1993) and Armero and Love (2000), on the other hand, is of a *total* type, because the initial undeformed configuration is taken as the reference.  $\square$

Due to the relative motion between the mesh and the material during the time–step (represented by  ${}^{n+1}\Delta\mathbf{u}_{\text{conv}}$ ), particles  ${}^n\mathbf{X}$  are no longer associated to grid points  $\boldsymbol{\chi}$  at the end of the time–step,  ${}^n\mathbf{X} \neq \mathbf{X}(\boldsymbol{\chi}, {}^{n+1}t)$ . For this reason, tensor  ${}^{n+1}\mathbf{b}^e$  must be convected before time–marching can proceed.

In exchange for this need of convecting variables, this approach offers a major advantage: since the material mapping  $\Psi$  is not used at all, only the quality of the spatial mesh (i.e. the mapping

---

FOR EVERY TIME-STEP  $[^n t, {}^{n+1} t]$ :

**Material phase**

- Neglect convective terms
- Advance the solution in an updated Lagrangian fashion: compute the increment of particle displacements  ${}^{n+1} \Delta \mathbf{u}$  and quantities  ${}^L \mathbf{b}^e$ ,  ${}^L \mathbf{p}$  and  $\det({}^L \mathbf{F})$  (superscript L denotes Lagrangian)

**Remeshing**

- Compute the increment of mesh displacements  ${}^{n+1} \Delta \mathbf{u}_\Phi$  and the increment of convective displacements  ${}^{n+1} \Delta \mathbf{u}_{\text{conv}}$  by means of a remeshing algorithm that reduces element distortion
- Compute the convective velocity  $\mathbf{c} = {}^{n+1} \Delta \mathbf{u}_{\text{conv}} / \Delta t$

**Convection phase**

- Account for convective terms
  - Use the Godunov-type technique to convect quantities  ${}^L \mathbf{b}^e$ ,  ${}^L \mathbf{p}$  and  $\det({}^L \mathbf{F})$  into  ${}^{n+1} \mathbf{b}^e$ ,  ${}^{n+1} \mathbf{p}$  and  $\det({}^{n+1} \mathbf{F})$
  - Compute stresses  ${}^{n+1} \boldsymbol{\tau}$  and  ${}^{n+1} \boldsymbol{\sigma}$
- 

Table 2.6: The proposed ALE approach for hyperelastoplasticity

of the finite element mesh in the referential domain  $R_\chi$  into the spatial domain  $R_x$ ) must be ensured by the ALE remeshing strategy. This is standard in ALE analysis of fluid dynamics and hypoelastoplasticity, and is in sharp contrast with the situation in Yamada and Kikuchi (1993), where both the spatial mesh *and* the material mesh (i.e. the mapping of the FE mesh in  $R_\chi$  into  $R_X$ ) must be kept undistorted, thus seriously limiting the potential of the ALE description as an  $r$ -adaptive technique.

Moreover, the need of convection cannot be regarded as a significant drawback of the proposed approach, since convecting variables is needed anyway in the ALE description of the plastic response.

**Hyperelastoplasticity** Indeed, if plastic strains are considered, a convective term appears in the equation that describes the evolution of plastic variables. For instance, Armero and Love (2000) work with the strain measure  $\mathbf{G}^p = (\mathbf{F}^{pT} \mathbf{F}^p)^{-1}$ , which is related to the elastic left Cauchy-Green tensor  $\mathbf{b}^e$  through  $\mathbf{b}^e = \mathbf{F} \mathbf{G}^p \mathbf{F}^T$ , and rewrite equation (2.2.10)<sub>1</sub> into

$$\dot{\mathbf{G}}^p = -2\dot{\gamma}(\mathbf{F}^{-1} \mathbf{m}_\tau \mathbf{F}) \mathbf{G}^p \quad (2.2.27)$$

in a Lagrangian setting, or

$$\frac{\partial \mathbf{G}^p}{\partial t} \Big|_{\chi} - \nabla_{\chi} \mathbf{G}^p \cdot \mathbf{F} \Psi^{-1} \frac{\partial \mathbf{X}}{\partial t} \Big|_{\chi} = -2\dot{\gamma}(\mathbf{F}^{-1} \mathbf{m}_\tau \mathbf{F}) \mathbf{G}^p \quad (2.2.28)$$

in an ALE setting. In equation (2.2.28),  $|_{\chi}$  denotes that the referential time derivative is computed holding the grid point  $\chi$  fixed, and  $\nabla_{\chi}$  is the gradient operator with respect to referential coordinates. As expected, the material time derivative in the left-hand-side of equation (2.2.27) is transformed, in equation (2.2.28), into a referential time derivative and a convective term which accounts for the relative motion between material particles  $\mathbf{X}$  and grid points  $\chi$ . A similar result is obtained for equation (2.2.10)<sub>2</sub>.

Alternatively, equation (2.2.10) can be reformulated into an ALE setting as

$$\frac{\partial \mathbf{b}^e}{\partial t} \Big|_{\mathbf{x}} + \mathbf{c} \nabla_{\mathbf{x}} \mathbf{b}^e = \mathbf{l} \mathbf{b}^e + \mathbf{b}^e \mathbf{l}^T - 2\dot{\gamma} \mathbf{m}_{\boldsymbol{\tau}}(\boldsymbol{\tau}, \mathbf{q}) \mathbf{b}^e \quad (2.2.29)$$

$$\frac{\partial \mathbf{p}}{\partial t} \Big|_{\mathbf{x}} + \mathbf{c} \nabla_{\mathbf{x}} \mathbf{p} = \dot{\gamma} \mathbf{m}_{\mathbf{q}}(\boldsymbol{\tau}, \mathbf{q}) \quad (2.2.30)$$

In equations (2.2.29) and (2.2.30), the material time derivative, see equations (2.2.10) and (2.2.11), has again been replaced by a referential time derivative and a convective term. The main difference between this approach and the one represented by equation (2.2.28) resides in the convective term: the relative motion is now expressed by the so-called convective velocity  $\mathbf{c}$  (i.e. the difference between the particle velocity and the mesh velocity), and the gradient operator is now with respect to spatial, not referential, coordinates. In fact, equations (2.2.29) and (2.2.30) are in the “quasi-Eulerian” format commonly encountered in ALE fluid dynamics and ALE hypoelastoplasticity (Huerta and Liu 1988).

Similarly, if the general case of non-isochoric response is considered  $\det(\mathbf{F})$  must also be convected, because it cannot be computed solely from  $\mathbf{b}^e$ . For doing so, it is convenient to rewrite equation (2.2.8) into

$$\frac{\partial |\mathbf{F}|}{\partial t} \Big|_{\mathbf{x}} + \mathbf{c} \nabla_{\mathbf{x}} |\mathbf{F}| = |\mathbf{F}| \nabla_{\mathbf{x}} \cdot \mathbf{v}. \quad (2.2.31)$$

Note that equation (2.2.31) has the same structure that equations (2.2.29) and (2.2.30): in the left-hand-side, a referential time derivative and a convective term; in the right-hand-side, the material terms.

In summary, the quantities to convect in the proposed ALE approach are  $\mathbf{b}^e$ ,  $\mathbf{p}$  and  $\det(\mathbf{F})$ . This is done by means of a fractional-step method, a very common strategy to treat ALE convective terms (Huétink et al. 1990, Baaijens 1993, Huerta and Casadei 1994, Rodríguez-Ferran et al. 1998, Askes et al. 1998, Armero and Love 2000). Every time-step is divided into two phases: the Lagrangian phase and the convection phase. During the Lagrangian phase, convection is neglected and the increment of particle displacements  ${}^{n+1}\Delta \mathbf{u}$  is computed in the usual Lagrangian fashion (i.e. elastic predictor and plastic corrector). After that, an ALE remeshing algorithm is employed to compute the increment of mesh displacements  ${}^{n+1}\Delta \mathbf{u}_{\Phi}$ . During the convection phase, the convective term is taken into account. A Godunov-like technique (Huerta, Casadei and Donea 1995, Rodríguez-Ferran et al. 1998) is used for that purpose. The proposed ALE approach for hyperelastoplasticity is summarized in table 2.6.

*Remark 2.2.4.* In the proposed approach, the time-integration of the elastic response is not exact. During the convection phase, truncation errors are introduced. It must be noted, however, that these numerical errors can be controlled by the time-step  $\Delta t$  and the mesh size. Moreover, these errors are completely unrelated with the drawbacks of hypoelastic-plastic models (i.e. elastic dissipation in a closed path). From the viewpoint of modelling, the proposed approach is fully hyperelastic-plastic.  $\square$

## 2.2.4 Numerical examples

The proposed ALE approach is illustrated and validated here by means of three representative numerical examples: a necking test, a coining test and a powder compaction test. Eight-noded quadrilateral elements with  $2 \times 2$  Gauss points are employed for all the computations.

### Necking test

The necking problem is a well-known benchmark test in large-strain solid mechanics (Simo 1988, Rodríguez-Ferran et al. 1998, Miehe 1998, Perić and de Souza Neto 1999). A cylindrical bar with circular cross-section, with a radius of 6.413 mm and 53.334 mm length, is subjected to uniaxial extension. A slight geometric imperfection (1% reduction in radius), see figure 2.22, induces necking in the central part of the bar. An axisymmetric analysis is carried out with the mesh of  $5 \times 10$  finite elements shown in figure 2.22.

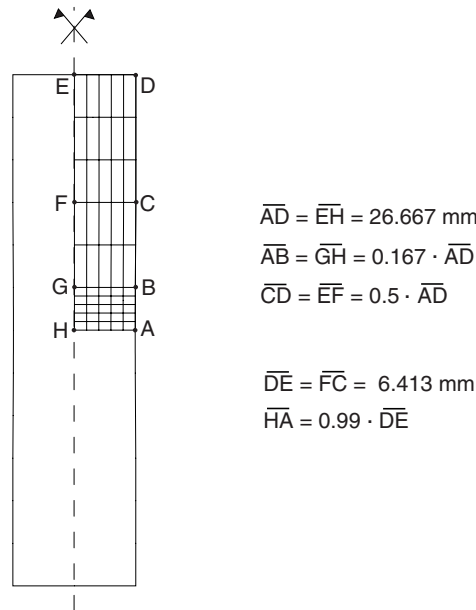


Figure 2.22: Necking of a cylindrical bar. Problem definition and computational mesh.

Bulk modulus	164.206 GPa
Shear modulus	80.1938 GPa
Initial flow stress	0.45 GPa
Residual flow stress	0.715 GPa
Linear hardening coefficient	0.12924 GPa
Saturation exponent	16.93
Yield shape exponent (Tresca-type model)	20

Table 2.7: Material parameters for the necking test.

Two hyperelastic–plastic models have been used: the classical von Mises model (Simo and Hughes 1998, Simo 1998) and a Tresca-type model (Miehe 1998). The two models are isochoric and exhibit hardening. In consequence, the quantities to transport in the convection phase are  $\mathbf{b}^e$  and  $\mathbf{p}$ , which contains one internal plastic variable. The material parameters for both models are summarized in table 2.7, see Simo (1988) and Pérez-Foguet and Armero (2000) for further details.

For comparative purposes, both Lagrangian and ALE analyses have been performed. A very simple ALE remeshing strategy is used (Rodríguez-Ferran et al. 1998): the outer region BDEG of the mesh is Lagrangian, and equal height of elements is prescribed in the central region ABGH.

The results with the von Mises model are discussed first. Figure 2.23 depicts the deformed shapes up to an elongation  $d$  of 8 mm for half the bar. As expected, the elements in the neck zone become very distorted with the Lagrangian description, see figure 2.23(a–c). The distortion is highly reduced with the ALE description, see figure 2.23(d–f). In the proposed ALE approach, the quality of these spatial meshes is the only concern of the ALE remeshing strategy. There is no need to ensure the quality of the material meshes (Yamada and Kikuchi 1993, Armero and Love 2000).

A more quantitative comparison is offered in figure 2.24, which shows the evolution of the vertical reaction and dimensionless radius (ratio of current radius to initial radius) with elongation. Very similar results are obtained up to an elongation of 6.5–7 mm. If pulling proceeds, however, discrepancies arise between the Lagrangian and ALE solutions. With only one row of (very distorted) elements in the necking zone, the Lagrangian simulation on the coarse mesh does not fully capture the plastification process, and this results in less necking. The ALE response is in much better agreement with a reference Lagrangian solution with a very fine mesh (not shown in the figure).

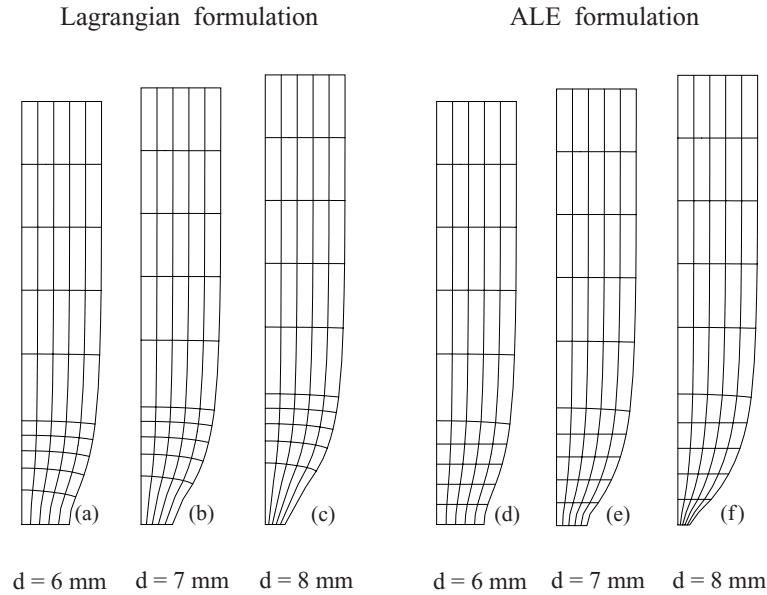


Figure 2.23: Necking test with the von Mises model. Mesh configurations for different top displacements  $d$ : (a-c) Lagrangian formulation and (d-f) ALE formulation.

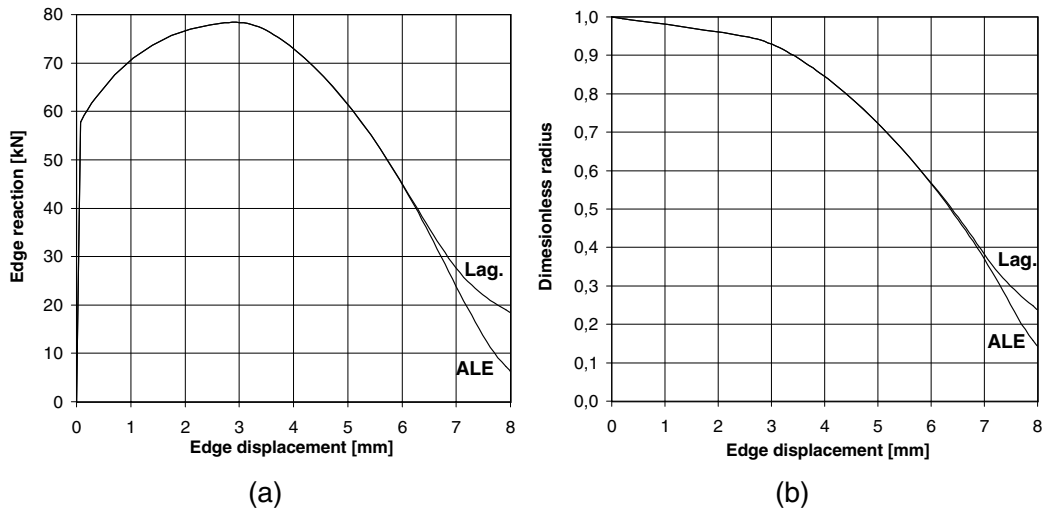


Figure 2.24: Necking test with the von Mises model. Lagrangian and ALE formulations. Global response: (a) vertical edge reaction and (b) dimensionless radius in the necking zone versus vertical edge displacement.

A final, qualitative assessment of the two simulations can be made by looking at the distribution of the von Mises stress. According to some empirical and semianalytical studies (Goicolea 1985) this field is constant in the neck zone, along the  $z = 0$  plane of symmetry. Figure 2.25 shows the distribution of the von Mises stress after an elongation of 7 mm. It can be seen that the Lagrangian analysis, figure 2.25(a), does not provide a constant value along  $z = 0$ , while the ALE analysis does, figure 2.25(b). The results reported in Rodríguez-Ferran et al. (1998) for the hypoelastic-plastic von Mises model are shown in figures 2.25(c) and 2.25(d). Since elastic strains are small compared to elastic strains for this test, the hyperelastic and hypoelastic approaches yield very similar results.

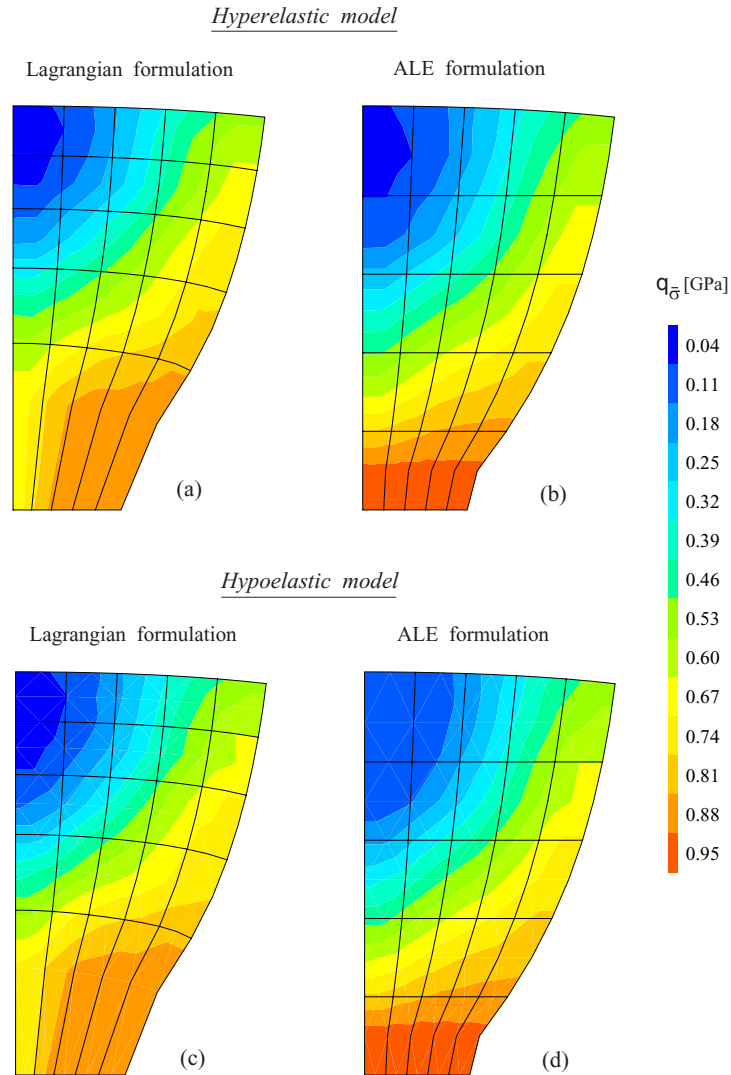


Figure 2.25: Necking test with the von Mises model. Distribution of the von Mises stress in the necking zone. Hyperelastic–plastic model: (a) Lagrangian formulation, (b) ALE formulation. Hypoelastic–plastic model (after Rodriguez–Ferran et al. 1998): (c) Lagrangian formulation, (d) ALE formulation.

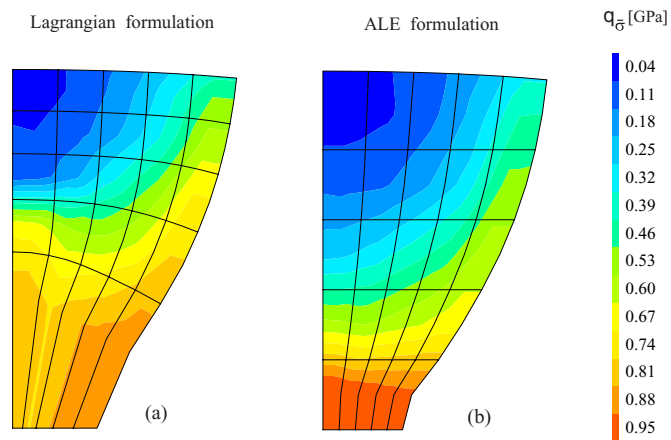


Figure 2.26: Necking test with the Tresca–type model. Distribution of the von Mises stress in the necking zone: (a) Lagrangian formulation, (b) ALE formulation.



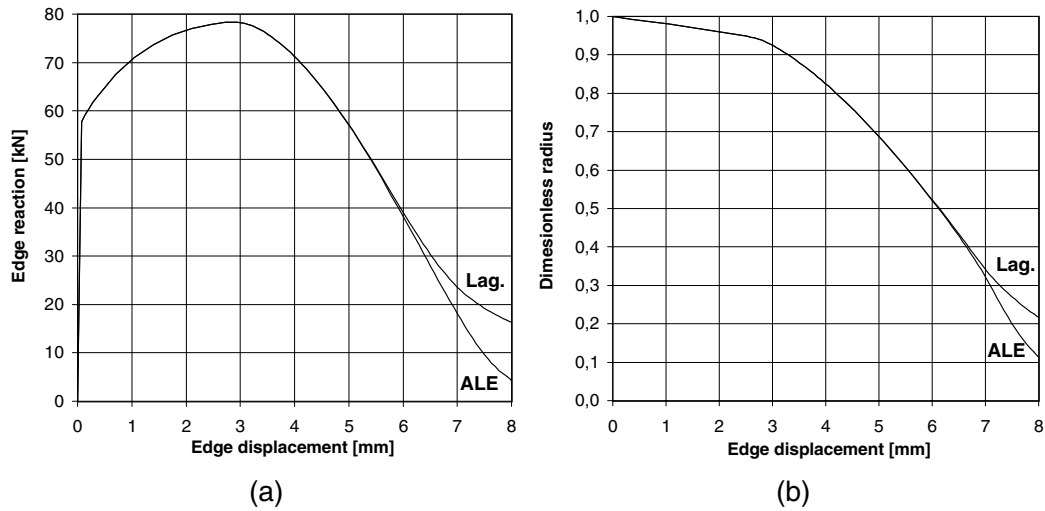


Figure 2.27: Necking test with the Tresca-type model. Lagrangian and ALE formulations. Global response: (a) vertical edge reaction and (b) dimensionless radius in the necking zone versus vertical edge displacement.

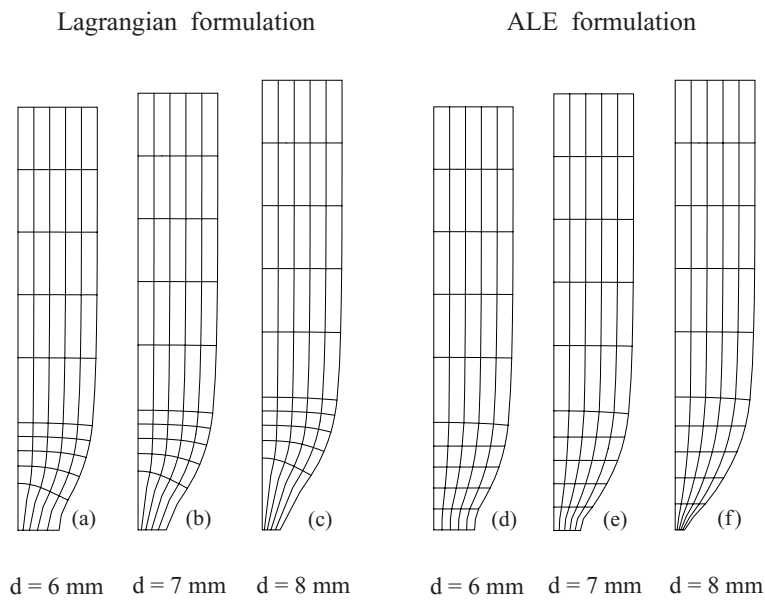


Figure 2.28: Necking test with the Tresca-type model. Mesh configurations for different top displacements,  $d$ : (a-c) Lagrangian formulation and (d-f) ALE formulation.

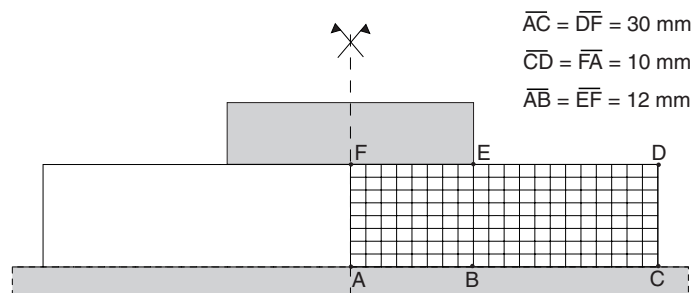


Figure 2.29: Coining test. Problem definition and computational mesh.

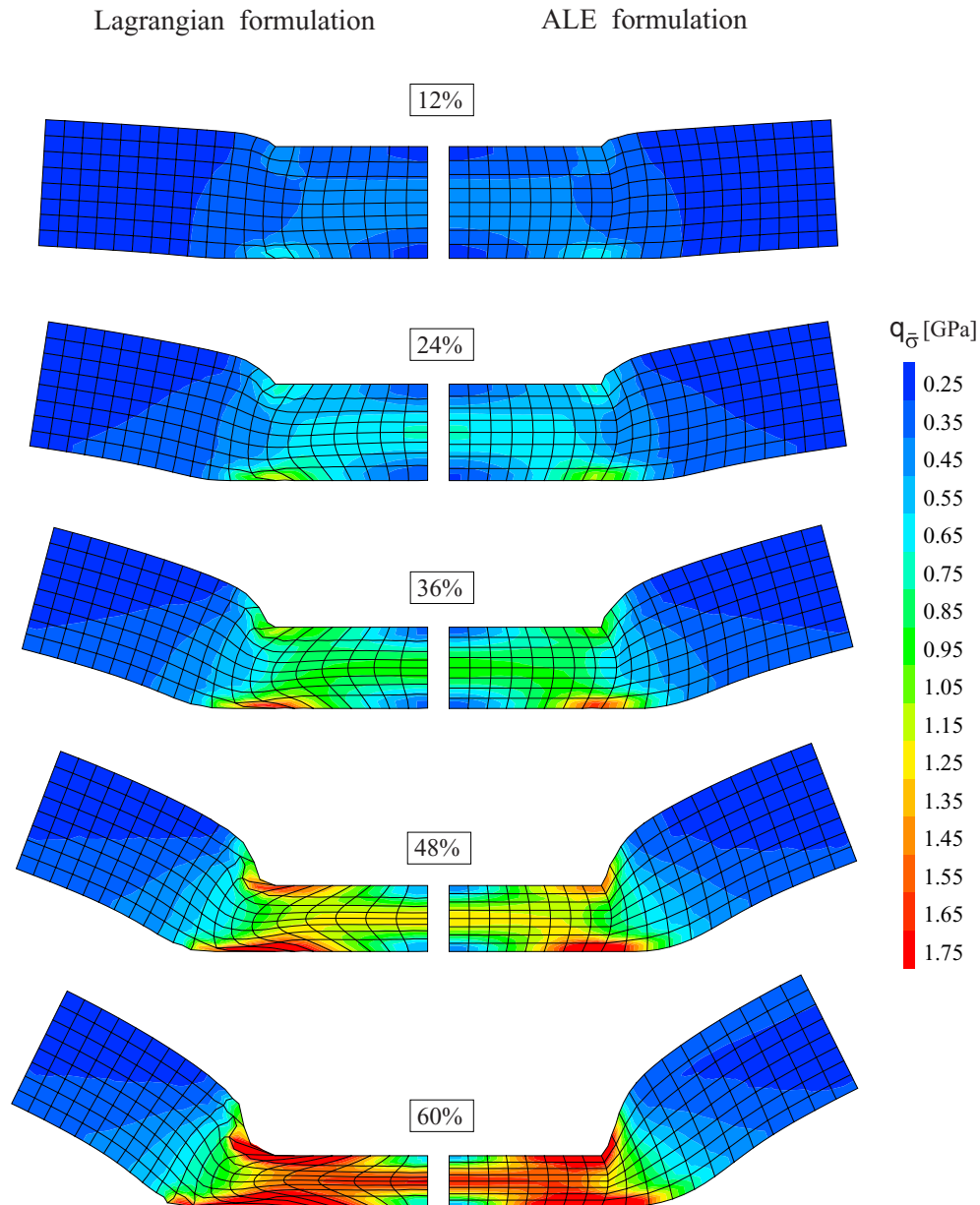


Figure 2.30: Coining test with the von Mises model. Mesh configurations and distribution of the von Mises stress for different height reductions. Lagrangian and ALE formulations.

The same test is performed with the Tresca-type model. Figure 2.28 shows the deformed shapes as elongation proceeds. The highly distorted Lagrangian meshes show the different failure pattern with respect to the von Mises model, compare figures 2.23(a–c) and 2.28(a–c). The ALE meshes, however, are very similar, compare figures 2.23(d–f) and 2.28(d–f), because the same ALE remeshing strategy is used. Thanks to the ALE description, the quality of the spatial mesh can be ensured independently of the material deformation.

Regarding the structural response and the von Mises stress distribution, results are qualitatively very similar to those with the von Mises model. Figure 2.27 shows that the global behaviour of the piece is captured correctly with the Lagrangian formulation only up to an elongation of 6.5–7 mm; figure 2.26 shows that only the ALE formulation correctly captures the constant stress distribution in the neck zone.

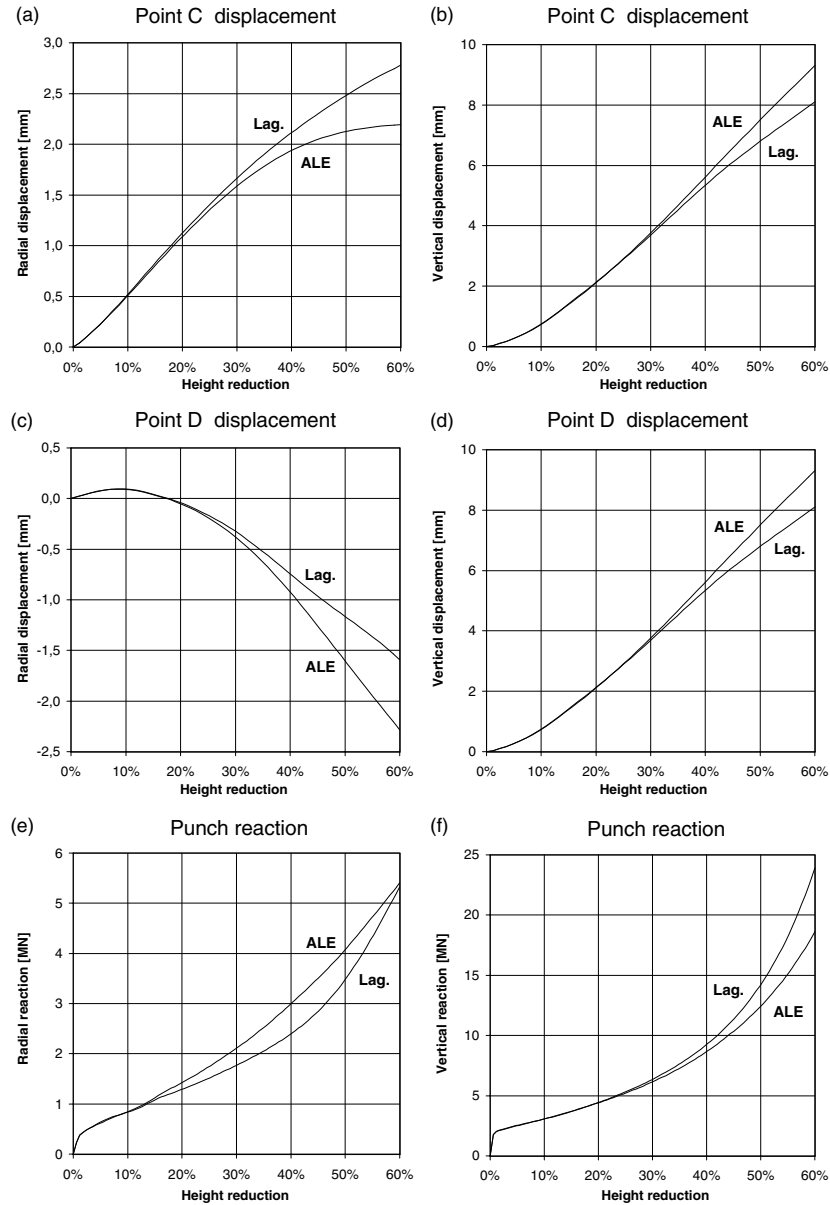


Figure 2.31: Coining test with the von Mises model. Lagrangian and ALE formulations. Representative results: (a-b) point C displacements, (c-d) point D displacements, and (e-f) punch reactions.

### Coining test

As a second example, a coining process is simulated (Rodríguez-Ferran et al. 1998). A metallic disk, with a radius of 30 mm and a height of 10 mm, is deformed by a punch 12 mm in radius, see figure 2.29. The von Mises hyperelastic–plastic model is employed, with elastic modulus  $E = 200$  GPa, Poisson’s coefficient  $\nu = 0.3$ , yield stress  $\sigma_y = 250$  MPa and plastic modulus  $E_p = 1$  GPa. Both the punch and the die are rigid. Perfect friction (stick) conditions are assumed in the punch–disk and disk–die interfaces. An axisymmetric analysis is performed to model a 60% height reduction with a mesh of  $20 \times 8$  finite elements.

Again, both a Lagrangian and an ALE analysis have been performed. The evolution of the deformed shape and the von Mises stress field is depicted in figure 2.30. Due to the stick conditions in the two interfaces, the material in the central part of the disk flows outward. This leads to a highly distorted Lagrangian mesh, especially under the punch corner and in the contact with the die. Remarkably, the convergence of the Lagrangian analysis is not disturbed by the mesh

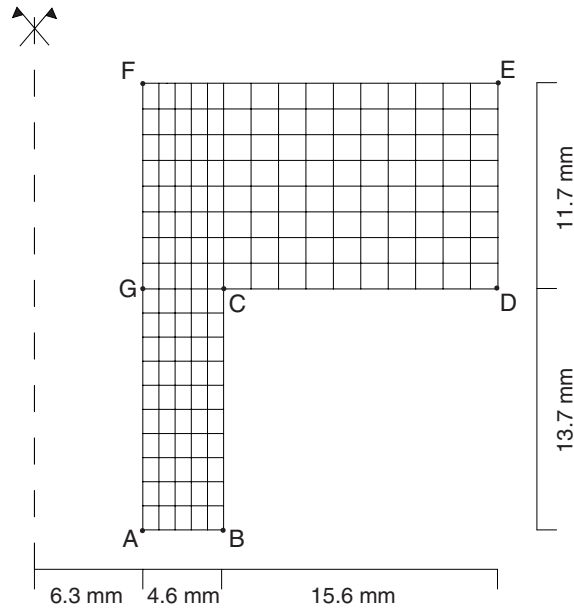


Figure 2.32: Flanged component. Problem definition and computational mesh, after Lewis and Khoei 1998.

distortion, thanks to the use of consistent tangent matrices and a  $2 \times 2$  Gauss–point quadrature, with negative Jacobians less likely than with a  $3 \times 3$  quadrature.

The mesh distortion is greatly reduced in the ALE analysis. The following remeshing strategy is used: (1) line  $\overline{AB}$  is Eulerian, lines  $\overline{CD}$  and  $\overline{EF}$  are Lagrangian and equal length of elements is prescribed in lines  $\overline{BC}$ ,  $\overline{CF}$  and  $\overline{DA}$ ; (2) parabolic profiles of horizontal mesh displacements are prescribed in region  $ABEF$ ; (3) mesh displacements in region  $BCDE$  are interpolated from the contour values.

As expected, the mesh distortion clearly affects the numerical solution. In figure 2.31, the Lagrangian and ALE solutions are compared in terms of the displacement of points C and D and the punch reaction (radial and vertical components shown separately). For all the outputs, the two descriptions provide very similar results up to a height reduction of 20%–30%, which induces a relatively small distortion in the Lagrangian mesh. Significant differences, however, are encountered for increasing height reductions and a more distorted Lagrangian mesh. The same type of behaviour is obtained with the Tresca–type model (with the same material parameters used for the von Mises analysis plus the yield shape exponent equal to 20).

### Compaction test

As a last example, the powder compaction of a flanged component is analyzed (Lewis and Khoei 1998). The axisymmetric computational domain and the structured mesh of 170 finite elements are depicted in figure 2.32. The plastic model is non-isochoric and has no internal variables. The yield function is elliptic and depends on the density. These are usual features in plastic models for powder compaction (Oliver et al. 1996). A detailed presentation of this model, together with the set of material parameters, can be found in section 4.4 (Pérez-Foguet et al. 2000b).

Friction effects are neglected both in section 4.4 and here, because the focus of these papers is respectively the consistent linearization for density–dependent plastic models and the ALE kinematical description of hyperelastoplasticity. A more realistic simulation of the compaction process can be found in chapter 5 (Pérez-Foguet, Rodríguez-Ferran and Huerta 2000a), where the friction in the die wall is accounted for.

Two different processes are analyzed: top punch compaction and bottom punch compaction. For comparative purposes, both Lagrangian and ALE analyses are performed. For the ALE computations,  $\mathbf{b}^e$  and  $\det(\mathbf{F})$  are transported during the convection phase.

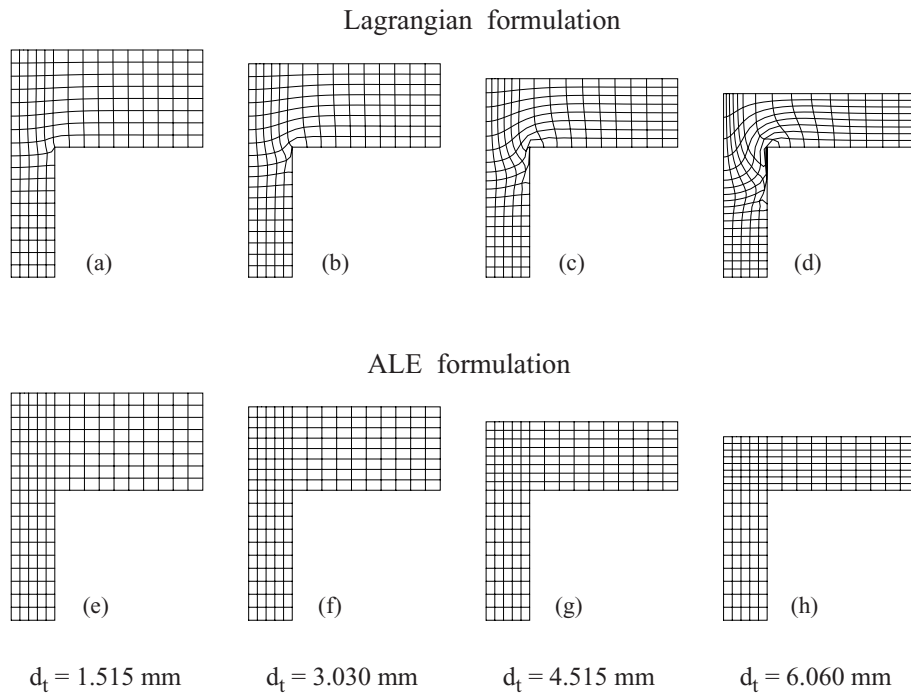


Figure 2.33: Top punch compaction of the flanged component. Mesh configurations for different punch displacements  $d_t$ : (a-d) Lagrangian formulation and (e-h) ALE formulation.

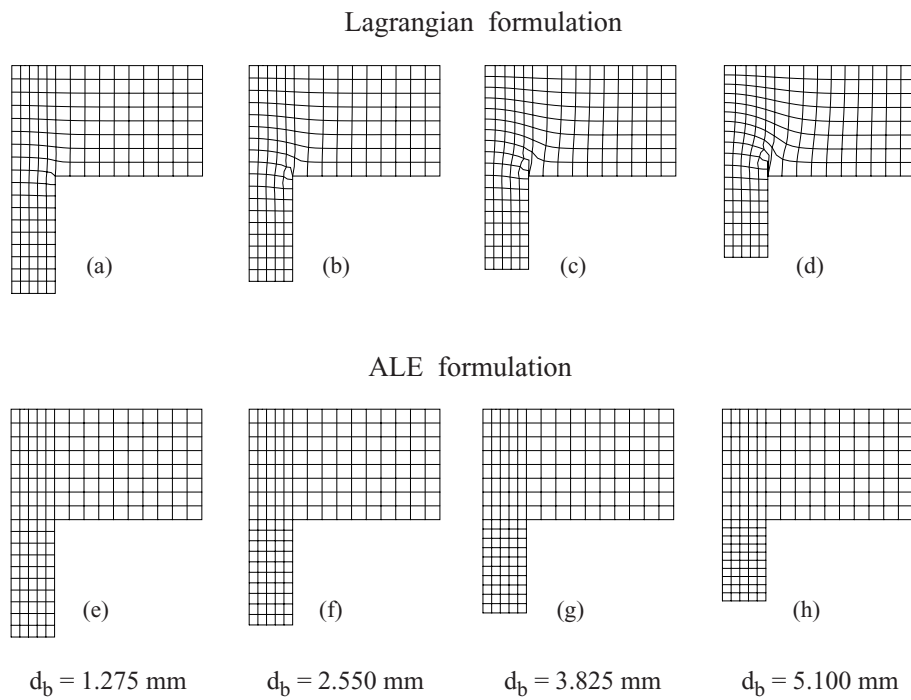


Figure 2.34: Bottom punch compaction of the flanged component. Mesh configurations for different punch displacements  $d_b$ : (a-d) Lagrangian formulation and (e-h) ALE formulation.

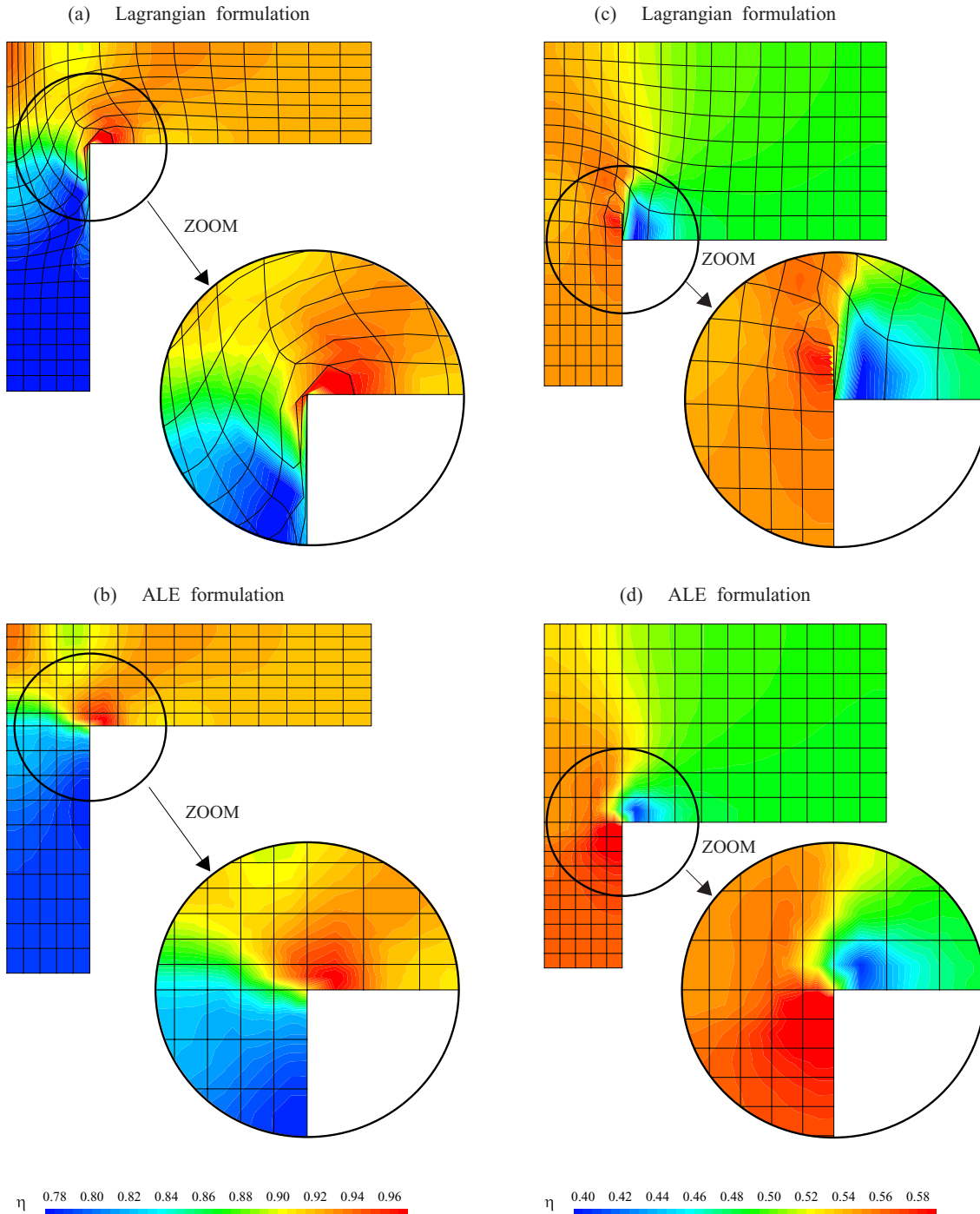


Figure 2.35: (a–b) Top and (c–d) bottom punch compactions of the flanged component. Final relative density distribution, Lagrangian and ALE formulations.

Figure 2.33 shows a sequence of deformed meshes for different values of the top punch displacement, up to a final value of 6.06 mm. The Lagrangian meshes, figures 2.33(a–d), clearly show the pattern of powder motion: as expected, the material flows to the left and to the bottom. This motion is especially important around the punch corner C. This leads to highly distorted elements in this zone, which in turn result in spurious oscillations of the relative density distribution, see figure 2.35(a).

Mesh distortion can be controlled in an effective way by means of a very simple ALE remeshing strategy: (1) region ABCG remains Eulerian; (2) in region GDEF, horizontal mesh displacements are restrained and an equal height for all elements is prescribed. By doing so, the original rect-

angular shape of the elements is maintained throughout the whole compaction process, see figures 2.33(e–h). As a consequence, a smoother field of relative densities is obtained, with no spurious oscillations, see figure 2.35(b).

A similar situation is encountered with the bottom compaction process. Due to the geometry of the piece, the material motion is predominantly upwards, as the Lagrangian meshes of figures 2.34(a–d) show. Note the high shear distortion around the punch corner C for the final punch displacement of 5.10 mm, which concentrates in a single element. This distortion is completely eliminated with the ALE analysis. The remeshing strategy is a straightforward adaptation of the one used before (i.e. region GDEF is Eulerian, and elements of equal shape are prescribed in region ABCG).

The quality of the mesh again affects the final density distribution, see figure 2.35(c–d). With the Lagrangian analysis, a spurious zone of high density results near point C. With the ALE analysis, on the other hand, a smoother density field is obtained.

### 2.2.5 Concluding remarks

The proposed approach allows the combination of the Arbitrary Lagrangian-Eulerian kinematical description and hyperelastic–plastic models in a straightforward and effective manner. Since a fractional–step method is chosen for numerical time–marching, the material terms and the convection terms of the ALE governing equations are treated separately. As a consequence, the standard predictor–corrector techniques of finite strain plasticity can be employed during the Lagrangian phase, and a simple Godunov–type algorithm for the convection phase.

Contrary to other approaches for ALE hyperelastoplasticity reported in the literature, the deformed configuration at the beginning of the time–step, rather than the initial configuration, provides the reference to describe the deformation. In exchange for the need of convecting the elastic strains—a marginal drawback, since plastic variables must be convected anyway—the strategy suggested here has a major advantage: only the quality of the spatial mesh, not of the spatial and material meshes, must be ensured. This is the standard situation in ALE fluid dynamics and ALE hypoelastoplasticity, and renders a flexible  $r$ –adaptive technique.

These aspects have been illustrated by means of various numerical examples involving different hyperelastic–plastic models. The comparison of Lagrangian and ALE analyses clearly show that it is essential to keep mesh distortion under control to ensure the quality of the numerical solution. In the ALE simulations, the distortion of the spatial mesh is controlled by means of very simple remeshing strategies, which do not have to worry about the distortion of the material mesh.





## Chapter 3

# Non-standard consistent tangent operators

Two topics related with the computation of consistent tangent operators in elastoplasticity are developed in this chapter. Both are of special interest for the solution of problems involving highly nonlinear constitutive models.

First, in section 3.1, numerical differentiation is applied to integrate the plastic constitutive laws and to compute the corresponding consistent tangent operators. In many cases, the plastic constitutive laws used in geomaterial modelling have complicated expressions of the flow vector and the internal variable flow direction. The derivatives of both are needed to achieve quadratic convergence in the numerical time-integration of the constitutive equations at Gauss-point level and in the solution of boundary value problems with an incremental-iterative strategy. In this context, it is shown that the numerical approximation of first derivatives is a simple, robust and competitive alternative to analytical derivatives. The behaviour of several numerical differentiation techniques is analyzed.

On the other hand, in section 3.2, a very simple expression of consistent tangent operators for substepping time-integration schemes is presented. Substepping schemes based on the forward Euler, the backward Euler and the midpoint rules are included. An adaptive strategy which activates a substepping scheme at Gauss points where the standard return mapping algorithms does not converge is used as an example. With this strategy, the most restrictive local problems no longer control the load increment of the global problem. This results in a large reduction of the number of load increments of the global problem, which typically implies a large reduction of the computational cost.

Examples involving the adaptive substepping scheme jointly with the proposed numerical differentiation approximations are included. It is shown that the use of both strategies lead to quadratic convergence in complex nonlinear elastoplastic problems.

### 3.1 Numerical differentiation for local and global tangent operators in computational plasticity

In this section, numerical differentiation is applied to integrate plastic constitutive laws and to compute the corresponding consistent tangent operators. The derivatives of the constitutive equations are approximated by means of difference schemes. These derivatives are needed to achieve quadratic convergence in the integration at Gauss-point level and in the solution of the boundary value problem. Numerical differentiation is shown to be a simple, robust and competitive alternative to analytical derivatives. Quadratic convergence is maintained, provided that adequate schemes and stepsizes are chosen. This point is illustrated by means of some numerical examples.

#### 3.1.1 Introduction

The main goal of this section is to show that numerical differentiation is a useful tool for achieving quadratic convergence in computational plasticity. Two different problems must be solved: 1) the

integration of the constitutive law at each Gauss point (the local problem) and 2) the boundary value problem (the global problem); see, for instance, Crisfield (1991, 1997).

If the constitutive law is integrated with an implicit method, the local problem is nonlinear. To solve it with the Newton-Raphson method, thus attaining quadratic convergence (Dennis and Schnabel 1983), it is necessary to compute the Jacobian of the residual at the Gauss-point level. The global problem, on the other hand, is typically solved via an incremental/iterative approach (Crisfield 1991). At each load increment, a nonlinear system of equations must be solved. To do it with the Newton-Raphson method and achieve quadratic convergence, the consistent tangent matrix (computed with the consistent elastoplastic moduli) must be used (Simo and Taylor 1985, Runesson et al. 1986). In both problems (local and global), the derivatives of the constitutive equation are needed. These derivatives are a key ingredient of both the Jacobian of the residual —local problem— and the consistent elastoplastic moduli —global problem.

Various approaches for computing these derivatives can be found in the literature. For simple plasticity models, analytical derivatives are readily available, and this leads to closed-form return mapping algorithms for the local problem and compact, explicit expressions of the consistent elastoplastic moduli for the global problem (Simo and Taylor 1985, Simo and Hughes 1998). In more complicated models, analytical differentiation is rather more cumbersome. Algebraic manipulators such as Maple or Mathematica can be a very effective tool for obtaining analytical derivatives.

Here a different approach is proposed: derivatives are approximated by means of classical difference schemes (Isaacson and Keller 1966, Dennis and Schnabel 1983, Hoffman 1982). The approximated derivatives are used both for the integration of the constitutive equations (local problem) and for the computation of the consistent tangent moduli (global problem). The resulting algorithm is both robust and computationally efficient. It maintains the characteristic quadratic convergence of the Newton-Raphson method, provided that adequate difference schemes and stepsizes (i.e. the perturbation in the difference scheme) are chosen.

Some applications of numerical differentiation to other problems of computational plasticity can be found in the literature. For instance, a first-order forward difference scheme is used by Miehe (1996) to compute the consistent tangent moduli needed in large-strain inelasticity. There, simple material models are used and closed expressions for the return mapping are available, so numerical derivatives are only applied to the global problem. The proposed numerical approach computes the derivatives of each stress component with respect to each strain component to get directly the consistent moduli. This implies a computational overhead (with respect to analytical derivatives) that ranges from 40% to 80% and, perhaps more importantly, its robustness is limited by the choice of the stepsize. More complicated models are considered by Jeremić and Sture (1994, 1997), but it is also concluded that analytical derivatives are clearly superior to numerical derivatives regarding computational cost.

In contrast to these approaches, the strategy proposed here, concerned with small strains, combines the three following features: 1) it can be used for both local and global problems, with complicated material models, see section 4.2 (Pérez-Foguet, Rodríguez-Ferran and Huerta 2000*e*), 2) it has a marginal computational overhead (around 1 — 2 %) and 3) it is very robust (i.e. insensitive to the choice of the stepsize).

An outline of this section follows. The local and the global problems of computational plasticity are briefly reviewed in subsection 3.1.2, with emphasis on the crucial role of the derivatives of the constitutive equation. In subsection 3.1.3 the various numerical differentiation techniques are summarized, and a simple rule for selecting the stepsize is presented. These numerical approximations are applied to several problems in subsection 3.1.4. Finally, some concluding remarks are made on subsection 3.1.5. For the sake of simplicity, the simple case of a single yield surface and the backward Euler integration rule is considered. However, the same derivatives are needed in multi-surface plasticity (Simo et al. 1988, Pramono and Willam 1989*b*) or with other implicit integration rules (Ortiz and Popov 1985, Runesson, Sture and Willam 1988, Chaboche and Cailletaud 1996), so numerical differentiation can also be applied in these general cases.

### 3.1.2 Problem statement

In small-strain elastoplasticity, the stress tensor  $\boldsymbol{\sigma}$  and the stress-like internal variables  $\mathbf{q}$  can be related with the small-strain tensor  $\boldsymbol{\varepsilon}$  and the strain-like internal variables  $\mathbf{p}$  (Lubliner 1990, Simo

and Hughes 1998) through

$$\boldsymbol{\sigma} = \nabla W^e(\boldsymbol{\varepsilon}^e) = \nabla W^e(\boldsymbol{\varepsilon} - \boldsymbol{\varepsilon}^p) \quad \text{and} \quad \mathbf{q} = -\nabla W^p(\mathbf{p}), \quad (3.1.1)$$

where  $\boldsymbol{\varepsilon}^e$  and  $\boldsymbol{\varepsilon}^p$  are the elastic and the plastic strain tensors,  $W^e$  and  $W^p$  are the elastic and the plastic part of the free-energy function per unit of volume, and  $\nabla \Psi(\chi)$  denotes the gradient of  $\Psi$  with respect to  $\chi$ . The yield function  $F$  defines the admissible stress states,  $F(\boldsymbol{\sigma}, \mathbf{q}) \leq 0$ . Its derivatives are denoted by  $\mathbf{n}_\sigma = \partial F / \partial \boldsymbol{\sigma}$  and  $\mathbf{n}_q = \partial F / \partial \mathbf{q}$ . The equations of evolution for  $\boldsymbol{\varepsilon}^p$  and  $\mathbf{p}$  are

$$\dot{\boldsymbol{\varepsilon}}^p = \dot{\lambda} \mathbf{m}_\sigma \quad \text{and} \quad \dot{\mathbf{p}} = \dot{\lambda} \mathbf{m}_q, \quad (3.1.2)$$

where  $\mathbf{m}_\sigma$  and  $\mathbf{m}_q$  are the corresponding flow directions, and  $\dot{\lambda}$  is the plastic consistency parameter. For convenience, the terms *generalized stress* and *generalized flow vector* are used to refer to  $(\boldsymbol{\sigma}, \mathbf{q})$  and  $(\mathbf{m}_\sigma, \mathbf{m}_q)$  respectively (Ortiz and Martin 1989, Simo and Hughes 1998). For some constitutive models, the generalized flow vector is expressed as the derivative of a generalized flow potential  $G(\boldsymbol{\sigma}, \mathbf{q})$  (Lubliner 1990, Runesson and Larsson 1993):  $\mathbf{m}_\sigma = \partial G / \partial \boldsymbol{\sigma}$  and  $\mathbf{m}_q = \partial G / \partial \mathbf{q}$ . The flow potential  $G$  may either coincide with (associate plasticity) or differ from (non-associate plasticity) the yield function  $F$ .

### Local problem: integration of the constitutive law

The integration of the constitutive law with an implicit rule results in a nonlinear problem. If the backward Euler rule is used, the equations are

$${}^{n+1}\boldsymbol{\sigma} = \nabla W^e ({}^{n+1}\boldsymbol{\varepsilon} - {}^n\boldsymbol{\varepsilon}^p - {}^{n+1}\lambda {}^{n+1}\mathbf{m}_\sigma) \quad (3.1.3)$$

$${}^{n+1}\mathbf{q} = -\nabla W^p ({}^n\mathbf{p} + {}^{n+1}\lambda {}^{n+1}\mathbf{m}_q) \quad (3.1.4)$$

$$F({}^{n+1}\boldsymbol{\sigma}, {}^{n+1}\mathbf{q}) = 0 \quad (3.1.5)$$

where the superscripts  $n$  and  $n+1$  refer to instants  ${}^n t$  and  ${}^{n+1} t = {}^n t + \Delta t$  respectively.

There are several ways to solve this nonlinear problem. For some very simple models, it can be solved analytically (Crisfield 1991, Simo and Hughes 1998). However, for general models an analytical solution is not possible, so a numerical method must be used. A typical choice is the Newton-Raphson method, because it converges quadratically (Dennis and Schnabel 1983). To use this method, the derivatives of equations (3.1.3–3.1.5) with respect to the unknowns  ${}^{n+1}\boldsymbol{\sigma}$ ,  ${}^{n+1}\mathbf{q}$ , and  ${}^{n+1}\lambda$  are needed. With the standard vector notation of computational mechanics (Zienkiewicz and Taylor 1988, Crisfield 1991), this Jacobian is

$${}^{n+1}\mathbf{J} = \begin{pmatrix} (\mathbf{I}_{n_\sigma} + \lambda \mathbf{E} \frac{\partial \mathbf{m}_\sigma}{\partial \boldsymbol{\sigma}}) & \lambda \mathbf{E} \frac{\partial \mathbf{m}_\sigma}{\partial \mathbf{q}} & \mathbf{E} \mathbf{m}_\sigma \\ \lambda \mathbf{H} \frac{\partial \mathbf{m}_q}{\partial \boldsymbol{\sigma}} & (\mathbf{I}_{n_q} + \lambda \mathbf{H} \frac{\partial \mathbf{m}_q}{\partial \mathbf{q}}) & \mathbf{H} \mathbf{m}_q \\ \mathbf{n}_\sigma^T & \mathbf{n}_q^T & 0 \end{pmatrix}_{t={}^{n+1}t}, \quad (3.1.6)$$

where  $\mathbf{E} = \nabla^2 W^e(\boldsymbol{\varepsilon}^e)$  is the tensor of elastic moduli,  $\mathbf{H} = \nabla^2 W^p(\mathbf{p})$  is the tensor of plastic moduli,  $T$  denotes transpose,  $n_\sigma$  is the dimension of the stress vector,  $n_q$  is the number of internal variables and  $\mathbf{I}_*$  is the identity matrix of order  $*$ . The expression of the Jacobian given in equation (3.1.6) can be compacted by multiplying the first row by  $\mathbf{E}^{-1}$  and the second row by  $\mathbf{H}^{-1}$  (Simo and Hughes 1998). This transformation (which must, of course, also be performed on the RHS residual vector of the Newton-Raphson iteration) is computationally appealing if matrices  $\mathbf{E}$  and  $\mathbf{H}$  are constant. However, the ideas presented in this section do not rely at all in this transformation. For this reason, the original expression of the Jacobian is retained here.

Of the terms in equation (3.1.6), the derivatives of the generalized flow vector with respect to the generalized stresses are usually the most difficult to compute. For complex material models, these derivatives are either not available or computationally too expensive (Pramono and Willam 1989b, Sture et al. 1989, Etse and Willam 1994, Jeremić and Sture 1997). The standard approach in these cases is to use nonlinear solvers (different from the Newton-Raphson method, i.e. a fully tangent approach) that do not need to compute all the derivatives of the generalized flow vector.

Some of these alternatives are: a tangent approach for the plastic multiplier, equation (3.1.5), with an explicit expression for internal variables, equation (3.1.4), and a secant approach for

stresses, equation (3.1.3) (Pramono and Willam 1989*b*); a tangent approach for the stresses, equation (3.1.3), and a direct substitution of the internal variable equations, equation (3.1.4) (Jeremić and Sture 1994, 1997); a two-level technique with a tangent approach for the stress invariants and a Picard iteration with an adaptive order inverse interpolation for the internal variables (Macari et al. 1997). However, quadratic convergence cannot be achieved with these methods, because they are not based on a consistent linearization of *all* the equations and unknowns.

The goal of this section is to show that numerical differentiation is a valid alternative to these approaches. By approximating numerically the derivatives of the generalized flow vector, the standard full Newton-Raphson method can be applied to equations (3.1.3–3.1.5). In this manner, quadratic convergence is obtained.

### Global problem: the consistent tangent matrix

Various nonlinear solvers may be used for the global problem (Dennis and Schnabel 1983, Crisfield 1991). Again, one of the best choices is the full Newton-Raphson method. To achieve quadratic convergence, the consistent tangent matrix must be used (Simo and Taylor 1985, Runesson et al. 1986). To compute this matrix, the consistent tangent moduli  $d^{n+1}\boldsymbol{\sigma}/d^{n+1}\boldsymbol{\varepsilon}$  are needed. They can be computed by linearizing the discrete constitutive equations (3.1.3–3.1.5). This linearization can be represented as

$${}^{n+1}\mathbf{J} \begin{pmatrix} d^{n+1}\boldsymbol{\sigma} \\ d^{n+1}\mathbf{q} \\ d^{n+1}\lambda \end{pmatrix} = \begin{pmatrix} \mathbf{E} d^{n+1}\boldsymbol{\varepsilon} \\ \mathbf{0} \\ \mathbf{0} \end{pmatrix} \quad (3.1.7)$$

where  ${}^{n+1}\mathbf{J}$  is the Jacobian of the local problem defined in equation (3.1.6). The upper-left block-matrix of the inverse of  ${}^{n+1}\mathbf{J}$  contains the consistent tangent moduli. In the literature, compact expressions (after inverting  ${}^{n+1}\mathbf{J}$  and taking the upper-left block-matrix) of these moduli can be found for particular models (Ortiz and Martin 1989, Crisfield 1991, Simo and Hughes 1998). However, the more general expression given in equation (3.1.7) is preferred here because it highlights an important fact in the context of this work: the derivatives of the generalized flow vector needed to solve the local problem are also required in the computation of the consistent tangent matrix.

Numerical differentiation is used by Miehe (1996) to approximate *directly* the consistent tangent moduli  $d^{n+1}\boldsymbol{\sigma}/d^{n+1}\boldsymbol{\varepsilon}$  (or, more precisely, an equivalent expression for the large-strain problems treated there). The resulting algorithm has a considerable CPU overhead in comparison to analytical derivation (40% to 80%) because the derivatives of *all* the stress components with respect to *all* the strain components are approximated numerically.

### 3.1.3 Numerical differentiation

The derivatives of the generalized flow vector with respect to the generalized stresses are approximated by means of classical difference schemes. The approximation will be used for both the local and the global problems defined in the previous section. Thus, it must be accurate enough to maintain the characteristic quadratic convergence of the Newton-Raphson method.

Some authors (Jeremić and Sture 1994, 1997) suggest to approximate numerically the second derivatives of the flow potential  $G$  (recall that the flow vector is the derivative of the flow potential). The standard approach to obtain second order of accuracy is the typical centered difference scheme (Isaacson and Keller 1966, Dennis and Schnabel 1983, Hoffman 1982) applied to a general  $n$ -dimensional function,  $f(\mathbf{x})$ :

$$\frac{\partial^2 f}{\partial x_i^2} = \frac{f(\mathbf{x} + h_i \mathbf{e}_i) - 2f(\mathbf{x}) + f(\mathbf{x} - h_i \mathbf{e}_i)}{h_i^2} + \mathcal{O}(h_i^2). \quad (3.1.8)$$

In equation (3.1.8),  $x_i$  is the  $i$ th component of  $\mathbf{x}$ ,  $\mathbf{e}_i$  the  $i$ th unit vector,  $h_i$  the stepsize in the  $i$ th direction and the  $\mathcal{O}$  denotes the order of convergence. The scheme represented by equation (3.1.8) will be denoted by 2ND- $\mathcal{O}(h^2)$ , see table 3.1.

The approach used in this section consists on approximating numerically the first derivatives of (the analytical expression of) the flow vector. That is, the flow vector can be obtained via analytical differentiation of the flow potential (this step is relatively simple, even for complex constitutive

Notation	Description
1ND-O( $h$ )	Forward difference scheme for first derivatives of the flow vector
1ND-O( $h^2$ )	Centered difference scheme for first derivatives of the flow vector
1CND-O( $h^2$ )	Approximation to first derivatives of the flow vector using complex variable
2ND-O( $h^2$ )	Centered difference scheme for second derivatives of the flow potential

Table 3.1: Numerical approximations to the derivatives of the flow vector.

laws) or it can be an input of the model. Then, numerical differentiation is applied to approximate the derivatives of the flow vector (which is the computationally involved step for complex models). Standard forward or centered difference schemes are used:

$$\frac{\partial f}{\partial x_i} = \frac{f(\mathbf{x} + h_i \mathbf{e}_i) - f(\mathbf{x})}{h_i} + \mathcal{O}(h_i) \quad (3.1.9)$$

$$\frac{\partial f}{\partial x_i} = \frac{f(\mathbf{x} + h_i \mathbf{e}_i) - f(\mathbf{x} - h_i \mathbf{e}_i)}{2h_i} + \mathcal{O}(h_i^2) . \quad (3.1.10)$$

The schemes represented by equations (3.1.9) and (3.1.10) will be denoted by 1ND-O( $h$ ) and 1ND-O( $h^2$ ) respectively, see table 3.1.

It must be noted that the generic function  $f$  plays the role of a component of the flow vector in equations (3.1.9) and (3.1.10), whereas it denotes the flow potential in equation (3.1.8).

### Error analysis

The key issue in numerical differentiation is the choice of the stepsize  $h_i$ . Approximations based on difference schemes are affected by truncation and rounding errors (Stepleman and Winarsky 1979, Dennis and Schnabel 1983). The truncation errors (represented in equations (3.1.8–3.1.10) with the  $\mathcal{O}$  symbol) decrease as the stepsize tends to zero. The rounding errors, on the contrary, increase as the stepsize tends to zero. Therefore, there is an *optimal* stepsize  $h^{\text{opt}}$  that minimizes the summation of both errors.

Dennis and Schnabel (1983) present an expression of this optimal stepsize for first and second-order approximations to first derivatives (1ND-O( $h$ ) and 1ND-O( $h^2$ )) and for first-order approximation to second derivatives (not used in this section). Their work has been extended here to the case of second-order approximation to second derivatives (2ND-O( $h^2$ )).

The optimal stepsize  $h^{\text{opt}}$  can be written as

$$h^{\text{opt}} = h_r^{\text{opt}} \max\{|x|, \text{typ}_x\} , \quad (3.1.11)$$

where  $h_r^{\text{opt}}$  is the optimal *relative* stepsize and  $\text{typ}_x$  is a typical value of  $x$  used to avoid choosing a null (or extremely small)  $h^{\text{opt}}$  for null (or extremely small)  $x$ . Numerical experimentation shows that  $\text{typ}_x$  can be chosen in a rather arbitrary manner, because it has a very small influence on the results (in all the numerical examples of section 4,  $\text{typ}_x = 1$ ). The main idea behind equation (3.1.11) is that  $h_r^{\text{opt}}$  is independent of  $x$ . This means that a constant value of  $h_r^{\text{opt}}$  can be used all over the domain, for every load step, and all the stress components.

In general, it is not possible to compute the exact value of  $h_r^{\text{opt}}$ . This would require the rigorous minimization of the sum of truncation and rounding errors. However, the following expressions can be found after some simplifying assumptions:

$$1\text{ND} - \text{O}(h) : \quad h_r^{\text{opt}} = \sqrt{r_f} \quad (3.1.12)$$

$$1\text{ND} - \text{O}(h^2) : \quad h_r^{\text{opt}} = \sqrt[3]{r_f} \quad (3.1.13)$$

$$2\text{ND} - \text{O}(h^2) : \quad h_r^{\text{opt}} = \sqrt[4]{r_f} . \quad (3.1.14)$$

In equations (3.1.12–3.1.14),  $r_f$  is the accuracy in the evaluation of  $f$ . The expressions (3.1.12) and (3.1.13) are given by Dennis and Schnabel (1983). Expression (3.1.14) has been derived following the same arguments, as described next.

Consider equation (3.1.8). A standard error propagation analysis renders the following bound on the rounding error  $E^{\text{Ro}}$  in the approximation to the second derivative, i.e. errors induced by finite precision computations of the first term in the RHS of equation (3.1.8):

$$|E^{\text{Ro}}| \leq \frac{(4r_f + 12r)\hat{f}}{h^2}. \quad (3.1.15)$$

In equation (3.1.15),  $r$  is the machine precision ( $r \approx 10^{-16}$  in IEEE double precision),  $\hat{f}$  is an upper bound of  $|f|$  in the neighborhood of  $x$  and the subscript  $i$  is omitted from the stepsize  $h$  to ease the notation.

Regarding the truncation error  $E^{\text{Tr}}$ , i.e. the second term in the RHS of equation (3.1.8), a bound can be easily derived (Isaacson and Keller 1966, Hoffman 1982) as

$$|E^{\text{Tr}}| \leq \frac{\gamma h^2}{12}, \quad (3.1.16)$$

where  $\gamma$  is a bound on the fourth derivative of  $f$ . Putting equations (3.1.15) and (3.1.16) together, the following bound on the total error  $E^{\text{Tot}}$  is obtained:

$$|E^{\text{Tot}}| \leq |E^{\text{Tr}}| + |E^{\text{Ro}}| \leq \frac{\gamma h^2}{12} + \frac{(4r_f + 12r)\hat{f}}{h^2}. \quad (3.1.17)$$

The effect of the truncation error and the rounding error on the total error is clearly highlighted in a double logarithmic graph of  $E^{\text{Tot}}$  versus  $h$ : the rounding error contributes with a line of slope 2 (because second derivatives are approximated) and the truncation error with a line of slope  $-2$  (because a second-order scheme is used). Similar results are obtained for the other schemes, see Dennis and Schnabel (1983) and figures 3.1 and 3.3 of subsection 3.1.4.

The optimal value of the stepsize, which minimizes the bound of  $|E^{\text{Tot}}|$  given by equation (3.1.17) is

$$h^{\text{opt}} = \sqrt[4]{12(4r_f + 12r)\frac{\hat{f}}{\gamma}}. \quad (3.1.18)$$

The value of  $h^{\text{opt}}$  cannot be computed from equation (3.1.18): the values of  $\hat{f}$  and  $\gamma$  depend on  $x$ , and, in general, they are very difficult to approximate. Following Dennis and Schnabel (1983), it is assumed that

$$\frac{\hat{f}}{\gamma} \propto (\max\{|x|, \text{typ}_x\})^4, \quad (3.1.19)$$

where the fourth power is obtained as the sum of the degree of derivation and the order of the approximation (2 and 2), and  $\propto$  means “is proportional to”. This assumption is rather reasonable; it is verified, for instance, for monomials  $f(x) = x^\alpha$ . Combining equations (3.1.18) and (3.1.19) yields

$$h^{\text{opt}} \propto \sqrt[4]{\max\{r_f, r\} \max\{|x|, \text{typ}_x\}}. \quad (3.1.20)$$

Two further assumptions are needed: 1)  $r_f$  is larger or equal to  $r$  (if function  $f$  is simple, then  $r_f$  is similar to  $r$ , but if many operations are involved,  $r_f$  can be quite larger than  $r$ ) and 2) the proportionality constant can be taken as 1 (again a reasonable assumption, as illustrated by monomials  $f(x) = x^\alpha$ ). With these assumptions, one finally gets the expression of the relative optimal stepsize given in equation (3.1.14).

The concept of *relative* stepsize is essential in computational plasticity. In a global problem the range of values of the generalized stresses is usually very large, and the values of the different components at a certain Gauss point are very different. For this reason, the optimal stepsize  $h^{\text{opt}}$  can show huge variations. However, the previous analysis shows that the optimal relative stepsize  $h_r^{\text{opt}}$  can be assumed to be constant. Since a simple technique is wanted, the same value of  $h_r^{\text{opt}}$  (obtained from equations 3.1.12, 3.1.13 or 3.1.14, depending on the scheme) will be used for all

the computation. In fact, equations (3.1.12–3.1.14) are only used to select the *order of magnitude* of  $h_r^{\text{opt}}$ , because there is a wide range of relative stepsizes for which the difference schemes (3.1.8–3.1.10) are accurate enough to attain quadratic convergence. In this context, the assumptions needed to deduce the simplified expressions of  $h_r^{\text{opt}}$ , equations (3.1.12–3.1.14), do not restrict at all the applicability of the proposed approach. This point is illustrated in the next section by means of several numerical examples.

*Remark 3.1.1.* An unconventional approximation of first derivatives has also been used in this work. It is based on the theory of functions of complex variable (Lyness and Moler 1967, Squire and Trapp 1998). If  $f : \mathbb{C} \rightarrow \mathbb{C}$  is analytic in a neighborhood that contains the point  $z = (x, 0)$  (with  $z \in \mathbb{C}$  and  $x \in \mathbb{R}$ ) the first derivative of  $f : \mathbb{R} \rightarrow \mathbb{R}$  at  $x$  can be approximated with second order of accuracy as

$$\frac{df}{dx} = \frac{\text{Im}(f(x + ih))}{h} + \mathcal{O}(h^2) \quad (3.1.21)$$

where  $i = \sqrt{-1}$  and  $\text{Im}(f)$  represents the imaginary part of  $f$ . The main feature of this approximation is that it involves no subtractions, so the cancellation error typical of finite difference schemes (see equations 3.1.9 and 3.1.10) is avoided. The scheme represented by equation (3.1.21) will be denoted by 1CND- $\mathcal{O}(h^2)$ , see table 3.1. In many applications, but not in all, this approach has the advantage that it is not necessary to choose a stepsize close to the optimal one. In the next section, this approach is applied to some examples of computational plasticity, and the main issues are discussed. Further applications are presented in section 4.2.  $\square$

### 3.1.4 Examples

In this subsection, the applicability of numerical differentiation to solve the local and the global problem is assessed. Two plasticity models are used: the von Mises model, with perfect plasticity and with exponential hardening (Simo and Taylor 1985, Crisfield 1991), and the Rounded Hyperbolic Mohr-Coulomb (RHMC) model (Sloan and Booker 1986, Abbo and Sloan 1995). The von Mises flow potential depends only on the second invariant of the stress tensor, thus the analytical derivatives of the flow vector are simple to compute. It is used just as a validation test. The RHMC flow potential depends on the three invariants through a complicated expression. The analytical derivatives of the flow vector have quite involved expressions. Thus, it is a good model to check the performance of numerical differentiation.

First, the analytical derivatives of the flow vector are compared with the numerical approximations. Four possibilities for the evaluation of the numerical derivatives are analyzed (see table 3.1). The values of the optimal relative stepsize and the influence of the rounding and truncation errors are presented. After that, the numerical differentiation is applied to the computation of the Jacobian of the residual of the local problem. An example with the RHMC model is presented. It will be shown that any of the four numerical approximations defined in table 3.1 can be used to solve the local problem.

Finally, the numerical differentiation is applied to the computation of the consistent tangent matrix (global problem). Four examples are presented, two with von Mises plasticity and two with the RHMC model. With von Mises plasticity, a perforated strip under traction is analyzed (Simo and Taylor 1985), first considering perfect plasticity and after with exponential hardening. With the RHMC model, the vertical displacement of a pile (Potts and Gens 1985) and the behavior of a rigid footing (Abbo and Sloan 1996) are simulated. It will be shown that approximating numerically the first derivatives of the flow vector maintains the quadratic convergence of the Newton-Raphson method for a wide range of relative stepsizes, and that approximating the second derivatives of the flow potential does not.

### Comparison of numerical differentiation with analytical derivatives

In the following, analytical derivatives are compared with four numerical approximations: difference schemes of first and second-order of accuracy for first derivatives of the flow vector, 1ND- $\mathcal{O}(h)$  and 1ND- $\mathcal{O}(h^2)$  respectively; a difference scheme of second-order of accuracy for second derivatives of the flow potential, 2ND- $\mathcal{O}(h^2)$ ; and the approximation to the first derivatives of the flow vector

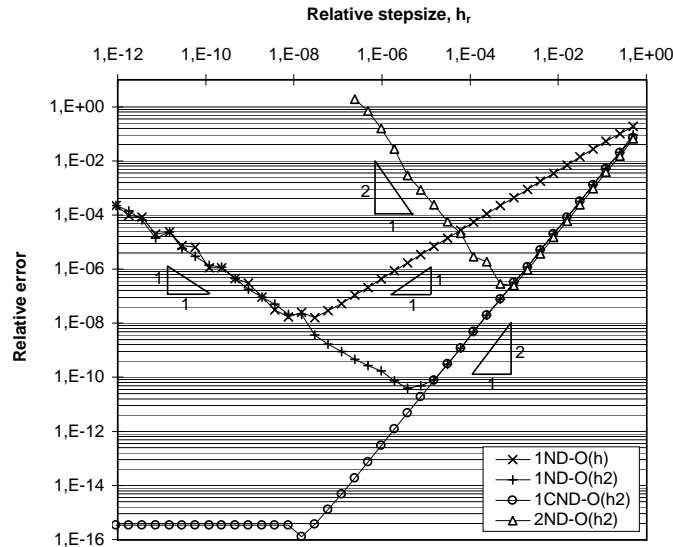


Figure 3.1: Relation between the relative error of the numerical approximations to the flow vector derivatives versus the relative stepsize, von Mises model.

based on complex variable theory defined in equation (3.1.21),  $1\text{CND-O}(h^2)$ . The four approximations are summarized in table 3.1. The influence of the relative stepsize on the rounding, truncation and total errors is analyzed. After that, the numerical differentiation will be applied to the local and the global problems.

**Von Mises model** The first example deals with the derivatives of the von Mises flow vector. The difference schemes present the typical relationship between the relative error of the approximation versus the relative stepsize (see figure 3.1). The influence of the different errors is clear: the left part of the curves correspond to the rounding errors and the right part to the truncation errors. Each of them have the expected slope. Moreover, the optimal relative stepsize  $h_r^{\text{opt}}$  of each approximation is in agreement with the corresponding expression, equations (3.1.12–3.1.14), with  $r_f \approx 10^{-16}$ . The value of  $r_f$  is close to  $r$  because the computation of the flow vector is very simple. In figure 3.1 the relative error of the  $1\text{CND-O}(h^2)$  approximation is also depicted. The main advantage of this approximation is that rounding errors are typically constant (i.e., they do not increase as the stepsize tends to zero) and very small. Thus, an arbitrarily small stepsize may be used. Below, this approach will be applied to the global problem and the main advantages will be highlighted.

The curves of figure 3.1 have been computed with a stress state where all the stress components are of the same order of magnitude. If this situation is maintained, the level of stress does not affect figure 3.1: the same curves are obtained for any level of stress. However, in a typical global problem the various components of the stress tensor can be very different (up to four orders of magnitude). It has been verified experimentally that, in these cases, the curves depicted in figure 3.1 are shifted to the right (the value of the  $h_r^{\text{opt}}$  can grow up to three orders of magnitude). For the numerical approximations to first derivatives of the flow vector ( $1\text{ND-O}(h)$ ,  $1\text{ND-O}(h^2)$  and  $1\text{CND-O}(h^2)$ ), this situation does not represent any practical problem. It will be shown in the applications to local and global problems that the range of relative stepsizes that give good results is large enough. Nevertheless, for the numerical approximation to second derivatives of the flow potential ( $2\text{ND-O}(h^2)$ ), the curve is also shifted upwards: the value of the minimum relative error (i.e., the relative error at  $h_r^{\text{opt}}$ ) can grow up to three orders of magnitude. Therefore, it can be anticipated that approximating the second derivatives of the flow potential is less adequate than approximating the first derivatives of the flow vector.

**Rounded Hyperbolic Mohr-Coulomb model** The numerical approximations to the flow vector derivatives of the Rounded Hyperbolic Mohr-Coulomb (RHMC) model have been also analyzed. The definition of the flow potential and its derivatives is presented by Abbo and Sloan



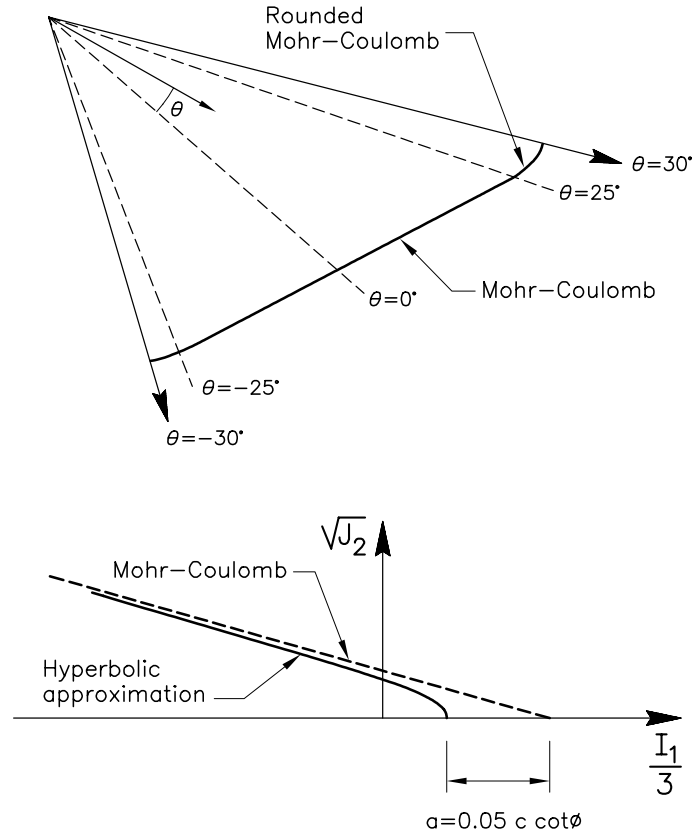


Figure 3.2: Main features of the Rounded Hyperbolic Mohr-Coulomb yield surface: trace on the deviatoric and meridian planes (after Abbo 1997).

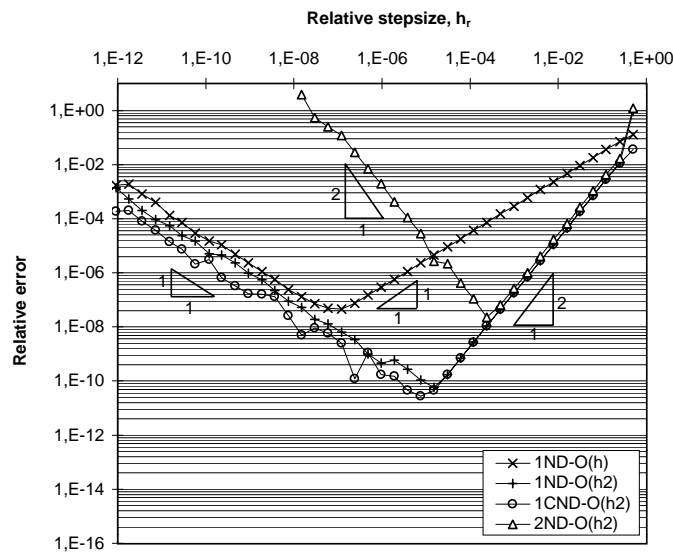


Figure 3.3: Relation between the relative error of the numerical approximations to the flow vector derivatives versus the relative stepsize, RHMC model.

(1995). The main features of the flow potential are summarized in figure 3.2 (associated plasticity is considered, so the yield function and the flow potential coincide). The definition of the flow potential is divided into two regions: one corresponding to the Hyperbolic Mohr-Coulomb zone that smoothes the apex of the classical Mohr-Coulomb model on the hydrostatic axis, and the other corresponding to the rounding zones, that smooth the corners present on the deviatoric

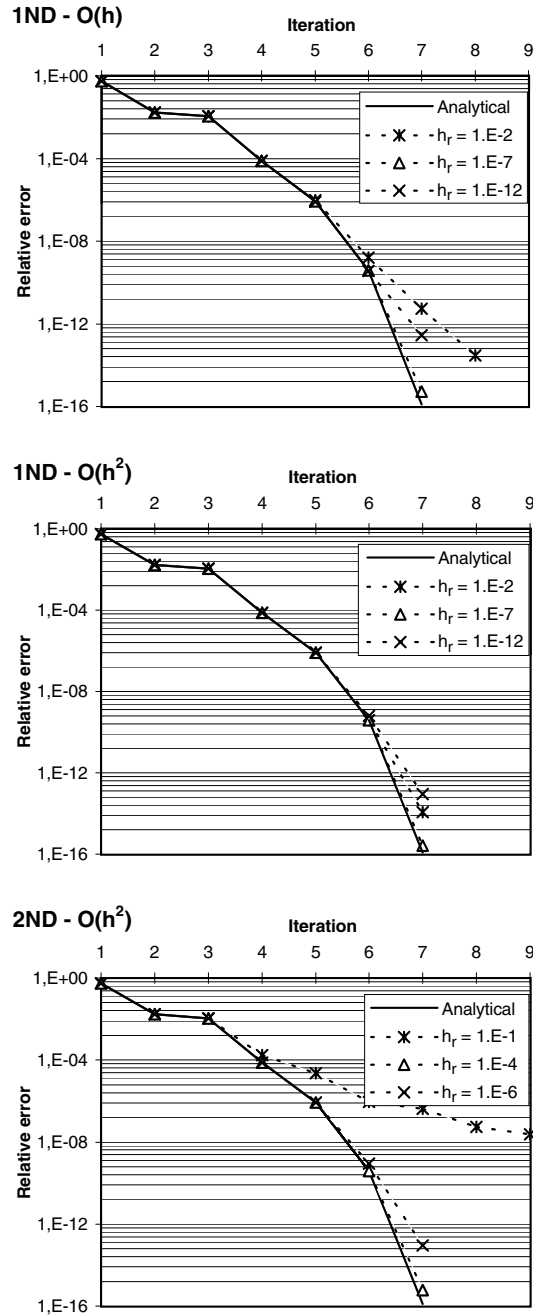


Figure 3.4: Convergence results of the local problem with RHC model.

plane. The dimensionless material parameters are a cohesion of  $\sqrt{3/2}$ , a friction angle of  $30^\circ$ , a Young modulus of 1040 and a Poisson coefficient of 0.3.

The relation between the relative error and the relative stepsize for the four numerical approximations (summarized in table 3.1) is depicted in figure 3.3. Results are very similar to those obtained with von Mises plasticity (figure 3.1). The main difference between the two models is the behavior of the 1CND- $O(h^2)$  approximation. For the RHC model, this approximation presents the same features of 1ND- $O(h^2)$ , the standard second-order approximation to the first derivative: rounding errors are not constant. This is caused by the routine used for the evaluation of the arcsin function (which appears in the RHC model, see Abbo and Sloan 1995) of a complex argument. FORTRAN compilers typically do not include the arcsin of a complex argument as an intrinsic

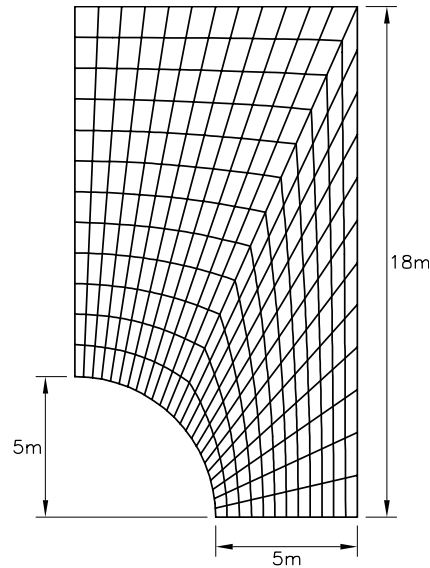


Figure 3.5: Perforated strip under traction (after Simo 1985). Due to symmetry, only one quarter is considered.

function. For this reason, a transformation based on logarithms was used for the computations shown here. This transformation is the origin of the non-constant rounding errors. If the arcsin is computed in a more accurate way (like the algebraic manipulator Maple does, for instance), constant and very small rounding errors are obtained, and the 1CND- $O(h^2)$  approximation exhibits its general behavior, illustrated in figure 3.1. However, with the routine used here rounding errors are not constant, so there is no improvement in using complex variables. In consequence, the approximation 1CND- $O(h^2)$  will not be used in the following examples of local and global problems with the RHMC model.

### Application to the local problem

Numerical differentiation is applied in order to compute the Jacobian shown in equation (3.1.6). Only the RHMC model is considered. Examples with von Mises model are not presented because with perfect plasticity the local problem is linear, and with exponential hardening the (nonlinear) local problem is so simple that the numerical approximations perform almost identically to the analytical derivatives.

In the local problem of the RHMC model, the Newton-Raphson method with the standard elastic predictor (the trial stresses, without any additional improvement) presents regions of non-convergence in the stress space, see section 3.2. However, in large regions of the stress space the local problem converges in few iterations, due to the special linear form of the yield surface. In order to check the applicability of numerical differentiation, a trial stress point located in an intermediate position has been chosen.

Figure 3.4 shows the convergence results of the local problem obtained with analytical derivatives and with the numerical approximations 1ND- $O(h)$ , 1ND- $O(h^2)$  and 2ND- $O(h^2)$  (the 1CND- $O(h^2)$  approximation is not used with the RHMC model because it presents the same behavior that 1ND- $O(h^2)$ , see figure 3.3). It is a plane strain problem, and the values of the material parameters are in figure 3.2. The trial stresses are  $\sigma_{xx} = -15$ ,  $\sigma_{yy} = -10$ ,  $\sigma_{zz} = -5$  and  $\sigma_{xy} = 15$ . The converged stresses are  $\sigma_{xx} = -20.5$ ,  $\sigma_{yy} = -17.2$ ,  $\sigma_{zz} = -10.2$  and  $\sigma_{xy} = 9.98$ . The problem is highly nonlinear: the Lode angle (defined in figure 3.2) changes from  $16^\circ$  at the trial state (Hyperbolic Mohr-Coulomb zone) to  $26.5^\circ$  at the converged state (Rounded zone).

The results of figure 3.4 show that, for the approximations 1ND- $O(h)$  and 1ND- $O(h^2)$ , quadratic convergence is achieved for a wide range of stepsizes. It is only lost if the relative stepsize is very different from the optimal one. On the contrary, the 2ND- $O(h^2)$  approximation is quite more sensible to the value of  $h_r$ . Numerical experimentation reveals that the key point for quadratic convergence is to use a  $h_r$  such that the relative error of the corresponding approximation of the

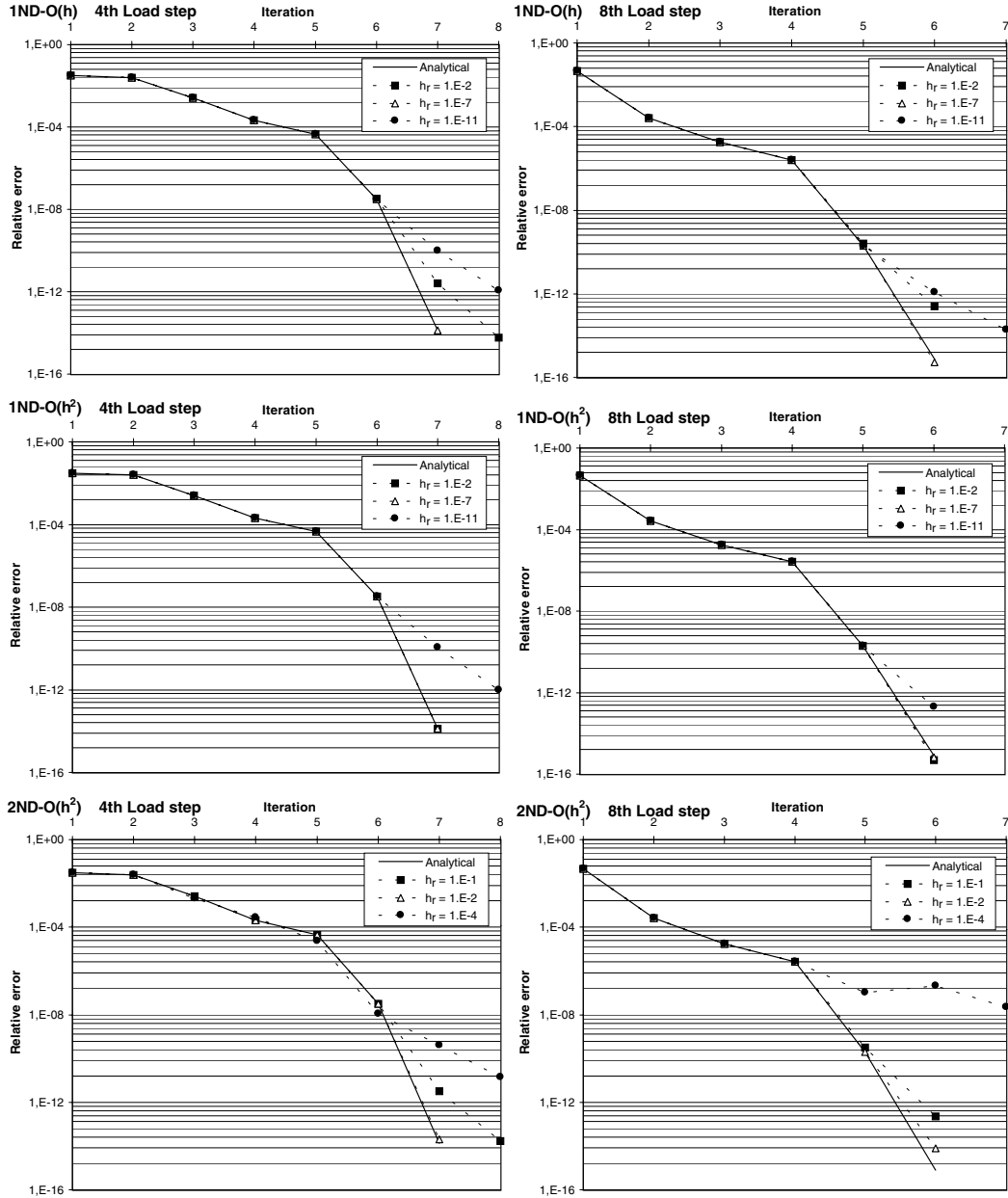


Figure 3.6: Convergence results for the fourth and the eighth load steps. Von Mises perfect plasticity.

analytical derivatives is less than  $10^{-5}$  —  $10^{-6}$ . It can be checked in figure 3.3 that this constraint yields a large interval of acceptable relative stepsizes for the numerical approximations to first derivatives of the flow vector, and a quite narrower one for the numerical approximation to second derivatives of the flow potential. In any case, the three difference schemes (1ND- $O(h)$ , 1ND- $O(h^2)$  and 2ND- $O(h^2)$ ) are valid for the local problem.

#### Application to the global problem

Numerical differentiation is applied to solve several boundary value problems (i.e., global problems). That is, the numerical approximations of table 3.1 are employed to compute consistent tangent matrices. Moreover, in the examples with the RHMC model, they are also used to solve the local problem. For all the stress components and over the whole domain a constant relative stepsize has been used.

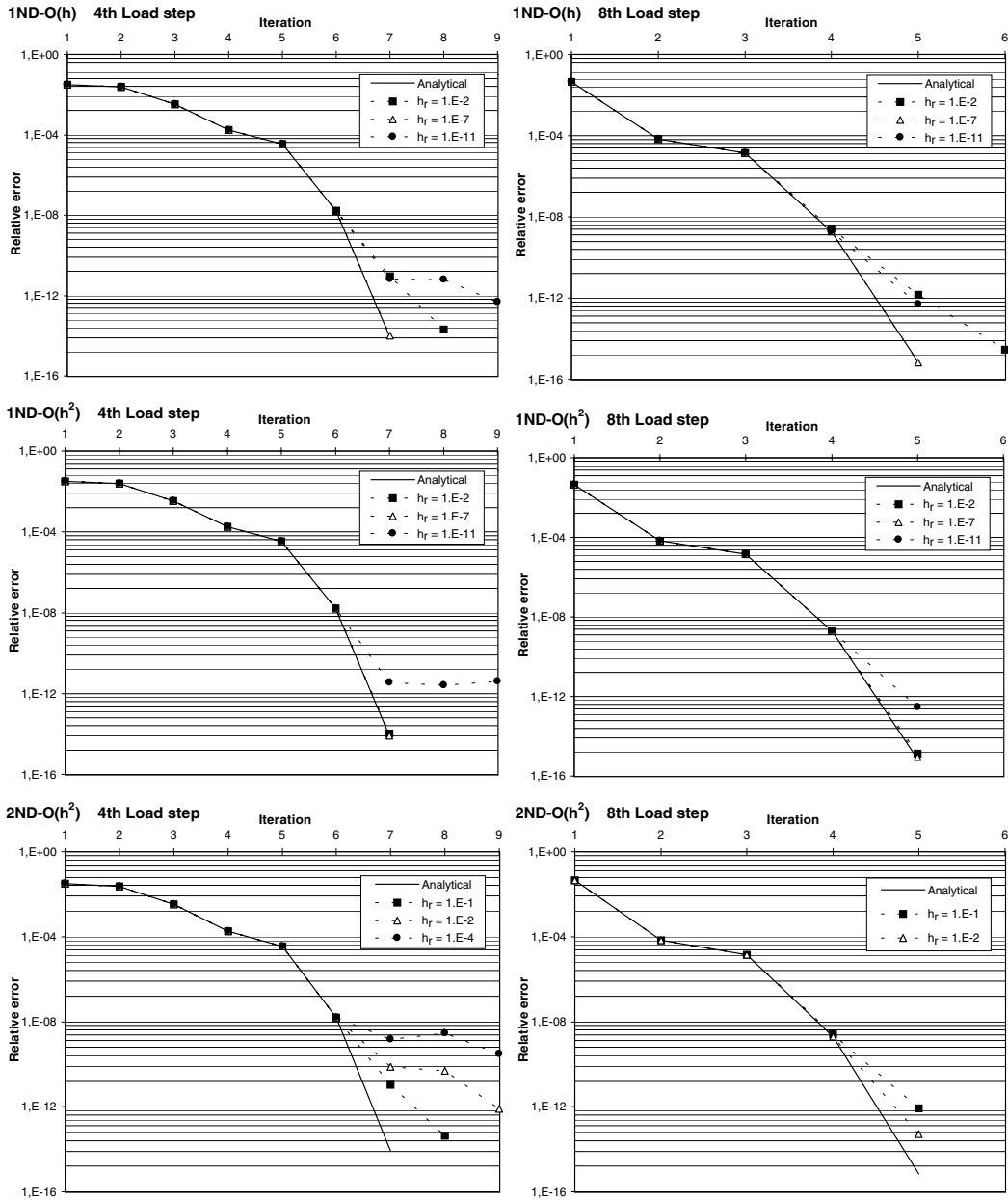


Figure 3.7: Convergence results for the fourth and the eighth load steps. Von Mises exponential hardening plasticity.

Four examples are presented: two with von Mises plasticity and two more with the RHMC model. These examples will illustrate that any numerical approximation to first derivatives of the flow vector (1ND- $O(h)$ , 1ND- $O(h^2)$  and 1CND- $O(h^2)$ ) is useful to solve the global problem with quadratic convergence. On the contrary, approximating numerically the second derivatives of the flow potential (2ND- $O(h^2)$ ) is not robust enough to achieve quadratic convergence.

**Von Mises model with perfect plasticity** First, a perforated strip under uniaxial traction is analyzed with von Mises perfect plasticity. This test is presented by Simo and Taylor (1985), and it is depicted in figure 3.5. A total displacement of 0.2 m is imposed in ten steps.

The convergence results for the fourth and the eighth load steps obtained with the analytical consistent tangent matrix and with numerical differentiation are compared in figure 3.6. The ranges of relative stepsizes that give the *same* convergence results that analytical consistent tangent

Num. approx.	Range of $h_r$
1ND-O( $h$ )	$(10^{-4}) - 10^{-5} - 10^{-7} - (10^{-8})$
1ND-O( $h^2$ )	$(10^{-2}) - 10^{-3} - 10^{-8} - (10^{-9})$
1CND-O( $h^2$ )	$(10^{-2}) - 10^{-3} - \dots$
2ND-O( $h^2$ )	$(10^{-2})$

Table 3.2: Relative stepsizes that give the same convergence results as analytical derivatives, for the von Mises perfect plasticity global problem.

Num. approx.	Range of $h_r$
1ND-O( $h$ )	$(10^{-4}) - 10^{-5} - (10^{-6})$
1ND-O( $h^2$ )	$10^{-3} - 10^{-5} - (10^{-6}) - (10^{-7})$
1CND-O( $h^2$ )	$10^{-3} - \dots$
2ND-O( $h^2$ )	—

Table 3.3: Relative stepsizes that give the same convergence results as analytical derivatives, for the von Mises exponential hardening global problem.

matrix (up to a relative error in energy of  $10^{-12}$ ) are presented in table 3.2 (convergence results are considered to be the *same* if the energy error has the same order of magnitude during all the iterations of all the load steps). Also in table 3.2, between parenthesis, the values of  $h_r$  that give *almost the same* results as the analytical derivatives are indicated (convergence results are considered to be *almost the same* if the energy error has the same order of magnitude during all the iterations except the last one of each load step). It can be seen that the difference schemes for first derivatives, 1ND-O( $h$ ) and 1ND-O( $h^2$ ), give the same result that analytical differentiation for a wide range of relative stepsizes, even though a very strict tolerance has been used. As expected, second-order of accuracy presents a wider range of adequate relative stepsizes than first-order. The 1CND-O( $h^2$ ) approximation presents the same convergence results as the 1ND-O( $h^2$ ) one for relative stepsizes higher than the optimal one. Moreover, in agreement with the previous results (see figure 3.1), it maintains the quadratic convergence for arbitrarily small relative stepsizes. On the other hand, the numerical difference scheme for second derivatives of the flow potential, 2ND-O( $h^2$ ), does not give very good results even in this simple boundary value problem (the typical quadratic convergence is lost).

**Von Mises model with exponential isotropic hardening** The perforated strip under traction has also been simulated using the von Mises model with exponential isotropic hardening. The problem definition is the same of Simo and Taylor (1985), except for the plastic parameters: the initial yield stress is equal to 0.243 MPa, the yield stress at infinite equivalent plastic strain is 0.729 MPa and the exponential parameter is 0.1 MPa. In figure 3.7, the convergence results for the fourth and the eighth load steps are depicted, and in table 3.3 the ranges of relative stepsizes that give the same convergence results that analytical consistent tangent matrices are presented. The results are more strict than those obtained with perfect plasticity: numerical first derivatives present a narrower range of relative stepsizes that give the same results as analytical derivatives, and the numerical second derivatives do not attain quadratic convergence. Moreover, note that the optimal relative stepsize is higher than the one of figure 3.1. This is in agreement with the previous comments about the value of  $h_r^{\text{opt}}$  when the components of the stress tensor have very different values. On the other hand, the 1CND-O( $h^2$ ) approximation presents the same behavior as in perfect plasticity: the results are the same as the 1ND-O( $h^2$ ) approximation for  $h_r$  higher than the optimal one, and quadratic convergence is achieved for arbitrarily small  $h_r$ .

The main conclusion of the two examples with von Mises plasticity is that numerical first derivatives of the flow vector do not affect the properties of convergence of the Newton-Raphson method (i.e., the global consistent tangent matrix is accurately approximated). The typical difference schemes present an adequate behavior for a wide range of relative stepsizes. And the unconventional approximation based on complex variable theory allows to use stepsizes as small as wanted. On the other hand, it has been shown that the numerical second derivatives of flow potential are not robust enough: they do not work properly in demanding boundary value problems.

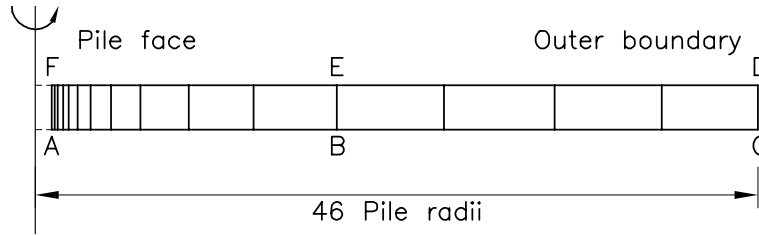


Figure 3.8: Pile problem (after Potts and Gens 1985).

(a)	Analytic	$10^{-3}$	$10^{-5}$	$10^{-7}$	$10^{-9}$
1	2.2 E+00	2.2 E+00	2.2 E+00	2.2 E+00	2.2 E+00
2	1.5 E-03	1.5 E-03	1.5 E-03	1.5 E-03	1.5 E-03
3	3.1 E-05	3.1 E-05	3.1 E-05	3.1 E-05	3.1 E-05
4	8.6 E-09	1.3 E-07	8.6 E-09	8.6 E-09	8.6 E-09
5	4.6 E-15	1.7 E-09	4.7 E-15	1.4 E-13	8.0 E-12
6		2.6 E-11			8.7 E-12
7		3.4 E-13			1.1 E-11
8					...

(b)	Analytic	$10^{-2}$	$10^{-3}$
1	2.2 E+00	2.2 E+00	2.2 E+00
2	1.5 E-03	1.5 E-03	1.5 E-03
3	3.1 E-05	4.0 E-05	3.0 E-05
4	8.6 E-09	7.2 E-06	1.8 E-07
5	4.6 E-15	8.6 E-07	1.7 E-08
6		1.3 E-07	1.5 E-09
7		1.7 E-08	1.4 E-10
8		2.4 E-09	1.3 E-11
9		3.2 E-10	1.2 E-12
10		4.5 E-11	2.1 E-13
11		...	

Table 3.4: The convergence results for sixth load step of the pile problem: (a) 1ND- $O(h)$ , (b) 2ND- $O(h^2)$ .

In the following, the applicability of the approximations 1ND- $O(h)$ , 1ND- $O(h^2)$  and 2ND- $O(h^2)$  to the Rounded Hyperbolic Mohr-Coulomb (RHMC) model is assessed by means of two boundary value problems. In both problems numerical differentiation is applied to the local and the global problem simultaneously.

**RHMC model: vertical displacement of a pile** The first problem is the vertical displacement of a pile. The definition of the problem is presented by Potts and Gens (1985), and it is only summarized here. Figure 3.8 shows the finite element mesh. It corresponds to a horizontal disc of soil. The thickness of the disc is 5 units of length (u.l.) and the pile radius is 7.5 u.l. To model the loading of the pile, a vertical displacement of 2 u.l. is imposed over the boundary AF in 20 load steps. To model the infinite extension of the disc, zero vertical displacement is imposed over the boundary CD. Due to the essentially one-dimensional nature of the problem, vertical lines (such as EB) are prescribed to remain vertical during loading.

Table 3.4 shows the convergence results for the tenth load step, and in table 3.5 the ranges of relative stepsizes that give the same convergence results that analytical consistent tangent matrices are presented. It is clear that the numerical approximations to the second derivatives of the flow potential, 2ND- $O(h^2)$ , do not yield quadratic convergence. To reach quadratic convergence it would be necessary to do a supplementary effort to choose a correct stepsize at each Gauss point. The results of the approximation 1ND- $O(h)$  are quite similar to the previous example, see table

Num. approx.	Range of $h_r$
1ND-O( $h$ )	$(10^{-4}) - 10^{-5} - (10^{-6})$
1ND-O( $h^2$ )	$10^{-4} - 10^{-6} - (10^{-7})$
2ND-O( $h^2$ )	—

Table 3.5: Relative stepsizes that give the same convergence results as analytical derivatives, for the pile problem.

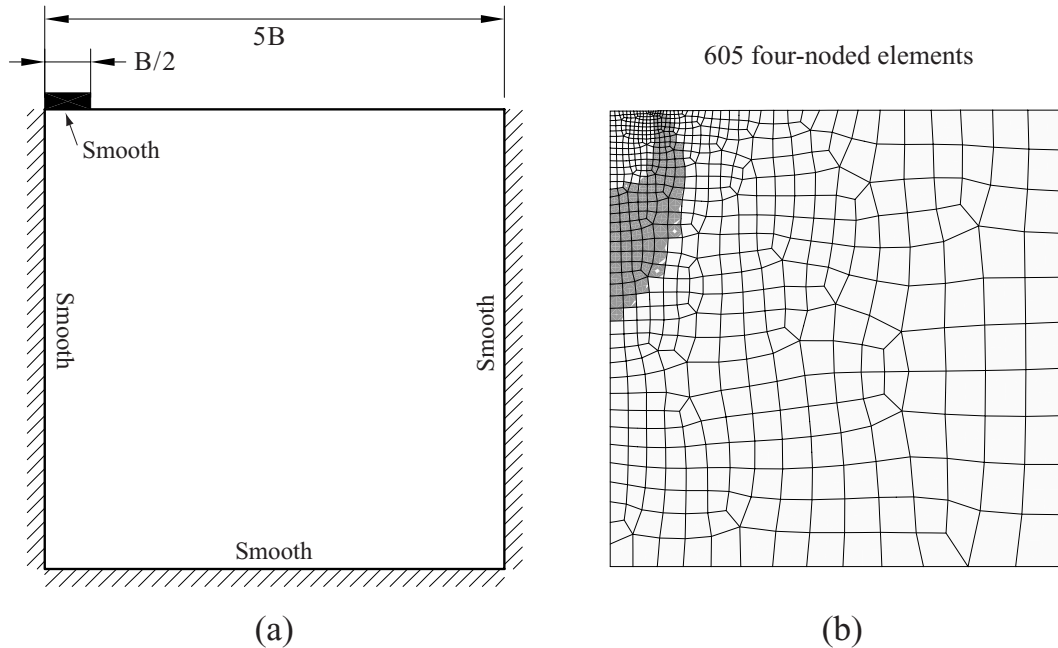


Figure 3.9: Rigid footing: (a) problem definition, (b) mesh and final plastic strains. Due to symmetry, only one half is considered.

3.3. The  $h_r$  that gives quadratic convergence in the global problem is higher than the estimated value from an analysis of the approximations to the flow vector derivatives (see figure 3.3). This is in agreement with the previous analysis of the influence of the stresses on the value  $h_r^{\text{opt}}$ . On the other hand, although one may conclude from table 3.5 that the range of adequate  $h_r$  is quite small, it must be pointed out that the comparison has been done up to a very strict tolerance of  $10^{-12}$ . If the results are compared to a tolerance of  $10^{-8}$  (that for a relative energy error is still a strict tolerance), the range becomes  $10^{-4}$  to  $10^{-9}$ . Thus, the 1ND-O( $h$ ) approximation is accurate enough.

The results of 1ND-O( $h^2$ ) are also similar to previous ones: the range of adequate  $h_r$  is larger than for 1ND-O( $h$ ), see table 3.5. Nevertheless, if realistic tolerances are considered (i.e.,  $10^{-8}$  or higher), the advantage of second order approximation is lost: the two alternatives give good results for a very wide range of relative stepsizes. Moreover, since the computational cost (the number of evaluations of the flow vector) of the first-order approximation is half of the second-order one, it can be concluded that the first-order scheme is more suitable.

**RHMC model: vertical displacement of a rigid footing** The second global problem solved using the RHMC model is the vertical displacement of a rigid footing (Abbo and Sloan 1996). The scheme of the problem is depicted in figure 3.9(a), and the mesh and the final distribution of plastic strains are shown in figure 3.9(b). The dimension of the rigid footing,  $B$ , is 20 units of length (u.l.) and a vertical displacement of 0.02 u.l. is imposed in 20 increments.

The convergence results for the load steps fifteen and twenty are shown in figure 3.10, and the ranges of relative stepsizes that give the same convergence results that analytical consistent tangent matrices are presented in table 3.6. The results are similar to previous ones: the 1ND-O( $h$ ) approximation gives quadratic convergence with a small range of relative stepsizes if a very strict



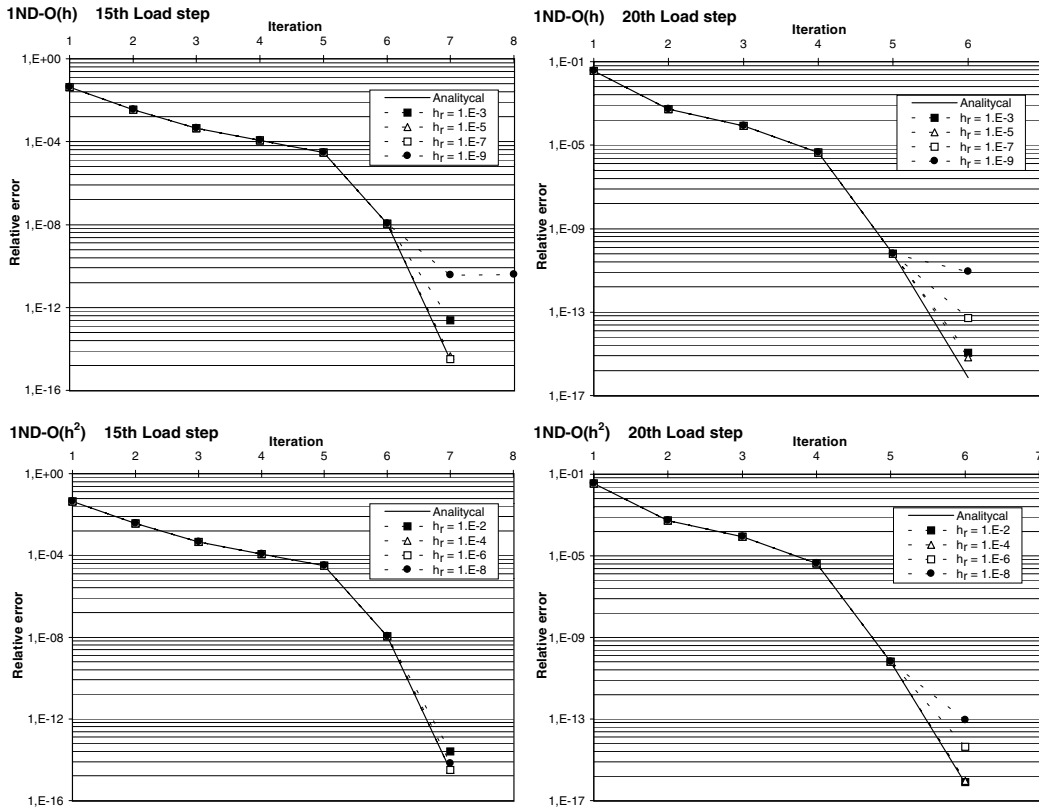


Figure 3.10: Convergence results for the load steps fifteen and twenty. Rigid footing with RHMIC model.

Num. approx.	Range of $h_r$
1ND-O( $h$ )	$(10^{-4}) - 10^{-5} - (10^{-6}) - (10^{-7})$
1ND-O( $h^2$ )	$(10^{-2}) - 10^{-3} - 10^{-5} - (10^{-6}) - (10^{-8})$

Table 3.6: Relative stepsizes that give the same convergence results as analytical derivatives, for the rigid footing problem.

tolerance is used ( $10^{-12}$ ), and with second-order of accuracy, 1ND-O( $h^2$ ), the range of relative stepsizes is wider. However, as in the pile problem example, with a tolerance of  $10^{-8}$  almost any relative stepsize gives good results for both approximations. Therefore, for practical applications the first-order difference scheme approximation, 1ND-O( $h$ ), is accurate enough. Moreover, the choice of the relative stepsize is not a problem (as in the previous example, the values of  $h_r$  between  $10^{-4}$  and  $10^{-9}$  give quadratic convergence up to a relative error less than  $10^{-8}$ ).

In this global problem, the computing time of the alternatives 1ND-O( $h$ ) and 1ND-O( $h^2$ ) has been analyzed. In table 3.7 there are the time overheads with respect to the problems solved with analytical consistent tangent matrices. All the approximations, except 1ND-O( $h$ ) with  $h_r = 10^{-3}$ , have needed the same number of iterations. For this particular case, the 1ND-O( $h$ ) approximation is between 1 — 1.5% more expensive than the one computed with the analytical derivatives, and the 1ND-O( $h^2$ ) is between 2.6 — 2.8%. Therefore, the computational cost of the proposed approach is marginal, even in the context of material models (von Mises and RHMIC) where analytical derivatives are available and relatively simple to compute.

The main conclusion of these last two examples is that typical difference schemes applied to first derivatives of the flow vector are adequate to approximate the consistent tangent matrix and the Jacobian of the residual of the integration rule for highly nonlinear flow potentials. The convergence properties are the same that with analytical derivatives for a wide range of relative stepsizes. The first-order approximation is enough to maintain quadratic convergence up to a tolerance of less

$h_r$	1ND-O( $h$ )	1ND-O( $h^2$ )
$10^{-3}$	4.1%	2.8%
$10^{-4}$	2.5%	3.4%
$10^{-5}$	1.5%	2.6%
$10^{-6}$	1.0%	2.8%
$10^{-7}$	1.4%	2.6%
$10^{-8}$	1.2%	3.8%

Table 3.7: Time overheads of the numerical approximations, for the rigid footing problem.

than  $10^{-8}$ . Nevertheless, for tolerances less or equal to  $10^{-12}$ , second-order accuracy is needed in order to have a wide range of relative stepsizes. Finally, for complex models the numerical second derivatives of the flow potential are not robust enough to maintain quadratic convergence, even in simple boundary value problems.

### 3.1.5 Concluding remarks

It has been shown that numerical differentiation is a useful tool in computational plasticity, both in the integration of the constitutive law (local problem) and in the computation of the consistent tangent matrix (global problem).

The analytical derivatives of the generalized flow vector with respect to the generalized stresses are the components most difficult to compute in the consistent tangent matrix and the Jacobian of the local residual. In some cases, they are not even available. The main conclusion of this section is that numerical differentiation is a valid alternative to analytical derivatives.

Two approaches are possible: 1) approximating the second derivatives of the flow potential (recall that the flow vector is the first derivative of the flow potential) or 2) approximating the first derivatives of the (analytical) flow vector. The first approach, suggested in the literature, is not robust enough. It can be used to solve the local problem, but not the global problem. The resulting consistent tangent matrices are not accurate enough and the Newton-Raphson method loses its characteristic quadratic convergence. The second approach, on the contrary, is a simple and robust alternative to analytical differentiation. Quadratic convergence is achieved, both for simple (von Mises) and more complicated (Rounded Hyperbolic Mohr-Coulomb) material models.

Various schemes may be used to approximate the first derivatives of the flow vector: the classical first-order and second-order difference schemes, and an unconventional second-order approximation based on complex variable theory. The first-order approximation maintains quadratic convergence up to a tolerance of less than  $10^{-8}$ , and the second-order approximations up to less than  $10^{-12}$ . Thus, all of them are accurate enough for any practical application.

The choice of an adequate stepsize (a typical problem of difference schemes) does not present any difficulty. The concept of the relative stepsize has been presented, and it has been verified that the three approximations to first derivatives of the flow vector give good results with a wide range of relative stepsizes. That is, the proposed strategy is very robust in the sense that the choice of the stepsize has a very small influence on its performance. Moreover, the complex variable approximation presents a very interesting property: the rounding errors are very small and constant (i.e., they do not increase as the stepsize tends to zero), so arbitrarily small stepsizes may be used.

The computational overhead of the proposed strategy (with respect to analytical derivatives) is marginal, even for material models where the analytical derivatives have relatively simple expressions. This result is in sharp contrast with previous applications of numerical differentiation to computational plasticity (Jeremić and Sture 1994, 1997, Miehe 1996). In section 4.2 (Pérez-Foguet et al. 2000e), numerical differentiation is applied to more complex constitutive models, where analytical derivatives are not available.

## 3.2 Consistent tangent matrices for substepping schemes

A very simple and general expression of the consistent tangent matrix for substepping time-integration schemes is presented. If needed, the derivatives required for the computation of the

consistent tangent moduli can be obtained via numerical differentiation. These two strategies (substepping and numerical differentiation) lead to quadratic convergence in complex nonlinear inelasticity problems.

### 3.2.1 Introduction

Consistent tangent matrices (Simo and Taylor 1985, Runesson et al. 1986) are an essential ingredient for the efficient solution via implicit methods of complex problems in nonlinear computational mechanics. The expression of the consistent tangent matrix for a wide variety of material models can be found in the literature. *Consistent* means consistent with the numerical time-integration scheme used to solve the local problems (i.e. the time-integration of the constitutive equation at the Gauss-point level), which is typically the backward Euler or the midpoint rule. Consistent tangent matrices are needed to solve the so-called global problem (i.e. the elastoplastic boundary value problem) with quadratic convergence, via a full Newton-Raphson linearization. The local counterpart is also needed to integrate the local problem and obtain quadratic convergence.

For complex models (for instance, with a highly nonlinear coupling between hardening-softening parameters), the convergence of these local problems can be a major issue, and pose severe restrictions to the time increment. This situation is also found with relatively simple models (i.e., perfect plasticity models) at Gauss points with stress states in zones of high curvature of the yield function. In both cases the plastic corrector often has difficulties in returning back to the yield surface (Bićanić and Pearce 1996).

A possible approach would be to use smaller time-steps. However, this amounts to letting the most restrictive Gauss point control the global problem. Various alternative strategies can be found in the literature. For instance, better initial approximations for the local nonlinear problem can be obtained by defining specific auxiliary predictor surfaces (Bićanić and Pearce 1996), or line-search schemes can be used to enlarge the convergence region of the Newton-Raphson method (Armero and Pérez-Foguet 2000, Pérez-Foguet and Armero 2000). These two strategies have been applied successfully to several plasticity models. However they cannot be regarded as the ultimate solution, especially for problems where complex models are involved.

Another approach, also successfully applied in various situations, is substepping (Sloan 1987, Sloan and Booker 1992, Potts and Ganendra 1994, Abbo and Sloan 1996). The time-step is subdivided into a number of substeps (which can be different for each Gauss point), and a single-step integration rule is employed within each one. If an explicit rule (forward Euler) is chosen, no iterations are needed at the local level. In fact, substepping is sometimes used in combination with explicit time-marching schemes for dynamic problems, to meet the stability constraints without resorting to very small time-steps. If an implicit rule (backward Euler or midpoint rule) is preferred, then the corresponding single-step nonlinear problems have to be solved. This can be done, for instance, by means of the standard Newton-Raphson method, eventually combined with any acceleration technique such as auxiliary predictor surfaces or line-search.

If an implicit time-marching scheme is used for the boundary value problem, global iterations are needed, whatever the choice of the integration rule at the local level (even if an explicit rule is used at the local level, the global problem is implicit). To achieve quadratic convergence with the Newton-Raphson method, the local problem must be consistently linearized.

The major contribution of this section is the expression of the consistent tangent matrix in the framework of substepping schemes. The proposed expression is general: it can be used for any subdivision of the step into (uniform or non-uniform) substeps, and for any single-step integration scheme within each substep. It is also simple: the expression of the consistent tangent moduli has the same structure of the corresponding scheme without substepping. From a practical viewpoint, the proposed expression allows to use substepping, thus circumventing the use of very small load increments, and attain quadratic convergence at global level. The substeps at each Gauss point are automatically chosen by monitoring the convergence of the local problem. In many applications, the demand for substepping is concentrated in a reduced number of Gauss points, while substepping is not activated in the rest of the domain. As a consequence, the computational cost of substepping is marginal in comparison with the cost of global equilibrium iterations. These aspects are illustrated by means of some numerical examples regarding the Rounded Hyperbolic Mohr-Coulomb model (Sloan and Booker 1986, Abbo and Sloan 1995).

The most involved step in obtaining consistent tangent matrices (either with or without substepping) is computing the derivatives of the constitutive equation with respect to stresses and internal variables. These derivatives are also needed to solve the local problems via the Newton-Raphson method.

For simple models, analytical derivatives are readily available, and this leads to compact, explicit expressions of the consistent tangent matrix. In more complicated models, analytical differentiation is rather more cumbersome. For this reason, a different approach is proposed: derivatives are approximated by means of classical difference schemes. The approximated derivatives are then used to solve the local problems and to compute the consistent tangent matrix. As shown in sections 3.1 and 4.2 (Pérez-Foguet et al. 2000*d*, 2000*e*), this approach is both robust and computationally efficient. Quadratic convergence is maintained, provided that adequate difference schemes and stepsizes (i.e. the perturbation of the difference scheme) are chosen.

Going beyond sections 3.1 and 4.2, where only the single-step backward Euler rule is considered, this section shows that substepping and numerical differentiation can be combined to obtain the consistent tangent matrix leading to quadratic convergence in complex situations, where 1) analytical derivatives of the constitutive equation are not available and 2) the use of single-step integration rules would demand prohibitively small time-steps. This point is illustrated in some examples with the MRS-Lade model (Sture et al. 1989, Pérez-Foguet and Huerta 1999, Pérez-Foguet et al. 2000*e*).

### 3.2.2 Problem statement

#### Preliminaries

Many elastoplastic models for small strains can be put in the general form (Ortiz and Popov 1985)

$$\begin{aligned}\boldsymbol{\varepsilon} &= \boldsymbol{\varepsilon}^e + \boldsymbol{\varepsilon}^p \\ \boldsymbol{\sigma} &= \mathbf{E}\boldsymbol{\varepsilon}^e \\ \dot{\boldsymbol{\varepsilon}}^p &= \dot{\lambda}\mathbf{m}(\boldsymbol{\sigma}, \boldsymbol{\kappa}) \\ \dot{\boldsymbol{\kappa}} &= \dot{\lambda}\mathbf{h}(\boldsymbol{\sigma}, \boldsymbol{\kappa}),\end{aligned}\tag{3.2.1}$$

where  $\boldsymbol{\varepsilon}$ ,  $\boldsymbol{\varepsilon}^e$  and  $\boldsymbol{\varepsilon}^p$  are the total, elastic and plastic strain tensors respectively,  $\boldsymbol{\sigma}$  is the Cauchy stress tensor,  $\mathbf{E}$  is the elastic stiffness tensor,  $\mathbf{m}$  is the flow vector,  $\boldsymbol{\kappa}$  is the set of internal variables and  $\mathbf{h}$  are the plastic moduli. The plastic multiplier  $\dot{\lambda}$  is determined with the aid of the loading-unloading criterion, that can be expressed in Kuhn-Tucker form as

$$F(\boldsymbol{\sigma}, \boldsymbol{\kappa}) \leq 0 \quad \dot{\lambda} \geq 0 \quad F(\boldsymbol{\sigma}, \boldsymbol{\kappa})\dot{\lambda} = 0,\tag{3.2.2}$$

where  $F(\boldsymbol{\sigma}, \boldsymbol{\kappa})$  is the yield function that defines the admissible stress states.

#### Single-step numerical time-integration

Time-integration of equation (3.2.1) with the backward Euler scheme yields the following nonlinear local problem (Ortiz and Popov 1985, Simo and Hughes 1998):

$$\begin{aligned}{}^{n+1}\boldsymbol{\sigma} + \lambda\mathbf{E}\mathbf{m}({}^{n+1}\boldsymbol{\sigma}, {}^{n+1}\boldsymbol{\kappa}) &= {}^n\boldsymbol{\sigma} + \mathbf{E}\Delta\boldsymbol{\varepsilon} \\ {}^{n+1}\boldsymbol{\kappa} - \lambda\mathbf{h}({}^{n+1}\boldsymbol{\sigma}, {}^{n+1}\boldsymbol{\kappa}) &= {}^n\boldsymbol{\kappa} \\ F({}^{n+1}\boldsymbol{\sigma}, {}^{n+1}\boldsymbol{\kappa}) &= 0.\end{aligned}\tag{3.2.3}$$

In equation (3.2.3), the state at time  ${}^nt$  (i.e., quantities  ${}^n\boldsymbol{\sigma}$  and  ${}^n\boldsymbol{\kappa}$ ) and the increment of *total* strains from time  ${}^nt$  to time  ${}^{n+1}t$ ,  $\Delta\boldsymbol{\varepsilon}$ , are known. The unknowns of this local problem are the stresses  ${}^{n+1}\boldsymbol{\sigma}$  and the internal variables  ${}^{n+1}\boldsymbol{\kappa}$  at time  ${}^{n+1}t$ , and the incremental plastic multiplier  $\lambda$ .

To solve this nonlinear local problem with the Newton-Raphson method, the Jacobian of the residual is needed. Using standard vector notation in computational mechanics (Zienkiewicz and

(Taylor 1988, Crisfield 1991), the Jacobian at  ${}^{n+1}t$  can be written as

$${}^{n+1}\mathbf{J} = \begin{pmatrix} (\mathbf{I}_{n_\sigma} + \lambda \mathbf{E} \frac{\partial \mathbf{m}}{\partial \boldsymbol{\sigma}}) & \lambda \mathbf{E} \frac{\partial \mathbf{m}}{\partial \boldsymbol{\kappa}} & \mathbf{E} \mathbf{m} \\ -\lambda \frac{\partial \mathbf{h}}{\partial \boldsymbol{\sigma}} & (\mathbf{I}_{n_\kappa} - \lambda \frac{\partial \mathbf{h}}{\partial \boldsymbol{\kappa}}) & -\mathbf{h} \\ \mathbf{n}^T & \boldsymbol{\xi}^T & 0 \end{pmatrix}_{t={}^{n+1}t}, \quad (3.2.4)$$

where  $\mathbf{n}$  and  $\boldsymbol{\xi}$  are the derivatives of  $F(\boldsymbol{\sigma}, \boldsymbol{\kappa})$  with respect to  $\boldsymbol{\sigma}$  and  $\boldsymbol{\kappa}$  respectively, the superscript  $T$  denotes transpose,  $n_\sigma$  is the dimension of the stress vector,  $n_\kappa$  is the number of internal variables and  $\mathbf{I}_*$  is the identity matrix of order  $*$ .

In order to solve the local problem, an initial approximation for the unknowns is also needed. The standard choice is the *elastic trial* state, which is

$${}^{n+1}\boldsymbol{\sigma}^0 = {}^n\boldsymbol{\sigma} + \mathbf{E} \Delta \boldsymbol{\varepsilon}, \quad {}^{n+1}\boldsymbol{\kappa}^0 = {}^n\boldsymbol{\kappa} \quad \text{and} \quad \lambda^0 = 0. \quad (3.2.5)$$

Moreover, to solve the global problem with quadratic convergence it is necessary to use the consistent tangent matrix (Simo and Taylor 1985, Runesson et al. 1986). To compute this matrix, the consistent tangent moduli  $d{}^{n+1}\boldsymbol{\sigma}/d{}^{n+1}\boldsymbol{\varepsilon}$  at each Gauss point are needed. They are obtained by linearizing equation (3.2.3). This linearization can be represented in a compact form as (Ortiz and Martin 1989)

$$\mathbf{P}^T ({}^{n+1}\mathbf{J})^{-1} \mathbf{P} \mathbf{E}, \quad (3.2.6)$$

where  $\mathbf{P}^T = (\mathbf{I}_{n_\sigma}, \mathbf{0}_{n_\sigma, n_\kappa+1})$  is the projection matrix on stress space; note that  $\mathbf{0}_{n_\sigma, n_\kappa+1}$  is a null rectangular matrix with  $n_\sigma$  rows and  $n_\kappa + 1$  columns.

### Substepping technique

In some cases, especially with complex material models and when large strain increments are imposed, the local problem with the standard initial approximation, equation (3.2.5), does not converge. This can be solved using an auxiliary predictor surface in order to find a better initial approximation (Bićanić and Pearce 1996). However, a specific auxiliary predictor surface must be devised for each material model. A different approach is followed here: an adaptive substepping technique, which is activated when the local problem requires more than a prescribed number of iterations. With this technique, the regions of non-convergence of the local problem are avoided.

The constitutive law is integrated from  ${}^n t$  to  ${}^{n+1} t$  in  $m$  substeps. This means that it is integrated first from  ${}^n t$  to  ${}^{n+\frac{1}{m}} t$ , then from  ${}^{n+\frac{1}{m}} t$  to  ${}^{n+\frac{2}{m}} t$ , and up to the last substep, from  ${}^{n+\frac{m-1}{m}} t$  to  ${}^{n+1} t$ . The integration of the constitutive law is driven by the total strain increment. Thus, the total strain increment from  ${}^n t$  to  ${}^{n+1} t$ ,  $\Delta \boldsymbol{\varepsilon}$ , is divided in  $m$  parts (not necessarily equal), one for each substep. The following division is considered:

$$\Delta \boldsymbol{\varepsilon} = \Delta \boldsymbol{\varepsilon}_1 + \Delta \boldsymbol{\varepsilon}_2 + \cdots + \Delta \boldsymbol{\varepsilon}_m = \sum_{k=1}^m \Delta \boldsymbol{\varepsilon}_k = \sum_{k=1}^m \alpha_k \Delta \boldsymbol{\varepsilon}. \quad (3.2.7)$$

Each substep is integrated with a single-step scheme. Except in trivial cases, each substep is a nonlinear problem. Obviously, these problems have the same structure of the local problem if the constitutive law is integrated directly from  ${}^n t$  to  ${}^{n+1} t$  with the same single-step scheme. Here the backward Euler scheme is used. Subsection 3.2.6 shows the consistent tangent moduli for substepping with the generalized midpoint rule.

The nonlinear problem corresponding to a generic substep  $k$  integrated with the backward Euler method can be expressed as

$$\mathbf{f}\left({}^{n+\frac{k}{m}}\boldsymbol{\sigma}, {}^{n+\frac{k}{m}}\boldsymbol{\kappa}, \lambda_k\right) = \begin{pmatrix} \mathbf{I}_{n_\sigma} & \mathbf{0}_{n_\sigma, n_\kappa} & \mathbf{0}_{n_\sigma, 1} \\ \mathbf{0}_{n_\kappa, n_\sigma} & \mathbf{I}_{n_\kappa} & \mathbf{0}_{n_\kappa, 1} \\ \mathbf{0}_{1, n_\sigma} & \mathbf{0}_{1, n_\kappa} & 0 \end{pmatrix} \begin{pmatrix} {}^{n+\frac{k-1}{m}}\boldsymbol{\sigma} \\ {}^{n+\frac{k-1}{m}}\boldsymbol{\kappa} \\ \lambda_{k-1} \end{pmatrix} + \begin{pmatrix} \mathbf{E} \\ \mathbf{0}_{n_\kappa, 1} \\ 0 \end{pmatrix} \Delta \boldsymbol{\varepsilon}_k \quad (3.2.8)$$

with  $\mathbf{f}$  defined as

$$\mathbf{f}\left({}^{n+\frac{k}{m}}\boldsymbol{\sigma}, {}^{n+\frac{k}{m}}\boldsymbol{\kappa}, \lambda_k\right) = \begin{pmatrix} {}^{n+\frac{k}{m}}\boldsymbol{\sigma} + \lambda_k \mathbf{E} \mathbf{m}\left({}^{n+\frac{k}{m}}\boldsymbol{\sigma}, {}^{n+\frac{k}{m}}\boldsymbol{\kappa}\right) \\ {}^{n+\frac{k}{m}}\boldsymbol{\kappa} - \lambda_k \mathbf{h}\left({}^{n+\frac{k}{m}}\boldsymbol{\sigma}, {}^{n+\frac{k}{m}}\boldsymbol{\kappa}\right) \\ F\left({}^{n+\frac{k}{m}}\boldsymbol{\sigma}, {}^{n+\frac{k}{m}}\boldsymbol{\kappa}\right) \end{pmatrix}. \quad (3.2.9)$$

Equations (3.2.8) and (3.2.9) represent the extension of equation (3.2.3) to the case of substepping. They are valid for any substep ( $k \in \{1, \dots, m\}$ ) within the time-step. For a given instant  $n + \frac{k}{m}t$ , the stresses and the internal variables are  $n + \frac{k}{m}\boldsymbol{\sigma}$  and  $n + \frac{k}{m}\boldsymbol{\kappa}$  respectively, whereas the incremental plastic multiplier of the substep  $i$  (from time  $n + \frac{i-1}{m}t$  to  $n + \frac{i}{m}t$ ) is  $\lambda_i$ . In equation (3.2.8) everything is known at  $i = k - 1$ , and must be computed for  $i = k$ , except for  $\Delta\boldsymbol{\varepsilon}_k$  which is the prescribed total strain increment of substep  $k$ .

Note that, in fact,  $\lambda_{k-1}$  is not involved in equation (3.2.8). It has been included in order to simplify the development of the consistent tangent matrix in subsection 3.2.3.

### 3.2.3 The consistent tangent matrix for the substepping technique

To compute the consistent tangent matrix for the substepping technique, the corresponding consistent tangent moduli  $d^{n+1}\boldsymbol{\sigma}/d^{n+1}\boldsymbol{\varepsilon}$  at each Gauss point are needed. They are obtained by linearizing recursively the  $m$  systems of equations solved to integrate the constitutive equation with substepping, i.e. equation (3.2.8) for  $k = 1, \dots, m$ . In order to linearize these  $m$  systems of equations, it is necessary to highlight the dependence of  $n+1\boldsymbol{\sigma}$  on  $\Delta\boldsymbol{\varepsilon}$ .

The stresses  $n+1\boldsymbol{\sigma}$  are defined implicitly, together with  $n+1\boldsymbol{\kappa}$ , as functions of  $n + \frac{m-1}{m}\boldsymbol{\sigma}$ ,  $n + \frac{m-1}{m}\boldsymbol{\kappa}$  and  $\Delta\boldsymbol{\varepsilon}_m$ . The dependence of  $\Delta\boldsymbol{\varepsilon}_m$  on  $\Delta\boldsymbol{\varepsilon}$  is simple,  $\Delta\boldsymbol{\varepsilon}_m = \alpha_m\Delta\boldsymbol{\varepsilon}$ . But the stresses  $n + \frac{m-1}{m}\boldsymbol{\sigma}$  and the internal variables  $n + \frac{m-1}{m}\boldsymbol{\kappa}$  are defined as functions of  $n + \frac{m-2}{m}\boldsymbol{\sigma}$ ,  $n + \frac{m-2}{m}\boldsymbol{\kappa}$  and  $\Delta\boldsymbol{\varepsilon}_{m-1}$ . In fact, the dependence of stresses and internal variables at  $n + \frac{k}{m}t$ , with  $k = m, \dots, 1$ , on the state at  $n + \frac{k-1}{m}t$  and  $\Delta\boldsymbol{\varepsilon}_k$  has always the same structure. The process finishes at  $k = 1$ , because  $n + \frac{1}{m}\boldsymbol{\sigma}$  and  $n + \frac{1}{m}\boldsymbol{\kappa}$  only depend on  $\Delta\boldsymbol{\varepsilon}_1 = \alpha_1\Delta\boldsymbol{\varepsilon}$ . Note that  $n\boldsymbol{\sigma}$  and  $n\boldsymbol{\kappa}$  are inputs of the integration from  $n t$  to  $n+1 t$ .

#### The consistent tangent moduli

The  $m$  systems of equations are linearized: first a generic substep  $k$ , with  $k = m, \dots, 2$ , is shown, then the first substep ( $k = 1$ ) is presented. A different treatment is required for the first substep because it only depends on  $\Delta\boldsymbol{\varepsilon}_1$ . Finally, the expression of the consistent tangent moduli is presented.

Both sides of equation (3.2.8) are linearized with respect to  $\Delta\boldsymbol{\varepsilon}$ ,

$$\frac{d\mathbf{f}}{d(n + \frac{k}{m}\boldsymbol{\sigma}, n + \frac{k}{m}\boldsymbol{\kappa}, \lambda_k)} \frac{d(n + \frac{k}{m}\boldsymbol{\sigma}, n + \frac{k}{m}\boldsymbol{\kappa}, \lambda_k)}{d\Delta\boldsymbol{\varepsilon}} = \begin{pmatrix} \mathbf{I}_{n_\sigma + n_\kappa} & \mathbf{0}_{n_\sigma + n_\kappa, 1} \\ \mathbf{0}_{1, n_\sigma + n_\kappa} & 0 \end{pmatrix} \frac{d(n + \frac{k-1}{m}\boldsymbol{\sigma}, n + \frac{k-1}{m}\boldsymbol{\kappa}, \lambda_{k-1})}{d\Delta\boldsymbol{\varepsilon}} + \begin{pmatrix} \mathbf{E} \\ \mathbf{0}_{n_\kappa, n_\sigma} \\ \mathbf{0}_{1, n_\sigma} \end{pmatrix} \frac{d\Delta\boldsymbol{\varepsilon}_k}{d\Delta\boldsymbol{\varepsilon}} \quad (3.2.10)$$

where

$$\frac{d\mathbf{f}}{d(n + \frac{k}{m}\boldsymbol{\sigma}, n + \frac{k}{m}\boldsymbol{\kappa}, \lambda_k)} = n + \frac{k}{m}\mathbf{J} = \begin{pmatrix} (\mathbf{I}_{n_\sigma} + \lambda\mathbf{E}\frac{\partial\mathbf{m}}{\partial\boldsymbol{\sigma}}) & \lambda\mathbf{E}\frac{\partial\mathbf{m}}{\partial\boldsymbol{\kappa}} & \mathbf{E}\mathbf{m} \\ -\lambda\frac{\partial\mathbf{h}}{\partial\boldsymbol{\sigma}} & (\mathbf{I}_{n_\kappa} - \lambda\frac{\partial\mathbf{h}}{\partial\boldsymbol{\kappa}}) & -\mathbf{h} \\ \mathbf{n}^T & \boldsymbol{\xi}^T & 0 \end{pmatrix}_{t = n + \frac{k}{m}t} \quad (3.2.11)$$

and

$$\frac{d\Delta\boldsymbol{\varepsilon}_k}{d\Delta\boldsymbol{\varepsilon}} = \alpha_k \mathbf{I}_{n_\sigma}. \quad (3.2.12)$$

Note that the first matrix in the RHS of equation (3.2.10) is simply a compact expression of a matrix already encountered in equation (3.2.8).

Assuming that  $\det({}^{n+\frac{k}{m}}\mathbf{J}) \neq 0$ , equation (3.2.10) is transformed into

$$\frac{d({}^{n+\frac{k}{m}}\boldsymbol{\sigma}, {}^{n+\frac{k}{m}}\boldsymbol{\kappa}, \lambda_k)}{d\Delta\boldsymbol{\varepsilon}} = \left({}^{n+\frac{k}{m}}\mathbf{J}\right)^{-1} \begin{pmatrix} \mathbf{I}_{n_\sigma+n_\kappa} & \mathbf{0}_{n_\sigma+n_\kappa,1} \\ \mathbf{0}_{1,n_\sigma+n_\kappa} & 0 \end{pmatrix} \left( \frac{d({}^{n+\frac{k-1}{m}}\boldsymbol{\sigma}, {}^{n+\frac{k-1}{m}}\boldsymbol{\kappa}, \lambda_{k-1})}{d\Delta\boldsymbol{\varepsilon}} + \alpha_k \begin{pmatrix} \mathbf{E} \\ \mathbf{0}_{n_\kappa, n_\sigma} \\ \mathbf{0}_{1, n_\sigma} \end{pmatrix} \right), \quad (3.2.13)$$

which can be rewritten as

$$\frac{d({}^{n+\frac{k}{m}}\boldsymbol{\sigma}, {}^{n+\frac{k}{m}}\boldsymbol{\kappa}, \lambda_k)}{d\Delta\boldsymbol{\varepsilon}} = {}^{n+\frac{k}{m}}\mathbf{A} \left( \alpha_k \mathbf{PE} + \frac{d({}^{n+\frac{k-1}{m}}\boldsymbol{\sigma}, {}^{n+\frac{k-1}{m}}\boldsymbol{\kappa}, \lambda_{k-1})}{d\Delta\boldsymbol{\varepsilon}} \right) \quad (3.2.14)$$

using  $\mathbf{P}^T = (\mathbf{I}_{n_\sigma}, \mathbf{0}_{n_\sigma, n_\kappa+1})$  and

$${}^{n+\frac{k}{m}}\mathbf{A} = \left({}^{n+\frac{k}{m}}\mathbf{J}\right)^{-1} \begin{pmatrix} \mathbf{I}_{n_\sigma+n_\kappa} & \mathbf{0}_{n_\sigma+n_\kappa,1} \\ \mathbf{0}_{1,n_\sigma+n_\kappa} & 0 \end{pmatrix}. \quad (3.2.15)$$

Equation (3.2.14) is valid for  $k = m, \dots, 2$ . For  $k = 1$ , the first substep, equation (3.2.8) is linearized as follows:

$$\frac{d({}^{n+\frac{1}{m}}\boldsymbol{\sigma}, {}^{n+\frac{1}{m}}\boldsymbol{\kappa}, \lambda_1)}{d\Delta\boldsymbol{\varepsilon}} = \alpha_1 \left({}^{n+\frac{1}{m}}\mathbf{J}\right)^{-1} \begin{pmatrix} \mathbf{E} \\ \mathbf{0}_{n_\kappa, n_\sigma} \\ \mathbf{0}_{1, n_\sigma} \end{pmatrix} = \alpha_1 {}^{n+\frac{1}{m}}\mathbf{APE}. \quad (3.2.16)$$

The final expression is obtained after substitution of equation (3.2.16) into equation (3.2.14) particularized at  $k = 2$ , and a recursive use of (3.2.14) from  $k = 3$  up to  $k = m$ . Finally,

$$\frac{d({}^{n+1}\boldsymbol{\sigma}, {}^{n+1}\boldsymbol{\kappa}, \lambda_m)}{d\Delta\boldsymbol{\varepsilon}} = {}^{n+1}\mathbf{A} \left( \alpha_m \mathbf{PE} + {}^{n+\frac{m-1}{m}}\mathbf{A} \left( \alpha_{m-1} \mathbf{PE} + \dots \dots \left( \alpha_2 \mathbf{PE} + \alpha_1 {}^{n+\frac{1}{m}}\mathbf{APE} \right) \dots \right) \right). \quad (3.2.17)$$

The consistent tangent moduli are in the leading principal minor of order  $n_\sigma$  of the LHS of equation (3.2.17). They are obtained by means of the projection matrix  $\mathbf{P}$ , and have the compact expression

$$\frac{d{}^{n+1}\boldsymbol{\sigma}}{d\Delta\boldsymbol{\varepsilon}} = \mathbf{P}^T \left[ \sum_{i=1}^m \left( \alpha_i \prod_{j=m}^i {}^{n+\frac{j}{m}}\mathbf{A} \right) \right] \mathbf{PE}. \quad (3.2.18)$$

Equation (3.2.18) has the same structure of equation (3.2.6). The summation in brackets of equation (3.2.18) plays the same role that the inverse of the Jacobian of equation (3.2.6). In fact, equation (3.2.18) is identical to equation (3.2.6) if only one substep is considered,  $m = 1$ .

Note that the computation of the consistent tangent moduli involves matrix inversions, even in the case of single-step integration rules with no substepping, equation (3.2.6). It must be remarked, however, that small matrices are considered, so numerical inversion poses no difficulties. The order of the Jacobian matrices to be inverted is only  $n_\sigma + n_\kappa + 1$ , see equations (3.2.4) and (3.2.11), and it can be further reduced. A computationally efficient expression of the consistent tangent moduli, with smaller matrices and a recursive structure, is presented in subsection 3.2.7.

### 3.2.4 Examples

In this subsection, two global problems are solved using the consistent tangent matrix for substepping presented in subsection 3.2.3. Quadratic convergence is attained.

The first example is the simulation of a rigid footing with the Rounded Hyperbolic Mohr-Coulomb model. When solving this problem with single-step integration rules, the Gauss points located under the corner of the footing restrict the load increment to a forbidding small value. When substepping is used, on the contrary, the load increment no longer depends on local demands.

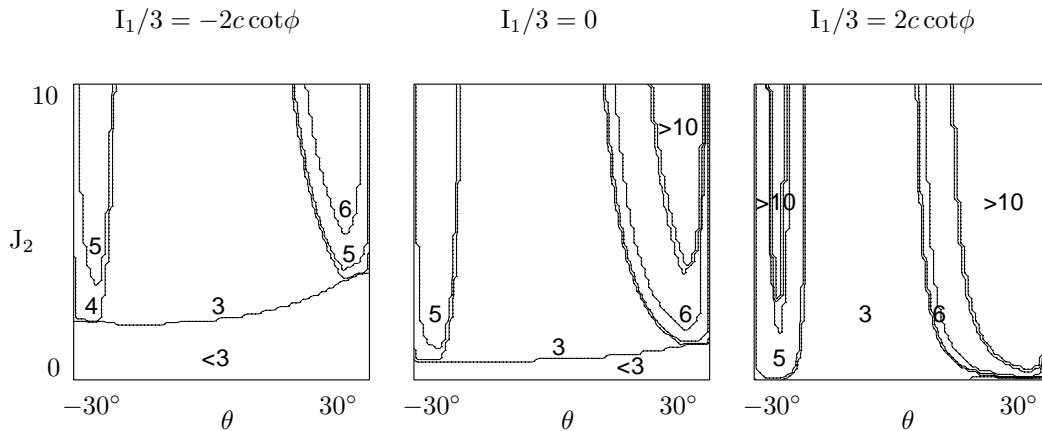


Figure 3.11: Rounded Hyperbolic Mohr-Coulomb model. Number of iterations of the local problem for trial stresses in the deviatoric plane ( $\theta$ - $J_2$ ) at various levels of confinement ( $I_1/3$ ).

As a consequence, larger load increments can be used. Until now, the use of substepping was incompatible with quadratic convergence at the global level. However, thanks to the consistent tangent matrix presented in subsection 3.2.3, quadratic convergence results are presented in the following.

The second example is the simulation of a triaxial test with the MRS-Lade model. In this example substepping is combined with numerical differentiation. For the MRS-Lade model, not all the derivatives needed to compute the Jacobian of the residual, equation (3.2.4), have a readily available analytical expression. Because of this, and following sections 3.1 and 4.2, numerical differentiation is used to approximate the Jacobian. In these references, numerical differentiation is combined with the backward Euler integration rule and quadratic convergence is obtained at local and global level. In this subsection, numerical differentiation is combined with substepping and quadratic results are also obtained.

### Simulation of a rigid footing with the Rounded Hyperbolic Mohr-Coulomb model

In the following a rigid footing is analysed with the Rounded Hyperbolic Mohr-Coulomb model and substepping (Abbo and Sloan 1995, 1996). The consistent tangent matrix developed in subsection 3.2.3 is employed to achieve quadratic convergence at the global level. The model is presented by Abbo and Sloan (1995). The flow potential-yield surface is divided into two regions: one corresponding to the Hyperbolic Mohr-Coulomb zone that smoothes the apex of the classical Mohr-Coulomb model on the hydrostatic axis, and the other corresponding to the rounding zones, that smoothes the corners present on the deviatoric plane. The traces of the flow potential-yield surface on the meridian and the deviatoric planes are presented in figure 3.2. The dimensionless material parameters are a cohesion of 1, a friction angle of  $30^\circ$ , a Young modulus of 3000 and a Poisson coefficient of 0.3. Associated plasticity is considered.

First, the convergence of the local problem is analysed. Figure 3.11 depicts the number of iterations for convergence (up to a tolerance of  $10^{-12}$ ) with the standard initial approximation, equation (3.2.5). Note that the Newton-Raphson method does not converge in 10 iterations in some regions of the stress space. This is due to the high curvature of the yield function close to the apex ( $I_1/3 \geq 0$ ) combined with the non-differentiability of the flow vector at  $|\theta| = 25^\circ$ . In order to avoid these regions of non-convergence of the local problem, the adaptive substepping scheme is activated at the Gauss points that require more than 6 iterations at the local level for convergence (to a tolerance of  $10^{-12}$ ).

Due to symmetry, only one half of domain is considered for the global problem, see figure 3.12. The soil mass is modelled as a square of 20 units of length (u.l.), twenty times the footing half-width,  $B = 2$  u.l. It has been checked that this domain is large enough to preclude any undesired influence of the boundary on the results. An unstructured mesh of 1784 quadrilateral eight-noded elements is used. A vertical displacement of the footing of 0.1 u.l. is prescribed in 100, 200, 400 and



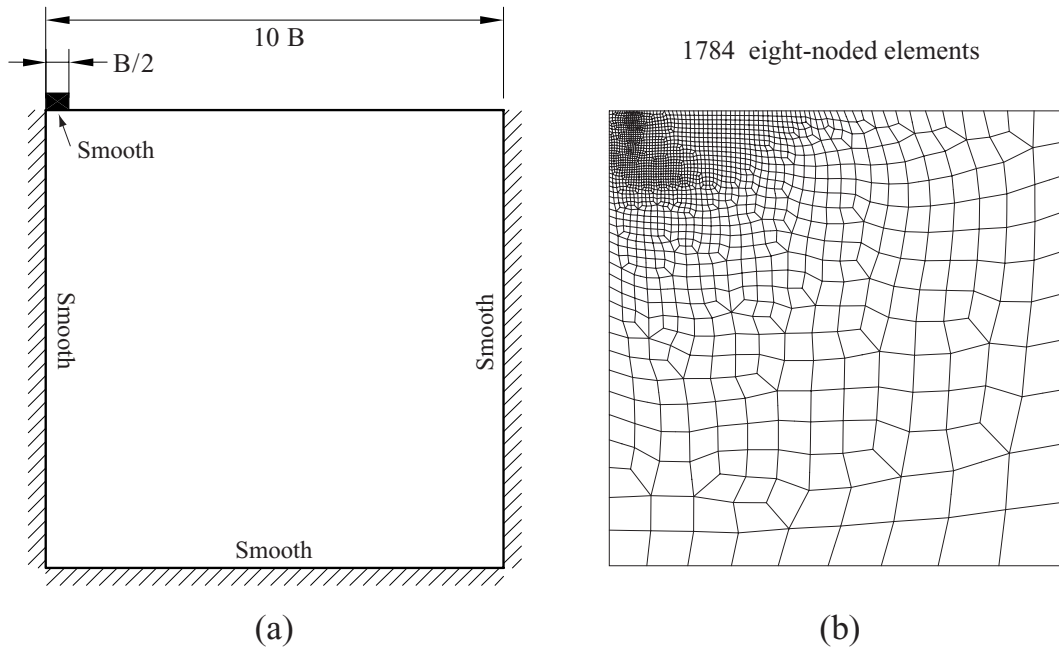


Figure 3.12: Rigid footing: (a) problem definition, (b) mesh.

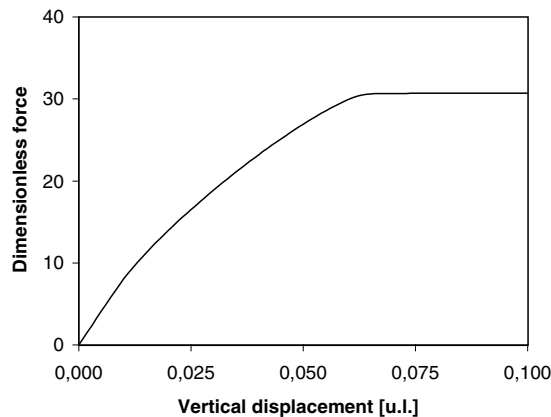


Figure 3.13: Rigid footing problem. Dimensionless force versus vertical displacement.

800 uniform increments. The relationship between force and vertical displacement is depicted in figure 3.13. The computed limit dimensionless force is 30.71, 2% above the exact Prandtl collapse dimensionless force of 30.14. Figure 3.14 shows the distribution of equivalent plastic strain for different values of the load level (i.e. fraction of the total prescribed displacement). Note that the failure mechanism is well captured. Very similar results are obtained for the four problems, with 100, 200, 400 and 800 load increments (l.i.).

The substepping has been activated just under the right corner of the footing. This agrees with the fact that the non-convergence regions of the local problem are close to the rounded apex. Figure 3.15 shows the evolution of the number of Gauss points with substepping activated, the sum of substeps over all the domain and the maximum number of substeps for all the Gauss points, for the problem solved with 100, 200, 400 and 800 l.i. The number of Gauss points with substepping activated is not very different in the four problems (it is reduced by a factor of less than 2 when the number of load increments increases by a factor of 8). On the other hand, the total number of substeps and the maximum number of substeps are in inverse proportion to the number of steps; if the number of load increments is doubled, the maximum number of substeps is divided by two. This indicates that a very large number of steps would be needed to solve the problem without substepping (extrapolating the results of figure 3.15, the number of uniform l.i. would be greater

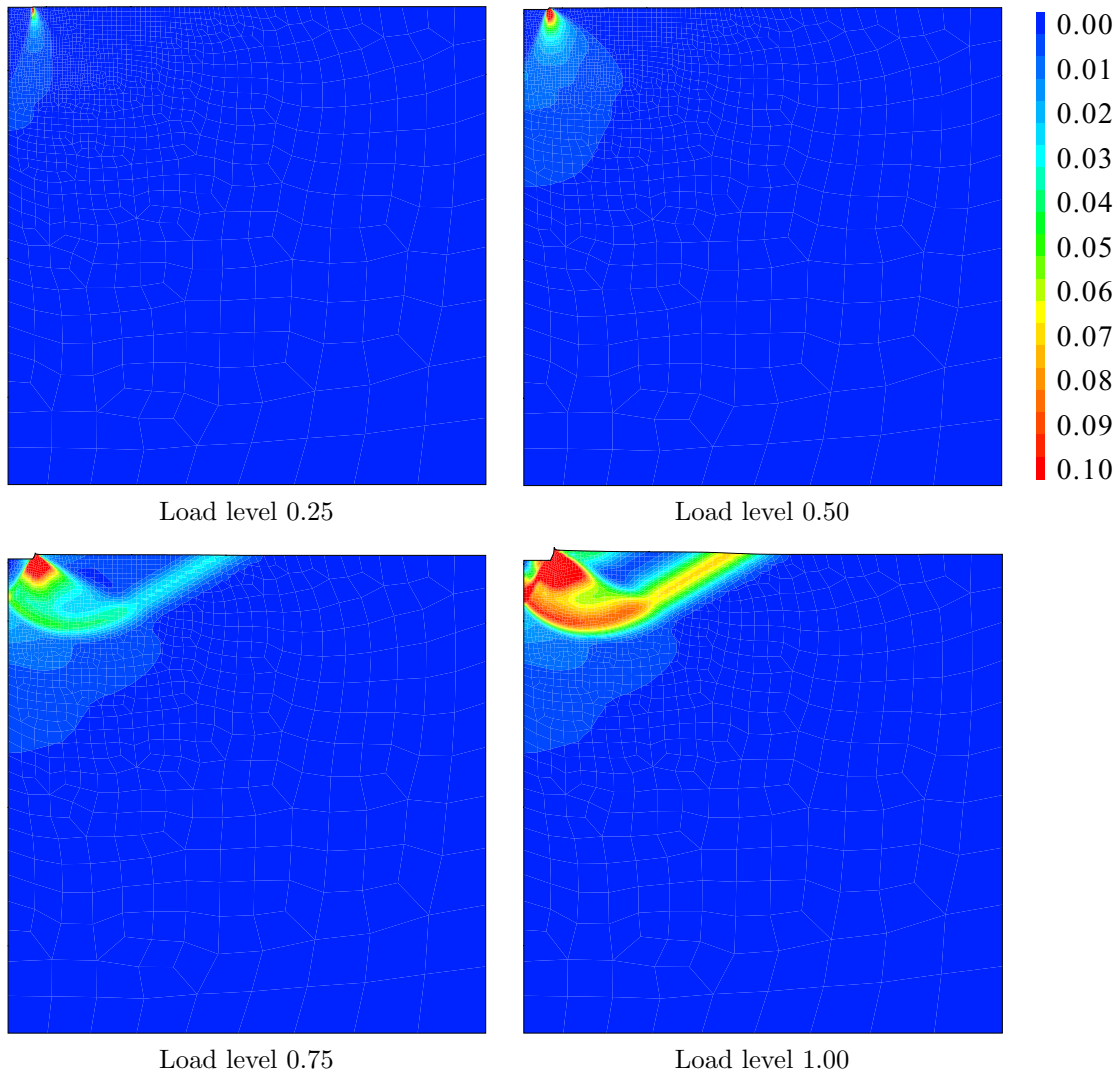


Figure 3.14: Rigid footing problem. Equivalent plastic strain for different load levels.

than 50 000).

The convergence results for several load levels and for the four problems (with 100, 200, 400 and 800 l.i.) are shown in figure 3.16. All the results are quadratic. As expected, the number of iterations per load increment decreases as the number of load increments increases. In fact, the problem with 100 l.i. requires up to 11 Newton-Raphson iterations at the increments previous to the plateau in the load–displacement curve. This indicates that larger increments should not be used in this part of the problem. It has been checked that the influence of the substepping criterion is marginal. If the threshold for activating the substepping is set at 12 iterations (instead of 6), the same results are found (except for the sum of substeps over the domain, which is a little lower).

The computational cost of the four load discretizations is compared in table 3.8 (relative CPU time) and in figure 3.17 (accumulated iterations). The computational cost increases with the number of load increments. Within the range presented in table 3.8, twice the number of load increments implies a computational cost 1.6 times greater. The case with no substepping (i.e. 50 000 uniform increments) is also shown in figure 3.17. Note that the computational cost is much higher: the number of accumulated iterations exceeds 10 000 after only one–eighth of the analysis. This clearly illustrates the computational efficiency of the substepping scheme with consistent tangent matrix.

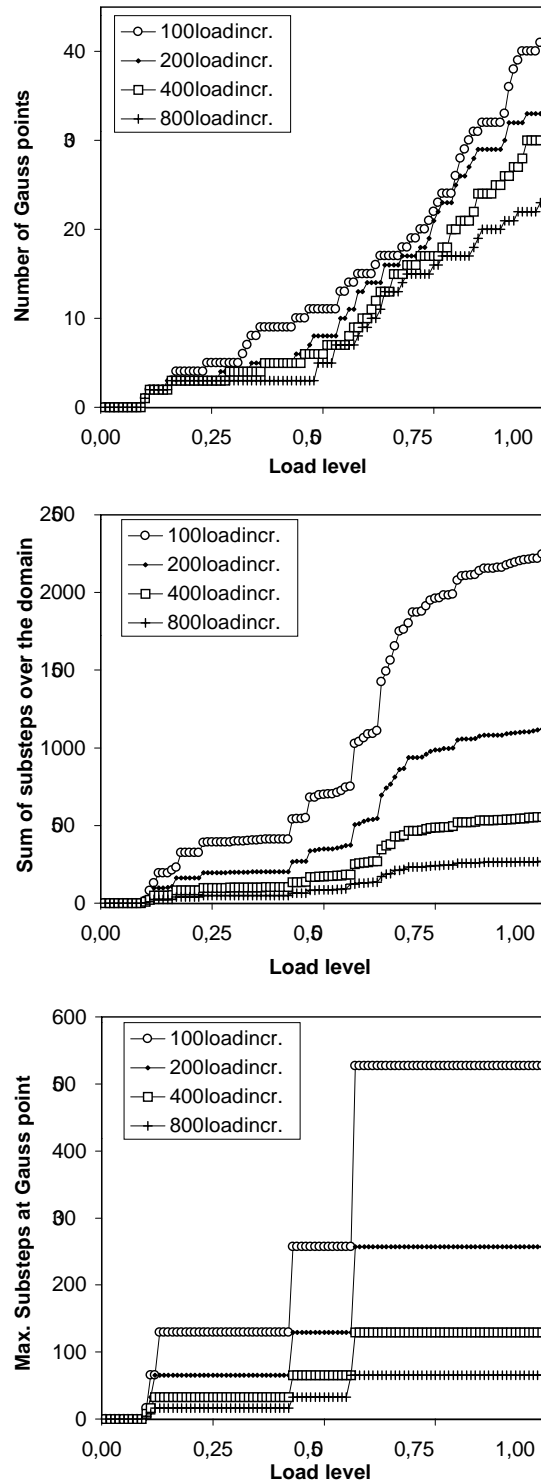


Figure 3.15: Rigid footing problem. Evolution of the number of Gauss points with substepping activated (top), the sum of substeps over the domain (center) and the maximum number of substeps for all the Gauss points (bottom).

### Triaxial test with the MRS–Lade model

In the following, a triaxial test with end–platen friction is analysed with the MRS–Lade model (Sture et al. 1989, Pérez-Foguet and Huerta 1999, Pérez-Foguet et al. 2000e) and substepping. The MRS–Lade model is used to simulate the behaviour of granular materials under both low and high

Load increments	100	200	400	800
Relative CPU time	100%	160%	263%	432%

Table 3.8: Rigid footing problem. Relationship between number of global load increments and relative CPU time.

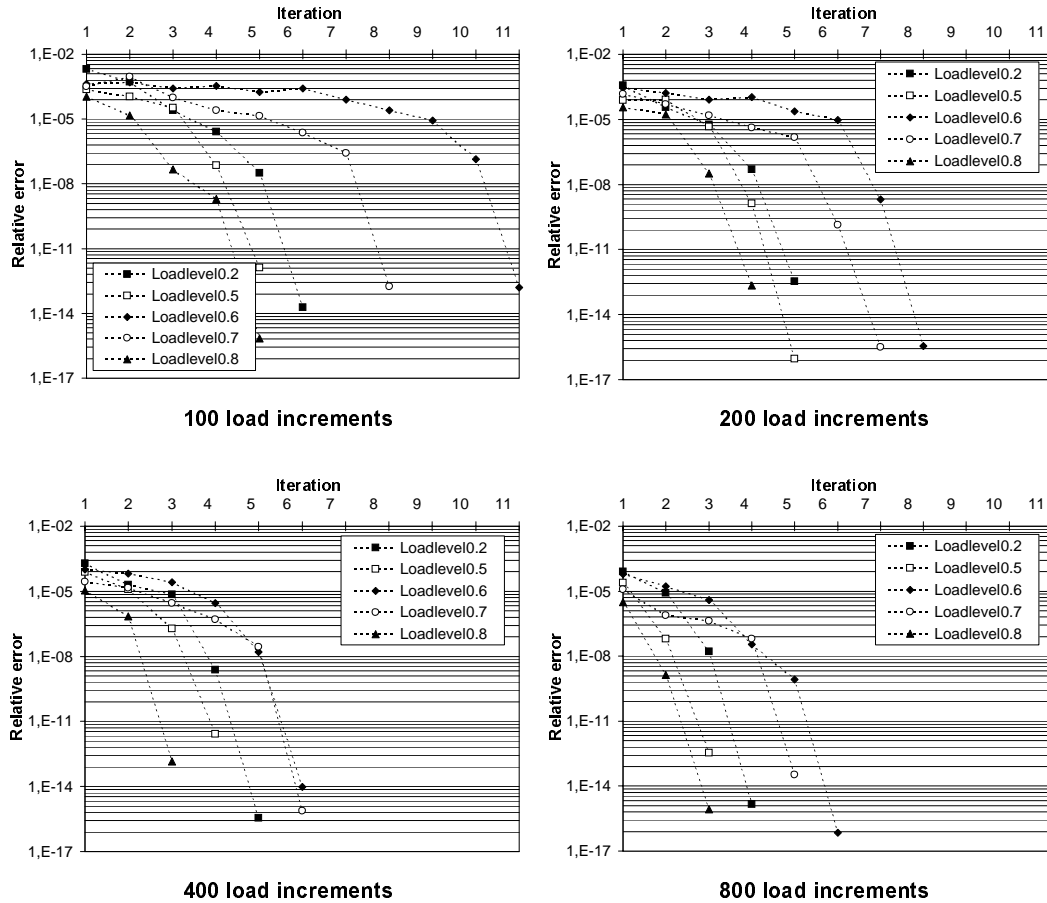


Figure 3.16: Rigid footing problem. Convergence results for different load levels.

confinement stresses (Macari et al. 1994, Macari et al. 1997). It features 1) a two-surface yield function, comprising a smooth cone surface and a smooth cap surface, 2) hardening and softening variables that depend on dissipated plastic work, and 3) a non-associated flow rule in the meridian plane of the cone region. Several slight modifications to the original formulation of the model have been devised (Jeremić and Sture 1994, Macari et al. 1997, Pérez-Foguet and Huerta 1999). In this section the modification presented in section 4.1 (Pérez-Foguet and Huerta 1999) is used. It consists on a new definition of the flow vector for the cone region that avoids the corner problem or the flip-over of previous formulations.

The traces of the yield surface on the meridian plane and on the deviatoric plane are depicted in figure 4.4, and the hardening-softening function  $\eta_{\text{con}}(\kappa_{\text{con}})$  of the cone in figure 4.5. The value of  $\eta_{\text{con}}$  is directly related with the friction angle (slope of the cone in the meridian plane) and  $\kappa_{\text{con}}$  is the cone internal variable, which depends on the plastic work. The softening at Gauss point level starts for  $\kappa_{\text{con}} = 1$ .

The MRS-Lade model exhibits a high coupling between the flow vector and the plastic moduli. This coupling makes the analytical computation of the derivatives a very cumbersome task. However, using any of the numerical differentiation techniques presented in sections 3.1 and 4.2, all the derivatives are computed in a simple and efficient way.

Going beyond sections 3.1 and 4.2, substepping and numerical differentiation are combined here. Like in the first example, the adaptive substepping technique is activated at the Gauss

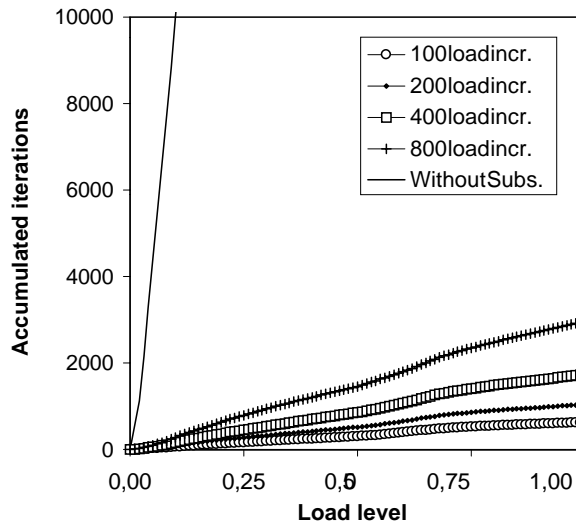


Figure 3.17: Rigid footing problem. Relationship between accumulated iterations and load level.

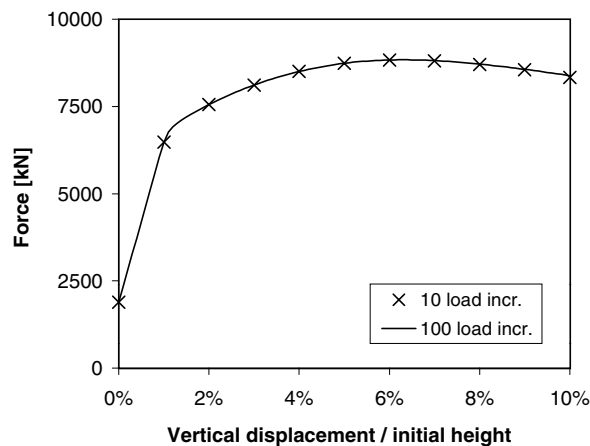


Figure 3.18: Triaxial test problem. Force versus relative vertical displacement.

Load increments	10	20	50	100
Relative CPU time	119%	100%	120%	215%

Table 3.9: Triaxial test problem. Relationship between number of global load increments and relative CPU time.

points where the local problem requires more than 6 iterations for convergence (up to a tolerance of  $10^{-12}$ ). As shown in section 4.2, quadratic convergence at the local level is obtained in all the stress–internal variable space, even with large total strain increments and no substepping. Substepping is used for this problem to ensure proper time–integration of the constitutive law and a reduction of the computational cost, not to avoid non-convergence regions as with the Rounded Hyperbolic Mohr–Coulomb model.

A structured mesh of 1350 ( $30 \times 45$ ) quadrilateral eight–nodded elements has been used. Due to double symmetry only the upper right quarter of the sample is modelled. The end–platen friction is imposed by restraining the radial displacement of the sample top during loading. The same material parameters used by Macari et al. (1997) to simulate the triaxial test at local level of a Sacramento River sand are used in this example. Since the MRS–Lade model is not regularized and includes non-associated plasticity and softening, the problem can localize. However, the low degree of softening of the material parameters used and the axisymmetric nature of the test prevent

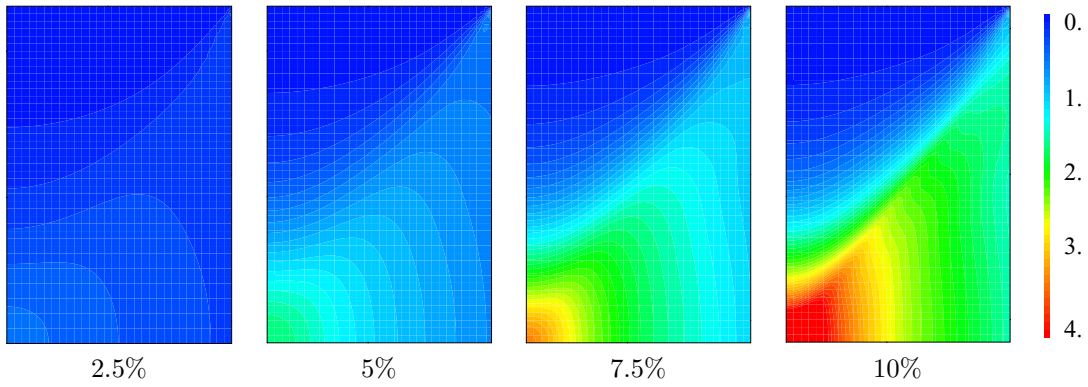


Figure 3.19: Triaxial test problem. Distribution of the cone internal variable for different values of the relative vertical displacement.

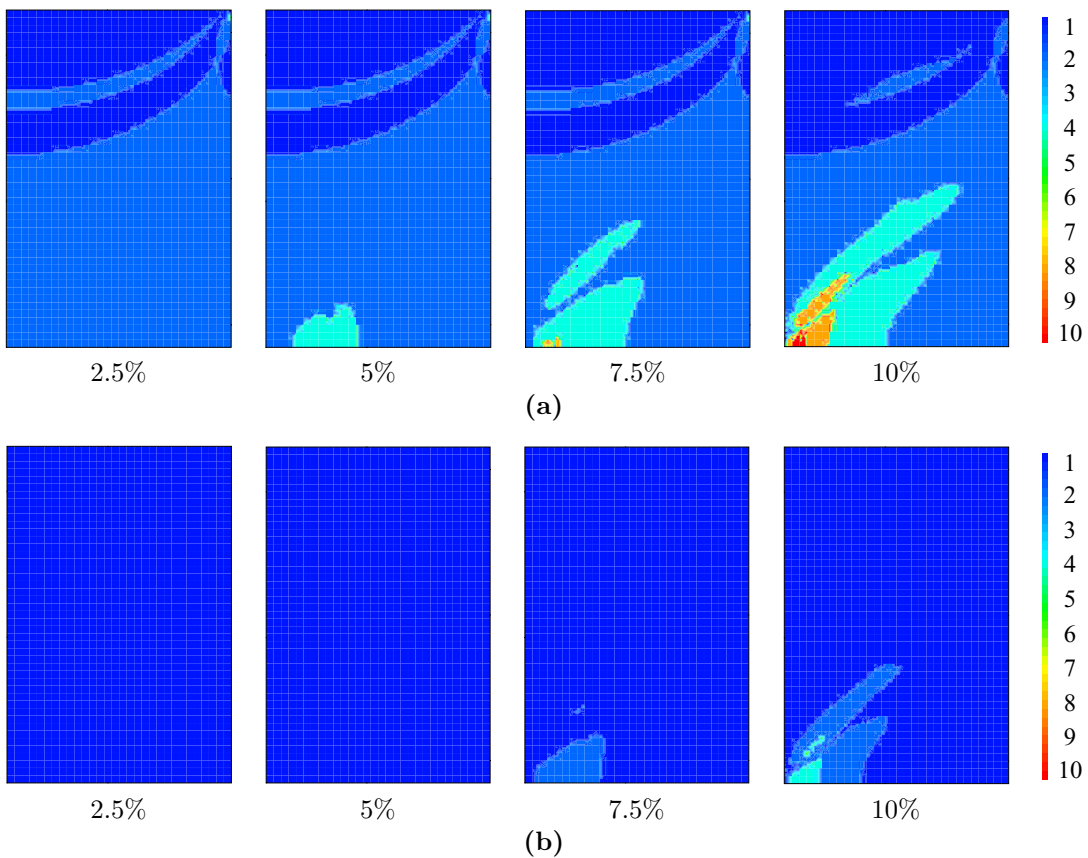


Figure 3.20: Triaxial test problem. Distribution of the number of substeps required for different values of the relative vertical displacement. Problem solved with (a) 20 l.i., and (b) with 50 l.i.

localization (Rudnicki and Rice 1975). The results do not depend significantly on the space or time discretization. The problem has been solved with 10, 20, 50 and 100 load increments. The curves of force versus relative vertical displacement (i.e. vertical displacement over initial height) for 10 and 100 l.i. are depicted in figure 3.18. The results are almost identical for all load discretizations (the relative error of the force at the end of the simulation computed with 10 l.i. is less than 0.6%). Figure 3.19 shows the evolution of the distribution of the cone internal variable. As expected, the material response is clearly non-homogeneous. Note that a wide region at the top of the sample does not enter in the softening regime ( $\kappa_{\text{con}} < 1$ ), even for large vertical displacements, while in the center of the sample (lower left corner of the computational domain) softening starts before the global limit force is reached.

Figure 3.20 shows the distribution of the number of substeps required at various load levels.

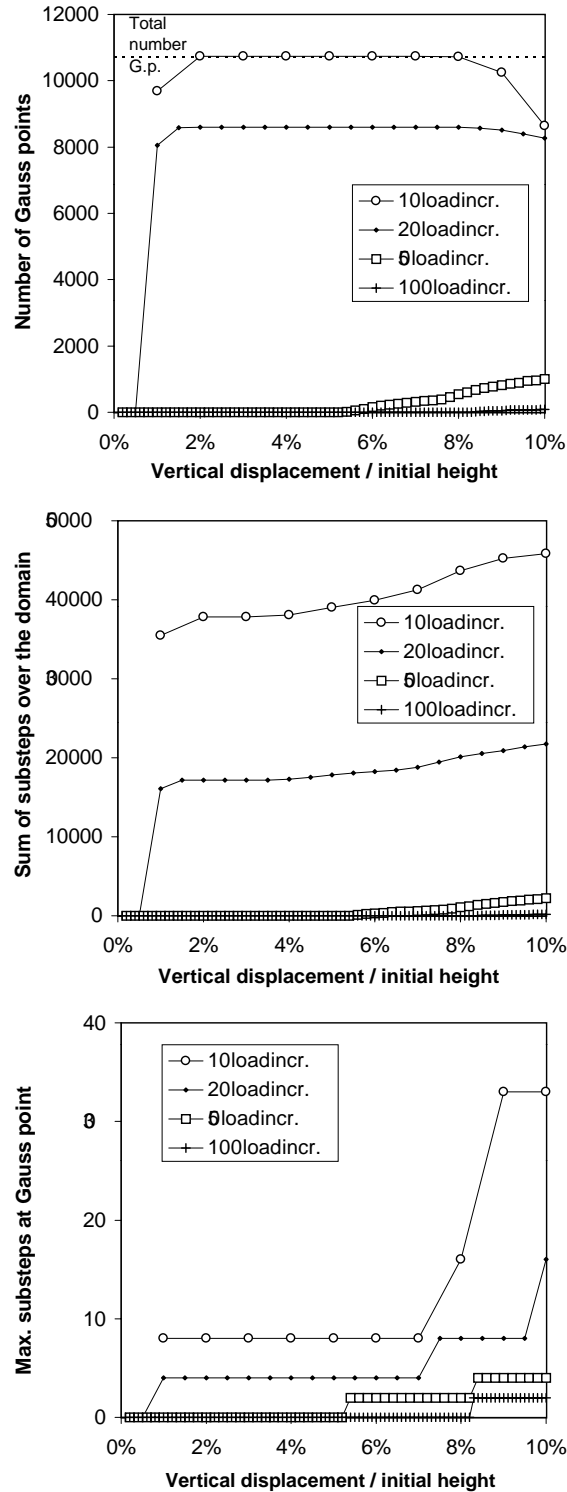


Figure 3.21: Triaxial test problem. Evolution of the number of Gauss points with substepping activated (top), the sum of substeps over the domain (center) and the maximum number of substeps for all the Gauss points (bottom).

Figure 3.21 shows the evolution of the number of Gauss points with substepping activated, the sum of substeps over the domain and the maximum number of substeps for the four problems (with 10, 20, 50 and 100 l.i.). In the problems with 10 and 20 l.i., substepping is activated from the beginning of the analysis and almost everywhere in the domain. At the end of the test, part

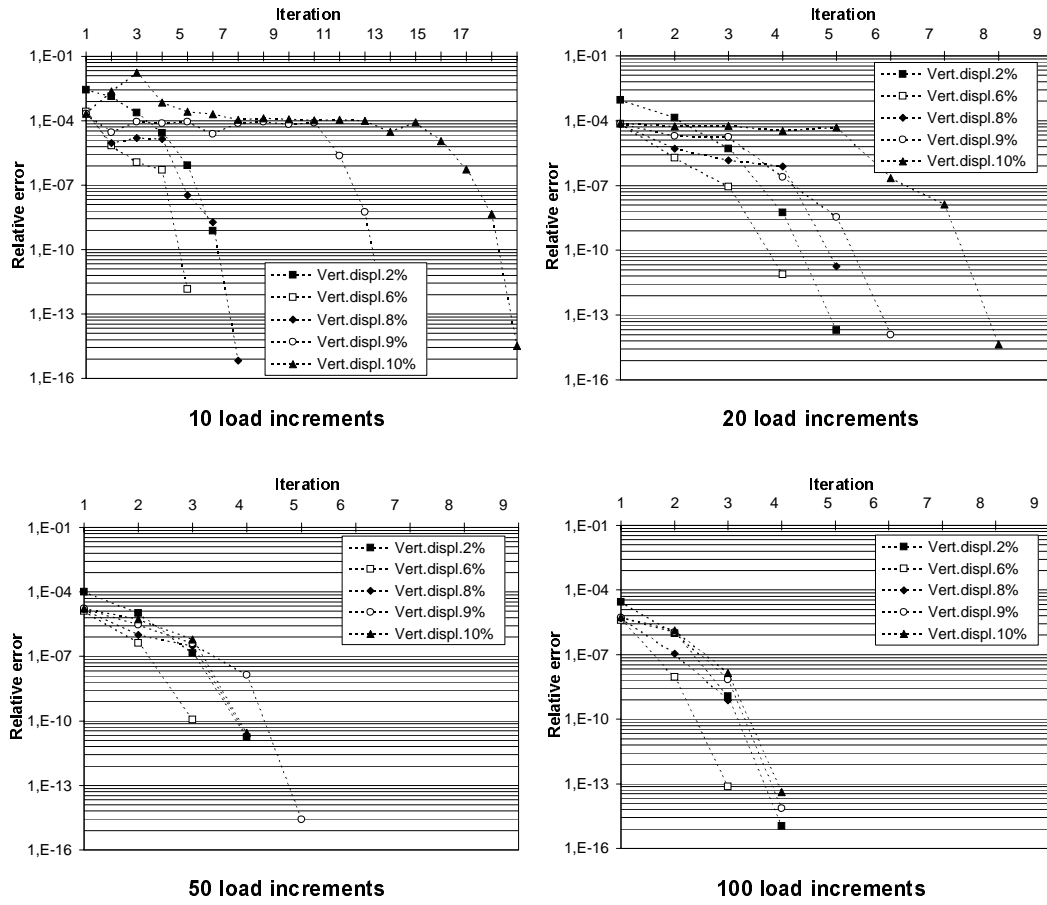


Figure 3.22: Triaxial test problem. Convergence results for different values of the relative vertical displacement.

of the domain changes from plastic loading to elastic unloading. In that region the substepping is deactivated. This results in a decrease in the number of Gauss points with substepping activated, see figures 3.21(top) and 3.20(a). However, the number of substeps at each Gauss point is very low, compared with the previous example. On the other hand, with 50 l.i., substepping is activated only in the region of the domain where the local problems are more demanding. Finally, note that with 100 l.i. there are only a few Gauss points with substepping activated at the end of the test, and they require only two substeps.

The convergence results for several load levels and for the four problems (with 10, 20, 50 and 100 l.i.) are depicted in figure 3.22. Quadratic convergence is attained at all load levels and in the four problems. As in the previous example, the number of iterations per load increment decreases as the number of load increments increases. It is noticeable that the last load increments of the problem solved with 10 l.i., which correspond to a relative vertical displacement of 9% and 10%, require up to 13 and 18 iterations respectively. Thus, although convergence is achieved, this load discretization is too coarse. On the other hand, the problem solved with 100 l.i. converges in four iterations at most during all the analysis.

The computational cost (relative CPU time) of the four load discretizations is shown in table 3.9. The solutions with 10, 20 and 50 l.i. have a similar computational cost. If only 10 or 20 l.i. are used, substepping is activated in a large part of the domain, see Figures 3.20(a) and 3.21, and more global iterations per increment are needed. If 50 l.i. are used, on the other hand, substepping is restricted to a smaller zone and less iterations per increment are required. This is why the total computational cost is similar in the three cases. It must be remarked, however, that the computational cost is halved with respect to the solution with 100 l.i., where almost no substepping is performed. In conclusion, the substepping scheme with consistent tangent matrix is computationally efficient.



### 3.2.5 Concluding remarks

A general expression of the consistent tangent matrix for substepping schemes has been presented. The consistent tangent moduli are computed via recursive linearization of the nonlinear constitutive equations within each substep. In each substep, any single-step scheme may be used. The expression for the generalized midpoint rule (which includes backward and forward Euler schemes as particular cases) has been derived. A simple and compact formula is obtained, with a structure very similar to the case with no substepping.

An adaptive substepping scheme based on the backward Euler rule has been chosen for illustrative purposes. Substepping is activated only at the Gauss points where the local problem requires more than a prescribed number of iterations. With this strategy, the most restrictive Gauss points no longer control the load increment of the global problem. This allows a large reduction of the number of load increments of the global problem, which typically implies a large reduction of the computational cost.

These aspects have been illustrated with the Rounded Hyperbolic Mohr-Coulomb model. The substepping scheme ensures local-level quadratic convergence over all the domain even for large load increments. The corresponding consistent tangent matrix presented in this section ensures quadratic convergence at the global level. The combination of both techniques lead to a large reduction of computational cost.

Moreover, if needed, the derivatives required for the evaluation of the consistent tangent moduli can be approximated via numerical differentiation. With numerical differentiation, quadratic convergence is also attained, both at the local and the global levels. This has been illustrated with the MRS-Lade model.

From a practical viewpoint, it has been shown that the combination of consistent tangent matrices, substepping and numerical differentiation lead to the efficient and simple solving of complex nonlinear inelasticity problems.

### 3.2.6 Appendix: Consistent tangent moduli for substepping with the generalized midpoint rule

In subsection 3.2.3, each substep is integrated with the backward Euler rule. Here, the generalized midpoint rule (Ortiz and Popov 1985), which includes the forward and backward Euler rules as particular cases, is considered. The expression of the consistent tangent moduli is obtained with the same ideas and notation of subsection 3.2.3.

The nonlinear problem corresponding to a generic substep  $k$  integrated with the generalized midpoint integration rule is

$$\hat{\mathbf{f}}\left(n+\frac{k}{m}\boldsymbol{\sigma}, n+\frac{k}{m}\boldsymbol{\kappa}, \lambda_k, n+\frac{k-1}{m}\boldsymbol{\sigma}, n+\frac{k-1}{m}\boldsymbol{\kappa}, \lambda_{k-1}\right) = \begin{pmatrix} \mathbf{I}_{n_\sigma} & \mathbf{0}_{n_\sigma, n_\kappa} & \mathbf{0}_{n_\sigma, 1} \\ \mathbf{0}_{n_\kappa, n_\sigma} & \mathbf{I}_{n_\kappa} & \mathbf{0}_{n_\kappa, 1} \\ \mathbf{0}_{1, n_\sigma} & \mathbf{0}_{1, n_\kappa} & 0 \end{pmatrix} \begin{pmatrix} n+\frac{k-1}{m}\boldsymbol{\sigma} \\ n+\frac{k-1}{m}\boldsymbol{\kappa} \\ \lambda_{k-1} \end{pmatrix} + \begin{pmatrix} \mathbf{E} \\ \mathbf{0}_{n_\kappa, 1} \\ 0 \end{pmatrix} \Delta\varepsilon_k \quad (3.2.19)$$

with  $\hat{\mathbf{f}}$  defined as

$$\hat{\mathbf{f}} = \begin{pmatrix} n+\frac{k}{m}\boldsymbol{\sigma} + \lambda_k \mathbf{E} n+\frac{k-1+\theta}{m}\mathbf{m} \\ n+\frac{k}{m}\boldsymbol{\kappa} - \lambda_k n+\frac{k-1+\theta}{m}\mathbf{h} \\ F\left(n+\frac{k}{m}\boldsymbol{\sigma}, n+\frac{k}{m}\boldsymbol{\kappa}\right) \end{pmatrix} \quad (3.2.20)$$

and

$$\begin{aligned} n+\frac{k-1+\theta}{m}\mathbf{m} &= \mathbf{m}\left(n+\frac{k-1+\theta}{m}\boldsymbol{\sigma}, n+\frac{k-1+\theta}{m}\boldsymbol{\kappa}\right) \\ n+\frac{k-1+\theta}{m}\mathbf{h} &= \mathbf{h}\left(n+\frac{k-1+\theta}{m}\boldsymbol{\sigma}, n+\frac{k-1+\theta}{m}\boldsymbol{\kappa}\right) \\ n+\frac{k-1+\theta}{m}\boldsymbol{\sigma} &= (1-\theta)n+\frac{k-1}{m}\boldsymbol{\sigma} + \theta n+\frac{k}{m}\boldsymbol{\sigma} \\ n+\frac{k-1+\theta}{m}\boldsymbol{\kappa} &= (1-\theta)n+\frac{k-1}{m}\boldsymbol{\kappa} + \theta n+\frac{k}{m}\boldsymbol{\kappa}. \end{aligned} \quad (3.2.21)$$

In equations (3.2.20) and (3.2.21),  $\theta$  can range from  $\theta = 0$  (forward Euler rule) to  $\theta = 1$  (backward Euler rule). The variable  $\lambda_{k-1}$  has been included in both sides of equation (3.2.19) in order to simplify the following deduction of the consistent tangent moduli.

Note that for  $\theta = 1$  the backward Euler scheme is recovered, and equations (3.2.19) and (3.2.20) coincide with equations (3.2.8) and (3.2.9) respectively.

Both sides of equation (3.2.19) are linearized with respect to  $\Delta\boldsymbol{\varepsilon}$ ,

$$\begin{aligned} \frac{\partial \hat{\mathbf{f}}}{\partial(n+\frac{k}{m}\boldsymbol{\sigma}, n+\frac{k}{m}\boldsymbol{\kappa}, \lambda_k)} \frac{d(n+\frac{k}{m}\boldsymbol{\sigma}, n+\frac{k}{m}\boldsymbol{\kappa}, \lambda_k)}{d\Delta\boldsymbol{\varepsilon}} + \\ \frac{\partial \hat{\mathbf{f}}}{\partial(n+\frac{k-1}{m}\boldsymbol{\sigma}, n+\frac{k-1}{m}\boldsymbol{\kappa}, \lambda_{k-1})} \frac{d(n+\frac{k-1}{m}\boldsymbol{\sigma}, n+\frac{k-1}{m}\boldsymbol{\kappa}, \lambda_{k-1})}{d\Delta\boldsymbol{\varepsilon}} = \\ \begin{pmatrix} \mathbf{I}_{n_\sigma+n_\kappa} & \mathbf{0}_{n_\sigma+n_\kappa,1} \\ \mathbf{0}_{1,n_\sigma+n_\kappa} & 0 \end{pmatrix} \frac{d(n+\frac{k-1}{m}\boldsymbol{\sigma}, n+\frac{k-1}{m}\boldsymbol{\kappa}, \lambda_{k-1})}{d\Delta\boldsymbol{\varepsilon}} + \alpha_k \begin{pmatrix} \mathbf{E} \\ \mathbf{0}_{n_\kappa, n_\sigma} \\ \mathbf{0}_{1, n_\sigma} \end{pmatrix}. \end{aligned} \quad (3.2.22)$$

The derivatives of  $\hat{\mathbf{f}}$  can be expressed as

$$\begin{aligned} \frac{\partial \hat{\mathbf{f}}}{\partial(n+\frac{k}{m}\boldsymbol{\sigma}, n+\frac{k}{m}\boldsymbol{\kappa}, \lambda_k)} = {}^{n+\frac{k}{m}}\mathbf{J}_\theta = \\ \begin{pmatrix} \theta\lambda_k\mathbf{E}\frac{\partial\mathbf{m}}{\partial\boldsymbol{\sigma}} & \theta\lambda_k\mathbf{E}\frac{\partial\mathbf{m}}{\partial\boldsymbol{\kappa}} & \mathbf{E}\mathbf{m} \\ -\theta\lambda_k\frac{\partial\mathbf{h}}{\partial\boldsymbol{\sigma}} & -\theta\lambda_k\frac{\partial\mathbf{h}}{\partial\boldsymbol{\kappa}} & -\mathbf{h} \\ \mathbf{0}_{1,n_\sigma} & \mathbf{0}_{1,n_\kappa} & 0 \end{pmatrix}_{t=n+\frac{k-1+\theta}{m}t} + \begin{pmatrix} \mathbf{I}_{n_\sigma} & \mathbf{0}_{n_\sigma, n_\kappa} & \mathbf{0}_{n_\sigma, 1} \\ \mathbf{0}_{n_\kappa, n_\sigma} & \mathbf{I}_{n_\kappa} & \mathbf{0}_{n_\kappa, 1} \\ \mathbf{n}^T & \boldsymbol{\xi}^T & 0 \end{pmatrix}_{t=n+\frac{k}{m}t} \end{aligned} \quad (3.2.23)$$

and

$$\begin{aligned} \frac{\partial \hat{\mathbf{f}}}{\partial(n+\frac{k-1}{m}\boldsymbol{\sigma}, n+\frac{k-1}{m}\boldsymbol{\kappa}, \lambda_{k-1})} = \\ \begin{pmatrix} (1-\theta)\lambda_k\mathbf{E}\frac{\partial\mathbf{m}}{\partial\boldsymbol{\sigma}} & (1-\theta)\lambda_k\mathbf{E}\frac{\partial\mathbf{m}}{\partial\boldsymbol{\kappa}} & \mathbf{0}_{n_\sigma, 1} \\ -(1-\theta)\lambda_k\frac{\partial\mathbf{h}}{\partial\boldsymbol{\sigma}} & -(1-\theta)\lambda_k\frac{\partial\mathbf{h}}{\partial\boldsymbol{\kappa}} & \mathbf{0}_{n_\kappa, 1} \\ \mathbf{0}_{1, n_\sigma} & \mathbf{0}_{1, n_\kappa} & 0 \end{pmatrix}_{t=n+\frac{k-1+\theta}{m}t}. \end{aligned} \quad (3.2.24)$$

Assuming that  $\det({}^{n+\frac{k}{m}}\mathbf{J}_\theta) \neq 0$  and after some arrangements, equation (3.2.22) is rewritten as

$$\begin{aligned} \frac{d(n+\frac{k}{m}\boldsymbol{\sigma}, n+\frac{k}{m}\boldsymbol{\kappa}, \lambda_k)}{d\Delta\boldsymbol{\varepsilon}} = ({}^{n+\frac{k}{m}}\mathbf{J}_\theta)^{-1} \\ \left( \alpha_k \mathbf{P}\mathbf{E} + {}^{n+\frac{k}{m}}\mathbf{G}_\theta \frac{d(n+\frac{k-1}{m}\boldsymbol{\sigma}, n+\frac{k-1}{m}\boldsymbol{\kappa}, \lambda_{k-1})}{d\Delta\boldsymbol{\varepsilon}} \right) \end{aligned} \quad (3.2.25)$$

with

$$\begin{aligned} {}^{n+\frac{k}{m}}\mathbf{G}_\theta = \\ \begin{pmatrix} (\mathbf{I}_{n_\sigma} - (1-\theta)\lambda_k\mathbf{E}\frac{\partial\mathbf{m}}{\partial\boldsymbol{\sigma}}) & -(1-\theta)\lambda_k\mathbf{E}\frac{\partial\mathbf{m}}{\partial\boldsymbol{\kappa}} & \mathbf{0}_{n_\sigma, 1} \\ (1-\theta)\lambda_k\frac{\partial\mathbf{h}}{\partial\boldsymbol{\sigma}} & (\mathbf{I}_{n_\kappa} + (1-\theta)\lambda_k\frac{\partial\mathbf{h}}{\partial\boldsymbol{\kappa}}) & \mathbf{0}_{n_\kappa, 1} \\ \mathbf{0}_{1, n_\sigma} & \mathbf{0}_{1, n_\kappa} & 0 \end{pmatrix}_{t=n+\frac{k-1+\theta}{m}t}. \end{aligned} \quad (3.2.26)$$

The first substep is linearized into

$$\frac{d(n+\frac{1}{m}\boldsymbol{\sigma}, n+\frac{1}{m}\boldsymbol{\kappa}, \lambda_1)}{d\Delta\boldsymbol{\varepsilon}} = \alpha_1 ({}^{n+\frac{1}{m}}\mathbf{J}_\theta)^{-1} \mathbf{P}\mathbf{E}. \quad (3.2.27)$$

Finally, following the same process of section 3.2.3, the consistent tangent moduli are obtained. The final expression is

$$\frac{d^{n+1}\boldsymbol{\sigma}}{d\Delta\boldsymbol{\varepsilon}} = \mathbf{P}^T \left[ \sum_{i=1}^m \left( \alpha_i \prod_{j=m}^i {}^{n+\frac{j}{m}}\mathbf{A}_\theta \right) \right] \mathbf{P}\mathbf{E}, \quad (3.2.28)$$

where,  $\forall k \in \{1, \dots, m-1\}$ ,

$${}^{n+\frac{k}{m}}\mathbf{A}_\theta = {}^{n+\frac{k+1}{m}}\mathbf{G}_\theta \left( {}^{n+\frac{k}{m}}\mathbf{J}_\theta \right)^{-1} \quad (3.2.29)$$

and, for  $k = m$ ,

$${}^{n+1}\mathbf{A}_\theta = ({}^{n+1}\mathbf{J}_\theta)^{-1}. \quad (3.2.30)$$

For the particular case of  $\theta = 1$  (backward Euler scheme) equation (3.2.28) reduces to equation (3.2.18).

### Consistent tangent moduli for substepping with the forward Euler method

In general, numerical inversion of the Jacobian matrices is required to compute the consistent tangent moduli, see equations (3.2.29) and (3.2.30). However, for the particular case of  $\theta = 0$  (forward Euler method), a closed-form expression of the inverse of the Jacobian can be derived, so numerical inversion is not needed.

The Jacobian is

$${}^{n+\frac{k}{m}}\mathbf{J}_0 = \begin{pmatrix} \mathbf{I}_{n_\sigma} & \mathbf{0}_{n_\sigma, n_\kappa} & \mathbf{E}^{n+\frac{k-1}{m}} \mathbf{m} \\ \mathbf{0}_{n_\kappa, n_\sigma} & \mathbf{I}_{n_\kappa} & -n+\frac{k-1}{m} \mathbf{h} \\ {}^{n+\frac{k}{m}}\mathbf{n}^T & {}^{n+\frac{k}{m}}\boldsymbol{\xi}^T & 0 \end{pmatrix}, \quad (3.2.31)$$

and its inverse is

$$\left( {}^{n+\frac{k}{m}}\mathbf{J}_0 \right)^{-1} = \begin{pmatrix} (\mathbf{I}_{n_\sigma} - a\mathbf{E}\mathbf{m}\mathbf{n}^T) & -a\mathbf{E}\mathbf{m}\boldsymbol{\xi}^T & a\mathbf{E}\mathbf{m} \\ a\mathbf{h}\mathbf{n}^T & (\mathbf{I}_{n_\kappa} + a\mathbf{h}\boldsymbol{\xi}^T) & -a\mathbf{h} \\ a\mathbf{n}^T & a\boldsymbol{\xi}^T & -a \end{pmatrix} \quad (3.2.32)$$

where  $\mathbf{n}$  and  $\boldsymbol{\xi}$  are referred to time  ${}^{n+\frac{k}{m}}t$ ,  $\mathbf{m}$  and  $\mathbf{h}$  to  ${}^{n+\frac{k-1}{m}}t$ , and with

$$a = \frac{1}{\mathbf{n}^T \mathbf{E} \mathbf{m} - \boldsymbol{\xi}^T \mathbf{h}}. \quad (3.2.33)$$

Equations (3.2.32) and (3.2.33) can be obtained using Sherman and Morrison's lemma (Dennis and Moré 1977). Note that these equations only involve matrix products.

### 3.2.7 Appendix: Computationally efficient expression of the consistent tangent moduli for substepping with the backward Euler method

The expression of the consistent tangent moduli obtained in subsection 3.2.3, equation (3.2.18), can be rearranged to render it computationally more efficient. In the following, an equivalent expression that involves smaller matrices is presented. In the new expression, moreover, the computation of the inverse of the Jacobians is simplified.

First, the equivalence

$$\begin{pmatrix} \mathbf{I}_{n_\sigma} & \mathbf{0}_{n_\sigma, n_\kappa} & \mathbf{0}_{n_\sigma, 1} \\ \mathbf{0}_{n_\kappa, n_\sigma} & \mathbf{I}_{n_\kappa} & \mathbf{0}_{n_\kappa, 1} \\ \mathbf{0}_{1, n_\sigma} & \mathbf{0}_{1, n_\kappa} & 0 \end{pmatrix} = \begin{pmatrix} \mathbf{I}_{n_\sigma} & \mathbf{0}_{n_\sigma, n_\kappa} \\ \mathbf{0}_{n_\kappa, n_\sigma} & \mathbf{I}_{n_\kappa} \\ \mathbf{0}_{1, n_\sigma} & \mathbf{0}_{1, n_\kappa} \end{pmatrix} \begin{pmatrix} \mathbf{I}_{n_\sigma} & \mathbf{0}_{n_\sigma, n_\kappa} & \mathbf{0}_{n_\sigma, 1} \\ \mathbf{0}_{n_\kappa, n_\sigma} & \mathbf{I}_{n_\kappa} & \mathbf{0}_{n_\kappa, 1} \end{pmatrix} \quad (3.2.34)$$

is employed in order to rewrite equation (3.2.13) into

$$\frac{d({}^{n+\frac{k}{m}}\boldsymbol{\sigma}, {}^{n+\frac{k}{m}}\boldsymbol{\kappa}, \lambda_k)}{d\Delta\varepsilon} = \left( {}^{n+\frac{k}{m}}\mathbf{J} \right)^{-1} \begin{pmatrix} \mathbf{I}_{n_\sigma} & \mathbf{0}_{n_\sigma, n_\kappa} \\ \mathbf{0}_{n_\kappa, n_\sigma} & \mathbf{I}_{n_\kappa} \\ \mathbf{0}_{1, n_\sigma} & \mathbf{0}_{1, n_\kappa} \end{pmatrix} \left( \begin{pmatrix} \mathbf{I}_{n_\sigma} & \mathbf{0}_{n_\sigma, n_\kappa} & \mathbf{0}_{n_\sigma, 1} \\ \mathbf{0}_{n_\kappa, n_\sigma} & \mathbf{I}_{n_\kappa} & \mathbf{0}_{n_\kappa, 1} \end{pmatrix} \frac{d({}^{n+\frac{k-1}{m}}\boldsymbol{\sigma}, {}^{n+\frac{k-1}{m}}\boldsymbol{\kappa}, \lambda_{k-1})}{d\Delta\varepsilon} + \alpha_k \begin{pmatrix} \mathbf{E} \\ \mathbf{0}_{n_\kappa, n_\sigma} \end{pmatrix} \right). \quad (3.2.35)$$

Then, equation (3.2.35) is pre-multiplied by

$$\begin{pmatrix} \mathbf{I}_{n_\sigma} & \mathbf{0}_{n_\sigma, n_\kappa} & \mathbf{0}_{n_\sigma, 1} \\ \mathbf{0}_{n_\kappa, n_\sigma} & \mathbf{I}_{n_\kappa} & \mathbf{0}_{n_\kappa, 1} \end{pmatrix} \quad (3.2.36)$$

in order to get

$$\frac{d\left({}^{n+\frac{k}{m}}\boldsymbol{\sigma}, {}^{n+\frac{k}{m}}\boldsymbol{\kappa}\right)}{d\Delta\boldsymbol{\varepsilon}} = {}^{n+\frac{k}{m}}\mathbf{A}_c \left( \frac{d\left({}^{n+\frac{k-1}{m}}\boldsymbol{\sigma}, {}^{n+\frac{k-1}{m}}\boldsymbol{\kappa}\right)}{d\Delta\boldsymbol{\varepsilon}} + \alpha_k \mathbf{P}_c \mathbf{E} \right) \quad (3.2.37)$$

where

$$\begin{aligned} \mathbf{P}_c &= \begin{pmatrix} \mathbf{I}_{n_\sigma} \\ \mathbf{0}_{n_\kappa, n_\sigma} \end{pmatrix}, \\ {}^{n+\frac{k}{m}}\mathbf{A}_c &= \begin{pmatrix} \mathbf{I}_{n_\sigma} & \mathbf{0}_{n_\sigma, n_\kappa} & \mathbf{0}_{n_\sigma, 1} \\ \mathbf{0}_{n_\kappa, n_\sigma} & \mathbf{I}_{n_\kappa} & \mathbf{0}_{n_\kappa, 1} \end{pmatrix} \left({}^{n+\frac{k}{m}}\mathbf{J}\right)^{-1} \begin{pmatrix} \mathbf{I}_{n_\sigma} & \mathbf{0}_{n_\sigma, n_\kappa} \\ \mathbf{0}_{n_\kappa, n_\sigma} & \mathbf{I}_{n_\kappa} \\ \mathbf{0}_{1, n_\sigma} & \mathbf{0}_{1, n_\kappa} \end{pmatrix}, \end{aligned} \quad (3.2.38)$$

and use is made of the relation

$$\begin{pmatrix} \mathbf{I}_{n_\sigma} & \mathbf{0}_{n_\sigma, n_\kappa} & \mathbf{0}_{n_\sigma, 1} \\ \mathbf{0}_{n_\kappa, n_\sigma} & \mathbf{I}_{n_\kappa} & \mathbf{0}_{n_\kappa, 1} \end{pmatrix} \frac{d\left({}^{n+\frac{k}{m}}\boldsymbol{\sigma}, {}^{n+\frac{k}{m}}\boldsymbol{\kappa}, \lambda_k\right)}{d\Delta\boldsymbol{\varepsilon}} = \frac{d\left({}^{n+\frac{k}{m}}\boldsymbol{\sigma}, {}^{n+\frac{k}{m}}\boldsymbol{\kappa}\right)}{d\Delta\boldsymbol{\varepsilon}}. \quad (3.2.39)$$

Finally, following the same process of section 3.2.3, the consistent tangent moduli are obtained. The final expression is

$$\frac{d^{n+1}\boldsymbol{\sigma}}{d\Delta\boldsymbol{\varepsilon}} = \mathbf{P}_c^T \left[ \sum_{i=1}^m \left( \alpha_i \prod_{j=m}^i {}^{n+\frac{j}{m}}\mathbf{A}_c \right) \right] \mathbf{P}_c \mathbf{E}. \quad (3.2.40)$$

Equation (3.2.40) has the same structure of equation (3.2.18). However, the matrices involved here are smaller. In fact, the consistent tangent moduli are computed with the following expression:

$$\begin{aligned} \frac{d^{n+1}\boldsymbol{\sigma}}{d\Delta\boldsymbol{\varepsilon}} &= \mathbf{P}_c^T {}^{n+1}\mathbf{A}_c \left( \alpha_m \mathbf{P}_c + {}^{n+\frac{m-1}{m}}\mathbf{A}_c \left( \alpha_{m-1} \mathbf{P}_c + \cdots \right. \right. \\ &\quad \left. \left. \cdots \left( \alpha_2 \mathbf{P}_c + \alpha_1 \underbrace{{}^{n+\frac{1}{m}}\mathbf{A}_c \mathbf{P}_c}_{m-1} \right) \cdots \right) \right) \mathbf{E}, \end{aligned} \quad (3.2.41)$$

which is equivalent to equation (3.2.40). As suggested by equation (3.2.41), the consistent tangent moduli are computed recursively during time-integration: when the substep  $j$  is integrated, the matrix  ${}^{n+\frac{j}{m}}\mathbf{A}_c$  is computed and the corresponding part of the consistent tangent moduli is calculated. The process is always the same, except for the first and the last substeps.

Moreover, because of the special structure of the Jacobian, the matrices  ${}^{n+\frac{j}{m}}\mathbf{A}_c$  are computed inverting only the leading principal minor of order  $n_\sigma + n_\kappa$  of the Jacobian. This result can be obtained using Sherman and Morrison's lemma (Dennis and Moré 1977).

## Chapter 4

# Elastoplastic models for granular materials

In this chapter, the highly nonlinear elastoplastic behaviour of granular materials is modelled following two different approaches. In both cases the attention is focused in the efficient solution of the nonlinear constitutive equations and the boundary value problems by means of the corresponding tangent operators.

The first part, sections 4.1 to 4.3, is devoted to the analysis of a work hardening cone–cap model for small–strain problems. In section 4.1 a new formulation of the plastic potential of the model is presented. This formulation avoids the grey zone and the flip–over found at cone–cap intersection of previous ones. A detailed analysis of the model features and its application to various boundary value problems is presented in section 4.2. The consistent linearization of all equations with respect to all unknowns and the application of the numerical differentiation techniques presented in section 3.1 lead to quadratic convergence results in both the time–integration of constitutive laws and the solution of boundary value problems. Previous applications found in the literature do not exhibit quadratic convergence. Finally, in section 4.3, an extension of the model which includes the modelling of cohesive behaviour is discussed.

In the second part, section 4.4, several examples involving different density–dependent models within the framework of isotropic finite strain multiplicative plasticity are presented. The flow directions and yield functions of these models are expressed in terms of the Kirchhoff stresses and the relative density. This type of models include the finite strain multiplicative plasticity based on the Cauchy stresses as a particular case. The consistent linearization of the constitutive equations, including the density influence, is presented. Moreover, it is shown that the standard numerical time–integration based on the exponential return mapping also apply, without any modification, to this type of models.

### 4.1 Plastic flow potential for the cone region of the MRS–Lade model

The original formulation of the MRS–Lade model, with non-associated flow rule on the meridian plane in the cone region, has a corner. In order to reduce the computational effort of corner solution algorithms, a modified plastic flow potential for the cone part is found in the literature. This modification may have a non-admissible *flip over* of the flow vector in the cone–cap intersection if the plastic flow potential is not correctly defined. Here a corrected plastic flow potential for the cone region is defined to obtain a continuous transition of the flow vector.

#### 4.1.1 Introduction

In computational plasticity, the definition of the plastic flow vector is more useful than the definition of the plastic flow potential. The flow vector is needed for the integration of the constitutive law and for the resolution of the global finite element problem, see Ortiz and Popov (1985), Simo and

Taylor (1985), Runesson et al. (1988) and Crisfield (1991, 1997) among others. In fact, the flow potential is hardly ever employed, it is defined mainly for convenience (Lubliner 1990). Nevertheless the flow potential is useful in theoretical analysis (Kim and Lade 1988, Lubliner 1990, Lade 1994) and in the formal description of the model, for instance, Pramono and Willam (1989a), Etse and Willam (1994) and Khan and Huang (1995).

In order to implement a non-associated flow rule three approaches are possible. The first one defines the flow rule (usually the flow potential) directly from experimental analysis, independently of other characteristics of model, see Lade and Duncam (1975), Nova and Wood (1979) and Lade and Kim (1988b) among others. The second one prescribes the flow vector modifying the normal to the yield function (the corresponding flow potential is obtained by integration), see for instance, Runesson (1987), Alawaji, Runesson and Sture (1992) and Larsson and Runesson (1996). The third one defines the flow potential as a direct modification of the yield function, Macari et al. (1994), Jeremić and Sture (1994), Macari et al. (1997); this must be done carefully in order to get the desired properties in the flow vector.

### 4.1.2 MRS–Lade model

This work focuses in the non-associated flow rule for the cone region of the MRS–Lade model. This model has been developed at the University of Colorado by Macari-Pasqualino, Runesson and Sture (Sture et al. 1989, Jeremić and Sture 1994, Macari et al. 1997) and it is a further development of Lade’s three-invariant model for cohesionless soils (Lade and Duncam 1975, Lade 1989).

The model has been used to simulate the behavior of granular materials, such as sand, under both low and high confinement stresses (Macari et al. 1994, Macari et al. 1997). Quoting Jeremić and Sture (1997), the MRS–Lade model features:

- a two-surface formulation, comprising a smooth cone surface and a smooth cap surface intersecting in plane curve (ellipse segment) in the deviatoric plane,
- hardening and softening variables for both surfaces are based on dissipated plastic work,
- a non-associated flow rule in the meridian plane and an associated flow rule in the deviatoric plane of the cone region, and an associated flow rule in the cap region,
- ability to model cohesive strength and a curved meridian in the cone region.

In order to center in the essential issue of this work, a simplified version of the original model is described here. Detailed discussion is presented by Sture et al. (1989) and Jeremić and Sture (1994).

The following expressions define the yield function

$$\begin{aligned} F_{\text{con}} &= qq(\theta) - \eta_{\text{cone}}p = 0 \\ F_{\text{cap}} &= \left( \frac{p - \alpha p_{\text{cap}}}{(1 - \alpha)p_{\text{cap}}} \right)^2 + \left( \frac{qq(\theta)}{\eta_{\text{cone}}\alpha p_{\text{cap}}} \right)^2 - 1 = 0 \quad , \end{aligned} \quad (4.1.1)$$

where  $p$ ,  $q$  and  $\theta$  are functions of the stress invariants,  $g(\theta)$  is a function that defines the shape in the deviatoric plane,  $\eta_{\text{cone}}$  and  $p_{\text{cap}}$  are the hardening–softening functions, and  $\alpha$  is a parameter of the model. A scheme of the trace of the yield function in the  $p - q$  plane is depicted in figure 4.1.

The flow rule is associated on the entire cap region and in the deviatoric plane of the cone region. Thus, in the cap region, the flow potential is equal to  $F_{\text{cap}}$ , and, in the cone region, it has the same dependence of  $q$  and  $\theta$  that  $F_{\text{con}}$  does. Following the original formulation of the model, Sture et al. (1989), the non-associated flow defined in correspondence with the expansive behavior in the cone region is represented by a plastic potential function of the form

$$G_{\text{cone}} = qq(\theta) - n\eta_{\text{cone}}p \quad , \quad (4.1.2)$$

where  $n$  is a non-negative *constant*. Typical values for  $n$  are close to 0.1. This potential reduces the dilatancy of the associated flow rule in the cone region. Note that for  $n$  equal to zero incompressibility is enforced for values of  $p$  between zero and  $\alpha p_{\text{cap}}$ . The components of the flow vector on the meridian plane,  $\mathbf{m} = (m_p, m_q)$ , are

$$m_p = -n\eta_{\text{cone}} \quad m_q = g(\theta) \quad . \quad (4.1.3)$$

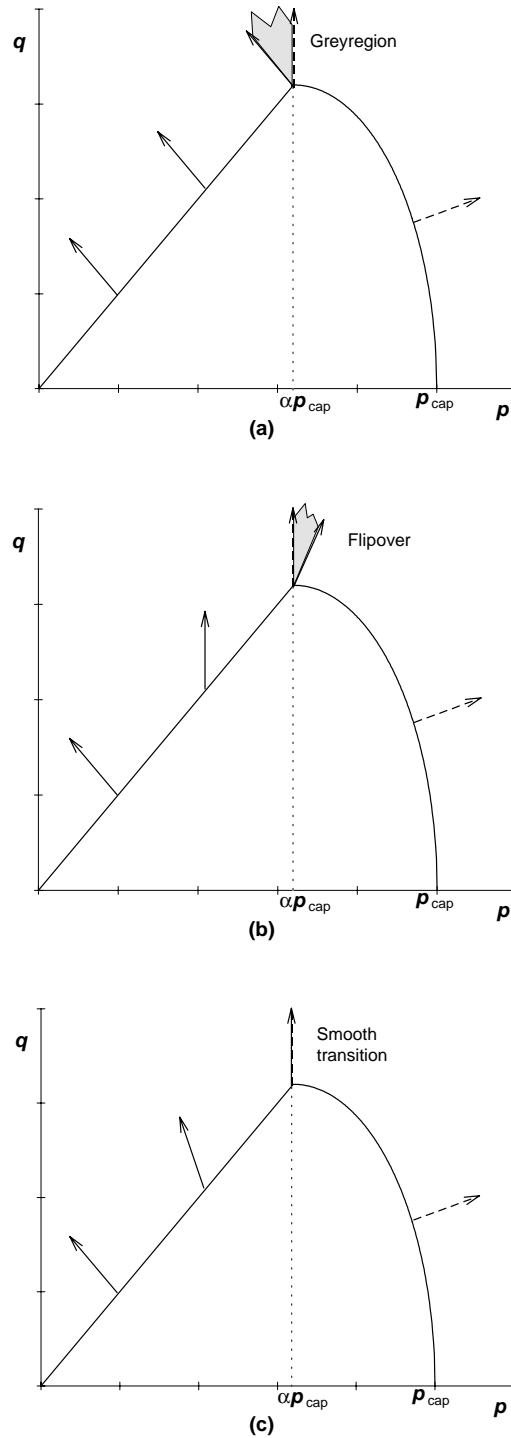


Figure 4.1: Trace of the simplified MRS-Lade yield function and characteristic flow vectors on the  $p$ - $q$  plane. Original formulation (a), modified flow potential (b) and corrected flow potential (c).

### 4.1.3 Modified plastic flow potential

For the usual case,  $n$  different than zero, this flow rule has a *grey region* at the intersection of cone and cap surfaces, see figure 4.1(a). In this region there is not continuity of the flow vector. This implies that the Koiter's rule must be applied: the direction of the plastic strain rate is

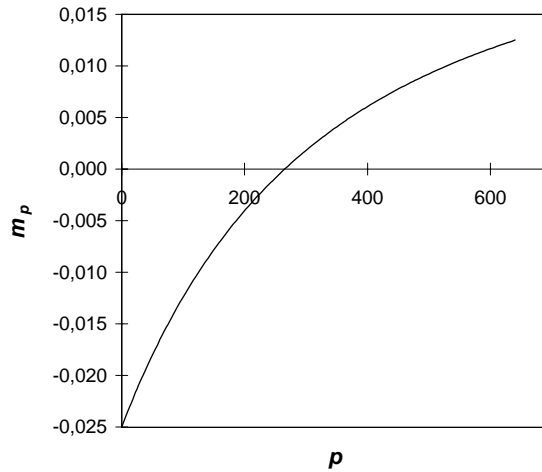


Figure 4.2:  $p$ -component of modified flow vector as function of  $p$ .

defined as a linear combination of the cone and cap flow vectors. Therefore, a corner solution algorithm is needed (Simo et al. 1988, Pramono and Willam 1989b, Hofstetter et al. 1993, Jeremić and Sture 1994). Such algorithms are usually expensive from a computational point of view. Thus, in order to reduce the computational effort, an alternative definition of the flow potential for the MRS–Lade model is presented in Macari et al. (1994) and Macari et al. (1997). To avoid the grey zone, the flow vectors corresponding to cone and cap regions at the corner, i.e.  $p = \alpha p_{\text{cap}}$ , must have the same direction, see figure 4.1(c). Thus the  $p$ -component of the cone flow vector must be zero at the corner.

The previously cited references propose the use of a pressure dependent  $n$ ,

$$n = -\gamma \frac{p - \alpha p_{\text{cap}}}{p + \alpha p_{\text{cap}}} \quad , \quad (4.1.4)$$

where  $\gamma$  is a non-negative constant. If equation (4.1.4) is used in (4.1.3) and the expression of the flow potential is not necessary at all, the grey zone disappears and a continuous variation of the flow vector is obtained. However, if equation (4.1.4) is directly substituted in (4.1.2), as Macari et al. (1994) and Macari et al. (1997) seem to indicate, a modified flow potential is defined which induces the following components of the flow vector on the meridian plane,

$$m_p = \gamma \eta_{\text{cone}} \left( \frac{2p - \alpha p_{\text{cap}}}{p + \alpha p_{\text{cap}}} - \frac{(p - \alpha p_{\text{cap}})p}{(p + \alpha p_{\text{cap}})^2} \right) \quad m_q = g(\theta) \quad . \quad (4.1.5)$$

Then,  $m_p$  varies from a negative value,  $-\gamma \eta_{\text{cone}}$ , at  $p = 0$  to a positive one,  $\gamma \eta_{\text{cone}}/2$  at the corner,  $p = \alpha p_{\text{cap}}$ . This variation is illustrated in figure 4.2, where characteristic values of  $\gamma = 0.125$ ,  $\eta_{\text{cone}} = 0.2$  and  $\alpha p_{\text{cap}} = 640$  are used, Macari et al. (1997). Thus the proposed objective is not attained. Moreover, since  $m_p$  at  $\alpha p_{\text{cap}}$  is strictly positive, there is a *flip over* of the vector flow at the corner, see figure 4.1(b). This situation is not desired and, in general, not admissible.

#### 4.1.4 Corrected plastic flow potential

In order to obtain the desired flow vector a different flow potential must be defined. With the desired expression of the flow vector a flow potential is obtained by integration. After substitution of equation (4.1.4) into (4.1.3) the components of the flow vector,  $\mathbf{m}^* = (m_p^*, m_q^*)$ , become

$$m_p^* = \gamma \eta_{\text{cone}} \frac{p - \alpha p_{\text{cap}}}{p + \alpha p_{\text{cap}}} \quad m_q^* = m_q = g(\theta) \quad . \quad (4.1.6)$$

As stated previously this flow vector induces the desired behavior. In figure 4.3, the variation of  $m_p^*$  with respect to  $p$  is presented. In this case, the component  $m_p^*$  remains negative for every  $p$  less



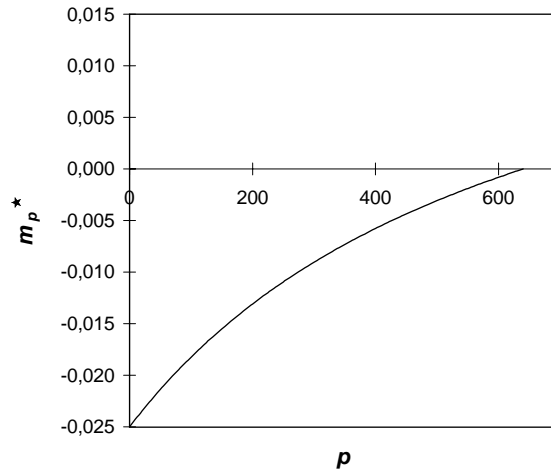


Figure 4.3:  $p$ -component of corrected flow vector as function of  $p$ .

then  $\alpha p_{\text{cap}}$  and reaches zero at this limit. Therefore, the *grey region* disappears, without any *flip over* of the flow vectors, and a specially designed corner algorithm is precluded. Note that other expressions for the evolution of  $m_p^*$  reaching zero from below at  $p = \alpha p_{\text{cap}}$  can be used, if they do conform with experimental results.

The plastic flow potential corresponding to the flow vector defined in (4.1.6) is obtained by integration:

$$G_{\text{cone}}^* = qg(\theta) + \gamma\eta_{\text{cone}}(p - 2\alpha p_{\text{cap}} \ln(p + \alpha p_{\text{cap}})) \quad , \quad (4.1.7)$$

where the integration constants are taken equal to zero since the purpose of (4.1.7) is simply the definition of a potential for the plastic strain rate.

Equation (4.1.7) represents a new plastic flow potential for the cone region of the MRS–Lade model. The corresponding flow vector components are defined in equation (4.1.6). This flow vector is justified from a physical view point in Macari et al. (1994). But, the flow potential presented here will not induce the undesired features of the one presented in Macari et al. (1994).

#### 4.1.5 Concluding remarks

Flow potentials are seldom employed in computational plasticity if the flow vector is known a priori. Nevertheless, if they are needed for theoretical or verification purposes they must agree with the desired behavior of the flow vectors. If the flow rule is modified by acting on the flow vector, the corresponding flow potential should be obtained by simple integration. Here, a new plastic flow potential for the cone region of the MRS–Lade model is presented. This potential induces a flow vector with continuous transition between cone and cap regions. Thus, the corner problem (*grey region*) inherent to the original formulation and the non-admissible flip over of previously published modifications, are avoided.

## 4.2 Numerical differentiation for non-trivial consistent tangent matrices: an application to the MRS-Lade model

Section 3.1 shows that numerical differentiation is a competitive alternative to analytical derivatives for the computation of consistent tangent matrices. Relatively simple models were treated in that reference. The approach is extended here to a complex model: the MRS–Lade model (Sture et al. 1989, Jeremić and Sture 1994). This plastic model has a cone–cap yield surface and exhibits strong coupling between the flow vector and the hardening moduli. Because of this, differentiating these quantities with respect to stresses and internal variables —the crucial step in obtaining consistent tangent matrices— is rather involved. Numerical differentiation is used

here to approximate these derivatives. The approximated derivatives are then used 1) to compute consistent tangent matrices (global problem) and 2) to integrate the constitutive equation at each Gauss point (local problem) with the Newton-Raphson method. The choice of the stepsize (i.e. the perturbation in the approximation schemes), based on the concept of relative stepsize, poses no difficulties. In contrast to previous approaches for the MRS–Lade model, quadratic convergence is achieved, for both the local and the global problems. The computational efficiency (CPU time) and robustness of the proposed approach is illustrated by means of several numerical examples, where the major relevant topics are discussed in detail.

### 4.2.1 Introduction

Consistent or algorithmic (as opposed to continuum) tangent matrices are a key ingredient in computational plasticity (Simo and Taylor 1985, Runesson et al. 1986). They are needed to solve the so-called *global problem* (i.e. the elastoplastic boundary value problem) with quadratic convergence, via a full Newton-Raphson linearization.

The most involved step in obtaining consistent tangent matrices is computing the derivatives of the flow vector and the hardening moduli with respect to the stresses and the internal variables. These derivatives are also required to achieve quadratic convergence with the full Newton-Raphson method for the *local problem* (i.e. the integration of the elastoplastic constitutive relation at the Gauss-point level).

In complex material models, these derivatives are difficult to obtain analytically, because there is a high coupling between stresses and internal variables. This is the situation, for instance, for the MRS–Lade model (Sture et al. 1989, Jeremić and Sture 1994, Macari et al. 1997). This model is used to describe the behaviour of granular materials, such as sand, under both low and high confinement stresses (Macari et al. 1994, Macari et al. 1997). It features a yield surface consisting of a cone and a cap, hardening and softening variables based on dissipated plastic work and a non-associated flow rule in the meridian plane of the cone region.

Because of the highly coupled nature of the MRS–Lade model, not all the required derivatives are readily available. Without these derivatives, it is not possible to compute a full consistent tangent matrix. In the literature, there are two techniques to integrate the MRS–Lade model which do not require the computation of the derivatives of the hardening moduli (which are rather more involved to obtain than the derivatives of the stresses): 1) a tangent approach for the stresses and a direct substitution of the internal variable equations Jeremić and Sture (1994, 1997) and 2) a two-level technique with a tangent approach for the stress invariants and a Picard iteration with an adaptive order inverse interpolation for the internal variables (Macari et al. 1997). However, in both cases quadratic convergence is never achieved, because these approaches are not based on a consistent linearization of *all* equations with respect to *all* unknowns.

In the context of computational plasticity, section 3.1 (Pérez-Foguet et al. 2000*d*) shows that numerical differentiation is a simple and competitive alternative to classical analytical derivatives, provided that adequate schemes and stepsizes are chosen. It maintains the characteristic quadratic convergence of the Newton-Raphson method, both for the local and the global problems. In section 3.1, the results obtained with numerical differentiation are compared with those obtained with the analytical derivatives for two material models with analytical derivatives available: von Mises and Rounded Hyperbolic Mohr-Coulomb. The main conclusion is that numerical differentiation is an efficient and robust strategy, which maintains quadratic convergence and has a very marginal CPU time overhead (with respect to analytical derivatives).

In this paper numerical differentiation is applied to compute the derivatives of a quite more complex model: MRS–Lade. In contrast to section 3.1, this model does not have all the analytical derivatives of the flow vector and the hardening moduli available. However, the same conclusions are reached: robustness and efficiency.

Thus, the improvement of numerical differentiation over other techniques for the MRS–Lade model (Jeremić and Sture 1997, Macari et al. 1997) is more clear than for simpler material models: it is the first time that quadratic convergence results are presented for the global and the local problems for this model. As a final introductory remark, it is worth noting that the MRS–Lade model is used here for illustrative purposes. The same approach can be used to compute consistent tangent matrices for other complex material models.

An outline of this section follows. The problem is stated in subsection 4.2.2. After some preliminaries on small-strain elastoplasticity, the MRS–Lade model is briefly reviewed. The proposed approach, based on numerical differentiation, is presented in subsection 4.2.4. In subsection 4.2.5, several examples of local and global problems are discussed in detail, and the convergence results are highlighted. Finally, the main conclusions are summarized in subsection 4.2.6.

## 4.2.2 Problem statement

### Preliminaries

Many elastoplastic models for small strains can be put in the general form (Ortiz and Popov 1985)

$$\begin{aligned}\boldsymbol{\varepsilon} &= \boldsymbol{\varepsilon}^e + \boldsymbol{\varepsilon}^p \\ \boldsymbol{\sigma} &= \mathbf{E}\boldsymbol{\varepsilon}^e \\ \dot{\boldsymbol{\varepsilon}}^p &= \dot{\lambda}\mathbf{m}(\boldsymbol{\sigma}, \boldsymbol{\kappa}) \\ \dot{\boldsymbol{\kappa}} &= \dot{\lambda}\mathbf{h}(\boldsymbol{\sigma}, \boldsymbol{\kappa}),\end{aligned}\tag{4.2.1}$$

where  $\boldsymbol{\varepsilon}$ ,  $\boldsymbol{\varepsilon}^e$  and  $\boldsymbol{\varepsilon}^p$  are the total, elastic and plastic strain tensors respectively,  $\boldsymbol{\sigma}$  is the Cauchy stress tensor,  $\mathbf{E}$  is the elastic stiffness tensor,  $\mathbf{m}$  is the flow vector,  $\boldsymbol{\kappa}$  is the set of internal variables and  $\mathbf{h}$  are the plastic moduli. The plastic multiplier  $\dot{\lambda}$  is determined with the aid of the loading–unloading criterion, that can be expressed in Kuhn-Tucker form as

$$F(\boldsymbol{\sigma}, \boldsymbol{\kappa}) \leq 0 \quad \dot{\lambda} \geq 0 \quad F(\boldsymbol{\sigma}, \boldsymbol{\kappa})\dot{\lambda} = 0,\tag{4.2.2}$$

where  $F(\boldsymbol{\sigma}, \boldsymbol{\kappa})$  is the yield function that defines the admissible stress states.

### The MRS–Lade model

The MRS–Lade model has been developed at the University of Colorado by Macari, Runesson and Sture (Sture et al. 1989) and it is a further development of Lade’s three-invariant model for cohesionless soils. The model is used to simulate the behaviour of granular materials, such as sand, under both low and high confinement stresses (Macari et al. 1994, Macari et al. 1997). It features 1) a two-surface yield function, comprising a smooth cone surface and a smooth cap surface intersecting in a plane curve (ellipse segment) in the deviatoric plane, 2) hardening and softening variables that depend on dissipated plastic work, and 3) a non-associated flow rule in the meridian plane of the cone region.

Several slight modifications to the original formulation of the model have been devised (Jeremić and Sture 1994, Macari et al. 1997, Pérez-Foguet and Huerta 1999). In this paper the modification presented in section 4.1 (Pérez-Foguet and Huerta 1999) is used. It consists on a new definition of the flow vector for the cone region that avoids the corner problem or the flip-over of previous formulations.

In the following, the main formulas of the model are reviewed. The goal is to illustrate the complex dependence of  $\mathbf{m}$  and  $\mathbf{h}$  with respect to  $\boldsymbol{\sigma}$  and  $\boldsymbol{\kappa}$ . In subsection 4.2.7, some additional formulas and the expanded expressions of  $\mathbf{m}$  and  $\mathbf{h}$  can be found. The physical meaning of the different laws and parameters and the main characteristics of the model are widely discussed by Sture et al. (1989).

The yield function  $F$  depends on the three stress invariants ( $p$ ,  $q$  and  $\theta$ , defined in subsection 4.2.7) and two internal variables,  $\kappa_{\text{con}}$  and  $\kappa_{\text{cap}}$ . It is defined in two parts, the cone and the cap:

$$\begin{aligned}F_{\text{con}}(\boldsymbol{\sigma}, \kappa_{\text{con}}) &= q \left(1 + \frac{q}{q_a}\right)^m g(\theta) - \eta_{\text{con}}(\kappa_{\text{con}})p \\ F_{\text{cap}}(\boldsymbol{\sigma}, \kappa_{\text{con}}, \kappa_{\text{cap}}) &= \left(\frac{p - p_m}{p_r}\right)^2 + \left(\frac{q(1 + q/q_a)^m g(\theta)}{f_r}\right)^2 - 1\end{aligned}\tag{4.2.3}$$

with

$$\begin{aligned}p_m &= \alpha p_{\text{cap}}(\kappa_{\text{cap}}) \\ p_r &= (1 - \alpha)p_{\text{cap}}(\kappa_{\text{cap}}) \\ f_r &= \alpha \eta_{\text{con}}(\kappa_{\text{con}})p_{\text{cap}}(\kappa_{\text{cap}}),\end{aligned}\tag{4.2.4}$$

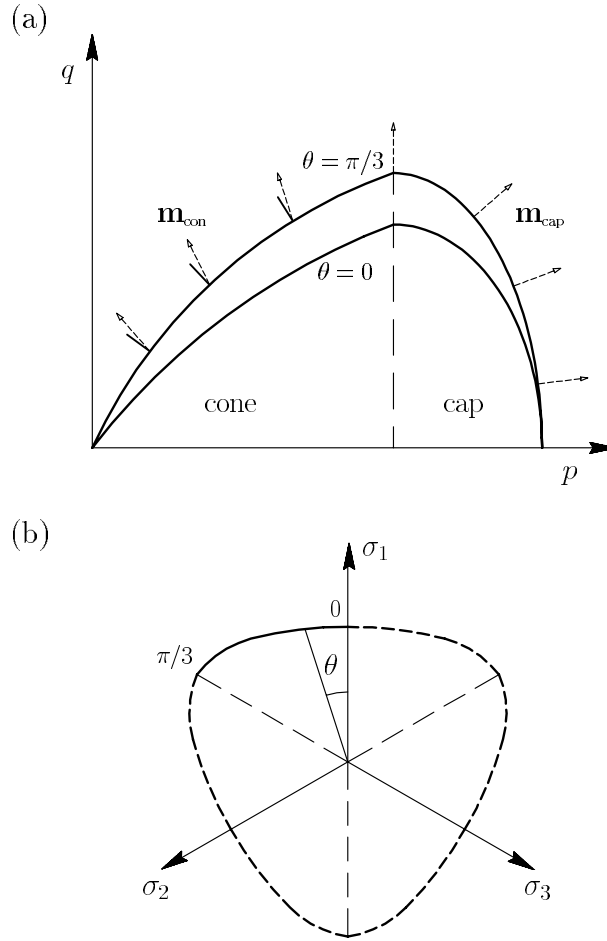


Figure 4.4: MRS–Lade model. Trace of the yield criterion: (a) on the meridian plane; (b) on the deviatoric plane.

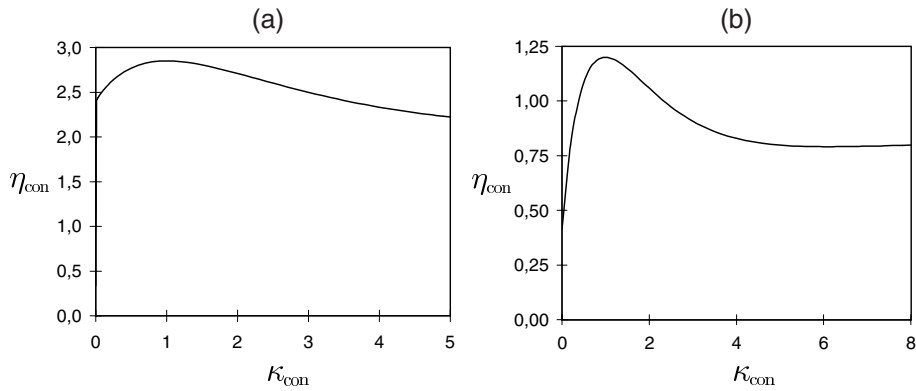


Figure 4.5: MRS–Lade model. Hardening–softening function  $\eta_{\text{con}}(\kappa_{\text{con}})$ . (a) Soil S1 and (b) soil S2; see table 4.2.

where  $q_a$ ,  $m$  and  $\alpha$  are parameters of the model,  $g(\theta)$  is the Willam–Warnke function,  $\eta_{\text{con}}(\kappa_{\text{con}})$  is a hardening–softening function related with the friction angle, and  $p_{\text{cap}}(\kappa_{\text{cap}})$  is a hardening function related with the triaxial compression strength. The definitions of  $g(\theta)$ ,  $\eta_{\text{con}}(\kappa_{\text{con}})$  and  $p_{\text{cap}}(\kappa_{\text{cap}})$  are in subsection 4.2.7. The trace of  $F_{\text{con}}$  and  $F_{\text{cap}}$  in the meridian plane and in the deviatoric plane are depicted in figure 4.4. The nonlinear shape of the hardening–softening function  $\eta_{\text{con}}(\kappa_{\text{con}})$  is shown in figure 4.5.

The plastic flow vector  $\mathbf{m}$  is also defined in two parts, cone and cap:

$$\mathbf{m}(\boldsymbol{\sigma}, \kappa_{\text{con}}, \kappa_{\text{cap}}) = \begin{cases} \mathbf{m}_{\text{con}} = \mathbf{A}\mathbf{n}_{\text{con}} & \text{if } p \leq \alpha p_{\text{cap}}(\kappa_{\text{cap}}) \\ \mathbf{m}_{\text{cap}} = \mathbf{n}_{\text{cap}} & \text{if } p > \alpha p_{\text{cap}}(\kappa_{\text{cap}}) \end{cases} \quad (4.2.5)$$

with

$$\begin{aligned} \mathbf{A}(\boldsymbol{\sigma}, \kappa_{\text{cap}}) &= \mathbf{I}_{n_\sigma} + \left( \frac{\gamma}{3} \frac{\alpha p_{\text{cap}}(\kappa_{\text{cap}}) - p}{\alpha p_{\text{cap}}(\kappa_{\text{cap}}) + p} - \frac{1}{3} \right) \boldsymbol{\delta} \boldsymbol{\delta}^T \\ \mathbf{n}_{\text{con}}(\boldsymbol{\sigma}, \kappa_{\text{con}}) &= \frac{\partial F_{\text{con}}}{\partial \boldsymbol{\sigma}} \\ \mathbf{n}_{\text{cap}}(\boldsymbol{\sigma}, \kappa_{\text{con}}, \kappa_{\text{cap}}) &= \frac{\partial F_{\text{cap}}}{\partial \boldsymbol{\sigma}}, \end{aligned} \quad (4.2.6)$$

where  $\gamma$  is a parameter of the model,  $\mathbf{I}_*$  is the identity matrix of order  $*$ ,  $n_\sigma$  is the number of stress components (i.e.  $n_\sigma = 4$  for plane-strain or axisymmetric 2-D problems and  $n_\sigma = 6$  for 3-D problems),  $T$  denotes transpose and  $\boldsymbol{\delta}$  is the vector Kronecker delta (for three-dimensional problems,  $\boldsymbol{\delta}^T = (1, 1, 1, 0, 0, 0)$ ). The expanded expressions of  $\mathbf{n}_{\text{con}}$  and  $\mathbf{n}_{\text{cap}}$  are in subsection 4.2.7. Matrix  $\mathbf{A}$  represents the non-associated behaviour of the model in the cone region (i.e.  $\mathbf{m}_{\text{con}} \neq \mathbf{n}_{\text{con}}$ ). At  $p = \alpha p_{\text{cap}}(\kappa_{\text{cap}})$ ,  $\mathbf{m}_{\text{con}}$  and  $\mathbf{m}_{\text{cap}}$  are equal and they only have a deviatoric component. Thus, the transition of the flow vector between cone and cap regions is smooth. In the original formulation of the model (Sture et al. 1989), the matrix  $\mathbf{A}$  is constant. As a consequence, the expression of  $\mathbf{m}_{\text{con}}$  is a little simpler, but the transition of the flow vector at the cone-cap intersection is non-smooth and an expensive corner algorithm must be implemented to solve the local problem.

The evolution of the internal variables is defined as

$$\begin{aligned} \dot{\kappa}_{\text{con}} &= \frac{1}{c_{\text{con}} p_a} \left( \frac{p}{p_a} \right)^{-l} \dot{w}^p \\ \dot{\kappa}_{\text{cap}} &= \frac{1}{c_{\text{cap}} p_a} \left( \frac{p_{\text{cap},0}}{p_a} \right)^{-r} \dot{w}^p \end{aligned} \quad (4.2.7)$$

where  $c_{\text{con}}$ ,  $c_{\text{cap}}$ ,  $p_a$ ,  $p_{\text{cap},0}$ ,  $l$  and  $r$  are parameters of the model and  $\dot{w}^p$  is the rate of plastic work dissipated during loading along the stress path:

$$\dot{w}^p = \boldsymbol{\sigma}^T \dot{\boldsymbol{\varepsilon}}^p. \quad (4.2.8)$$

Combining equations (4.2.7–4.2.8) and the last equation in (4.2.1) shows that the hardening moduli  $\mathbf{h} = (h_{\text{con}}, h_{\text{cap}})$  are

$$\begin{aligned} h_{\text{con}}(\boldsymbol{\sigma}, \kappa_{\text{con}}, \kappa_{\text{cap}}) &= \frac{1}{c_{\text{con}} p_a} \left( \frac{p}{p_a} \right)^{-l} \boldsymbol{\sigma}^T \mathbf{m} \\ h_{\text{cap}}(\boldsymbol{\sigma}, \kappa_{\text{con}}, \kappa_{\text{cap}}) &= \frac{1}{c_{\text{cap}} p_a} \left( \frac{p_{\text{cap},0}}{p_a} \right)^{-r} \boldsymbol{\sigma}^T \mathbf{m}. \end{aligned} \quad (4.2.9)$$

Equations (4.2.5–4.2.6) and (4.2.9) clearly exhibit a complex dependence of the flow vector  $\mathbf{m}$  and the hardening moduli  $\mathbf{h}$  with respect to the stresses  $\boldsymbol{\sigma}$  and the internal variables  $\boldsymbol{\kappa}$ . This makes the efficient time-integration of the MRS-Lade model a challenging issue, as discussed in the following.

### 4.2.3 Proposed approach

#### Numerical time-integration: the local and global problems

Time-integration of equation (4.2.1) with the backward Euler scheme yields the following nonlinear local problem (Ortiz and Popov 1985, Simo and Hughes 1998):

$$\begin{aligned} {}^{n+1}\boldsymbol{\sigma} + \lambda \mathbf{E} \mathbf{m}({}^{n+1}\boldsymbol{\sigma}, {}^{n+1}\boldsymbol{\kappa}) &= \mathbf{E}({}^{n+1}\boldsymbol{\varepsilon} - {}^n\boldsymbol{\varepsilon}^p) \\ {}^{n+1}\boldsymbol{\kappa} - \lambda \mathbf{h}({}^{n+1}\boldsymbol{\sigma}, {}^{n+1}\boldsymbol{\kappa}) &= {}^n\boldsymbol{\kappa} \\ F({}^{n+1}\boldsymbol{\sigma}, {}^{n+1}\boldsymbol{\kappa}) &= 0. \end{aligned} \quad (4.2.10)$$

In equation (4.2.10), the state at time  ${}^n t$  (i.e., quantities  ${}^n \boldsymbol{\varepsilon}^p$  and  ${}^n \boldsymbol{\kappa}$ ) and the *total* strains  ${}^{n+1} \boldsymbol{\varepsilon}$  at time  ${}^{n+1} t$  are known. The unknowns of this local problem are the stresses  ${}^{n+1} \boldsymbol{\sigma}$  and the internal variables  ${}^{n+1} \boldsymbol{\kappa}$  at time  ${}^{n+1} t$ , and the incremental plastic multiplier  $\lambda$ .

To solve this nonlinear local problem with the Newton-Raphson method the Jacobian of the residual is needed. Using standard vector notation of computational mechanics (Zienkiewicz and Taylor 1988, Crisfield 1991) the Jacobian can be written as

$${}^{n+1} \mathbf{J} = \begin{pmatrix} (\mathbf{I}_{n_\sigma} + \lambda \mathbf{E} \frac{\partial \mathbf{m}}{\partial \boldsymbol{\sigma}}) & \lambda \mathbf{E} \frac{\partial \mathbf{m}}{\partial \boldsymbol{\kappa}} & \mathbf{E} \mathbf{m} \\ -\lambda \frac{\partial \mathbf{h}}{\partial \boldsymbol{\sigma}} & (\mathbf{I}_{n_\kappa} - \lambda \frac{\partial \mathbf{h}}{\partial \boldsymbol{\kappa}}) & -\mathbf{h} \\ \mathbf{n}^t & \boldsymbol{\xi}^t & 0 \end{pmatrix}_{t={}^{n+1} t} \quad (4.2.11)$$

where  $\mathbf{n}$  and  $\boldsymbol{\xi}$  are the derivatives of  $F(\boldsymbol{\sigma}, \boldsymbol{\kappa})$  with respect to  $\boldsymbol{\sigma}$  and  $\boldsymbol{\kappa}$  respectively, and  $n_\kappa$  is the number internal variables (i.e.  $n_\kappa = 2$  for the MRS–Lade model).

On the other hand, to solve the global problem with quadratic convergence it is necessary to use the consistent tangent matrix (Simo and Taylor 1985, Runesson et al. 1986). To compute this matrix, the consistent tangent moduli  $d{}^{n+1} \boldsymbol{\sigma} / d{}^{n+1} \boldsymbol{\varepsilon}$  at each Gauss point are needed. They are obtained by linearizing equation (4.2.10). This linearization can be represented in a compact form as (Ortiz and Martin 1989)

$$\mathbf{P}^T ({}^{n+1} \mathbf{J})^{-1} \mathbf{P} \mathbf{E}, \quad (4.2.12)$$

where  $\mathbf{P}^T = (\mathbf{I}_{n_\sigma}, \mathbf{0}_{n_\kappa+1})$  is the projection matrix on stress space. Therefore, the Jacobian matrix, equation (4.2.11), is needed for both the local and the global problems.

The most difficult components to compute of the Jacobian are typically the derivatives of  $\mathbf{m}$  and  $\mathbf{h}$  with respect to  $\boldsymbol{\sigma}$  and  $\boldsymbol{\kappa}$ . This is the case for the MRS–Lade model, which exhibits a high coupling of all the components. Note, for instance, that the hardening moduli  $\mathbf{h}$  are defined in terms of the flow vector  $\mathbf{m}$ . This is caused by the fact that plastic work drives the hardening, see equation (4.2.7). Thus  $\mathbf{h}$  depends on  $\boldsymbol{\sigma}$  and  $\boldsymbol{\kappa}$  both explicitly and through  $\mathbf{m}$ , see equation (4.2.9). This coupling makes the analytical computation of the derivatives a very cumbersome task. Jeremić and Sture (1994), for instance, only present the analytical expression of *some* of the required derivatives for the original formulation of the model (that is, for  $\mathbf{A}$  constant). They use these derivatives to solve the local problem and to compute an approximation to the consistent tangent matrix for the global problem. However, quadratic convergence is not achieved, because not all the required derivatives are used.

#### 4.2.4 Numerical differentiation

Indeed, quadratic convergence can only be attained by means of a *full* Newton-Raphson method. That is, *all* the derivatives of  $\mathbf{m}$  and  $\mathbf{h}$  with respect to  $\boldsymbol{\sigma}$  and  $\boldsymbol{\kappa}$  are needed. One possibility would be to obtain the analytical expression of the missing derivatives. However, this is rather involved, even with the help of an algebraic manipulator. For this reason, a different course is followed here: all required derivatives are approximated numerically. Three of the techniques discussed in section 3.1 will be employed: the forward difference scheme, 1ND- $O(h)$ , the centered difference scheme, 1ND- $O(h^2)$ , and the scheme based on complex variables, 1CND- $O(h^2)$ , see table 4.1. The forward difference scheme is first-order accurate, and the other two schemes are second-order accurate. With these schemes, the derivative of  $m_i$  with respect to  $\kappa_j$  (recall that vector notation is used), for instance, is approximated either by

$$\begin{aligned} \text{1ND} - O(h) \quad \frac{\partial m_i}{\partial \kappa_j}(\boldsymbol{\sigma}, \boldsymbol{\kappa}) &= \frac{m_i(\boldsymbol{\sigma}, \boldsymbol{\kappa} + h \mathbf{e}_j) - m_i(\boldsymbol{\sigma}, \boldsymbol{\kappa})}{h}, \\ \text{1ND} - O(h^2) \quad \frac{\partial m_i}{\partial \kappa_j}(\boldsymbol{\sigma}, \boldsymbol{\kappa}) &= \frac{m_i(\boldsymbol{\sigma}, \boldsymbol{\kappa} + h \mathbf{e}_j) - m_i(\boldsymbol{\sigma}, \boldsymbol{\kappa} - h \mathbf{e}_j)}{2h}, \\ \text{1CND} - O(h^2) \quad \frac{\partial m_i}{\partial \kappa_j}(\boldsymbol{\sigma}, \boldsymbol{\kappa}) &= \frac{\text{Im}(m_i(\boldsymbol{\sigma}, \boldsymbol{\kappa} + \sqrt{-1} h \mathbf{e}_j))}{h}, \end{aligned} \quad (4.2.13)$$

where  $h$  is the stepsize and  $\mathbf{e}_j$  is the  $j$ th unit vector. Similar expressions are used for  $\partial \mathbf{m} / \partial \boldsymbol{\sigma}$ ,  $\partial \mathbf{h} / \partial \boldsymbol{\sigma}$  and  $\partial \mathbf{h} / \partial \boldsymbol{\kappa}$ . The approximated derivatives are then used to solve the local and the global problems.

Notation	Description
1ND-O( $h$ )	Forward difference scheme (1 <sup>st</sup> order accurate)
1ND-O( $h^2$ )	Centered difference scheme (1 <sup>st</sup> order accurate)
1CND-O( $h^2$ )	Approximation based on complex variables (2 <sup>nd</sup> order accurate)

Table 4.1: Numerical approximations to first derivatives.

	S1	S2		S1	S2
$E$ [MPa]	1.46 E5	1.46 E5	$\bar{\eta}_{\text{con}}$	2.8499	1.2
$\nu$	0.2	0.2	$v$	1.15	1.15
$p_a$ [kPa]	1.	1.	$k_1$	0.2	0.2
$q_a$ [kPa]	1.	1.	$k_2$	0.7256	0.7256
$p_{\text{cap},0}$ [kPa]	5. E3	5. E3	$c_{\text{con}}$	4.3067 E-2	4. E-3
$e$	0.7	0.7	$c_{\text{cap}}$	1.59 E-4	1.59 E-4
$m$	7.423 E-2	7.423 E-2	$l$	1.0867654	1.0867654
$\gamma$	0.5	0.5	$r$	1.592	1.592
$\alpha$	0.8	0.8	$\epsilon$	7.5 E-5	7.5 E-1

Table 4.2: Sets of material parameters. S1 is a Sacramento River sand (Macari et al. 1997). S2 is a modification of S1.

A crucial issue in numerical differentiation is the choice of the stepsize  $h$ . In this work it is selected as shown in section 3.1, by using the concept of *relative* stepsize,  $h_r$ . The optimal value of the relative stepsize can be approximated by  $\sqrt{\text{macheps}}$  for the first-order scheme, 1ND-O( $h$ ), and by  $\sqrt[3]{\text{macheps}}$  for the second-order accurate schemes, 1ND-O( $h^2$ ) and 1CND-O( $h^2$ ), with *macheps* the machine precision.

Numerical experiments reveal a good behaviour of numerical differentiation (that is, quadratic convergence for both the local and the global problems) for a wide range of relative stepsizes,  $h_r$ . In order to reduce the effect of rounding errors,  $h_r$  is taken as a negative power of 2 ( $h_r = 2^{-k}$ ), not of 10 ( $h_r = 10^{-k}$ ). This choice is relevant in some critical zones, as illustrated in next subsection.

## 4.2.5 Examples

In this subsection, several local and global problems are solved quadratically with numerical differentiation. The three techniques of table 4.1 are compared and the main features of each one are remarked.

Two sets of parameters have been used, see table 4.2. Soil S1 is a dense Sacramento River sand (Macari et al. 1997). Soil S2 is a small modification of soil S1. The modifications are 1) a smaller value of  $\bar{\eta}_{\text{con}}$ , which reduces the size of the elastic domain ( $\bar{\eta}_{\text{con}}$  is the maximum value of  $\eta_{\text{con}}$ , see equations (4.2.17) and (4.2.18) in subsection 4.2.7, and 2) different values of  $c_{\text{con}}$  and  $\epsilon$ , which result in a more nonlinear evolution of the cone internal variable,  $\kappa_{\text{con}}$ , see equations (4.2.9), (4.2.17) and (4.2.18). With these two modifications, soil S2 is quite more demanding from a numerical point of view than soil S1.

First part of subsection 4.2.5 deals with local problems. The relative error of the vector of unknowns  $\mathbf{x} = (\boldsymbol{\sigma}, \boldsymbol{\kappa}, \lambda)$  measured in the maximum norm is used to control the convergence. Global problems are treated in second part of subsection 4.2.5. Convergence is checked with the relative error in energy norm.

All the computations (except where the opposite is explicitly stated) have been performed by using a negative power of 2, not of 10, as the relative stepsize ( $h_r = 2^{-k}$ ), to reduce the effect of rounding errors. However, relative stepsizes are expressed as powers of 10 to indicate clearly the order of magnitude. For instance,  $h_r = 10^{-6}$  in the text or in a table means that the actual computation is performed with  $h_r = 2^{-19}$ .

Strict tolerances have been used:  $10^{-14}$  for local problems and  $10^{-8}$  to  $10^{-10}$  for global problems. This allows for a comparative assessment of the three differentiation techniques. Quite larger values may be chosen in practice.

	Path A	Path B	Path C
$\boldsymbol{\sigma}_{\text{ini}}$	(1000, 1000, 1000, 0)	(4800, 4800, 4800, 0)	(4800, 4800, 4800, 0)
$\boldsymbol{\kappa}_{\text{ini}}$	(0, 0)	(0, 0)	(0, 0)
$\Delta\boldsymbol{\varepsilon}$	(0, 0, 0, 0.2)	(0, 0, 0, 0.2)	(-0.1, 0, 0, 0)
$n$	50	50	50

Table 4.3: Definition of the three stress paths for the local problems.

Step	1	5	10	25	50
Path A	40.3°	51.5°	53.1°	54.1°	53.9°
Path B	30.0°	35.8°	42.2°	54.7°	54.1°
Path C	60.0°	60.0°	60.0°	60.0°	60.0°

Table 4.4: Evolution of the Lode angle  $\theta$  (in degrees) during the three stress paths defined in table 4.3.

Num. approx.	Path A	Path B
1ND- $O(h)$	$10^{-6} - 10^{-9}$	$10^{-6} - 10^{-10}$
1ND- $O(h^2)$	$10^{-4} - 10^{-10}$	$10^{-4} - 10^{-10}$
1CND- $O(h^2)$	$10^{-4} - 10^{-11}$	$10^{-4} - 10^{-11}$

Table 4.5: Range of relative stepsizes  $h_r$  that give quadratic convergence in the local problem, stress paths A and B.

### Local problems

In the local problem, numerical differentiation is applied to compute the Jacobian shown in equation (4.2.11) at each Gauss point.

In order to show that quadratic convergence is obtained in all stress–internal variable space, three different deformation paths are considered. The paths are characterized by an initial stress–internal variable state,  $\boldsymbol{\sigma}_{\text{ini}}$  and  $\boldsymbol{\kappa}_{\text{ini}}$ , and a total strain increment,  $\Delta\boldsymbol{\varepsilon}$  (applied in 50 steps) see table 4.3. The material parameters of soil S2 have been used.

In figure 4.6 the trace on the meridian plane of the three stress paths and the trace of the initial and final yield criteria are depicted. Paths A and B correspond to pure shear deformation, see  $\Delta\boldsymbol{\varepsilon}$  in table 4.3. Path A develops in the cone region, and path B starts in the cap region and then changes to the cone region. Path C corresponds to uniaxial compression, see table 4.3, and it develops in the cap region. In table 4.4 the evolution of the Lode angle,  $\theta$ , is shown. Note that, in general, the paths are three–dimensional curves in the three–invariant space  $(p, q, \theta)$ . Indeed,  $\theta$  changes during loading in paths A and B. For path C, on the other hand,  $\theta$  remains constant and equal to  $\pi/3$ . Finally, note that the three paths start in hardening regime and finish during softening. Therefore, a wide range of different local problems is covered.

In the following, quadratic convergence results are presented and analyzed for moderate strain increments. After that, the behaviour of the three numerical differentiation schemes, see table 4.1, is compared. Finally, quadratic convergence results for large excursions outside the elastic domain are also shown.

**Convergence illustration** The convergence results for different steps of the three stress paths are depicted in figure 4.7. These results correspond to local problems in the cone and the cap regions and to hardening and softening regimes. All the convergence results are quadratic up to a (very strict) tolerance of  $10^{-14}$ . These results have been obtained with the approximation 1ND- $O(h)$  and with  $h_r = 10^{-6}$ , see equation (4.2.13) and table 4.1. The convergence is also quadratic if checked independently for each unknown of the local problem ( $\boldsymbol{\sigma}$ ,  $\boldsymbol{\kappa}$  and  $\lambda$ ), see figure 4.8. In figure 4.9 the stress invariants and the yield criterion during the iterations are depicted. In three iterations the approximations are very close to the final result. The remaining iterations are just to improve the accuracy.



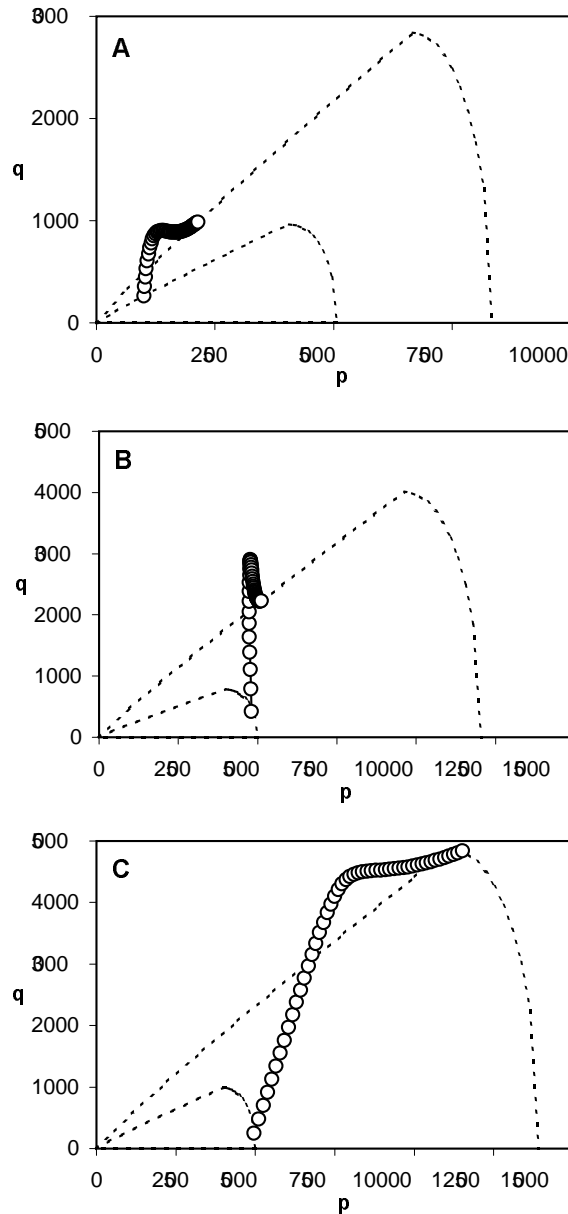


Figure 4.6: Trace of the three paths and of their initial and final yield criteria on the meridian plane.

**Comparison of numerical differentiation schemes** The three numerical differentiation schemes of table 4.1 have been compared through the integration of paths A, B and C defined in table 4.3. The convergence results of step 31 of path A with different relative stepsizes  $h_r$  are depicted in figure 4.10. They are quadratic up to a tolerance of  $10^{-14}$  for a wide range of  $h_r$  with the three schemes. The same results are obtained with the other steps of paths A and B. In table 4.5, the ranges of  $h_r$  that give quadratic convergence during all the steps of paths A and B are summarized. The main difference between the three techniques is that second order of accuracy provides quadratic convergence with larger  $h_r$ . This is in agreement with section 3.1 and it is due to the fact that the truncation error of the second-order schemes is lower than for the first-order scheme.

The ranges of  $h_r$  that give quadratic convergence during all the steps of path C are summarized in table 4.6. Both the ranges obtained using  $h_r = 10^{-k}$  and  $h_r = 2^{-k}$  are indicated. Two aspects are important: first, the ranges are quite narrower than for paths A and B; and second, with the approximation 1ND- $O(h)$  the improvement of using  $h_r = 2^{-k}$  is notorious. This is because path

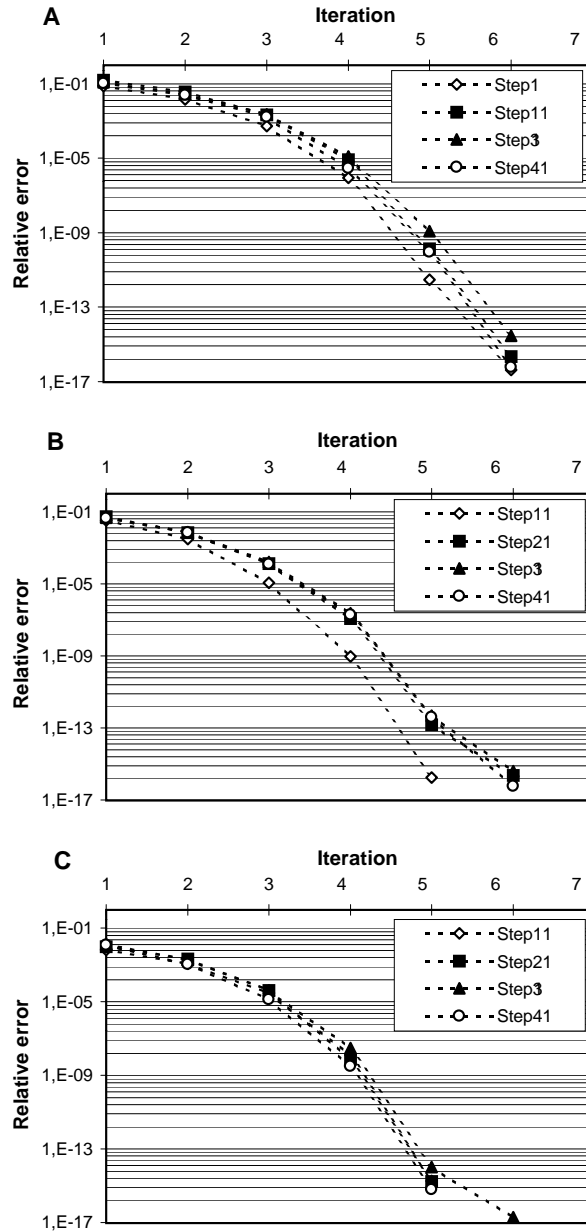


Figure 4.7: Convergence results for various steps of paths A, B and C

Num. approx.	$h_r = 10^{-k}$	$h_r = 2^{-k}$
1ND- $O(h)$	$10^{-5} - 10^{-6}$	$10^{-5} - 10^{-8}$
1ND- $O(h^2)$	$10^{-3} - 10^{-7}$	$10^{-3} - 10^{-7}$
1CND- $O(h^2)$	$10^{-4} - 10^{-9}$	$10^{-4} - 10^{-9}$

Table 4.6: Range of relative stepsizes  $h_r$  that give quadratic convergence in the local problem, stress path C.

C develops at Lode angle equal to  $\pi/3$ . In this zone, the influence of the rounding errors is quite more important than in the other regions of the stress space. Nevertheless, the range in which one can choose  $h_r$  is still wide enough and includes the approximation indicated before.

**Large excursions outside the elastic domain** In order to show that quadratic convergence is also attained for large excursions outside the elastic domain, path A defined in table 4.3 is

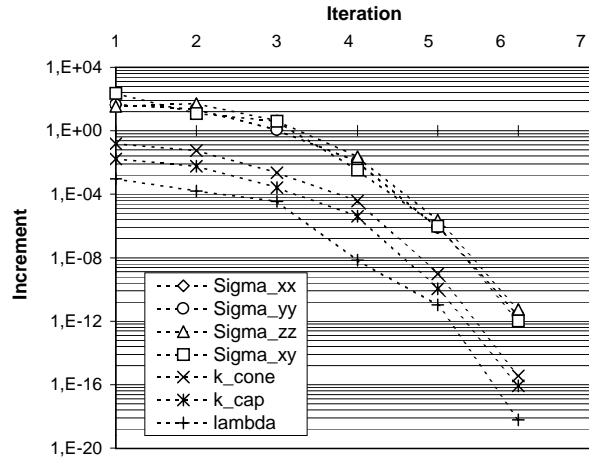


Figure 4.8: Convergence of the different unknowns of the local problem for step 31 of path A.

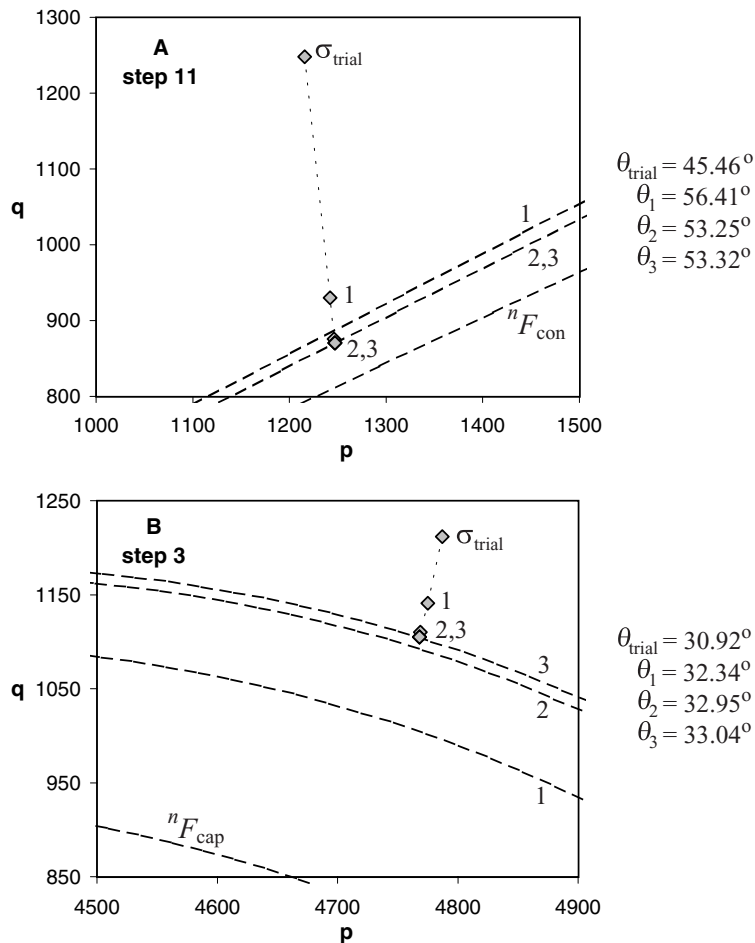


Figure 4.9: Evolution of the stress invariants and the yield criterion during the iterations of step 11 of path A and step 3 of path B.

solved with only 10 steps. The convergence results for various steps, depicted in figure 4.11, are again quadratic. On the other hand, note that, as expected, more iterations than in the original integration of path A with 50 steps are needed (compare Figures 4.11 and 4.7). This is clearly due to the use of the solution of one step as the initial approximation for the next step. Larger steps

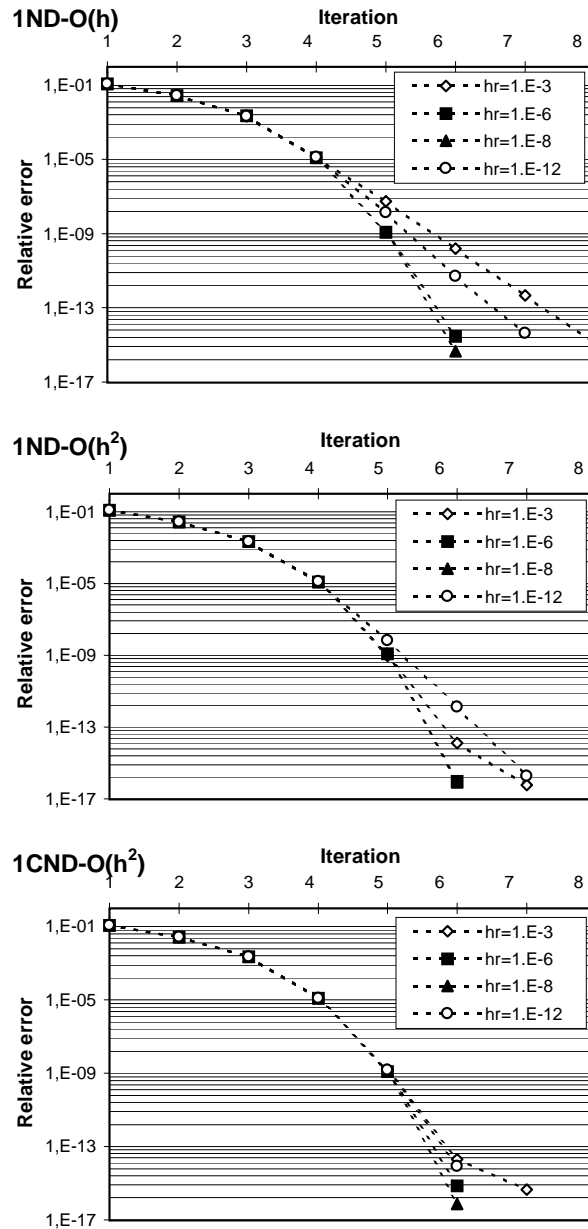


Figure 4.10: Convergence results for step 31 of path A using the approximations defined in table 4.1 with several relative stepsizes  $h_r$

mean worse initial approximations and, thus, more iterations.

To summarize these examples on local problems: quadratic convergence can be attained in a simple manner with any of the three techniques of numerical differentiation. This is valid for any stress path (cone and cap regions, hardening and softening regimes), and for both moderate and large steps. The choice of the stepsize presents no difficulties, because quadratic convergence is obtained for a wide range of relative stepsizes.

### Global problems

In the following, numerical differentiation is applied to solve several boundary value problems (i.e., global problems). That is, the numerical approximations of table 4.1 are employed to compute consistent tangent matrices, see equation (4.2.12). Moreover, they are also used to solve the corresponding local problems.

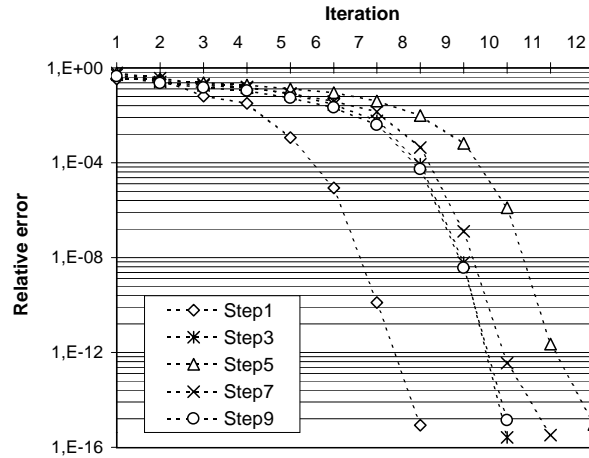


Figure 4.11: Convergence results for path A with only 10 steps

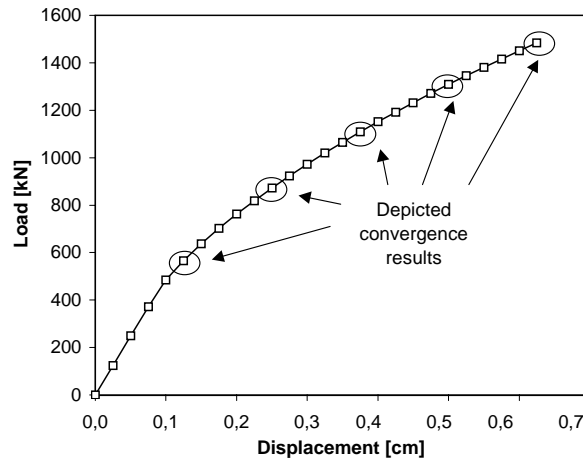


Figure 4.12: Load versus displacement curve for the pile problem.

Three examples are presented: the vertical displacement of a pile, a triaxial test with an homogeneous sample and a triaxial test with a non-homogeneous sample. These examples illustrate that the three numerical approximations to first derivatives of the flow vector and the hardening moduli, see table 4.1, are useful to solve the global problem with quadratic convergence. Moreover, their main features (range of adequate relative stepsizes and computational cost) are compared.

**Vertical displacement of a pile** The first example is the vertical displacement of a pile. The definition of the problem is presented by Potts and Gens (1985), and it is only summarized here. Figure 3.8 shows the finite element mesh. It corresponds to a horizontal disc of soil. The thickness of the disc is 5 cm and the pile radius is 7.5 cm. A hydrostatic initial stress state of  $-250$  kPa is imposed. To model the loading of the pile, a vertical displacement of 0.625 cm is prescribed over the boundary AF in 25 load steps. To model the infinite extension of the disc, zero vertical displacements are prescribed over the boundary CD. Due to the essentially one-dimensional nature of the problem, vertical lines (such as EB) are prescribed to remain vertical during loading. The material parameters correspond to the dense Sacramento River sand, see table 4.2.

The load versus displacement curve is depicted in figure 4.12. The most stressed points are those next to the boundary AF. Because of the one-dimensional behaviour of the problem, the limit state is reached when the integration points close to AF start the softening regime. After that, stresses are no longer transferred to the rest of the disc. Thus, this simple example only tests the behaviour during hardening. The convergence results for several load steps (indicated in figure 4.12) are shown in figure 4.13. Convergence is quadratic up to a strict tolerance of  $10^{-10}$ . These

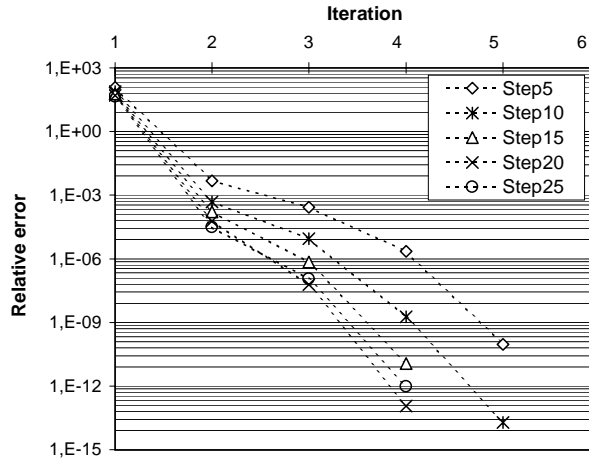


Figure 4.13: Convergence results for various load steps of the pile problem

Num. approx.	Range of $h_r$
1ND-O( $h$ )	$10^{-5} - 10^{-9}$
1ND-O( $h^2$ )	$10^{-3} - 10^{-9}$
1CND-O( $h^2$ )	$10^{-3} - 10^{-9}$

Table 4.7: Range of relative stepsizes  $h_r$  that give quadratic convergence up to a tolerance of  $10^{-10}$  in the pile problem.

$h_r$	$10^{-3}$	$10^{-4}$	$10^{-5}$	$10^{-6}$	$10^{-7}$	$10^{-8}$	$10^{-9}$
1ND-O( $h$ )	113%	106%	107%	101%	101%	100%	101%
1ND-O( $h^2$ )	122%	122%	124%	124%	122%	122%	122%
1CND-O( $h^2$ )	141%	143%	139%	139%	139%	140%	138%

Table 4.8: Relative CPU time of the three numerical differentiation techniques with several relative stepsizes  $h_r$  in the pile problem.

particular results have been obtained with the approximation 1CND-O( $h^2$ ) and with  $h_r = 10^{-5}$ . However, similar results are obtained with the other techniques and other relative stepsizes. In table 4.7, the ranges of  $h_r$  that give quadratic convergence during all the test are summarized.

In table 4.8 the computational cost (CPU time) of the three techniques with several  $h_r$  is summarized. The values are given in % with respect to 1ND-O( $h$ ) with  $h_r = 10^{-8}$ . The number of iterations during all the load process is equal for all the entries in table 4.8, except for 1ND-O( $h$ ) with  $h_r = 10^{-3}$  and  $10^{-4}$  (which require 6 and 1 extra iterations respectively). The results are quite independent of  $h_r$  and are mainly related with the derivation technique. The 1ND-O( $h^2$ ) and 1CND-O( $h^2$ ) approximations are respectively 20% and 40% more expensive than the 1ND-O( $h$ ) approximation. These results are in agreement with the fact that the cost of a complex function evaluation can be approximated (when additions and products are balanced) by the cost of four real function evaluations. Thus, the overhead of complex approximation (one complex evaluation of the flow vector and the hardening moduli) is twice that of centered differences (that needs two real evaluations).

Quadratic convergence results have been obtained without difficulties in a simple global problem. There are not significant differences between the convergence results of the three techniques. The ranges of optimal relative stepsize are wide in all cases. Differences appear regarding computational cost.

**Triaxial test: homogeneous sample** The second example is the triaxial test with an homogeneous sample. The material parameters, defined in table 4.2, correspond to a Sacramento River sand. These parameters are the same that Macari et al. (1997) used to simulate the triaxial test at Gauss point level. Note that  $\epsilon$  is not defined in that reference, so an inverse problem has been

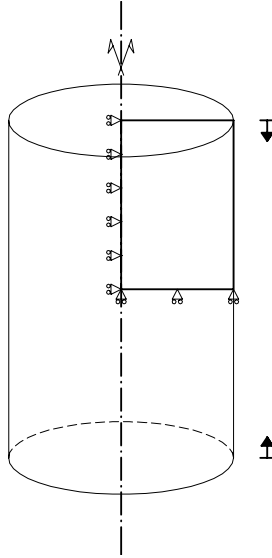


Figure 4.14: Triaxial test. Problem statement.

Num. approx.	Range of $h_r$
1ND- $O(h)$	$10^{-3} - 10^{-5}$
1ND- $O(h^2)$	$10^{-3} - 10^{-5}$
1CND- $O(h^2)$	$10^{-3} - 10^{-7}$

Table 4.9: Range of relative stepsizes  $h_r$  that give quadratic convergence in the homogeneous triaxial problem up to a tolerance of  $10^{-8}$  (1ND- $O(h)$  approximation) or  $10^{-10}$  (the other two).

solved to determine its value. Here, the triaxial test is solved at the global level, and, as expected, the results are homogeneous and equal to those presented by Macari et al. (1997).

The definition of the problem is summarized in figure 4.14. The sample is axisymmetric. The top and bottom are assumed perfectly smooth and the vertical displacement is imposed simultaneously in both faces. Thus, just a half of the sample is considered in the numerical simulation. The load is divided in two phases: first the sample is precompressed, and second a vertical displacement is imposed at the top. A structured mesh of 150 ( $10 \times 15$ ) elements has been used. In figure 4.15, the relationship between  $q$  and the axial strain for several precompressions is depicted. They coincide with those presented by Macari et al. (1997).

In the following, attention is focused in the test with a precompression of 600 kPa. In figure 4.16 three nonlinear solvers are compared, by showing the accumulated iterations versus the axial strain relationship. The advantage of using the consistent tangent matrix is clear: the number of iterations needed with the full (Kt) or modified (K1) Newton-Raphson methods is much lower than with the initial-stress (K0) method, that only uses the elastic tangent matrix. All the steps are in the plastic regime. However, figure 4.16 clearly shows that the step with a convergence more sensible to the computation of the consistent tangent matrix is step 2. It is the first step with a significant change in the internal variables (more specifically, in  $\kappa_{\text{con}}$ ). For that reason, the three differentiation schemes have been compared in that load step. The convergence results are shown in figure 4.17, and the range of relative stepsizes that keep quadratic convergence is summarized in table 4.9.

The convergence results of figure 4.17 show that the first-order scheme, 1ND- $O(h)$ , keeps quadratic convergence up to a tolerance of  $10^{-8}$ , and that second-order schemes reach a tolerance of  $10^{-10}$ . This difference is due to the fact that the Lode angle  $\theta$  is equal to  $\pi/3$  for all the Gauss points (recall that the global problem is homogeneous). This region of stress space is the most demanding one for approximating the derivatives of the flow vector. For this reason, the differences between order 1 and order 2 in the truncation error are clear. However, it must be noted that the indicated tolerances are very strict for any practical application. Thus, even the 1ND- $O(h)$  approximation is accurate enough if a tolerance of, say,  $10^{-6}$  is used. With this tolerance, the

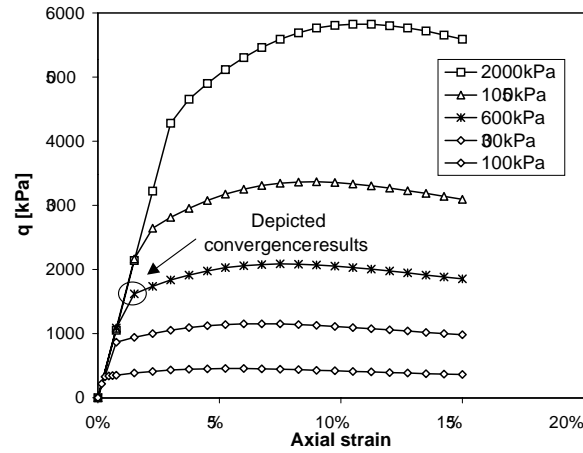


Figure 4.15: Invariant  $q$  versus axial strain curves for the homogeneous triaxial problem with various precompressions.

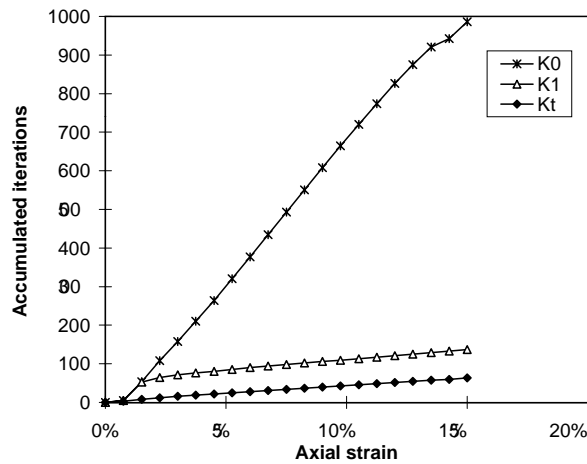


Figure 4.16: Accumulated iterations versus load level for the homogeneous triaxial problem with three nonlinear solvers: initial stress method (K0), modified Newton-Raphson method (K1) and full Newton-Raphson method (Kt).

three techniques provide quadratic convergence for a wide range of relative stepsizes.

**Triaxial test: non-homogeneous sample** The third example is the triaxial test with an non-homogeneous sample. A structured mesh of 600 ( $20 \times 30$ ) elements, the material parameters of soil S2 and a precompression of 600 kPa have been used. The finite element in the the bottom left corner is weakened (the values of  $\bar{\eta}_{con}$  and  $p_{cap,0}$  are 10% lower) to induce a non-homogeneous response.

The evolution of the second invariant of the deviatoric part of the strain tensor is depicted in figure 4.18. Because the MRS-Lade model is not regularized and includes non-associated plasticity and softening, the problem localizes. However, the axisymmetric nature of the test delays localization (Rudnicki and Rice 1975). Thus, part of the behaviour after the limit load can be modelled without mesh dependence. Figure 4.19 shows the evolution of the load and the number of Gauss points which undergo plastic loading versus displacement. Note that after the limit load, a large reduction of number of Gauss points under plastic loading is found. Several Gauss points that were on plastic loading change to elastic unloading. Therefore, this part of the example is called *partial unloading*. During partial unloading, the mechanical behaviour of the sample becomes clearly non-homogeneous.

The convergence results for several load steps during partial unloading is depicted in figure



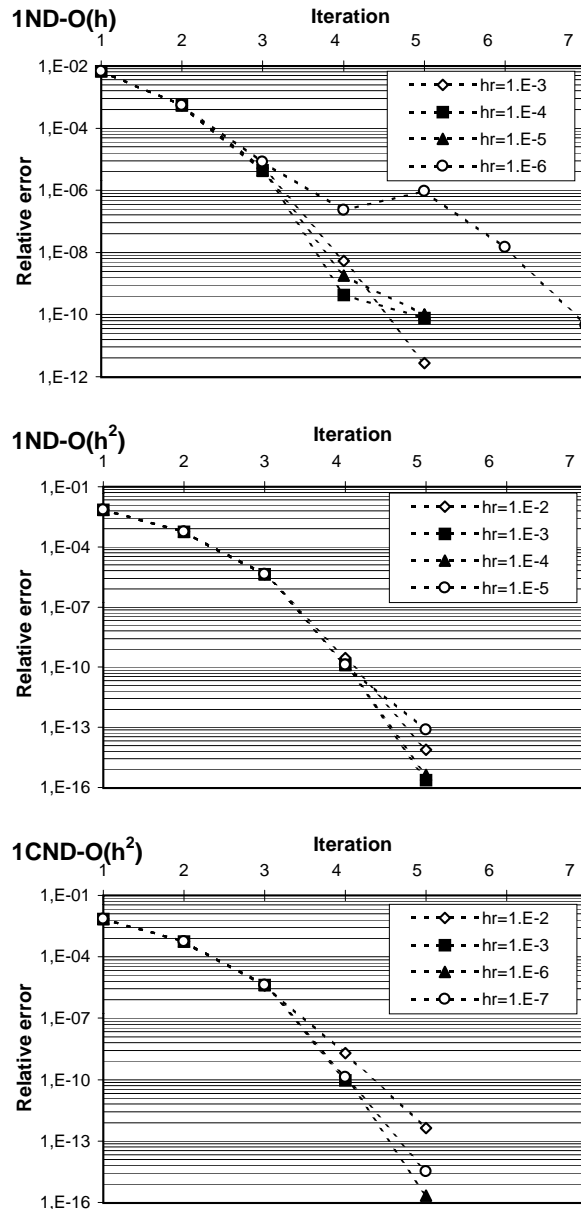


Figure 4.17: Convergence results for step 2 of the homogeneous triaxial problem with various relative stepsizes  $h_r$ .

4.20. Note that quadratic convergence is found. These results are obtained with the technique 1CND- $O(h^2)$ , with  $h_r = 10^{-5}$  and with a tolerance of  $10^{-10}$ . In these steps, the same results are found with the other techniques and other relative stepsizes  $h_r$ .

However, if a too strict tolerance is imposed, the convergence results obtained during the hardening regime depend on the differentiation technique and the relative stepsize. It has been already shown for the homogeneous triaxial test that the first-order technique only ensures quadratic convergence up to a tolerance of  $10^{-8}$ . In order to check the behaviour of the three techniques with this example, the number of accumulated iterations along all the loading process with several  $h_r$  are summarized in table 4.10. Two tolerances are considered:  $10^{-8}$  and  $10^{-10}$ .

Table 4.10(a) shows that, with a tolerance of  $10^{-8}$ , the three techniques need a very similar number of iterations for a wide range of relative stepsizes. This indicates quadratic convergence in all the entries of the table. On the other hand, only the 1CND- $O(h^2)$  approximation ensures quadratic convergence up to a tolerance of  $10^{-10}$  during all the loading, see table 4.10(b). For

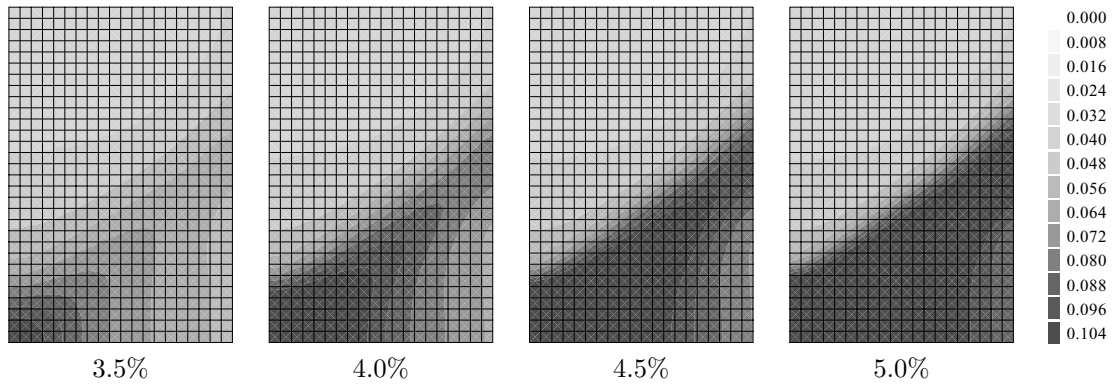


Figure 4.18: Second invariant of the deviatoric part of the strain tensor for different values of the axial strain (vertical displacement/initial height) in the non-homogeneous triaxial problem.

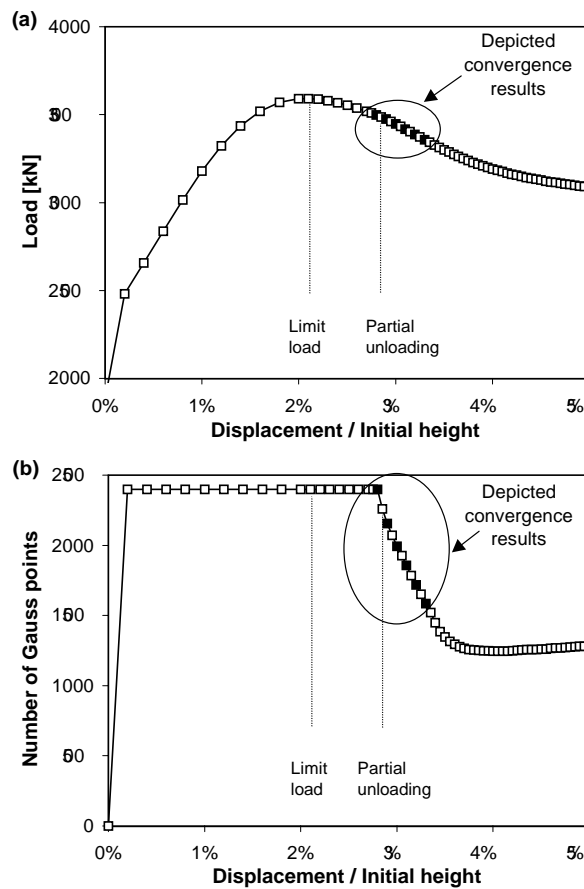


Figure 4.19: Non-homogeneous triaxial problem. Evolution of (a) load and (b) number of Gauss points with plastic loading versus displacement.

the other two approximations, there are variations in the number of iterations, caused by a loss of quadratic convergence.

A comparison of the computational cost (CPU time) of the three techniques with a tolerance of  $10^{-10}$  and with several  $h_r$  is presented in table 4.11. The values are given in % with respect to 1ND- $O(h)$  with  $h_r = 10^{-6}$ . The forward difference scheme has a relative cost of 100 — 110%, the centered difference scheme of 120 — 130 % and the approximation based on complex variables of 130 — 135 %.

Finally, in figure 4.21 several nonlinear solvers are compared. With the K0 method (which

(a)

$h_r$	$10^{-3}$	$10^{-4}$	$10^{-5}$	$10^{-6}$	$10^{-7}$	$10^{-8}$
1ND-O( $h$ )	255	225	226	226	230	—
1ND-O( $h^2$ )	225	227	226	225	228	—
1CND-O( $h^2$ )	225	225	225	225	225	225

(b)

$h_r$	$10^{-3}$	$10^{-4}$	$10^{-5}$	$10^{-6}$	$10^{-7}$	$10^{-8}$
1ND-O( $h$ )	315	271	268	251	260	—
1ND-O( $h^2$ )	264	245	243	249	257	—
1CND-O( $h^2$ )	253	236	235	235	239	236

Table 4.10: Number of accumulated iterations for the non-homogeneous triaxial problem: (a) with a tolerance of  $10^{-8}$ ; (b) with a tolerance of  $10^{-10}$ .

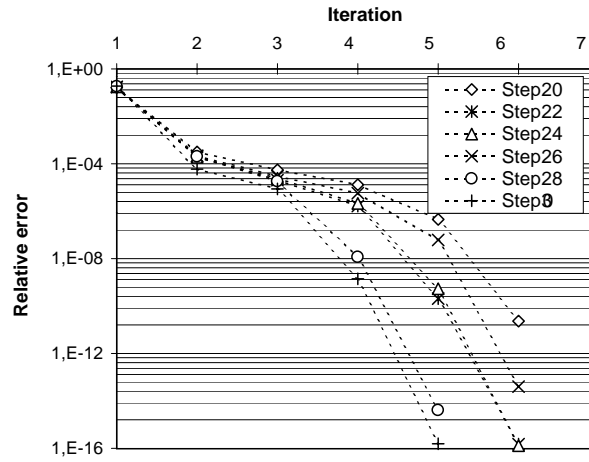


Figure 4.20: Convergence results for various load steps of the non-homogeneous triaxial problem.

$h_r$	$10^{-3}$	$10^{-4}$	$10^{-5}$	$10^{-6}$	$10^{-7}$	$10^{-8}$
1ND-O( $h$ )	145%	111%	112%	100%	105%	—
1ND-O( $h^2$ )	150%	122%	119%	122%	127%	—
1CND-O( $h^2$ )	150%	134%	132%	131%	134%	133%

Table 4.11: Relative CPU time of the three numerical differentiation techniques with several relative stepsizes  $h_r$  in the non-homogeneous triaxial problem up to a tolerance of  $10^{-10}$ .

does not use the consistent tangent matrix) the step right after the limit load needs more than 400 iterations. The K1 method (consistent tangent matrix updated at the beginning of each step) fails to converge when the partial unloading is starting. Only with a full Newton-Raphson method, Kt, or at least updating the consistent tangent matrix regularly within the step (each two iterations, Kd2, or each four, Kd4) can the analysis be completed.

## 4.2.6 Concluding remarks

Numerical differentiation of the flow vector and the hardening moduli allows to compute the consistent tangent matrix when the analytical derivatives are not available. This allows to solve boundary value problems (i.e. global problems) in computational plasticity with quadratic convergence.

Moreover, the approximated derivatives are also used to compute the Jacobian of the residual of the local problem (time-integration of the elastoplastic constitutive equations at each Gauss point). Thus, a full Newton-Raphson method can be applied over stresses and internal variables, and quadratic convergence is also obtained.

The proposed approach has been illustrated with a complex material model: the MRS-Lade model. It is a cap-cone model with highly nonlinear hardening-softening laws. Analytical deriva-

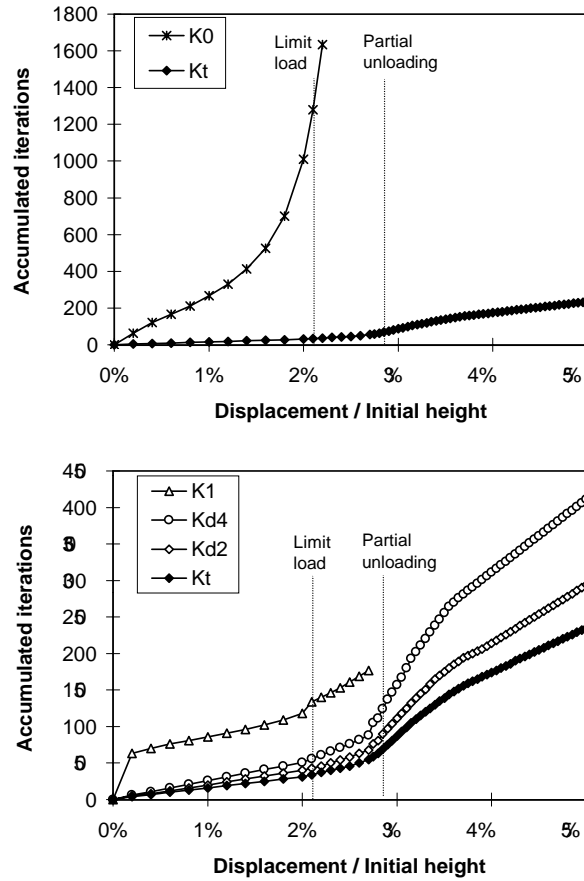


Figure 4.21: Accumulated iterations versus load level for the non-homogeneous triaxial problem with various nonlinear solvers.

tives of the flow vector and the hardening moduli are not available in the literature. In fact, it is first time that quadratic convergence results are presented for this model (both for local and global problems). Extension to other complex material models is straightforward, and consists only in changing the definition of the flow vector and the hardening moduli.

Three numerical differentiation schemes have been applied: forward and centered difference schemes (first and second order respectively) and an approximation based in complex variables (second order). The three schemes provide quadratic convergence. The choice of an adequate stepsize does not present any difficulty. The concept of relative stepsize introduced in section 3.1 (Pérez-Foguet et al. 2000d) has been exploited, and good results (i.e. quadratic convergence at the local and global level for a convergence tolerance of  $10^{-8}$  or even more strict) have been obtained for a wide range of relative stepsizes.

As a final concluding remark, it must be noted that the proposed approach has a modest computational cost. A direct comparison of analytical versus numerical differentiation cannot be made for this model, because analytical derivatives are not available. However, for other material models, an overhead in computational cost (of numerical derivatives with respect to analytical derivatives) of only 1% to 2% has been found, see section 3.1.

#### 4.2.7 Appendix: MRS–Lade model definition

In the following, the formulas needed to compute the flow vector and the hardening–softening moduli that have not been presented in subsection 4.2.2 are summarized.

The model is expressed through the following three invariants:

$$p = -\frac{1}{3} I_1 \quad q = \sqrt{3} J_2 \quad \theta = \frac{1}{3} \arccos \left( \frac{3\sqrt{3} J_3}{2J_2^{3/2}} \right) \quad (4.2.14)$$

with

$$I_1 = \boldsymbol{\sigma}^T \boldsymbol{\delta} \quad J_2 = \frac{1}{2} \mathbf{s}^T \mathbf{L} \mathbf{s} \quad J_3 = \det[\mathbf{s}] \quad (4.2.15)$$

where  $\mathbf{s} = \boldsymbol{\sigma} + p \boldsymbol{\delta}$ ,  $\mathbf{L}$  is a diagonal matrix with the diagonal terms equal to  $\{1, 1, 1, 2, 2, 2\}$  (in three-dimensional problems), and  $\det[*]$  is the determinant of  $*$ .

The expression of the Willam-Warnke function reads

$$g(\theta) = \frac{(2e-1)^2 + 4(1-e^2) \cos(\theta)^2}{2(1-e^2) \cos(\theta) - (2e-1) \sqrt{5e^2 - 4e + 4(1-e^2) \cos(\theta)^2}}, \quad (4.2.16)$$

where  $e$  is a parameter of the model.

The expressions of the hardening-softening laws are

$$\begin{aligned} \eta_{\text{con}}(\kappa_{\text{con}}) &= a \exp(-b\kappa_{\text{con}}) (k_1 + \kappa_{\text{con}})^{1/v} + k_2 \bar{\eta}_{\text{con}} \left( \frac{\kappa_{\text{con}}}{\epsilon + \kappa_{\text{con}}} \right) \\ p_{\text{cap}}(\kappa_{\text{cap}}) &= p_{\text{cap},0} \left( 1 + \kappa_{\text{cap}}^{1/r} \right), \end{aligned} \quad (4.2.17)$$

where  $k_1$ ,  $k_2$ ,  $v$ ,  $\bar{\eta}_{\text{con}}$  and  $\epsilon$  are parameters of the model, and

$$\begin{aligned} a &= \exp(b) \left( \frac{1}{1+k_1} \right)^{1/v} \left( 1 - \frac{k_2}{1+\epsilon} \right) \bar{\eta}_{\text{con}} \\ b &= \frac{1}{v(1+k_1)} + \frac{k_2 \epsilon}{(1+\epsilon)(1+\epsilon-k_2)}. \end{aligned} \quad (4.2.18)$$

Finally,  $\mathbf{n}_{\text{con}}$  and  $\mathbf{n}_{\text{cap}}$ , the derivatives of  $F_{\text{con}}$  and  $F_{\text{cap}}$  with respect to  $\boldsymbol{\sigma}$ , are obtained applying the chain rule:

$$\frac{\partial F_*}{\partial \boldsymbol{\sigma}} = \frac{\partial F_*}{\partial p} \frac{\partial p}{\partial \boldsymbol{\sigma}} + \frac{\partial F_*}{\partial q} \frac{\partial q}{\partial \boldsymbol{\sigma}} + \frac{\partial F_*}{\partial \theta} \frac{\partial \theta}{\partial \boldsymbol{\sigma}}, \quad (4.2.19)$$

where the subscript  $*$  stands for either cone or cap.

The derivatives of  $p$ ,  $q$  and  $\theta$  with respect to  $\boldsymbol{\sigma}$  are

$$\begin{aligned} \frac{\partial p}{\partial \boldsymbol{\sigma}} &= -\frac{1}{3} \boldsymbol{\delta} \\ \frac{\partial q}{\partial \boldsymbol{\sigma}} &= \frac{3}{2q} \mathbf{L} \mathbf{s} \\ \frac{\partial \theta}{\partial \boldsymbol{\sigma}} &= \left( \frac{3 \cos(3\theta)}{2q^2 \sin(3\theta)} \right) \mathbf{L} \mathbf{s} + \left( \frac{9}{2q^3 \sin(3\theta)} \right) \frac{\partial J_3}{\partial \boldsymbol{\sigma}}. \end{aligned} \quad (4.2.20)$$

The partial derivatives of  $F_{\text{con}}$  are

$$\begin{aligned} \frac{\partial F_{\text{con}}}{\partial p} &= -\eta_{\text{con}}(\kappa_{\text{con}}) \\ \frac{\partial F_{\text{con}}}{\partial q} &= \left( 1 + \frac{q}{q_a} \right)^m \left( 1 + \frac{mq}{q_a + q} \right) g(\theta) \\ \frac{\partial F_{\text{con}}}{\partial \theta} &= q \left( 1 + \frac{q}{q_a} \right)^m \frac{\partial g(\theta)}{\partial \theta}, \end{aligned} \quad (4.2.21)$$

and the partial derivatives of  $F_{\text{cap}}$  are

$$\begin{aligned} \frac{\partial F_{\text{cap}}}{\partial p} &= 2 \frac{p - p_m}{p_r^2} \\ \frac{\partial F_{\text{cap}}}{\partial q} &= \frac{2q g(\theta)^2}{f_r^2} \left( 1 + \frac{q}{q_a} \right)^{2m} \left( 1 + \frac{mq}{q_a + q} \right) \\ \frac{\partial F_{\text{cap}}}{\partial \theta} &= \frac{2q^2 g(\theta)}{f_r^2} \left( 1 + \frac{q}{q_a} \right)^{2m} \frac{\partial g(\theta)}{\partial \theta}. \end{aligned} \quad (4.2.22)$$

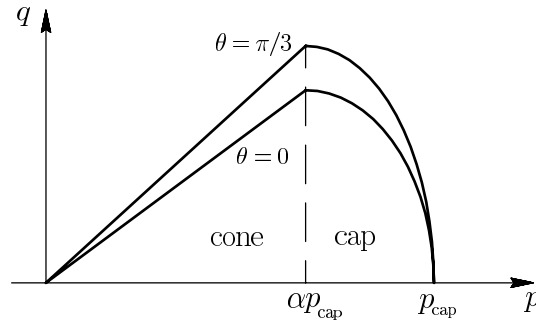


Figure 4.22: MRS–Lade model for cohesionless materials. Trace of the simplified yield criterion on the meridian plane.

### 4.3 The MRS-Lade model for cohesive materials

In the following, cohesion is included in the MRS–Lade model for granular materials. It is shown that both the cone and the cap yield surfaces must be modified to account for cohesion. Moreover, the cone flow potential is modified to preclude the so-called corner problem in the cone–cap intersection.

#### 4.3.1 Introduction

The MRS–Lade model is used to describe the behaviour of granular materials (Sture et al. 1989, Macari et al. 1994). It was developed by Macari, Runesson and Sture (Sture et al. 1989) on the basis of Lade’s three-invariant model for cohesionless soils. The yield function of the MRS–Lade model consists of two surfaces, a cone and a cap. Cohesion can be included to model the interlocking at very low confining stresses.

A formulation of the MRS–Lade model for cohesive materials is presented by Jeremić and Sture (1994) and Macari et al. (1997). However, these references suggest that only the cone yield function is modified to account for cohesion. As a result, a discontinuity (gap) appears in the cone–cap intersection, so the yield function is not closed and the model is not valid.

An alternative formulation is presented here. The key idea is that the constitutive equations for cohesionless materials can also be used for cohesive materials, if stresses are replaced with translated stresses along the hydrostatic axis. This rationale is proposed by Kim and Lade (1988) and Lade and Kim (1988a, 1988b). Therefore, both the cone *and* the cap yield functions change if cohesion is included. The proposed extension also precludes the so-called corner problem (i.e. the jump in the direction of the flow vector in the cone–cap intersection) of the original model. Following section 4.1 (Pérez-Foguet and Huerta 1999), where the cohesionless version of the model is considered, the corner is suppressed by (slightly) changing the flow potential in the cone region.

An outline of this paper follows. The original MRS–Lade model for cohesionless materials is briefly reviewed in subsection 4.3.2. The proposed formulation for cohesive materials is presented in subsections 4.3.3 to 4.3.5. Finally, some concluding remarks are made in subsection 4.3.6.

#### 4.3.2 The original MRS–Lade model for cohesionless materials

The original formulation of the model is briefly reviewed here. In order to clarify the presentation, a simplified version of the model is considered. A detailed presentation of the model can be found in Sture et al. (1989) and Jeremić and Sture (1994). The efficient numerical time-integration of the model, leading to quadratic convergence, is discussed in section 4.2 (Pérez-Foguet et al. 2000e).

#### Yield function

The yield function  $F$  depends on the stress tensor,  $\boldsymbol{\sigma}$ , through three stress invariants,  $p$ ,  $q$  and  $\theta$ , defined, for instance in section 4.2, and on two internal variables,  $\kappa_{\text{con}}$  and  $\kappa_{\text{cap}}$ , driven by

dissipated plastic work.  $F$  is defined in two parts, the cone and the cap.

The cone yield function is

$$F_{\text{con}} = qg(\theta) - \eta_{\text{con}}p, \quad (4.3.1)$$

where  $g(\theta)$  is the Willam-Warkne function and  $\eta_{\text{con}}(\kappa_{\text{con}})$  is the cone hardening–softening function. Figure 4.22 depicts the trace of the cone yield function on the meridian plane.

The cap yield function is

$$F_{\text{cap}} = \left( \frac{p - \alpha p_{\text{cap}}}{(1 - \alpha)p_{\text{cap}}} \right)^2 + \left( \frac{qg(\theta)}{\eta_{\text{con}}\alpha p_{\text{cap}}} \right)^2 - 1, \quad (4.3.2)$$

where  $p_{\text{cap}}(\kappa_{\text{cap}})$  is the cap hardening function, that corresponds to the isotropic yield stress under compression, and  $\alpha$  ( $0 < \alpha < 1$ ) is a parameter of the model. It can be seen directly from equation (4.3.2) that the trace of the cap yield function on the  $p$ – $q$  plane is an ellipse segment, centered at  $p = \alpha p_{\text{cap}}$ , see figure 4.22(a).

### Flow potential

The plastic strain rate,  $\dot{\epsilon}^p$ , is defined as

$$\dot{\epsilon}^p = \dot{\lambda} \frac{\partial G}{\partial \boldsymbol{\sigma}}, \quad (4.3.3)$$

where  $\dot{\lambda}$  is the plastic multiplier and  $G$  is the flow potential. The flow potential is associated in the cap region ( $G_{\text{cap}} = F_{\text{cap}}$ ) and non-associated in the cone region ( $G_{\text{cone}} \neq F_{\text{con}}$ ). The cone flow potential is

$$G_{\text{cone}} = qg(\theta) - n\eta_{\text{con}}p, \quad (4.3.4)$$

where  $n$  is a non-negative parameter that accounts for non-associativity.

### Internal variables

The evolution of the internal variables  $\kappa_{\text{con}}$  and  $\kappa_{\text{cap}}$  is defined as

$$\begin{aligned} \dot{\kappa}_{\text{con}} &= \frac{1}{c_{\text{con}}p_a} \left( \frac{p}{p_a} \right)^{-l} \dot{w}^p \\ \dot{\kappa}_{\text{cap}} &= \frac{1}{c_{\text{cap}}p_a} \left( \frac{p_{\text{cap},0}}{p_a} \right)^{-r} \dot{w}^p, \end{aligned} \quad (4.3.5)$$

where  $c_{\text{con}}$ ,  $p_a$ ,  $l$ ,  $c_{\text{cap}}$ ,  $p_{\text{cap},0}$  and  $r$  are parameters of the model and  $\dot{w}^p$  is the rate of plastic work dissipated during loading along the stress path,

$$\dot{w}^p = \boldsymbol{\sigma} : \dot{\epsilon}^p. \quad (4.3.6)$$

### 4.3.3 The proposed MRS–Lade model for cohesive materials

The model has been extended to cohesive materials following the work of Kim and Lade (1988) and Lade and Kim (1988a, 1988b). This is done by translating the principal stress space along the hydrostatic axis. Thus, a constant stress,  $p_c < 0$  (which reflects the effect of the tensile strength of the material), is added to the normal stress components before substitution in the constitutive equations for cohesionless materials of subsection 4.3.2.

This amounts to keeping the same constitutive equations but referred to a translated stress tensor,  $\bar{\boldsymbol{\sigma}}$ , defined as

$$\bar{\boldsymbol{\sigma}} = \boldsymbol{\sigma} + p_c \boldsymbol{\delta}, \quad (4.3.7)$$

where  $\boldsymbol{\delta}$  is Kronecker's delta. The three invariants of the translated stresses are

$$\bar{p} = p - p_c, \quad \bar{q} = q \quad \text{and} \quad \bar{\theta} = \theta. \quad (4.3.8)$$

In the following, the constitutive equations of the cohesive version of the model are derived. They are expressed in the original, non-translated stress  $\boldsymbol{\sigma}$ , to show that the inclusion of cohesion changes the meaning of some material parameters of the model. Moreover, the cone flow potential that precludes the corner problem, see section 4.1, is extended to cohesive materials.

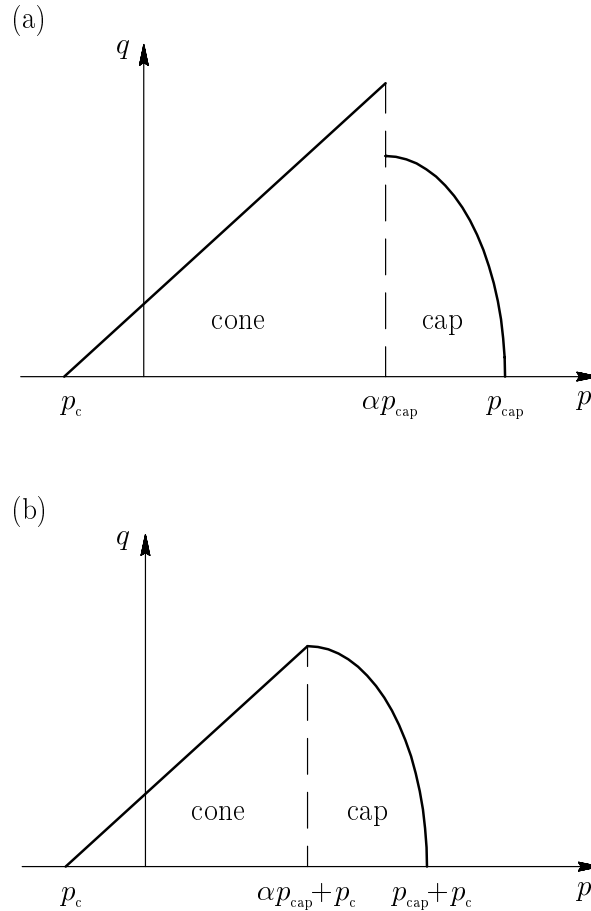


Figure 4.23: MRS–Lade model for cohesive materials. Trace of the yield criterion on the meridian plane: (a) incorrect open surface; (b) correct closed surface

### Yield function

As shown by Jeremić and Sture (1994) and Macari et al. (1997), the cone yield function for cohesive materials is

$$F_{\text{con}} = qq(\theta) - \eta_{\text{con}}\bar{p} = qq(\theta) - \eta_{\text{con}}(p - p_c), \quad (4.3.9)$$

so the cone apex is at  $p = p_c$ , see figure 4.23. This new cone yield function *cannot* be complemented with the cap of equation (4.3.2), as suggested in Jeremić and Sture (1994) and Macari et al. (1997). This leads to a yield surface with a gap at  $p = \alpha p_{\text{cap}}$ , which is clearly not admissible, see figure 4.23(a). It is necessary to redefine the cap yield function in terms of the translated stress invariants,  $\bar{p}$ ,  $\bar{q}$  and  $\bar{\theta}$ . After substituting the relationships of equation (4.3.8), the following expression is found:

$$F_{\text{cap}} = \left( \frac{p - p_c - \alpha p_{\text{cap}}}{(1 - \alpha)p_{\text{cap}}} \right)^2 + \left( \frac{qq(\theta)}{\eta_{\text{con}}\alpha p_{\text{cap}}} \right)^2 - 1. \quad (4.3.10)$$

With this new definition of the cap yield function, a closed yield surface is obtained, see figure 4.23(b).

Note that in the cohesive version of  $F_{\text{cap}}$ , equation (4.3.10),  $p_{\text{cap}}$  does not retain its original meaning of isotropic yield stress (Sture et al. 1989). The maximum value of  $p$  is now  $p_{\text{cap}} + p_c$ . Moreover, the cone–cap intersection has also changed; it is now located at  $\alpha p_{\text{cap}} + p_c$ . For cohesionless materials, for which  $p_c$  vanishes, the original values are recovered in both cases.



### Flow potential: suppressing the corner problem

The original formulation of the MRS–Lade model, reviewed in subsection 4.3.2, exhibits the so-called corner problem: a jump in the flow vector in the cone–cap intersection. From a constitutive standpoint this poses no trouble, because Koiter’s rule can be applied to unambiguously determine the flow direction. However, it is a source of numerical difficulties, because specific algorithms must be implemented for the integration of the constitutive equation at the local level.

In the context of the cohesionless version of the model, section 4.1 shows how to suppress the corner problem by modifying the cone flow potential of equation (4.3.4). After prescribing a smooth transition of the flow vector at the cone–cap intersection and integrating, the following corrected expression for the cone flow potential is obtained in section 4.1:

$$G_{\text{con}}^* = qg(\theta) - \gamma\eta_{\text{con}}(2\alpha p_{\text{cap}} \ln(\alpha p_{\text{cap}} + p) - p), \quad (4.3.11)$$

where  $\gamma$  is a non-negative constant that defines the degree of non-associativity at  $p = 0$  (the cone apex in the cohesionless version of the model).

The flow potential is extended to cohesive materials in the same way that the yield function. Therefore,  $G_{\text{cap}}$  is equal to  $F_{\text{cap}}$ , see equation (4.3.10), and  $p$  is replaced by  $p - p_c$  in equation (4.3.11)

$$G_{\text{con}}^* = qg(\theta) - \gamma\eta_{\text{con}}(2\alpha p_{\text{cap}} \ln(\alpha p_{\text{cap}} + p - p_c) - p + p_c). \quad (4.3.12)$$

Note that in equation (4.3.12), the parameter  $\gamma$  retains its original meaning: it is the degree of non-associativity at the apex, now located at  $p = p_c$ .

Since  $G_{\text{con}}^*$  is a potential for the plastic strain rate, it is arbitrary up to a constant. Thus, instead of equation (4.3.12) the following expression is recommended:

$$G_{\text{con}}^* = qg(\theta) - \gamma\eta_{\text{con}}(2\alpha p_{\text{cap}} \ln(\alpha p_{\text{cap}} + p - p_c) - p). \quad (4.3.13)$$

The plastic strain rate is redefined as Kim and Lade (1988)

$$\dot{\epsilon}^p = \dot{\lambda} \frac{\partial G(\bar{\sigma})}{\partial \bar{\sigma}} \quad (4.3.14)$$

that is equivalent to

$$\dot{\epsilon}^p = \dot{\lambda} \frac{\partial G(\sigma)}{\partial \sigma} : \frac{\partial \sigma}{\partial \bar{\sigma}} = \dot{\lambda} \frac{\partial G(\sigma)}{\partial \sigma} \quad (4.3.15)$$

because  $\partial \sigma / \partial \bar{\sigma}$  is equal to the fourth-order identity tensor.

### Internal variables

Finally, the evolution of the internal variables is changed into

$$\begin{aligned} \dot{\kappa}_{\text{con}} &= \frac{1}{c_{\text{con}} p_a} \left( \frac{\bar{p}}{p_a} \right)^{-l} \dot{w}^p = \frac{1}{c_{\text{con}} p_a} \left( \frac{p - p_c}{p_a} \right)^{-l} \dot{w}^p \\ \dot{\kappa}_{\text{cap}} &= \frac{1}{c_{\text{cap}} p_a} \left( \frac{p_{\text{cap},0}}{p_a} \right)^{-r} \dot{w}^p \end{aligned} \quad (4.3.16)$$

with  $\dot{w}^p$  equal to (Lade and Kim 1988a)

$$\dot{w}^p = \bar{\sigma} : \dot{\epsilon}^p = \sigma : \dot{\epsilon}^p + p_c \text{tr}(\dot{\epsilon}^p), \quad (4.3.17)$$

where  $\text{tr}(\ast)$  indicates the trace of  $\ast$ .

### 4.3.4 Recovering the meaning of cap parameters

In the formulation for cohesive materials just presented, parameters  $p_{\text{cap}}$  and  $\alpha$  have lost the meaning they originally had for cohesionless materials, see figure 4.24. The isotropic yield stress under compression is not  $p_{\text{cap}}$ , but  $p_{\text{cap}} + p_c$ ; the cone–cap intersection is not at  $p = \alpha p_{\text{cap}}$ , but at  $p = \alpha p_{\text{cap}} + p_c$ .

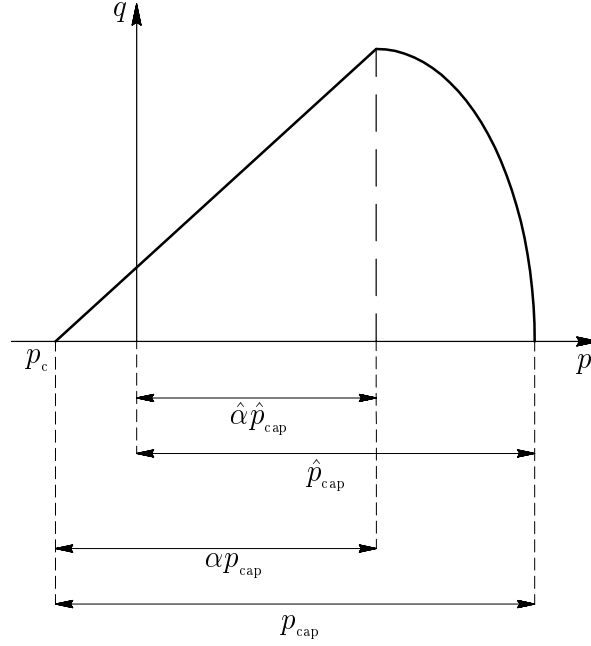


Figure 4.24: MRS–Lade model for cohesive materials. Relationships between  $\hat{p}_{\text{cap}}$ ,  $\hat{\alpha}$ ,  $p_{\text{cap}}$  and  $\alpha$ .

This change in meaning does not affect the validity of the model. However, the physical interpretation of  $p_{\text{cap}}$  and  $\alpha$  is not straightforward. In what follows, the cohesive MRS–Lade model is expressed in terms of two new parameters,  $\hat{p}_{\text{cap}}$  and  $\hat{\alpha}$ .  $\hat{p}_{\text{cap}}$  is the isotropic yield stress under compression of a cohesive material, and  $\hat{\alpha}\hat{p}_{\text{cap}}$  is the compression level at cone–cap intersection.

From the previous discussion and figure 4.24, it follows directly that the relationships between  $\hat{p}_{\text{cap}}$ ,  $\hat{\alpha}$ ,  $p_{\text{cap}}$  and  $\alpha$  is simply

$$\begin{aligned}\hat{p}_{\text{cap}} &= p_{\text{cap}} + p_c \\ \hat{\alpha}\hat{p}_{\text{cap}} &= \alpha p_{\text{cap}} + p_c\end{aligned}\quad (4.3.18)$$

In the following, equations (4.3.18) are used to express the cap yield function/flow potential, see equation (4.3.10), and the cone flow potential, see equation (4.3.13), as functions of  $\hat{p}_{\text{cap}}$  and  $\hat{\alpha}$ . The other constitutive equations (the cone yield function and the internal variable evolution laws, equations (4.3.9) and (4.3.16)) are not affected by the change of notation.

### 4.3.5 Yield function

By using equations (4.3.18), the cap yield function of equation (4.3.10) is transformed into

$$F_{\text{cap}} = \left( \frac{p - \hat{\alpha}\hat{p}_{\text{cap}}}{(1 - \hat{\alpha})\hat{p}_{\text{cap}}} \right)^2 + \left( \frac{qg(\theta)}{\eta_{\text{con}}(\hat{\alpha}\hat{p}_{\text{cap}} - p_c)} \right)^2 - 1. \quad (4.3.19)$$

Note that, in this new format, the cap yield function for cohesive materials is very similar to the cohesionless case, see equation (4.3.2) (of course, the hats of  $\hat{p}_{\text{cap}}$  and  $\hat{\alpha}$  can be dropped after completing the redefinition of parameters, to simplify the notation). However, there is an important difference: the value of  $q$  at cone–cap intersection increases in a length  $|\eta_{\text{con}}p_c|$  due to cohesion. This term, which is missing in Jeremić and Sture (1994) and Macari et al. (1997), ensures a closed yield surface, with no gaps.

### Flow potential

The cone flow potential also depends on  $p_{\text{cap}}$  and  $\alpha$ , see equation (4.3.13). Therefore, it must be also transformed to a function of  $\hat{p}_{\text{cap}}$  and  $\hat{\alpha}$ . After substituting equations (4.3.18) into (4.3.13),

the following expression is obtained

$$G_{\text{con}}^* = qg(\theta) - \gamma\eta_{\text{con}}(2(\hat{\alpha}\hat{p}_{\text{cap}} - p_c) \ln(\hat{\alpha}\hat{p}_{\text{cap}} + p - 2p_c) - p). \quad (4.3.20)$$

### 4.3.6 Concluding remarks

A formulation of the MRS–Lade model for cohesive materials has been presented. By means of a translation of the stress space, it is shown that both the cone and the cap yield surfaces must be modified to account for cohesion. If only the cone surface is modified, as suggested in the literature, a gap appears at the cone–cap intersection. Moreover, the proposed formulation is free from the so-called corner problem and its associated numerical difficulties.

## 4.4 Consistent tangent matrices for density–dependent finite plasticity models

In this section, the consistent tangent matrix for density–dependent plastic models within the theory of isotropic multiplicative hyperelastoplasticity is presented. Plastic equations expressed as general functions of the Kirchhoff stresses and density are considered. They include the Cauchy–based plastic models as a particular case. The standard exponential return–mapping algorithm is applied, with the density playing the role of a fixed parameter during the nonlinear plastic corrector problem. The consistent tangent matrix has the same structure as in the usual density–independent plastic models. A simple additional term takes into account the influence of the density on the plastic corrector problem. Quadratic convergence results are shown for several representative examples involving geomaterial and powder constitutive models.

### 4.4.1 Introduction

Consistent tangent matrices (Simo and Taylor 1985, Runesson et al. 1986) are an essential ingredient for the efficient solution via implicit methods of complex problems in nonlinear computational mechanics. Consistent tangent matrices are needed to solve the elastoplastic boundary value problem with quadratic convergence, via a full Newton–Raphson linearization. They are computed from the consistent tangent moduli at Gauss–point level.

The expression of the consistent tangent moduli for a wide variety of material models can be found in the literature. Consistent tangent moduli for different small–strain elastoplastic models and time–integration rules can be found in Simo and Taylor (1985), Runesson et al. (1986), Simo et al. (1988), Crisfield (1997) and Pérez-Foguet, Rodríguez-Ferran and Huerta (2000*c*) among many others.

In the context of finite–strain modelling of isotropic materials, both multiplicative hyperelastoplasticity theory with logarithmic strain measures and time–integration based on the exponential mapping are a standard approach (Simo 1992, Cuitiño and Ortiz 1992, Perić, Owen and Honnor 1992, Simo 1998). From a computational point of view, its attractiveness stems from the fact that it leads to the same return–mapping algorithm of the infinitesimal theory, and, therefore, the same linearization of the plastic corrector nonlinear equations. This approach was developed initially for plastic incompressible materials in terms of the Kirchhoff stresses (Simo 1992, 1998). Extensions to include thermal coupling (Simo and Miehe 1992), damage effects (de Souza Neto et al. 1994, Li 1995), and specific geomaterial plastic models (Simo and Meschke 1993, Meschke et al. 1996, Borja and Tamagnini 1998, Callari et al. 1998) have been presented. Applications to consolidation problems have also been developed (Borja and Alarcón 1995, 1998, Armero 1999). In all these cases, the consistent linearization of the numerical time–integration algorithm is included.

A key issue in the application of the multiplicative hyperelastoplasticity theory to geomaterials is the choice of the stress measure for the constitutive equations. This affects directly how to model the influence of the density, or, equivalently, the volumetric deformation, on the plastic behaviour. Recently, Menschke and Liu (1999) have presented a re-formulation of the return–mapping algorithm in terms of the Cauchy stresses. They present a discussion on the role of the stress measure that needs to be chosen as the argument of the plastic model and comparative examples. The corresponding consistent tangent moduli are also included.

A more general way to model the influence of the volumetric deformation on the plastic behaviour is to consider density-dependent plastic equations, this is, yield function and flow rules expressed in terms of the density and the Kirchhoff stresses. Here, it is shown that the standard exponential return-mapping algorithm applies to this type of models. Moreover, the consistent tangent moduli are presented. Note that the Cauchy-based models (Menschke and Liu 1999) are, implicitly, density-dependent plastic models due to the relationship between Cauchy and Kirchhoff stresses. Therefore, the approach presented here also applies to this type of models.

On the other hand, in powder compaction simulations, plasticity models expressed as a function of the stresses and the density are usual. In this context, some of these models are formulated within the multiplicative hyperelastoplasticity theory, with the Kirchhoff stresses as a reference measure, see for instance Oliver, Oller and Cante (1992, 1996), Brandt and Nilsson (1999) and Cante, Oliver and Hernández (1999). However, in all these cases the elastic deformation is assumed to be small with respect to the total deformation, and neglected. Specific return-mapping algorithms are devised, and, in some cases the corresponding consistent tangent moduli are presented (Oliver et al. 1992, 1996, Cante et al. 1999). The approach presented here, without simplifications of the general kinematic framework, has been applied successfully to powder compaction modelling in chapter 5 (Pérez-Foguet et al. 2000a). There, it is shown that considering the influence of large elastic deformations in this type of problems does not represent any drawback from a modelling point of view.

An outline of this section follows. The problem is stated in subsection 4.4.2. The constitutive model and the standard numerical time-integration algorithm are briefly reviewed. The consistent linearization of the algorithm is presented in subsection 4.4.3. First, the expression for density-independent models is shown. After that, the extension to the density-dependent case is devised. In subsection 4.4.4, representative examples are discussed in detail and the convergence results are highlighted. Three elastoplastic models with different degree of computational difficulty are used: a Drucker-Prager model (Menschke and Liu 1999), an elliptic model (Oliver et al. 1992, 1996, Jinka, Bellet and Fourment 1997, Ragab and Saleh 1999) and a cone-cap model (Aydin, Briscoe and Sanliturk 1996, Lewis and Khoei 1998, Brandt and Nilsson 1998, Khoei and Lewis 1999, Brandt and Nilsson 1999, Cante et al. 1999). The Arbitrary Lagrangian-Eulerian formulation for multiplicative elastoplasticity presented in section 2.2 (Rodríguez-Ferran et al. 2000) is used in some of the examples to avoid mesh distortion. The main conclusions are summarized in subsection 4.4.5.

#### 4.4.2 Problem statement

This subsection presents a brief description of the problem. First, the constitutive equations are summarized. After that, the key issues of the integration scheme are described. See Simo (1992, 1998), Menschke and Liu (1999) and references therein for further details on the general framework.

Here, the dependence of the plastic model on the density is included in the yield function and the flow rule in a general way. Moreover, it is shown that there is no influence of the density on the standard exponential return-mapping algorithm.

##### Constitutive model

Let  $\Omega \subset \mathbb{R}^{n_{\text{dim}}}$  ( $n_{\text{dim}} = 2, 3$ ) be the material configuration of a continuum body with particles labelled by  $\mathbf{X} \in \Omega$ . The motion of  $\Omega$  is described by the one-parameter family of mappings  $\varphi_t : \Omega \mapsto \mathbb{R}^{n_{\text{dim}}}$  with  $t \in [0, T]$  the time-like parameter. Let  $\Omega_t = \varphi_t(\Omega)$  be the placement of the body at time  $t$  and  $\mathbf{x} = \varphi_t(\mathbf{X}) = \varphi(\mathbf{X}, t) \in \Omega_t$  the position of the material particle  $\mathbf{X}$ . In that context, the deformation gradient,

$$\mathbf{F}(\mathbf{X}, t) = \frac{\partial \varphi}{\partial \mathbf{X}}(\mathbf{X}, t), \quad (4.4.1)$$

is assumed to be locally decomposed into elastic and plastic parts as

$$\mathbf{F} = \mathbf{F}^e \mathbf{F}^p. \quad (4.4.2)$$

Uncoupled isotropic hyperelastic behaviour is assumed. Therefore, the local thermodynamic state is defined by means of the elastic left Cauchy–Green tensor

$$\mathbf{b}^e = \mathbf{F}^e \mathbf{F}^{eT} \quad (4.4.3)$$

and a set of strain–like scalar internal variables  $\mathbf{p} \in \mathbb{R}^{n_p}$  (the superscript  $T$  means transpose). The Kirchhoff stress tensor,  $\boldsymbol{\tau}$ , and the stress–like internal variables,  $\mathbf{q}$ , are given by

$$\boldsymbol{\tau} = 2 \frac{dW^e}{d\mathbf{b}^e} \mathbf{b}^e \quad \text{and} \quad \mathbf{q} = -\frac{dW^p}{d\mathbf{p}}, \quad (4.4.4)$$

where  $W^e$  and  $W^p$  are the elastic and plastic parts of the free–energy function per unit of undeformed volume (Bonet and Wood 1997). The Cauchy stress tensor is given by

$$\boldsymbol{\sigma} = \frac{\boldsymbol{\tau}}{\det(\mathbf{F})}. \quad (4.4.5)$$

The mass conservation equation reads, in material formulation,

$$\rho(\mathbf{X}, t) = \frac{\rho_0(\mathbf{X})}{\det(\mathbf{F})}, \quad (4.4.6)$$

where  $\rho(\mathbf{X}, t)$  and  $\rho_0(\mathbf{X})$  are the densities of the particle  $\mathbf{X}$  at times  $t$  and  $t = 0$  respectively. In powder compaction modelling, equation (4.4.6) is rewritten in dimensionless format, in terms of the relative density,  $\eta(\mathbf{X}, t)$  (Oliver et al. 1992, 1996, Brandt and Nilsson 1998, 1999). Both sides of equation (4.4.6) are divided by the solid density of the compacted material, which is taken as a reference value. This leads to the equivalent expression

$$\eta(\mathbf{X}, t) = \frac{\eta_0(\mathbf{X})}{\det(\mathbf{F})}. \quad (4.4.7)$$

The plastic response of the material is assumed isotropic and density–dependent. The dependence on the density is incorporated through  $\eta$ . A generic yield function

$$f(\boldsymbol{\tau}, \mathbf{q}, \eta) = 0 \quad (4.4.8)$$

and flow rules

$$\mathcal{L}_v \mathbf{b}^e = -2 \dot{\gamma} \mathbf{m}_\tau(\boldsymbol{\tau}, \mathbf{q}, \eta) \mathbf{b}^e \quad \text{and} \quad \dot{\mathbf{p}} = \dot{\gamma} \mathbf{m}_q(\boldsymbol{\tau}, \mathbf{q}, \eta), \quad (4.4.9)$$

are considered, with  $\mathcal{L}_v$  the Lie derivative with respect to the spatial velocity,  $\mathbf{v}$ ,  $\mathbf{m}_\tau$  and  $\mathbf{m}_q$  the corresponding flow directions, and  $\dot{\gamma}$  the plastic multiplier. The plastic multiplier is determined with the classical Kuhn–Tucker conditions:

$$\dot{\gamma} \geq 0, \quad f(\boldsymbol{\tau}, \mathbf{q}, \eta) \leq 0 \quad \text{and} \quad \dot{\gamma} f(\boldsymbol{\tau}, \mathbf{q}, \eta) = 0. \quad (4.4.10)$$

*Remark 4.4.1.* The general constitutive model just presented includes as particular cases the plastic models expressed in terms of Cauchy stresses, Cauchy–based plastic models (Menschke and Liu 1999). This can be shown by considering a generic isotropic yield function expressed on terms of the Cauchy stress tensor,

$$f(\boldsymbol{\sigma}, \mathbf{q}) = 0, \quad (4.4.11)$$

and using equations (4.4.5) and (4.4.7), which relate Cauchy and Kirchhoff stresses through

$$\boldsymbol{\sigma} = \frac{\eta}{\eta_0} \boldsymbol{\tau}. \quad (4.4.12)$$

Then, a density–dependent yield function expressed in terms of the Kirchhoff stress tensor,  $\tilde{f}(\boldsymbol{\tau}, \mathbf{q}, \eta/\eta_0)$ , can be defined simply by substituting equation (4.4.12) into (4.4.11):

$$f(\boldsymbol{\sigma}, \mathbf{q}) = \tilde{f}(\boldsymbol{\tau}, \mathbf{q}, \eta/\eta_0) = 0. \quad (4.4.13)$$

The function  $\tilde{f}$  is not unique. Thus, the most convenient expression from a computational point of view should be chosen. On the other hand,  $\tilde{f}$  depends on  $\eta$  only through  $\eta/\eta_0$ . So an arbitrary

scale can be chosen, for instance  $\eta_0 = 1$  for all particles  $\mathbf{X}$ . See the example presented in sections 4.4.4 and 4.4.6 for further details.

The other components of the Cauchy-based models, i.e. hyperelastic relationships and flow rules, are equal to those presented for density-dependent Kirchhoff-based models, see equation (4.4.9). This can be shown following the developments of Menschke and Liu (1999) with a yield function  $\tilde{f}$  given by equation (4.4.13). Therefore, the numerical time-integration algorithm and consistent tangent moduli presented in the following apply to both types of models.  $\square$

### Numerical time-integration

The evolution from time  ${}^n t$  to time  ${}^{n+1} t = {}^n t + \Delta t$  of the different magnitudes associated with a prescribed material particle  $\mathbf{X}$  is computed by means of the time-integration of the state variables  $\mathbf{b}^e$ ,  $\mathbf{p}$  and  $\eta$ .

Let us assume that  ${}^n \mathbf{x} = \mathbf{x}(\mathbf{X}, {}^n t)$ ,  ${}^n \mathbf{b}^e$ ,  ${}^n \mathbf{p}$  and  ${}^n \eta$  are known values referred to time  ${}^n t$  and that the incremental displacement

$${}^{n+1} \Delta \mathbf{u} = {}^{n+1} \mathbf{x} - {}^n \mathbf{x}, \quad (4.4.14)$$

with  ${}^{n+1} \mathbf{x} = \mathbf{x}(\mathbf{X}, {}^{n+1} t)$ , is given. Then, the new values  ${}^{n+1} \mathbf{b}^e$ ,  ${}^{n+1} \mathbf{p}$  and  ${}^{n+1} \eta$  for time  ${}^{n+1} t$  are computed using the corresponding values for time  ${}^n t$  and the incremental deformation gradient,

$${}^{n+1} \mathbf{f} = \frac{\partial {}^{n+1} \mathbf{x}}{\partial {}^n \mathbf{x}} = \mathbf{I}_{\text{n}_{\text{dim}}} + \frac{\partial {}^{n+1} \Delta \mathbf{u}}{\partial {}^n \mathbf{x}}, \quad (4.4.15)$$

which relates the deformation gradients at times  ${}^n t$  and  ${}^{n+1} t$ ,  ${}^n \mathbf{F}$  and  ${}^{n+1} \mathbf{F}$ , through the relationship  ${}^{n+1} \mathbf{F} = {}^{n+1} \mathbf{f} {}^n \mathbf{F}$ .  $\mathbf{I}_{\text{n}_{\text{dim}}}$  denotes a identity matrix of order  $\text{n}_{\text{dim}}$ .

The relative density,  $\eta$ , is integrated exactly (in the sense that no numerical time-integration scheme is used) because of the Lagrangian expression of the mass conservation principle, equation (4.4.7), which leads to

$${}^{n+1} \eta = \frac{\eta_0}{\det({}^{n+1} \mathbf{F})} = \frac{{}^n \eta}{\det({}^{n+1} \mathbf{f})}. \quad (4.4.16)$$

The values of  ${}^{n+1} \mathbf{b}^e$  and  ${}^{n+1} \mathbf{p}$  are obtained by means of the standard elastic predictor-plastic corrector split strategy applied to equations (4.4.8–4.4.10). Remarkably, the dependence of the constitutive equations on the density does not modify the algorithm. The value of  ${}^{n+1} \eta$  is given by equation (4.4.16), and therefore it plays the role of a fixed parameter.

The result of the elastic predictor step is the so-called trial state. It is defined by

$$\mathbf{b}_{tr}^e = {}^{n+1} \mathbf{f} {}^n \mathbf{b}^e {}^{n+1} \mathbf{f}^T \quad \text{and} \quad \mathbf{p}_{tr} = {}^n \mathbf{p}. \quad (4.4.17)$$

If the trial state is admissible,  $f(\boldsymbol{\tau}_{tr}, \mathbf{q}_{tr}, {}^{n+1} \eta) \leq 0$ , the state at time  ${}^{n+1} t$  is set equal to the trial state. If it is not, a plastic corrector step is computed.

The plastic correction step requires the approximation of the flow rules, equations (4.4.9). A standard approximation consists in the use of the exponential map and the backward Euler integration scheme (Simo 1992, Cuitiño and Ortiz 1992, Simo 1998). Under the previous isotropy assumptions, this approach leads to a nonlinear system of equations with the same structure as that of infinitesimal elastoplasticity.

In order to obtain the nonlinear system of equations, three vectors of  $\mathbb{R}^{\text{n}_{\text{dim}}}$  are defined:  $\boldsymbol{\varepsilon}_{tr}^e$ ,  ${}^{n+1} \boldsymbol{\varepsilon}^e$  and  ${}^{n+1} \bar{\boldsymbol{\tau}}$ . The components of  $\boldsymbol{\varepsilon}_{tr}^e$  and  ${}^{n+1} \boldsymbol{\varepsilon}^e$  are related with the eigenvalues of the tensors  $\mathbf{b}_{tr}^e$  and  ${}^{n+1} \mathbf{b}^e$ , respectively, and the components of  ${}^{n+1} \bar{\boldsymbol{\tau}}$  are the eigenvalues of  ${}^{n+1} \boldsymbol{\tau}$ :

$$\begin{aligned} \mathbf{b}_{tr}^e &= \sum_{i=1}^{\text{n}_{\text{dim}}} (\exp([\boldsymbol{\varepsilon}_{tr}^e]_i))^2 \mathbf{n}_{tr}^i \otimes \mathbf{n}_{tr}^i \\ {}^{n+1} \mathbf{b}^e &= \sum_{i=1}^{\text{n}_{\text{dim}}} (\exp([{}^{n+1} \boldsymbol{\varepsilon}^e]_i))^2 \mathbf{n}_{tr}^i \otimes \mathbf{n}_{tr}^i \\ {}^{n+1} \boldsymbol{\tau} &= \sum_{i=1}^{\text{n}_{\text{dim}}} [{}^{n+1} \bar{\boldsymbol{\tau}}]_i \mathbf{n}_{tr}^i \otimes \mathbf{n}_{tr}^i, \end{aligned} \quad (4.4.18)$$

with  $\{\mathbf{n}_{tr}^i\}_{i=1,\dots,n_{\text{dim}}}$  the eigenvectors of the three tensors, and  $\{[*]_i\}_{i=1,\dots,n_{\text{dim}}}$  the components of the three vectors. The eigenvectors are the same for the three tensors because of the isotropy assumptions.

After some manipulations, the following expression of the nonlinear system of equations is found:

$$\begin{aligned} {}^{n+1}\boldsymbol{\varepsilon}^e + \Delta\gamma \mathbf{m}_{\bar{\boldsymbol{\tau}}}({}^{n+1}\bar{\boldsymbol{\tau}}, {}^{n+1}\mathbf{q}, {}^{n+1}\eta) &= \boldsymbol{\varepsilon}_{tr}^e \\ - {}^{n+1}\mathbf{p} + \Delta\gamma \mathbf{m}_{\mathbf{q}}({}^{n+1}\bar{\boldsymbol{\tau}}, {}^{n+1}\mathbf{q}, {}^{n+1}\eta) &= -\mathbf{p}_{tr} \\ f({}^{n+1}\bar{\boldsymbol{\tau}}, {}^{n+1}\mathbf{q}, {}^{n+1}\eta) &= 0, \end{aligned} \quad (4.4.19)$$

where  $\Delta\gamma = \Delta t \dot{\gamma}$  is the incremental plastic multiplier,  $\mathbf{m}_{\bar{\boldsymbol{\tau}}}$  is the flow vector in the principal direction space (that is,  $\mathbf{m}_{\bar{\boldsymbol{\tau}}} = \sum_{i=1}^{n_{\text{dim}}} [\mathbf{m}_{\bar{\boldsymbol{\tau}}}]_i \mathbf{n}_{tr}^i \otimes \mathbf{n}_{tr}^i$ ) and the three isotropic functions  $\mathbf{m}_{\bar{\boldsymbol{\tau}}}$ ,  $\mathbf{m}_{\mathbf{q}}$  and  $f$  are expressed as functions of  $\bar{\boldsymbol{\tau}}$ . Equations (4.4.19) are complemented with the restriction  $\Delta\gamma \geq 0$ , equation (4.4.4)<sub>2</sub>, and

$$\bar{\boldsymbol{\tau}} = \frac{d\bar{W}^e}{d\boldsymbol{\varepsilon}^e}, \quad (4.4.20)$$

with  $\bar{W}^e(\boldsymbol{\varepsilon}^e)$  defined so that equation (4.4.20) is equivalent to the hyperelastic relationship (4.4.4)<sub>1</sub>. Once equations (4.4.19) are solved, the variables at time  ${}^{n+1}t$  are fully determined.

### 4.4.3 Consistent tangent moduli for density–dependent finite plasticity models

The linearization of the previous algorithm with respect to the gradient of the incremental displacement is needed to solve the discrete boundary value problem with quadratic convergence. In the following, the expression of the consistent tangent moduli for density–independent plastic models is briefly reviewed. After that, the general expression including the density influence is derived.

#### Expression for density–independent models

The linearized problem is completely specified once the following consistent tangent moduli is given (Simo 1992, 1998):

$${}^{n+1}\mathbf{c} = \sum_{i=1}^{n_{\text{dim}}} \sum_{j=1}^{n_{\text{dim}}} [{}^{n+1}\mathbf{a}]_{ij} \mathbf{n}_{tr}^i \otimes \mathbf{n}_{tr}^i \otimes \mathbf{n}_{tr}^j \otimes \mathbf{n}_{tr}^j + 2 \sum_{i=1}^{n_{\text{dim}}} [{}^{n+1}\bar{\boldsymbol{\tau}}]_i \hat{\mathbf{c}}_{tr}^i, \quad (4.4.21)$$

where  ${}^{n+1}\mathbf{a}$  is a matrix of order  $n_{\text{dim}}$  defined as

$${}^{n+1}\mathbf{a} = \frac{d{}^{n+1}\bar{\boldsymbol{\tau}}}{d\boldsymbol{\varepsilon}_{tr}^e}. \quad (4.4.22)$$

The tensors  $\{\hat{\mathbf{c}}_{tr}^i\}_{i=1,\dots,n_{\text{dim}}}$  can be expressed on the basis  $\{\mathbf{n}_{tr}^i\}_{i=1,\dots,n_{\text{dim}}}$  and depend on the values  $\boldsymbol{\varepsilon}_{tr}^e$ . Therefore they are fully determined from the elastic trial state (Simo 1992, 1998).

Equation (4.4.21) corresponds to the linearization of the Kirchhoff stresses at time  ${}^{n+1}t$ ,  ${}^{n+1}\boldsymbol{\tau}$ , with respect to the gradient of the incremental displacements. It can be found by applying the chain rule to equation (4.4.18)<sub>3</sub>. The first term in the right–hand–side of equation (4.4.21) corresponds to the linearization of the eigenvalues of  ${}^{n+1}\boldsymbol{\tau}$ ,  ${}^{n+1}\bar{\boldsymbol{\tau}}$ . The second term corresponds to the linearization of its eigenvectors,  $\{\mathbf{n}_{tr}^i\}_{i=1,\dots,n_{\text{dim}}}$ .

The matrix  ${}^{n+1}\mathbf{a}$  has an expression identical to the consistent tangent moduli of infinitesimal elastoplasticity (Simo 1992, 1998). For elastic steps,  $\Delta\gamma = 0$ , it is equal to the Hessian of  $\bar{W}^e$ ,

$${}^{n+1}\mathbf{a} = \left. \frac{d^2\bar{W}^e}{d\boldsymbol{\varepsilon}^{e2}} \right|_{t={}^{n+1}t}. \quad (4.4.23)$$

For plastic steps,  $\Delta\gamma > 0$ , it can be expressed as (Ortiz and Martin 1989)

$${}^{n+1}\mathbf{a} = \mathbf{P}^T \tilde{\mathbf{G}} \mathbf{P} - \frac{\mathbf{P}^T \tilde{\mathbf{G}} \mathbf{m} \nabla f^T \tilde{\mathbf{G}} \mathbf{P}}{\nabla f^T \tilde{\mathbf{G}} \mathbf{m}}, \quad (4.4.24)$$

with all quantities evaluated at time  ${}^{n+1}t$  and where the following notation has been introduced:

- $\mathbf{P}$  is a projection matrix of  $n_{\text{dim}} + n_p$  rows and  $n_{\text{dim}}$  columns,  $\mathbf{P}^T = (\mathbf{I}_{n_{\text{dim}}}, \mathbf{0}_{n_{\text{dim}}, n_p})$ , and  $\mathbf{0}_{n_{\text{dim}}, n_p}$  is a null matrix of  $n_{\text{dim}}$  rows and  $n_p$  columns (recall that  $\mathbf{p} \in \mathbb{R}^{n_p}$ ).
- $\tilde{\mathbf{G}}$  is a matrix of order  $n_{\text{dim}} + n_p$  equal to  $(\mathbf{G}^{-1} + \Delta\gamma\nabla\mathbf{m})^{-1}$ , with  $\mathbf{G}$  a symmetric matrix defined as

$$\mathbf{G} = \begin{pmatrix} \frac{d^2\bar{W}^e}{d\boldsymbol{\varepsilon}^e{}^2} & 0 \\ 0 & \frac{d^2W^p}{d\mathbf{p}^2} \end{pmatrix}. \quad (4.4.25)$$

- $\mathbf{m}$  is a  $n_{\text{dim}} + n_p$  vector defined as  $\mathbf{m}^T = (\mathbf{m}_{\bar{\boldsymbol{\tau}}}^T, \mathbf{m}_{\mathbf{q}}^T)$ .
- And  $\nabla$  refers to the derivatives with respect to  $\bar{\boldsymbol{\tau}}$  and  $\mathbf{q}$ ,

$$\nabla f = \begin{pmatrix} \frac{\partial f}{\partial \bar{\boldsymbol{\tau}}} \\ \frac{\partial f}{\partial \mathbf{q}} \end{pmatrix} \quad \text{and} \quad \nabla \mathbf{m} = \begin{pmatrix} \frac{\partial \mathbf{m}_{\bar{\boldsymbol{\tau}}}}{\partial \bar{\boldsymbol{\tau}}} & \frac{\partial \mathbf{m}_{\bar{\boldsymbol{\tau}}}}{\partial \mathbf{q}} \\ \frac{\partial \mathbf{m}_{\mathbf{q}}}{\partial \bar{\boldsymbol{\tau}}} & \frac{\partial \mathbf{m}_{\mathbf{q}}}{\partial \mathbf{q}} \end{pmatrix}. \quad (4.4.26)$$

### Extension to the density–dependent case

In the following, the consistent linearization of the numerical–time integration scheme applied to density–dependent plastic models is presented. Although the dependence on the density of the plastic equations does not modify the standard integration algorithm, it affects the consistent tangent moduli.

In plastic steps, the relative density,  ${}^{n+1}\eta$ , affects the plastic response and thus the value of  ${}^{n+1}\boldsymbol{\tau}$ . It depends on the gradient of the incremental displacement through the relation

$${}^{n+1}\eta = \frac{{}^n\eta}{\det\left(\mathbf{I}_{n_{\text{dim}}} + \frac{\partial {}^{n+1}\Delta\mathbf{u}}{\partial {}^n\mathbf{x}}\right)}, \quad (4.4.27)$$

obtained substituting equation (4.4.15) in (4.4.16). The relative density is fixed during the return–mapping algorithm because it is integrated exactly (i.e. there is no need of a plastic correction for  ${}^{n+1}\eta$ ). For this reason, the standard integration algorithm remains unchanged. However, the value of  ${}^{n+1}\boldsymbol{\tau}$  depends on the incremental displacement through  ${}^{n+1}\eta$ , see equation (4.4.27). This influence has to be taken into account in the expression of the consistent tangent moduli to solve the boundary value problem with quadratic convergence.

The general expression of  ${}^{n+1}\mathbf{c}$ , equation (4.4.21), is valid for density–dependent plastic models. The dependence on the density does not affect the application of the chain rule nor the eigenvectors of  $\mathbf{b}_{tr}^e$ ,  $\{\mathbf{n}_{tr}^i\}_{i=1, \dots, n_{\text{dim}}}$ , and, therefore, neither the expression of  $\{\hat{\mathbf{c}}_{tr}^i\}_{i=1, \dots, n_{\text{dim}}}$ . Consequently, the influence of the density is restricted to the value of  ${}^{n+1}\bar{\boldsymbol{\tau}}$  and the matrix  ${}^{n+1}\mathbf{a}$ . The value of  ${}^{n+1}\bar{\boldsymbol{\tau}}$  is obtained directly from the numerical time–integration scheme, equations (4.4.19) and (4.4.19). On the other hand,  ${}^{n+1}\mathbf{a}$  only depends on the trial state for elastic steps. In summary, only the new expression of  ${}^{n+1}\mathbf{a}$  for plastic steps must be obtained to extend equation (4.4.21) to density–dependent plastic models.

In the following, the consistent linearization of the plastic corrector step is presented. It is shown that the new, more general, expression of the moduli  ${}^{n+1}\mathbf{a}$  is composed of two terms, one equal to the expression for density–independent models, equation (4.4.24), and another one which adds the influence of the density. In order to do that it is useful to rephrase the dependence of  ${}^{n+1}\eta$  on  ${}^{n+1}\mathbf{f}$ , equation (4.4.16), as

$${}^{n+1}\eta = {}^n\hat{\eta} \exp(-\text{tr}(\boldsymbol{\varepsilon}_{tr}^e)), \quad (4.4.28)$$

with  ${}^n\hat{\eta} = {}^n\eta\sqrt{\det({}^n\mathbf{b}^e)}$  a known value from the previous time step and where  $\text{tr}(\ast)$  means trace of  $\ast$  (that is,  $\sum_{i=1}^{n_{\text{dim}}}[\ast]_i$ ). Equation (4.4.28) is found by applying the determinant function to both sides of equation (4.4.17)<sub>1</sub> and substituting equation (4.4.18)<sub>1</sub> into it.

From the definition of  ${}^{n+1}\mathbf{a}$ , equation (4.4.22), and the application of the chain rule a new more convenient expression of  ${}^{n+1}\mathbf{a}$  is found:

$${}^{n+1}\mathbf{a} = \frac{d{}^{n+1}\bar{\boldsymbol{\tau}}}{d{}^{n+1}\boldsymbol{\varepsilon}^e} \frac{d{}^{n+1}\boldsymbol{\varepsilon}^e}{d\boldsymbol{\varepsilon}_{tr}^e} = \left. \frac{d^2\bar{W}^e}{d\boldsymbol{\varepsilon}^e{}^2} \right|_{t={}^{n+1}t} \frac{d{}^{n+1}\boldsymbol{\varepsilon}^e}{d\boldsymbol{\varepsilon}_{tr}^e}. \quad (4.4.29)$$



Equation (4.4.29) shows that  ${}^{n+1}\mathbf{a}$  is determined once the total influence of  $\boldsymbol{\varepsilon}_{tr}^e$  on  ${}^{n+1}\boldsymbol{\varepsilon}^e$  is found. This influence is given by the nonlinear system of equations (4.4.19) and the relationship between  ${}^{n+1}\eta$  and  $\boldsymbol{\varepsilon}_{tr}^e$ , equation (4.4.28). Thus, it can be computed by linearizing the nonlinear system of equations

$$\begin{aligned} {}^{n+1}\boldsymbol{\varepsilon}^e + \Delta\gamma \mathbf{m}_{\bar{\tau}}({}^{n+1}\bar{\tau}, {}^{n+1}\mathbf{q}, {}^{n+1}\eta) &= \boldsymbol{\varepsilon}_{tr}^e \\ -{}^{n+1}\mathbf{p} + \Delta\gamma \mathbf{m}_{\mathbf{q}}({}^{n+1}\bar{\tau}, {}^{n+1}\mathbf{q}, {}^{n+1}\eta) &= -\mathbf{p}_{tr} \\ f({}^{n+1}\bar{\tau}, {}^{n+1}\mathbf{q}, {}^{n+1}\eta) &= 0 \\ {}^{n+1}\eta &= {}^n\hat{\eta} \exp(-\text{tr}(\boldsymbol{\varepsilon}_{tr}^e)) \end{aligned} \quad (4.4.30)$$

and the relationships (4.4.20) and (4.4.4)<sub>2</sub>, that link  ${}^{n+1}\bar{\tau}$  and  ${}^{n+1}\mathbf{q}$  with  ${}^{n+1}\boldsymbol{\varepsilon}^e$  and  ${}^{n+1}\mathbf{p}$ .

The linearization of equations (4.4.30) reads, in compact matrix form,

$$\begin{pmatrix} \mathbf{J} & \frac{\partial(\Delta\gamma\mathbf{m},f)}{\partial\eta} \\ \mathbf{0}_{1,n_{\text{dim}}+n_p+1} & 1 \end{pmatrix} \begin{pmatrix} \mathbf{d}^{n+1}\boldsymbol{\varepsilon}^e \\ -\mathbf{d}^{n+1}\mathbf{p} \\ d\Delta\gamma \\ d{}^{n+1}\eta \end{pmatrix} = \begin{pmatrix} \mathbf{I}_{n_{\text{dim}}} \\ \mathbf{0}_{n_p+1,n_{\text{dim}}} \\ -\eta\mathbf{1}_{1,n_{\text{dim}}} \end{pmatrix} d\boldsymbol{\varepsilon}_{tr}^e \quad (4.4.31)$$

with all quantities evaluated at time  ${}^{n+1}t$ , and where  $\mathbf{d}^{n+1}\boldsymbol{\varepsilon}^e$  is a vector of  $\mathbb{R}^{n_{\text{dim}}}$ ,  $\mathbf{d}^{n+1}\mathbf{p}$  is a vector of  $\mathbb{R}^{n_p}$ ,  $d\Delta\gamma$  and  $d{}^{n+1}\eta$  are scalars,  $\mathbf{0}_{n_*,m_*}$  and  $\mathbf{1}_{n_*,m_*}$  are matrices of  $n_*$  rows and  $m_*$  columns with coefficients 0 and 1, respectively,

$$\mathbf{J} = \begin{pmatrix} \mathbf{I}_{n_{\text{dim}}+n_p} + \Delta\gamma\nabla\mathbf{m}\mathbf{G} & \mathbf{m} \\ \nabla f^T\mathbf{G} & 0 \end{pmatrix} \quad \text{and} \quad \frac{\partial(\Delta\gamma\mathbf{m},f)}{\partial\eta} = \begin{pmatrix} \Delta\gamma \frac{\partial\mathbf{m}}{\partial\eta} \\ \frac{\partial f}{\partial\eta} \end{pmatrix}. \quad (4.4.32)$$

From equation (4.4.31) and the relationship

$$\mathbf{d}^{n+1}\boldsymbol{\varepsilon}^e = \frac{d{}^{n+1}\boldsymbol{\varepsilon}^e}{d\boldsymbol{\varepsilon}_{tr}^e} d\boldsymbol{\varepsilon}_{tr}^e \quad (4.4.33)$$

it results that

$$\frac{d{}^{n+1}\boldsymbol{\varepsilon}^e}{d\boldsymbol{\varepsilon}_{tr}^e} = \begin{pmatrix} \mathbf{P}^T & \mathbf{0}_{n_{\text{dim}},1} & \mathbf{0}_{n_{\text{dim}},1} \end{pmatrix} \begin{pmatrix} \mathbf{J} & \frac{\partial(\Delta\gamma\mathbf{m},f)}{\partial\eta} \\ \mathbf{0}_{1,n_{\text{dim}}+n_p+1} & 1 \end{pmatrix}^{-1} \begin{pmatrix} \mathbf{P} \\ \mathbf{0}_{1,n_{\text{dim}}} \\ -\eta\mathbf{1}_{1,n_{\text{dim}}} \end{pmatrix} \quad (4.4.34)$$

which is equivalent to

$$\frac{d{}^{n+1}\boldsymbol{\varepsilon}^e}{d\boldsymbol{\varepsilon}_{tr}^e} = \begin{pmatrix} \mathbf{P}^T & \mathbf{0}_{n_{\text{dim}},1} \end{pmatrix} \mathbf{J}^{-1} \begin{pmatrix} \mathbf{P} \\ \mathbf{0}_{n_{\text{dim}},1} \end{pmatrix} + \eta \begin{pmatrix} \mathbf{P}^T & \mathbf{0}_{n_{\text{dim}},1} \end{pmatrix} \mathbf{J}^{-1} \frac{\partial(\Delta\gamma\mathbf{m},f)}{\partial\eta} \mathbf{1}_{1,n_{\text{dim}}}. \quad (4.4.35)$$

The expression of  ${}^{n+1}\mathbf{a}$  is found substituting equation (4.4.35) into equation (4.4.29). It has two parts, one for each term on the right-hand-side of equation (4.4.35),

$${}^{n+1}\mathbf{a} = {}^{n+1}\mathbf{a}_{\eta\text{-indep}}^{\text{ep}} + {}^{n+1}\mathbf{a}_{\eta}^{\text{ep}}. \quad (4.4.36)$$

The first part,  ${}^{n+1}\mathbf{a}_{\eta\text{-indep}}^{\text{ep}}$ , is equal to the standard one for density-independent plastic models, equation (4.4.24). The second part,  ${}^{n+1}\mathbf{a}_{\eta}^{\text{ep}}$ , takes into account the influence of the density. After some manipulations it can be expressed as

$${}^{n+1}\mathbf{a}_{\eta}^{\text{ep}} = \eta \Delta\gamma \mathbf{P}^T \left( \tilde{\mathbf{G}} - \frac{\tilde{\mathbf{G}}\mathbf{m}\nabla f\tilde{\mathbf{G}}}{\nabla f^T\tilde{\mathbf{G}}\mathbf{m}} \right) \frac{\partial\mathbf{m}}{\partial\eta} \mathbf{1}_{1,n_{\text{dim}}} + \eta \frac{\partial f}{\partial\eta} \mathbf{P}^T \frac{\tilde{\mathbf{G}}\mathbf{m}}{\nabla f^T\tilde{\mathbf{G}}\mathbf{m}} \mathbf{1}_{1,n_{\text{dim}}}. \quad (4.4.37)$$

In the density-independent case, symmetric tangent moduli are obtained for material models with a flow rule such that  $\mathbf{m} = \nabla f$ , see equation (4.4.24). On the contrary, unsymmetric moduli are found with all density-dependent material models because  ${}^{n+1}\mathbf{a}_{\eta}^{\text{ep}}$  is unsymmetric except for very particular problems (see subsection 4.4.4). For this reason, in density-dependent plasticity,

unsymmetric linear solvers have to be used in order to keep the characteristic quadratic convergence of the Newton-Raphson method.

On the other hand, it is important to remark that the expression of  $n+1$   $\mathbf{a}$  for density-dependent plastic models can be computed with just a few more matrix-vector products than the standard one for density-independent plastic models (compare equations (4.4.37) and (4.4.24)), and, as expected, the additional information

$$\frac{\partial \mathbf{m}_{\bar{\tau}}}{\partial \eta} , \quad \frac{\partial \mathbf{m}_{\mathbf{q}}}{\partial \eta} \quad \text{and} \quad \frac{\partial f}{\partial \eta} . \quad (4.4.38)$$

#### 4.4.4 Examples

In this subsection, quadratic convergence is shown for some representative boundary value problems with density-dependent plastic models. The consistent tangent moduli presented in the previous subsection are used.

Examples with three elastoplastic models are presented: a Drucker-Prager model, an elliptic model and a cone-cap model. The three models have no internal variables,  $n_p = 0$ , a usual feature in the density-dependent models found in the literature. This fact simplifies some equations presented in the previous subsection. However, the structure and the dependence on the density of the consistent tangent moduli remain unchanged, see equations (4.4.24) and (4.4.37), and, therefore, the examples are fully representative.

The three plastic models are complemented with the Hencky's hyperelastic law, which leads to a linear relationship between  $\bar{\tau}$  and  $\varepsilon^e$  equal to that of linear elasticity between stresses and small strains. The use of other hyperelastic laws is straightforward. The main features of the three models are described in this subsection. A more detailed presentation is included in subsection 4.4.6. Two invariants of the stresses are used to show some results. They are also defined in subsection 4.4.6.

The examples with the Drucker-Prager model show that the proposed approach (numerical time-integration and consistent tangent moduli) is valid for Cauchy-based elastoplastic models. The examples with the elliptic and the cone-cap models show that the consistent tangent moduli also give quadratic convergence for general density-dependent constitutive laws. The yield function and the flow vector of the three models are expressed as functions of the Kirchhoff stresses and the relative density, as presented in subsection 4.4.2.

Elliptic models are widely used in porous material modelling, see Ragab and Saleh (1999) and references therein, and specifically in powder compaction simulations, see Oliver et al. (1992, 1996) and Jinka, Bellet and Fourment (1997). The formulation used in this work is based on that presented by Oliver et al. (1992, 1996). In these references, the elastic strains are assumed small and the kinematic description of the model is simplified. A specific return mapping algorithm and the corresponding consistent tangent moduli are presented. In this work, the general finite hyperelastoplasticity framework is used. The results of both approaches are compared in some introductory examples. After that, a more demanding example is solved using the Arbitrary Lagrangian-Eulerian formulation for multiplicative elastoplasticity presented in section 2.2. Quadratic convergence is obtained in all cases.

The cone-cap model is an extension of the elliptic model. It is defined by a density-dependent Drucker-Prager yield surface and a non-centered ellipse. The yield function and the flow rule are similar to other cone-cap models used recently in powder compaction simulations, see for instance Aydin et al. (1996), Lewis and Khoei (1998), Khoei and Lewis (1999), Brandt and Nilsson (1998, 1999), and Cante et al. (1999). However, the cone-cap model used here is defined, like the elliptic model, in the general finite hyperelastoplasticity framework presented in subsection 4.4.2, without kinematic simplifying assumptions. The results obtained in a particular example are compared with those of the elliptic model. Quadratic convergence results are also shown.

*Remark 4.4.2.* In the examples involving the elliptic and the cone-cap models, the derivatives of the yield function and the flow vector, equations (4.4.38), are computed with a first-order numerical approximation, as proposed in section 3.1 for flow vector derivatives in a small-strain context. Also in the present application, numerical differentiation does not disturb the quadratic convergence of

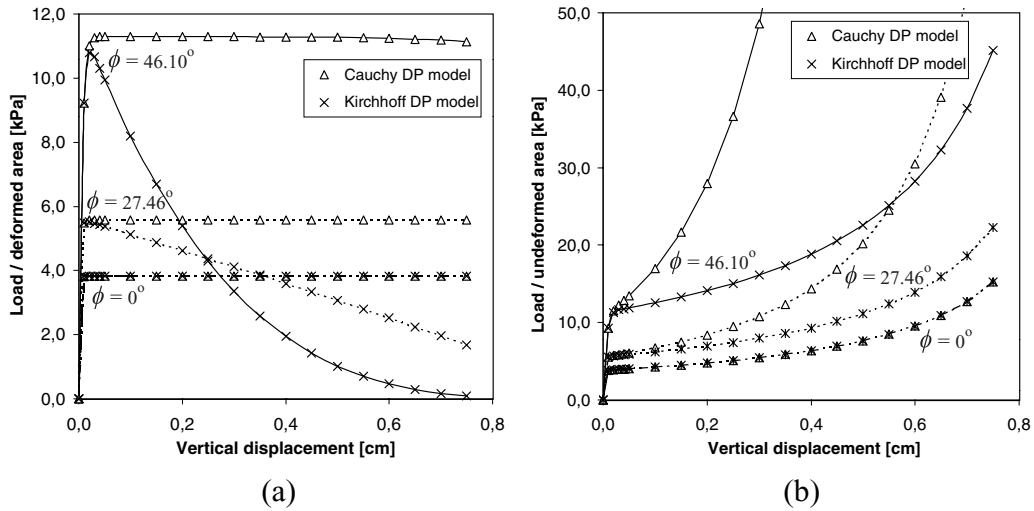


Figure 4.25: Load–displacement results of the uniaxial compression test. Cauchy–based and Kirchhoff–based Drucker–Prager models with different friction angles,  $\phi$ . (a) Load divided by deformed area and (b) load divided by undeformed area.

	Powder–A	Powder–B
$E$	2 000. [MPa]	50 000. [MPa]
$\nu$	0.37	0.37
$\sigma_y$	90. [MPa]	170. [MPa]
$\eta_0$	0.489	0.4
$n_1$	1.	0.3
$n_2$	2.7	5.4
$\phi_{\min}$	$45^\circ$	—
$\phi_{\max}$	$60^\circ$	—
$C_{\text{ref}}$	15. [MPa]	—
$n_c$	2.	—

Table 4.12: Sets of material parameters:  $(E, \nu, \sigma_y, \eta_0, n_1, n_2)$  for the elliptic model and  $(E, \nu, \sigma_y, \eta_0, n_1, n_2, \phi_{\min}, \phi_{\max}, C_{\text{ref}}, n_c)$  for the cone–cap model.

the Newton–Raphson method. Convergence is checked with the relative error in energy norm. A strict tolerance of  $10^{-10}$  has been used in all the examples in order to show clearly the quadratic convergence. Quite larger values may be chosen in practice.  $\square$

**Drucker–Prager model simulations** The following examples involve a Cauchy–based Drucker–Prager model (CDP). They illustrate that the proposed numerical time–integration approach, standard return–mapping algorithm, and the new consistent tangent moduli, equation (4.4.36), are valid for Cauchy–based elastoplastic models. A density–dependent Drucker–Prager model expressed in terms of the Kirchhoff stresses equivalent to the Cauchy–based Drucker–Prager model is used. The model is presented in subsection 4.4.6, equation (4.4.44).

Simulations with the standard density–independent Kirchhoff–based Drucker–Prager model (KDP), equation (4.4.42), are also included for comparative purposes. The flow vectors of both models, CDP and KDP, are equal to the partial derivative of the corresponding yield function with respect to the Kirchhoff stresses. Note that the two models are completely different from a modelling point of view (see Menschke and Liu 1999 for a discussion about the role of the stress measure in the plastic equations), so qualitatively different results are expected.

A square of 1 cm of length is subjected to a plane strain uniaxial compression test (Menschke and Liu 1999). The domain is modelled by a single bilinear element. A height reduction of 75% is imposed with five increments of 1% and 14 increments of 5%. The material parameters are a Young’s modulus,  $E$ , equal to 10 GPa, a Poisson’s ratio,  $\nu$ , equal to 0.3, and a cohesion of  $2.7 \sqrt{3/2}$

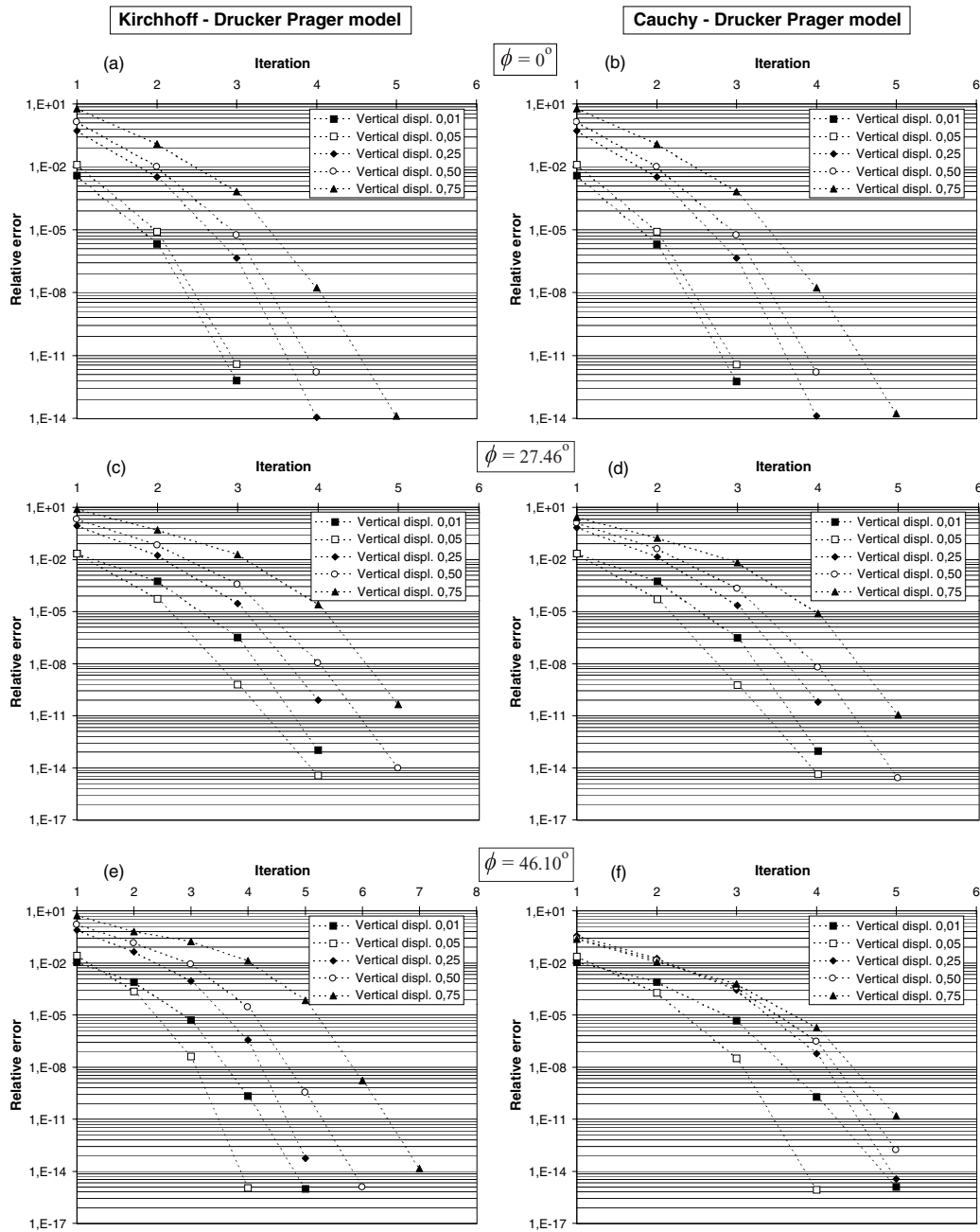


Figure 4.26: Uniaxial compression test. Left (a,c,e) Kirchhoff-based and right (b,d,f) Cauchy-based Drucker-Prager models with different friction angles,  $\phi$ . Convergence results for different vertical displacements.

GPa. The results for three values of the friction angle,  $\phi = 0^\circ$ ,  $27.46^\circ$ , and  $46.1^\circ$ , are computed (Menschke and Liu 1999).

The curves of load divided by deformed and undeformed area versus vertical displacement are depicted in figure 4.25. The KDP model with friction angles greater than  $0^\circ$  exhibits a post-peak softening in the load divided by deformed area—vertical displacement relationship. The softening increases with the friction angle. As Menschke and Liu (1999) indicate, this behaviour is related with the inelastic volume change produced by the flow rule. On the other hand, the results of both models, KDP and CDP, for  $\phi = 0^\circ$  differ only on the elastic volume change, which is not significant for the chosen material parameters.

The convergence results of both models for different vertical displacements and the three friction

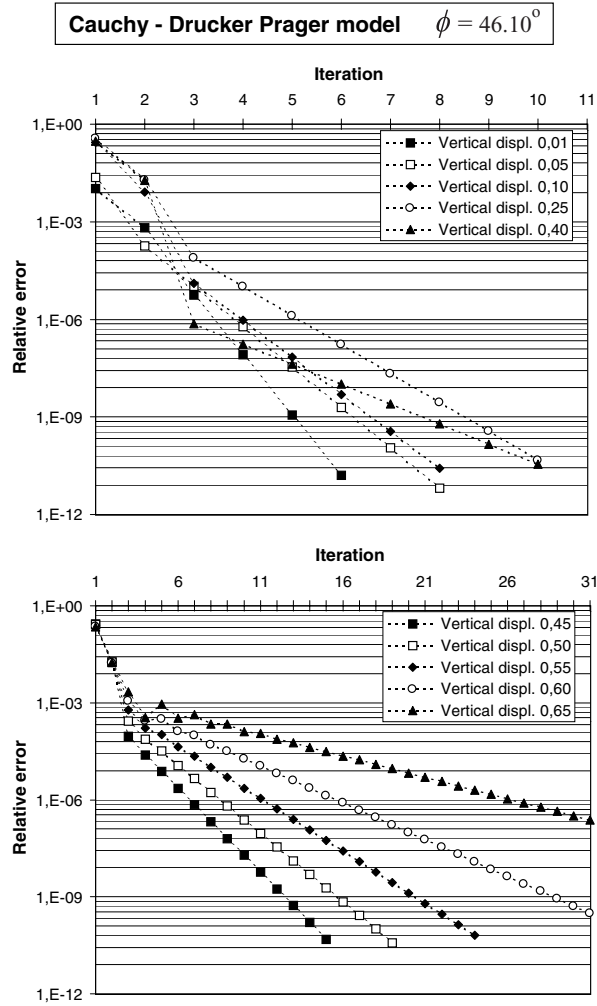


Figure 4.27: Convergence results for different vertical displacements obtained with the standard (density-independent) consistent tangent moduli,  ${}^{n+1}\mathbf{a} = {}^{n+1}\mathbf{a}_{\eta\text{-indep}}^{\text{ep}}$ .

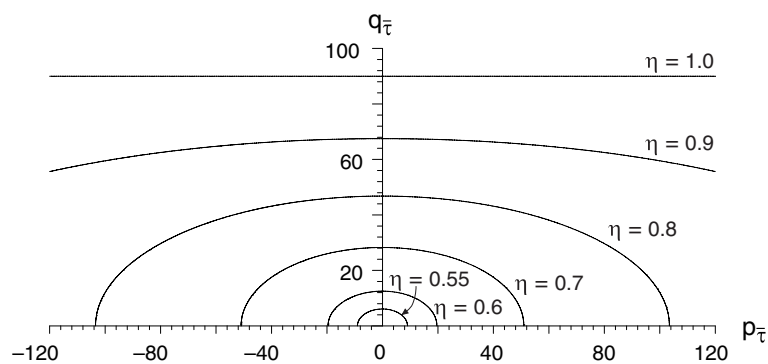


Figure 4.28: Traces of the elliptic yield function on the meridian plane  $q_{\bar{\tau}}-p_{\bar{\tau}}$  for different relative densities,  $\eta$ . Powder-A material parameters, see table 4.12.

angles are depicted in figure 4.26. All results are quadratic. The influence of neglecting the density contribution on the consistent tangent moduli is shown in figure 4.27. The convergence results for several load increments and the CDP model with a friction angle of  $46.1^\circ$  are depicted. Non-convergence is detected after a vertical displacement of 0.65 cm. In all convergent load increments, after the initial two or three iterations, the convergence becomes clearly linear. The influence of

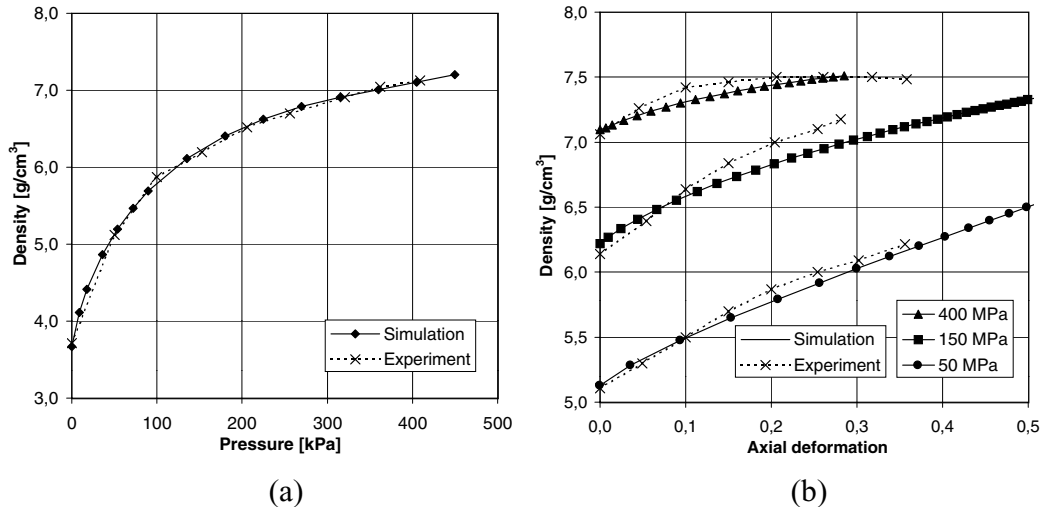


Figure 4.29: Results of (a) isostatic and (b) triaxial tests with powder-A material, see table 4.12. Experimental data from Doremus et al. (1994).

the density on the consistent tangent moduli is evident comparing figures 4.27 and 4.26(f).

**Elliptic model simulations** In the following, some examples of density-dependent multiplicative elastoplasticity with an elliptic yield function are analyzed. The yield function expression is presented in subsection 4.4.6. Its traces on the meridian plane  $q_{\bar{\tau}}-p_{\bar{\tau}}$  for different relative densities,  $\eta$ , and a particular set of material parameters are depicted in figure 4.28. The flow vector is equal to the partial derivatives of the yield function with respect to the Kirchhoff stresses.

Two sets of material parameters are used. Their values are summarized in table 4.12. Both are calibrated by Oliver et al. (1996) by comparing the results of numerical simulations with experiments.

The first set of compaction experiments (Dorémus, Geindreau, Martin, Lécot and Dao 1994) is modelled by Oliver et al. (1996) with powder-A parameters. A sample with an initial height of 24 mm and a diameter of 20 mm was used. Both isostatic compaction and triaxial tests were performed. The triaxial tests consisted of an initial isostatic compaction step up to a pressure of 50, 150 or 400 MPa, followed by an uniaxial compaction up to a vertical pressure of 1250 MPa (keeping the external radial pressure constant). The problem is axisymmetric. The sample is modelled by a 2D structured mesh of 100 bilinear elements. The friction effects are not considered (Oliver et al. 1996). The results of the numerical simulations and the experiments are compared in figure 4.29. The results of the simulations agree with the experimental ones and the results presented by Oliver et al. (1996), not shown in figure 4.29.

The convergence results for different load levels of the isostatic test are depicted in figure 4.30. Quadratic convergence is found for all load increments. However, if a consistent tangent matrix for density-independent problems is used divergence is found at the first load increment. This example is more demanding in the initial load levels than in the last ones. This fact is in agreement with the dependence of the density on the applied pressure, see figure 4.29(a). At the beginning of the test, a given increment of the pressure causes a larger variation of the density than at the end of the test.

The convergence results for the triaxial test with an initial isostatic pressure of 150 MPa are summarized in figure 4.31. Results for different load levels of the isostatic and the uniaxial compression parts of the test are depicted. The isostatic part is solved with 52 non-uniform increments (4 of 1%, 48 of 2%) and the uniaxial part with 20 equal increments. The results obtained using an unsymmetric solver for the linear systems of equations (recall that the full consistent tangent moduli  ${}^{n+1}\mathbf{a}$  is not symmetric) and a symmetric solver (with the symmetrized part of  ${}^{n+1}\mathbf{a}$ ) are shown. As expected, the results obtained with the unsymmetric consistent tangent moduli are quadratic, see figures 4.31(a,c). Remarkably, the convergence results obtained with the symmetric solver during the isostatic part of the test are also quadratic, see figure 4.31(b).

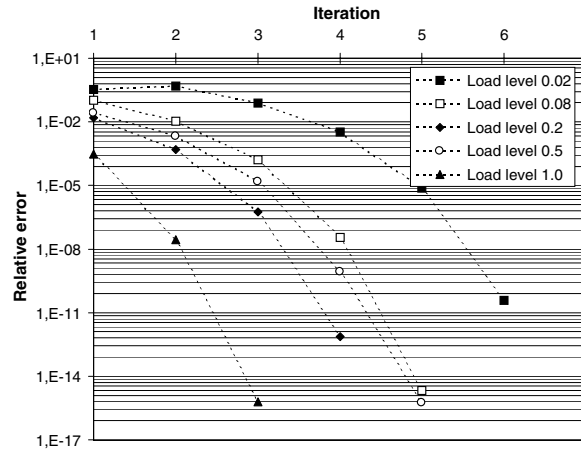


Figure 4.30: Powder–A isostatic test. Convergence results for different load levels.

This is due to the pure hydrostatic character of the test, which leads to a symmetric consistent tangent matrix, see equation (4.4.37). In the uniaxial compression part of the test the symmetric solver gives linear convergence, figure 4.31(d). The same influence on the convergence has been reported for other problems with unsymmetric consistent tangent matrices solved with a linear solver for symmetric matrices (Menschke and Liu 1999).

The second set of compaction experiments (Ernst and Barnekow 1994) is modelled by Oliver et al. (1996) with powder–B parameters of table 4.12. A sample with an initial height of 80 mm and a diameter of 14.3 mm was used. Both isostatic and uniaxial compaction tests were performed. The sample is modelled by a structured mesh of 100 bilinear elements, and no friction effects are considered. The results of the numerical simulations and the experiments are compared in figure 4.32. In general, the simulation results agree with the experimental ones. Nevertheless, for a fixed value of the pressure, the density predicted in this work is a little bit higher than the values shown by Oliver et al. (1996). These differences may be related with the large elastic strains, which in the present formulation are taken into account.

The convergence results for different load levels of the initial part of the isostatic test are depicted in figure 4.33. Small load increments are required at the beginning of the test to ensure convergence of the boundary value problem (4 increments of 0.025% and 3 increments of 0.3% of a total load of 250 MPa). After these initial steps, the load increments are quite larger (2 increments of 2% and 19 of 5%). Quadratic convergence is found for all steps.

The last example with the elliptic model is the frictionless compaction of a rotational flanged component. The component is modelled by an axisymmetric representation as illustrated in figure 2.32 (Lewis and Khoei 1998, Khoei and Lewis 1999). This example shows that quadratic convergence is also found in highly demanding boundary value problems. In the simulation presented in this section the friction effects are neglected. Therefore, the results are a qualitative approximation to the real compaction process, where the friction effects have to be taken into account (Lewis and Khoei 1998, Khoei and Lewis 1999). Complete compaction simulations with this material model and friction are presented in chapter 5.

A structured mesh of 170 eight–noded elements with reduced integration (four Gauss–points per element) is used. The radial displacement of segments  $\overline{BC}$ ,  $\overline{DE}$  and  $\overline{FA}$  and the vertical movement of segments  $\overline{AB}$  and  $\overline{CD}$  are set equal to zero (see figure 2.32). A vertical movement of  $-6.06$  mm is imposed to the segment  $\overline{EF}$  in 80 non-uniform increments. Small increments are needed at the beginning of the test (10 of 0.01%, 19 of 0.1%, 2 of 1%) in order to ensure convergence of the boundary value problem. Larger increments are used for the rest of the test (48 of 2%). This is directly related with the high curvature of the yield surface for  $\eta$  close to  $\eta_0$ , see figure 4.28.

The Arbitrary Lagrangian–Eulerian formulation for multiplicative elastoplasticity presented in section 2.2 is used to reduce the mesh distortion, see Lagrangian simulations of this test in section 2.2. The mesh region ABCG is Eulerian, and equal height elements are prescribed in the mesh region CDEFG. Material parameters are those of powder–A in table 4.12.

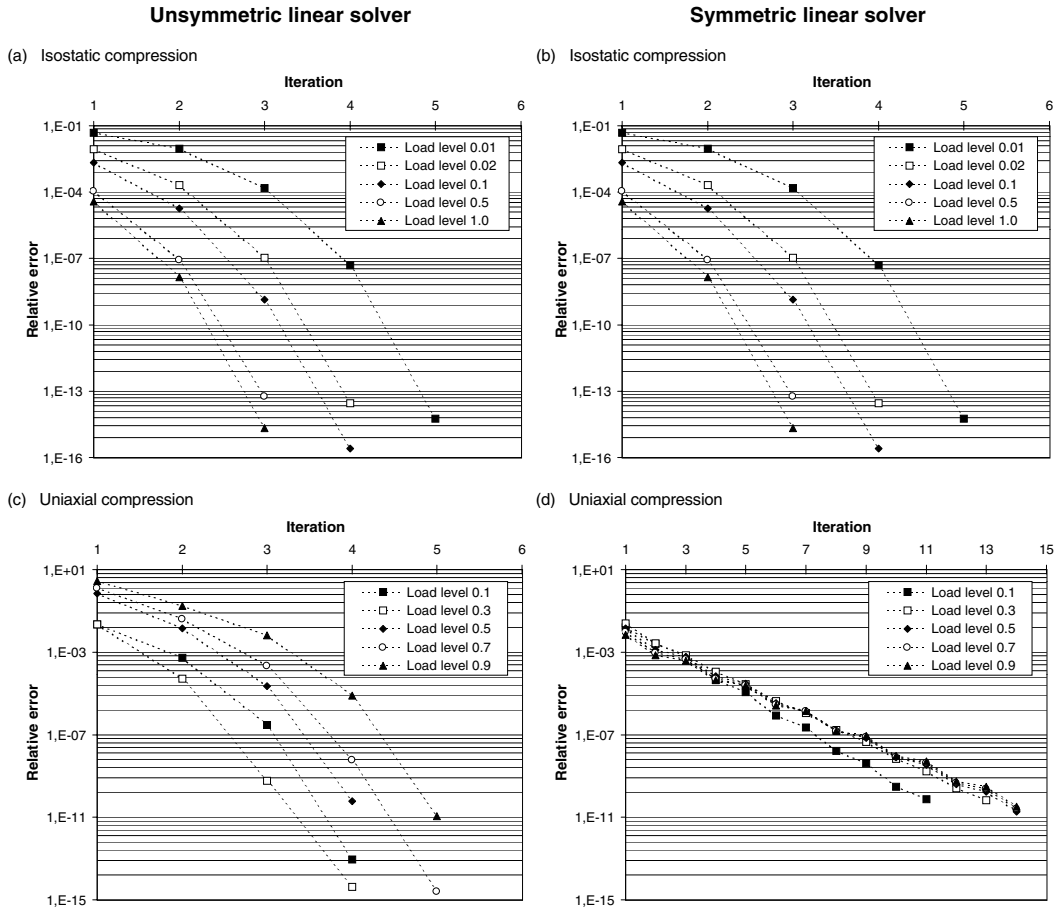


Figure 4.31: Powder-A triaxial test (150 MPa initial isostatic compaction). Convergence results for different load levels and with (a,c) unsymmetric and (b,d) symmetric linear solvers, left and right respectively.

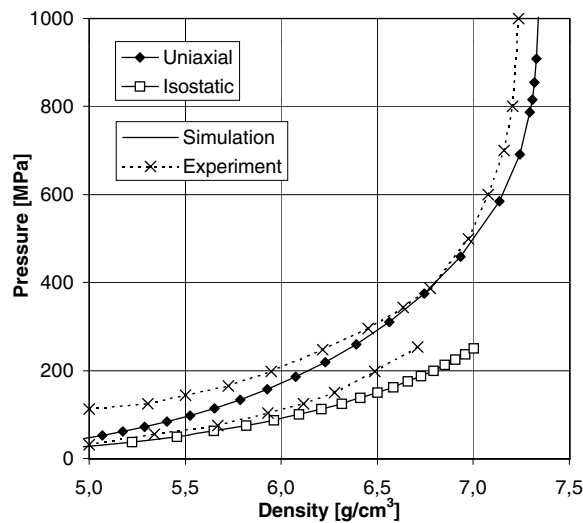


Figure 4.32: Results of isostatic and uniaxial tests with powder-B material, see table 4.12. Experimental data from Ernst and Barnekov (1994).



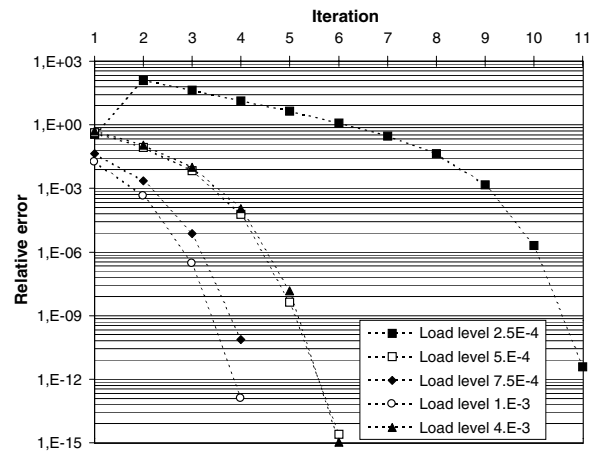


Figure 4.33: Powder-B isostatic test. Convergence results for different load levels.

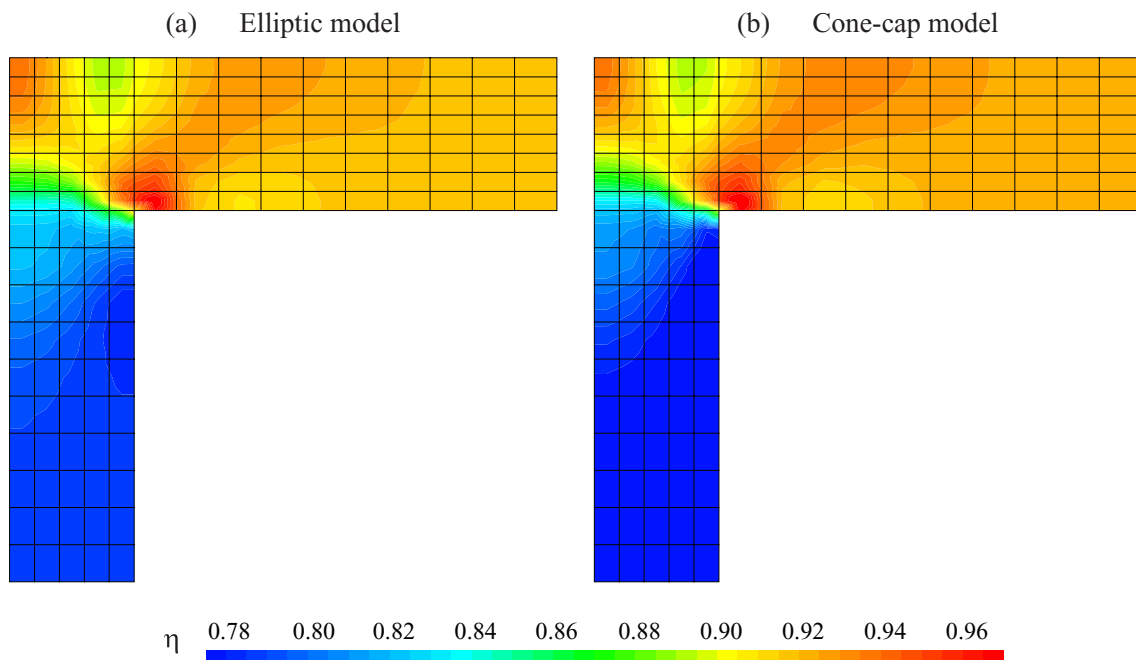


Figure 4.34: Frictionless compaction of the flanged component with (a) the elliptic model (b) the cone-cap model. Final relative density,  $\eta$ , distribution after a top displacement of 6.06 mm.

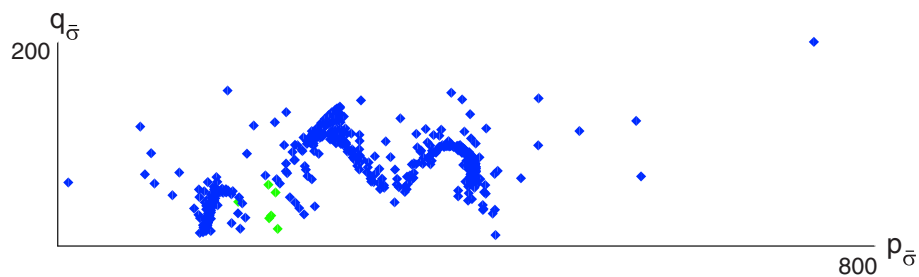


Figure 4.35: Frictionless compaction of the flanged component with the elliptic model. Final distribution of Cauchy stresses at Gauss-point level on the meridian plane  $q_{\bar{\sigma}}-p_{\bar{\sigma}}$ . Blue marks indicate plastic steps and green marks indicate elastic steps.

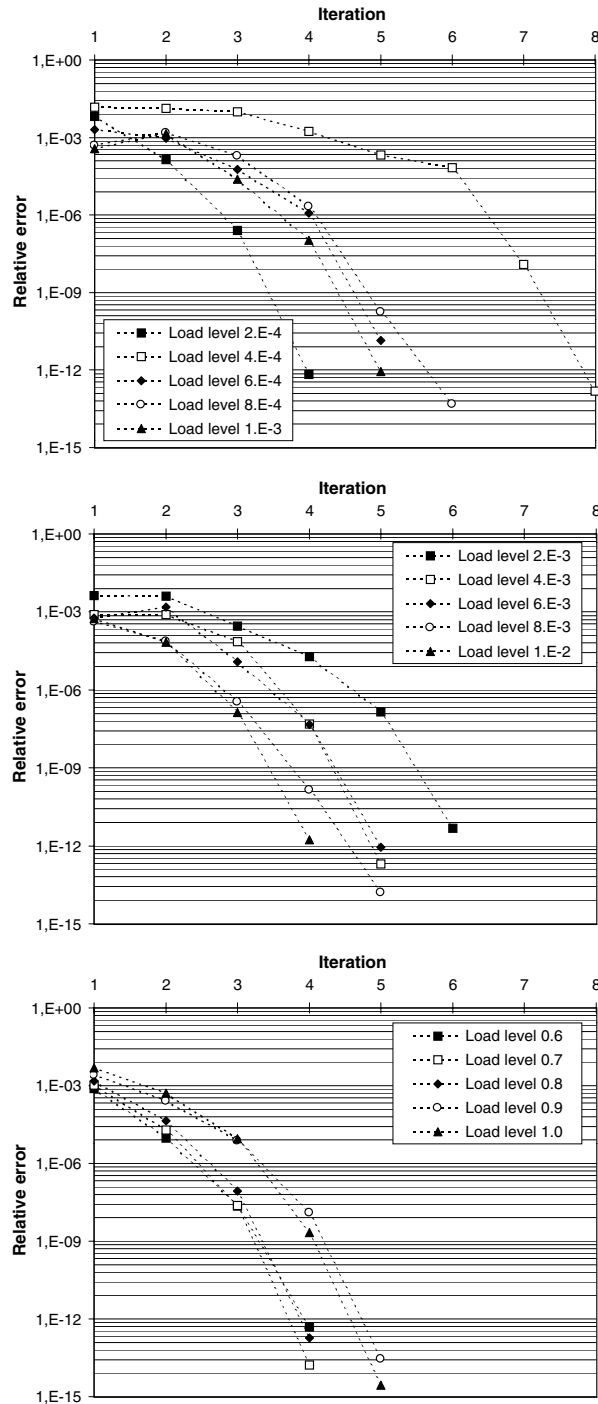


Figure 4.36: Frictionless compaction of the flanged component with the elliptic model. Convergence results for different load levels.

The final distribution of the relative density is shown in figure 4.34(a). The results are qualitatively similar to those presented by Lewis and Khoei (1998), although the lack of friction produces a relatively high compacted region near point F which is not reported in similar test simulations. The convergence results for different load levels are depicted in figure 4.36. Quadratic convergence is found in all cases.

The final distribution of Cauchy stresses at Gauss-point level on the meridian plane  $q_{\bar{\sigma}}-p_{\bar{\sigma}}$  is depicted in figure 4.35. This figure will be useful for comparing the results obtained with this model with those of the cone-cap simulation. During the major part of the load process all Gauss

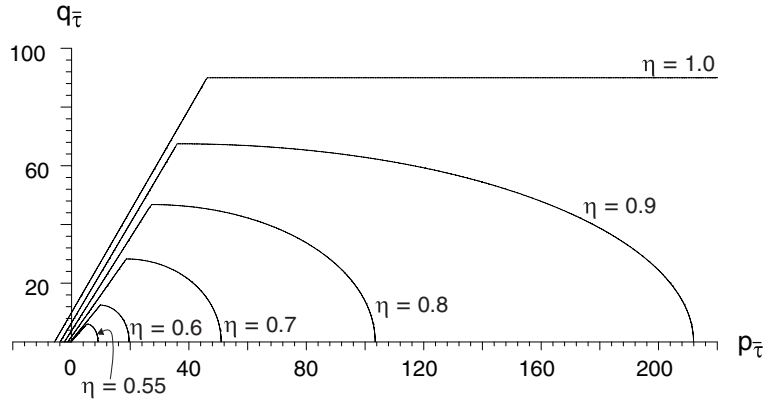


Figure 4.37: Traces of the cone–cap yield function on the meridian plane  $q_{\bar{\tau}}-p_{\bar{\tau}}$  for different relative densities,  $\eta$ . Powder–A material parameters, see table 4.12.

points are in plastic load, blue marks; however at the end of the test a small number of Gauss points, 6, are under elastic load, green marks. On the other hand, the Gauss points subjected to higher and lower Cauchy mean pressure are located respectively above and below point C.

**Cone–cap model simulations** In the following, the frictionless compaction of a flanged component (figure 2.32) is modelled with a cone–cap model. The traces of the yield function on the meridian plane  $q_{\bar{\tau}}-p_{\bar{\tau}}$  for different relative densities are depicted in figure 4.37. Powder–A material parameters for this model are summarized in table 4.12. The dependence on density of the cap yield function is similar to that of the elliptic model, compare figures 4.37 and 4.28. The cone is defined by a cohesion which increases up to  $C_{\text{ref}}$  for  $\eta = 1$ , and a friction angle which varies parabolically from  $\phi_{\text{min}}$  at  $\eta = \eta_0$  to  $\phi_{\text{max}}$  at  $\eta = 1$ . The friction angle range and dependence on the density has been set following results reported by Shinohara, Oida and Golman (2000) and with the aim of illustrating the convergence properties of the presented consistent tangent moduli. Lower constant (i.e. density–independent) values are used by Lewis and Khoei (1998), and higher constant values are reported by Dorémus and Toussaint (2000).

The flow vector is defined so there are no grey regions on the stress space (Pérez-Foguet and Huerta 1999) and therefore no corner return–mapping algorithms (Simo et al. 1988, Pramono and Willam 1989b, Hofstetter et al. 1993, Cante et al. 1999) are needed. Complete expressions of plastic equations are presented in subsection 4.4.6.

Note that the cone–cap model represents a more demanding test for the consistent tangent moduli than the elliptic model because the dependence on the density of the yield function and the flow rule is more complicate.

The numerical parameters of the simulation are the same that for the elliptic model, except for the number of load increments that has been increased to 103 (smaller initial load increments have been needed to obtain convergence of the boundary value problem). The distribution of Cauchy stresses at Gauss–point level on the meridian plane  $q_{\bar{\sigma}}-p_{\bar{\sigma}}$  for different load levels is depicted in figure 4.38. Red and blue marks correspond to points under plastic regime on the cone and cap regions respectively. Green marks denote elastic regime. The influence of the cone yield surface on the stress distribution is significant in the first steps of the test, but it reduces drastically to 1–3 Gauss points for the rest of test. The Gauss points with plastic loading in the cone region are those of the elements located on the left side of point C. The distribution of Cauchy stresses at the end of the test (figure 4.38, load level 1.0) is quite similar to that obtained with the elliptic model, figure 4.35. The distribution of the relative density at the end of the test is shown in figure 4.34(b). The results are also similar to those obtained with the elliptic model, figure 4.34(a). The influence of the cone is restricted to a slight reduction of the relative density in the ABCG region.

No direct comparison of powder compaction simulations with elliptic and cone–cap models has been found in the literature. The cone yield surface incorporates in the constitutive model the particle sliding that occurs at low pressures (Lewis and Khoei 1998). According to Cante et al. (1999), this effect could be relevant at the transfer stage (the beginning of the industrial process,

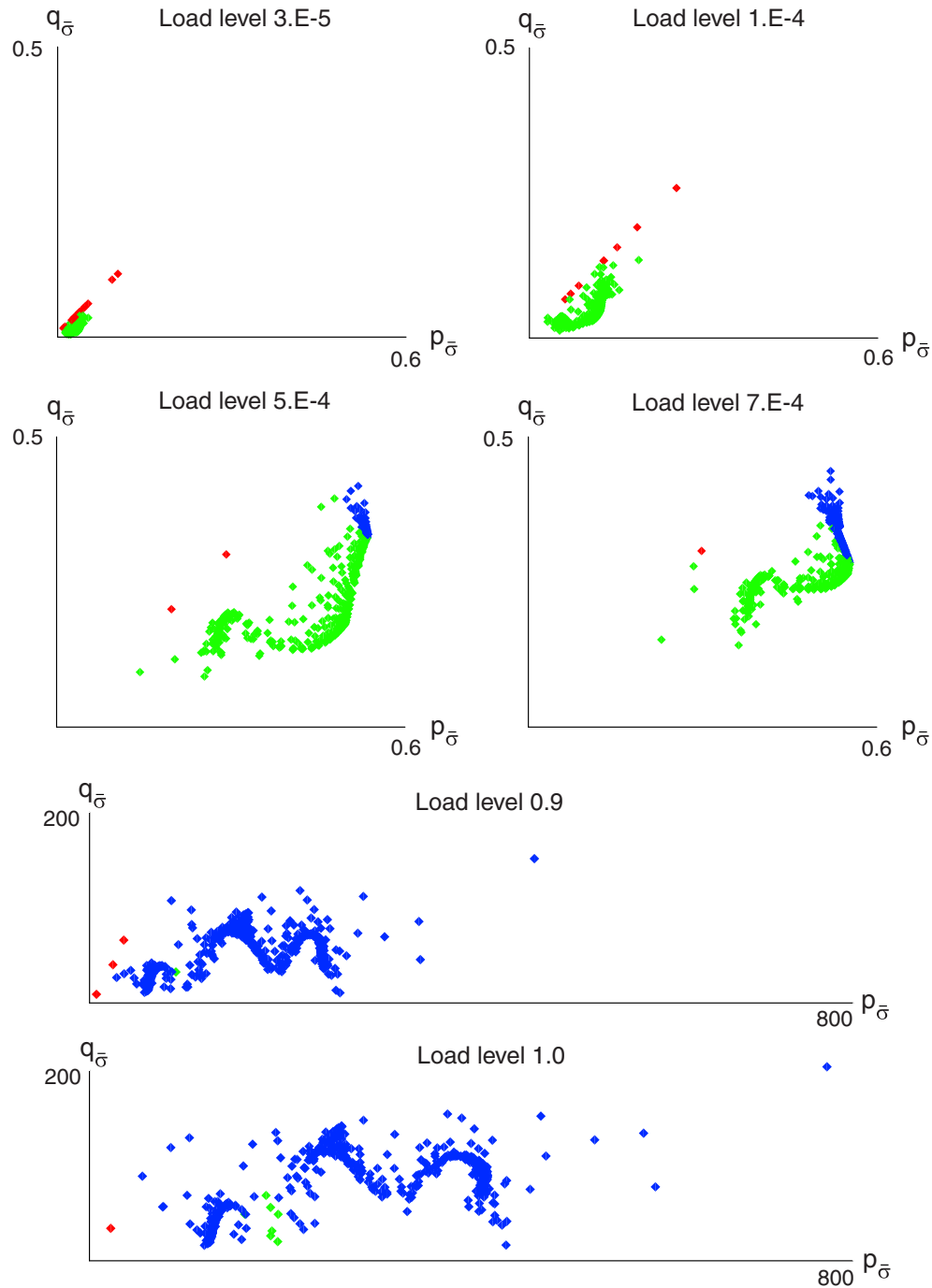


Figure 4.38: Frictionless compaction of the flanged component with the cone–cap model. Distribution of Cauchy stresses at Gauss–point level on the meridian plane  $q_{\sigma}$ – $p_{\sigma}$  for different load levels. Blue marks indicate plastic steps on the cap region, red marks plastic steps on the cone region and green marks elastic steps.

when an initial movement of the punches leads to the initial configuration of the sample). The present results show that, as expected, the effect of the cone yield surface is significant at the beginning of the compaction process, when a low pressure is applied. However, the influence is highly reduced as the compaction process advances, and the final results are quite similar with and without the cone (i.e. with the cone–cap model and with the elliptic model). The influence of the cone yield function when the friction effects between powder and compaction tools are important has not been established yet.

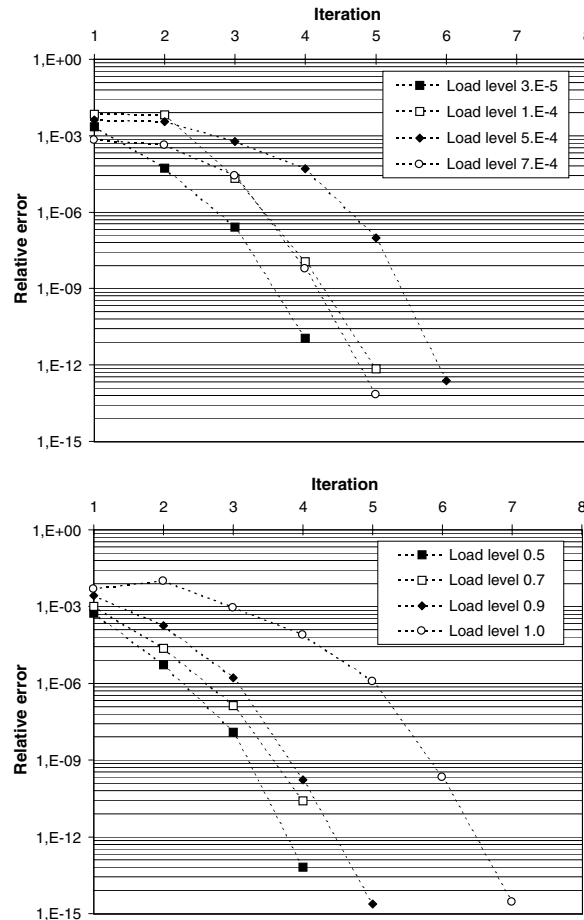


Figure 4.39: Frictionless compaction of the flanged component with the cone–cap model. Convergence results for different load levels.

The convergence results for different load levels are depicted in figure 4.39. These load levels include those used in figure 4.38 to show the distribution of Cauchy stresses at Gauss–point level. Quadratic convergence is found in all cases, for load increments with Gauss points under plastic loading in the cone region and with Gauss points under plastic loading in both regions.

#### 4.4.5 Concluding remarks

In this section, the consistent tangent moduli for general isotropic multiplicative hyperelastic and density–dependent plastic models have been presented. Moreover, it has been shown that the inclusion of the density in the plastic equations does not modify the standard backward Euler return–mapping algorithm based on the exponential map (Simo 1992, Cuitiño and Ortiz 1992).

Both elastic and plastic large deformations are included in the formulation. The yield function and flow rules are assumed to be expressed as general functions of the Kirchhoff stresses and the relative density. This includes the plastic models formulated in terms of Cauchy stresses (Menschke and Liu 1999) as a particular case.

As in the density–independent case, the expression of the consistent tangent moduli is composed of two terms, the geometric part, which only depends on the trial state and the elastic energy function, and the material part, which depends on the plastic model. The influence of the density is restricted to the material part. At Gauss points under plastic loading, the material part is found to be composed of two terms. The standard one for density–independent plastic models (Simo, 1992, 1998) and an additional one which includes density influence on the plastic equations.

The computation of the additional term only requires some vector–matrix products and the derivatives of the plastic equations with respect to the relative density. Therefore, it does not

represent any significant increase of the computational cost. On the other hand the consistent tangent moduli are, in general, unsymmetric. This has to be taken into account when solving the linear system of equations in order to obtain quadratic convergence with the Newton-Raphson method.

Some representative examples with a Cauchy-based Drucker–Prager model and elliptic and cone–cap density–dependent models have been presented. In the examples involving the elliptic and the cone–cap models, the derivatives with respect to the relative density have been approximated numerically, see sections 3.1 and 4.2 (Pérez–Foguet et al. 2000*d*, 2000*e*). In all the examples quadratic convergence has been found.

The influence of neglecting the density part of the consistent tangent moduli has been analyzed. It turns out that convergence is usually lost. When it is not, only linear convergence is obtained. The influence of symmetrizing the tangent is also assessed. Except for frictionless isostatic compaction tests (where the elliptic and cap model leads to symmetric tangents) linear convergence and, later, non-convergence are obtained.

A frictionless compaction test of an iron powder has also been simulated, as an example of a highly demanding boundary value problem from a computational point of view. The Arbitrary Lagrangian–Eulerian formulation presented in section 2.2 (Rodríguez-Ferran et al. 2000) for multiplicative elastoplasticity is used to avoid mesh distortion. The results obtained with the elliptic and the cone–cap models have been compared. Quadratic convergence has been found in both cases. Further analysis of compaction tests, including friction effects, are presented in chapter 5 (Pérez-Foguet et al. 2000*a*).

#### 4.4.6 Appendix: Density–dependent finite plasticity models

In the following, the three material models used in the examples, subsection 4.4.4, are presented. Attention is focused in the expression of the yield functions. The corresponding flow vectors are directly related with them. Thus, only their definition and main features are analyzed here. The complete expressions of the flow vectors can be derived in a straightforward manner.

The yield functions presented below are expressed in terms of the invariants

$$I_1(\bar{\boldsymbol{\tau}}) = \sum_{i=1}^{\text{n}_{\text{dim}}} [\bar{\boldsymbol{\tau}}]_i \quad \text{and} \quad J_2(\bar{\boldsymbol{\tau}}) = \frac{1}{2} \sum_{i=1}^{\text{n}_{\text{dim}}} ([\text{dev}(\bar{\boldsymbol{\tau}})]_i)^2, \quad (4.4.39)$$

where  $I_1(\bar{\boldsymbol{\tau}})$  denotes the first invariant of  $\bar{\boldsymbol{\tau}}$  and  $J_2(\bar{\boldsymbol{\tau}})$  the second invariant of the deviatoric part of  $\bar{\boldsymbol{\tau}}$ ,  $\{[\text{dev}(\bar{\boldsymbol{\tau}})]_i = [\bar{\boldsymbol{\tau}}]_i - I_1(\bar{\boldsymbol{\tau}})/3\}_{i=1, \dots, \text{n}_{\text{dim}}}$ . The following functions of  $I_1(\bar{\boldsymbol{\tau}})$  and  $J_2(\bar{\boldsymbol{\tau}})$  are also used

$$p_{\bar{\boldsymbol{\tau}}} = -\frac{I_1(\bar{\boldsymbol{\tau}})}{3} \quad \text{and} \quad q_{\bar{\boldsymbol{\tau}}} = \sqrt{3J_2(\bar{\boldsymbol{\tau}})}. \quad (4.4.40)$$

*Remark 4.4.3.* The invariants defined in equations (4.4.39) and (4.4.40) are also applied to the vector  $\bar{\boldsymbol{\sigma}}$ , whose components are the eigenvalues of the Cauchy stress tensor  $\boldsymbol{\sigma}$ ,  $\boldsymbol{\sigma} = \sum_{i=1}^{\text{n}_{\text{dim}}} [\bar{\boldsymbol{\sigma}}]_i \mathbf{n}_{tr}^i \otimes \mathbf{n}_{tr}^i$ . The relationship between  $\bar{\boldsymbol{\tau}}$  and  $\bar{\boldsymbol{\sigma}}$  follows from equations (4.4.5) and (4.4.12),

$$\bar{\boldsymbol{\sigma}} = \frac{\bar{\boldsymbol{\tau}}}{\det(\mathbf{F})} = \frac{\eta}{\eta_0} \bar{\boldsymbol{\tau}}. \quad (4.4.41)$$

Therefore,  $I_1(\bar{\boldsymbol{\sigma}})$ ,  $J_2(\bar{\boldsymbol{\sigma}})$ ,  $p_{\bar{\boldsymbol{\sigma}}}$  and  $q_{\bar{\boldsymbol{\sigma}}}$  are equal to the corresponding functions of  $\bar{\boldsymbol{\tau}}$  multiplied by  $\eta/\eta_0$ .  $\square$

#### Drucker–Prager model

Two expressions of the Drucker–Prager model are considered: one with the yield function based on the principal Kirchhoff stresses (Kirchhoff–based Drucker–Prager model) and another based on the principal Cauchy stresses (Cauchy–based Drucker–Prager model). In both cases, the flow vector  $\mathbf{m}_{\bar{\boldsymbol{\tau}}}$  is set equal to the derivatives of the yield function with respect to the principal Kirchhoff stresses,  $\mathbf{m}_{\bar{\boldsymbol{\tau}}} = \frac{\partial f}{\partial \bar{\boldsymbol{\tau}}}$ .

The Kirchhoff–based Drucker–Prager (KDP) yield function is defined as

$$f_{\text{KDP}}(\bar{\boldsymbol{\tau}}) = \sqrt{2J_2(\bar{\boldsymbol{\tau}})} + \sqrt{\frac{2}{3}} \left( \tan(\phi_{\text{DP}}) \frac{I_1(\bar{\boldsymbol{\tau}})}{3} - C_{\text{DP}} \right), \quad (4.4.42)$$

with  $\phi_{\text{DP}}$  the friction angle and  $C_{\text{DP}}$  the cohesion. The intersection with the deviatoric axis ( $p_{\bar{\tau}} = 0$ ) is at  $q_{\bar{\tau}} = C_{\text{DP}}$ , and the cone vertex (the intersection with the hydrostatic axis,  $q_{\bar{\tau}} = 0$ ) is at  $p_{\bar{\tau}} = -C_{\text{DP}}/\tan(\phi_{\text{DP}})$ . The von Mises yield function is recovered for  $\phi_{\text{DP}} = 0^\circ$ .

The Cauchy-based Drucker–Prager (CDP) yield function,  $f_{\text{CDP}}(\bar{\boldsymbol{\sigma}})$ , is obtained by substituting  $\bar{\boldsymbol{\tau}}$  by  $\bar{\boldsymbol{\sigma}}$  in equation (4.4.42). In order to apply the developments presented in this section,  $f_{\text{CDP}}(\bar{\boldsymbol{\sigma}})$  must be expressed in terms of the principal Kirchhoff stresses,  $\bar{\boldsymbol{\tau}}$ , and the relative density,  $\eta$ . This can be done by substituting equation (4.4.41) in  $f_{\text{CDP}}(\bar{\boldsymbol{\sigma}})$ , see remark 4.4.1, which leads to:

$$\tilde{f}_{\text{CDP}}(\bar{\boldsymbol{\tau}}, \eta) = \frac{\eta}{\eta_0} \sqrt{2J_2(\bar{\boldsymbol{\tau}})} + \sqrt{\frac{2}{3}} \left( \tan(\phi_{\text{DP}}) \frac{\eta}{\eta_0} \frac{I_1(\bar{\boldsymbol{\tau}})}{3} - C_{\text{DP}} \right). \quad (4.4.43)$$

However,  $\tilde{f}_{\text{CDP}}(\bar{\boldsymbol{\tau}}, \eta)$  is not used in the simulations of subsection 4.4.4. The equivalent yield function

$$\tilde{\tilde{f}}_{\text{CDP}}(\bar{\boldsymbol{\tau}}, \eta) = \frac{\eta_0}{\eta} \tilde{f}_{\text{CDP}}(\bar{\boldsymbol{\tau}}, \eta) = \sqrt{2J_2(\bar{\boldsymbol{\tau}})} + \sqrt{\frac{2}{3}} \left( \tan(\phi_{\text{DP}}) \frac{I_1(\bar{\boldsymbol{\tau}})}{3} - \frac{\eta_0}{\eta} C_{\text{DP}} \right) \quad (4.4.44)$$

is preferred because it leads to a density-independent flow vector,  $\frac{\partial \mathbf{m}_{\bar{\tau}}}{\partial \eta} = 0$ , contrary to equation (4.4.43), see remark 4.4.4 below. The parameter  $\eta_0$  is set equal to one for all  $\mathbf{X}$ , see remark 4.4.1.

*Remark 4.4.4.* The yield functions given in equations (4.4.43) and (4.4.44) are equivalent in the sense that, for a given trial state, both lead to the same solution on strains, stresses and internal variables of the plastic corrector problem, equation (4.4.19). Therefore, both yield functions model in the same way the elastoplastic behaviour of the material. However, the plastic corrector problems are not the same because the respective incremental plastic multipliers,  $\Delta\tilde{\gamma}$  and  $\Delta\tilde{\tilde{\gamma}}$ , are different. They are related through

$$\Delta\tilde{\gamma} = \frac{\eta_0}{\eta} \Delta\tilde{\tilde{\gamma}}. \quad (4.4.45)$$

On the other hand, the density-dependent part of the consistent tangent moduli of both problems is also different, see equation (4.4.37). The yield function that leads to the simpler consistent tangent moduli,  $\tilde{\tilde{f}}_{\text{CDP}}(\bar{\boldsymbol{\tau}}, \eta)$ , is used in this work.  $\square$

### Elliptic model

This model is defined by a density-dependent yield function (expressed in terms of the principal Kirchhoff stresses). The flow vector  $\mathbf{m}_{\bar{\tau}}$  is fixed equal to the derivatives of the yield function with respect to  $\bar{\boldsymbol{\tau}}$ .

The yield function is (Oliver et al. 1996)

$$f_{\text{ellip}}(\bar{\boldsymbol{\tau}}, \eta) = 2J_2(\bar{\boldsymbol{\tau}}) + a_1(\eta) \left( \frac{I_1(\bar{\boldsymbol{\tau}})}{3} \right)^2 - \frac{2}{3} a_2(\eta) (\sigma_y)^2, \quad (4.4.46)$$

with

$$a_1(\eta) = \begin{cases} \left( \frac{1-\eta^2}{2+\eta^2} \right)^{n_1} & \eta < 1 \\ 0 & \eta \geq 1 \end{cases} \quad (4.4.47)$$

$$a_2(\eta) = \begin{cases} \left( \frac{0.02\eta_0}{1-0.98\eta_0} \right)^{n_2} & \eta \leq \eta_0 \\ \left( \frac{\eta-0.98\eta_0}{1-0.98\eta_0} \right)^{n_2} & \eta > \eta_0 \end{cases}$$

The value of  $a_1(\eta)$  decreases from  $2^{-n_1}$  at  $\eta = 0$  to zero for  $\eta \geq 1$ . The value of  $a_2(\eta)$  increases monotonically from a minimum value for  $\eta \leq \eta_0$  Oliver et al. (1992) and its value at  $\eta = 1$  is one. The intersection with the deviatoric axis is at  $q_{\bar{\tau}} = \sqrt{a_2(\eta)} \sigma_y$  and the intersection with the hydrostatic axis is at  $p_{\bar{\tau}} = \pm \sqrt{\frac{2a_2(\eta)}{3a_1(\eta)}} \sigma_y$ . Note that  $f_{\text{ellip}}$  becomes the von Mises yield function for  $\eta \geq 1$ .

### Cone–cap model

This model is composed of two density–dependent yield functions: a *cone* defined by a Drucker–Prager yield function and a *cap* defined by an elliptic yield function. Both are expressed in terms of the principal Kirchhoff stresses. The flow vector is defined in two parts, one for the cone and the other for the cap. Both are presented in the following, after the yield function expressions.

The cone yield function is defined as

$$f_{\text{cone}}(\bar{\boldsymbol{\tau}}, \eta) = \sqrt{2J_2(\bar{\boldsymbol{\tau}})} + \sqrt{\frac{2}{3}} \left( \tan(\phi_{\text{cone}}(\eta)) \frac{I_1(\bar{\boldsymbol{\tau}})}{3} - C_{\text{cone}}(\eta) \right), \quad (4.4.48)$$

with

$$\begin{aligned} \phi_{\text{cone}}(\eta) &= \begin{cases} \phi_{\min} & \eta \leq \eta_0 \\ \left( \frac{\phi_{\min} - \phi_{\max}}{1 + \eta_0^2 - 2\eta_0} \right) (\eta^2 - 2\eta + 1) + \phi_{\max} & 1 \leq \eta < \eta_0 \\ \phi_{\max} & \eta > \eta_0 \end{cases} \\ C_{\text{cone}}(\eta) &= \begin{cases} C_{\text{ref}} \left( \frac{0.02\eta_0}{1 - 0.98\eta_0} \right)^{n_c} & \eta \leq \eta_0 \\ C_{\text{ref}} \left( \frac{\eta - 0.98\eta_0}{1 - 0.98\eta_0} \right)^{n_c} & \eta > \eta_0 \end{cases} \end{aligned} \quad (4.4.49)$$

The friction angle  $\phi_{\text{cone}}(\eta)$  varies parabolically from a minimum value  $\phi_{\min}$  at  $\eta = \eta_0$  to a maximum value  $\phi_{\max}$  at  $\eta = 1$ . The cohesion  $C_{\text{cone}}(\eta)$  increases as the function  $a_2(\eta)$  of the elliptic model, equation (4.4.47)<sub>2</sub>. The reference value  $C_{\text{ref}}$  is reached at  $\eta = 1$ .

The definition of the cap yield function is based on the elliptic yield function presented before, equation (4.4.46). It is defined so that it has the same maximum shear strength (maximum value of  $q_{\bar{\boldsymbol{\tau}}}$ ) and the same hydrostatic compression strength (maximum value of  $p_{\bar{\boldsymbol{\tau}}}$ ), as the elliptic yield function,  $\sqrt{a_2(\eta)} \sigma_y$  and  $\sqrt{\frac{2a_2(\eta)}{3a_1(\eta)}} \sigma_y$  respectively. Its expression is

$$f_{\text{cap}}(\bar{\boldsymbol{\tau}}, \eta) = 2J_2(\bar{\boldsymbol{\tau}}) + \tilde{a}_1(\eta) \left( \frac{I_1(\bar{\boldsymbol{\tau}}) - I_{\text{inter}}(\eta)}{3} \right)^2 - \frac{2}{3} a_2(\eta) (\sigma_y)^2, \quad (4.4.50)$$

with

$$\begin{aligned} I_{\text{inter}}(\eta) &= 3 \frac{C_{\text{cone}}(\eta) - \sqrt{a_2(\eta)} \sigma_y}{\tan(\phi_{\text{cone}}(\eta))}, \\ I_{\text{compr}}(\eta) &= - \sqrt{\frac{6 a_2(\eta)}{a_1(\eta)}} \sigma_y, \\ \tilde{a}_1(\eta) &= \frac{6 a_2(\eta) \sigma_y^2}{(I_{\text{compr}}(\eta) - I_{\text{inter}}(\eta))^2}, \end{aligned} \quad (4.4.51)$$

and  $a_1(\eta)$  and  $a_2(\eta)$  given by equations (4.4.47). Note that the maximum shear strength is reached at cone–cap intersection,  $I_{\text{inter}}(\eta)$ , instead of  $p_{\bar{\boldsymbol{\tau}}} = 0$  as the elliptic yield function does. Although Cante et al. (1999) use  $f_{\text{ellip}}$  defined in equation (4.4.46) as a cap yield function, in this work the expression of  $f_{\text{cap}}$  given by equation (4.4.50) is preferred because it simplifies the flow vector definition, as shown in the following.

The flow vector  $\mathbf{m}_{\bar{\boldsymbol{\tau}}}$  is defined by parts, one expression for the cone region,  $I_1(\bar{\boldsymbol{\tau}}) > I_{\text{inter}}(\eta)$ , and another for the cap region,  $I_1(\bar{\boldsymbol{\tau}}) \leq I_{\text{inter}}(\eta)$ . In the cap region, it is equal to the derivatives of the yield function with respect to  $\bar{\boldsymbol{\tau}}$ ,

$$\mathbf{m}_{\bar{\boldsymbol{\tau}} \text{ cap}} = \frac{\partial f_{\text{cap}}}{\partial \bar{\boldsymbol{\tau}}}, \quad (4.4.52)$$

and in the cone region, to

$$\mathbf{m}_{\bar{\boldsymbol{\tau}} \text{ cone}} = \mathbf{A}(\eta) \frac{\partial f_{\text{cone}}}{\partial \bar{\boldsymbol{\tau}}}, \quad (4.4.53)$$



with  $\mathbf{A}(\eta)$  a matrix of order  $n_{\text{dim}}$  defined so that  $\mathbf{m}_{\bar{\boldsymbol{\tau}}_{\text{cone}}}$  at cone–cap intersection is equal to  $\mathbf{m}_{\bar{\boldsymbol{\tau}}_{\text{cap}}}$  (pure deviatoric) and at cone vertex is pure hydrostatic:

$$\begin{aligned} \mathbf{A}(\eta) = \max \left\{ 1, \frac{3J_2(\bar{\boldsymbol{\tau}})}{a_2(\eta)(\sigma_y)^2} \right\} & \left( \mathbf{I}_{n_{\text{dim}}} - \frac{1}{3} \mathbf{1}\mathbf{1}^T \right) \\ & + \max \left\{ 1, \frac{I_{\text{inter}}(\eta) - I_1(\bar{\boldsymbol{\tau}})}{I_{\text{inter}}(\eta) + 3C_{\text{cone}}(\eta) \cot(\phi_{\text{cone}}(\eta))} \right\} \left( \frac{1}{3} \mathbf{1}\mathbf{1}^T \right) \end{aligned} \quad (4.4.54)$$

With the  $\mathbf{m}_{\bar{\boldsymbol{\tau}}_{\text{cone}}}$  given by equations (4.4.53) and (4.4.54) no corner return–mapping algorithm (Simo et al. 1988, Pramono and Willam 1989*b*, Hofstetter et al. 1993, Cante et al. 1999) is needed in the cone–cap intersection and neither in the cone vertex. This reduces the computational effort of the numerical time–integration algorithm. The same approach has already been used to avoid the grey zone at cone–cap intersection in plastic models for granular materials (Macari et al. 1997, Pérez-Foguet and Huerta 1999). A different technique, based on smoothing the yield function, has been used by Brandt and Nilsson (1999) with the same purpose.



## Chapter 5

# An application to powder compaction processes

Some of the new developments presented in previous chapters are applied here to the simulation of different quasistatic cold compaction processes of powders. These problems involve large boundary displacements, finite deformations and highly nonlinear material behaviour; thus, they represent demanding tests for the different numerical techniques presented in this report.

A density-dependent plastic model is used to describe the highly nonlinear material behaviour. The model is formulated within the framework of isotropic finite strain multiplicative hyperelastoplasticity. An elliptic plastic model expressed in terms of the Kirchhoff stresses and the relative density models the transition between the loose powder and the compacted sample. The Coulomb dry friction model is used to capture friction effects at die-powder contact.

Excessive distortion of Lagrangian meshes due to large mass fluxes are usual in powder compaction problems. For this reason, the ALE formulation presented in section 2.2 is used here to preclude any undesired mesh distortion. The ALE equations are integrated with a fractional-step method. This results in a Lagrangian phase and a convective phase. The Lagrangian phase is integrated with the standard return mapping for finite strain multiplicative plasticity and the convective phase with a simple explicit Godunov-like technique. Several representative compaction examples, involving structured and unstructured meshes, are simulated. The results obtained agree with the experimental data and other numerical results reported in the literature. On the other hand, in contrast with other simulations, the density distributions are smooth, i.e. without spurious oscillations, thanks to the use of an ALE formulation. Moreover, it is shown that, contrary to other Lagrangian and adaptive  $h$ -remeshing approaches recently reported for this type of problems, the present approach verifies the mass conservation principle with very low relative errors (less than 1% in all ALE examples and exactly in the pure Lagrangian examples).

### 5.1 Introduction

Cold compaction processes are a key ingredient in metallic and ceramic powder forming processes. They consist in the vertical compaction through the movement of a set of punches of a fine powder material at room temperature (Oliver et al. 1996, Jinka et al. 1997). The process transforms the loose powder into a compacted sample with a volume reduction (and therefore a density increase) of about 2–2.5 times. The design of these processes includes the definition of the initial dimensions of the sample and the movements of the punches that lead to compacted samples with uniform density distributions. In this context, efficient and reliable numerical simulations can play an important role as a complement of experimental tests.

Two ingredients are crucial for the numerical simulation of powder compaction processes: the constitutive model and the kinematic formulation of the problem. Several constitutive models have been proposed, including microscopic models, flow formulations and solid mechanics models, as elastic, plastic or visco-plastic models; see Oliver et al. (1996) and Lewis and Khoei (1998) for an general overview and references for each type of model. One of the most common approaches is the use of elastoplastic models based on porous or frictional materials. Here, the plastic model

presented by Oliver et al. (1996) is used. It consists in an elliptic yield function expressed in terms of the relative density and the Kirchhoff stresses. The plastic model is originally formulated within the framework of the multiplicative hyperelastoplasticity (Simo 1992, 1998), with some simplifications derived from the assumption of small elastic strains. In this work, large elastic strains are included in the formulation. As shown in the following, this does not represent any drawback from a modelling point of view. On the contrary, it allows to apply numerical techniques and material models developed for the general kinematic framework in a straightforward manner.

Up to date, a common characteristic of powder compaction simulations with solid mechanics constitutive models is the use of a Lagrangian kinematic formulation. This approach has shown to be adequate for problems that do not exhibit large mass fluxes among different parts of the sample (i.e. homogeneous tests). But in practical problems, as those which appear in realistic design processes, the Lagrangian approach leads to useless meshes (Lewis and Khoei 1998, Khoei and Lewis 1999) or violations of the boundary limits (Oliver et al. 1996). In order to solve these problems, different  $h$ -adaptive procedures have been presented recently (Khoei and Lewis 1999, Cante et al. 1999). However,  $h$ -refinement is computationally expensive and information must be interpolated from the old mesh to the new mesh. For these reasons, an Arbitrary Lagrangian–Eulerian formulation is preferred in this work. ALE formulations were first proposed for fluid problems with moving boundaries (Donald et al. 1977, Huerta and Liu 1988). Nowadays, ALE formulations for fluid problems are widely used in forming processes. On the other hand, the ALE formulation has been successfully employed in nonlinear solid mechanics (Liu et al. 1986, Benson 1986, Ghosh and Kikuchi 1991, Rodríguez-Ferran et al. 1998, Rodríguez-Ferran et al. 2000) and structural mechanics (Askes et al. 1998, Huerta et al. 1999). The formulation for multiplicative hyperelastoplasticity presented in section 2.2 is used here.

The main features of the ALE formulation and the time-integration scheme are presented in section 5.2, together with the description of the constitutive model. After that, in section 5.3, the proposed approach is applied to several representative examples. The present results are compared with experimental data and other results of numerical simulations presented in the literature. Section 5.4 contains some concluding remarks.

## 5.2 Problem statement

In this section, a brief description of the main features of the proposed approach is presented. First, the kinematics of the ALE formulation are reviewed. After that, the finite strain elliptic elastoplastic model is described, focusing in the yield function dependence on the density and the expression of the ALE evolution equations. Finally, the key points of the numerical time-integration algorithm are summarized. We refer to sections 2.2 and 4.4 for further details on these topics.

### 5.2.1 Kinematics

Let  $R_X \subset \mathbb{R}^{\text{ndim}}$  ( $\text{ndim} = 2, 3$ ) be the material configuration of a continuum body with particles labelled by their initial position vector  $\mathbf{X} \in R_X$ . In a Lagrangian setting,  $\mathbf{X}$  are used as the independent variables in the description of motion. The motion of the body is described by the one-parameter family of mappings  $\varphi_t : R_X \mapsto \mathbb{R}^{\text{ndim}}$  with  $t \in [0, T]$ .  $R_x = \varphi_t(R_X)$  is the spatial configuration of the body at time  $t$ , and  $\mathbf{x} = \varphi_t(\mathbf{X}) = \varphi(\mathbf{X}, t) \in R_x$  is the current position of the material particle  $\mathbf{X}$ .

The key ingredient of the ALE formulation is the referential configuration  $R_\chi$ , with grid (or reference) points  $\chi$  used as independent variables to describe body motion. This referential configuration  $R_\chi$  is mapped into the material and spatial configurations by  $\Psi$  and  $\Phi$  respectively, see figure 2.21. The initial and current positions of a material particle are expressed on the reference domain as  $\mathbf{X} = \Psi(\chi, t)$  and  $\mathbf{x} = \Phi(\chi, t)$  respectively. The three mappings  $\varphi$ ,  $\Phi$  and  $\Psi$  are related by  $\varphi = \Phi \circ \Psi^{-1}$ .

In an ALE setting, different displacement fields can be defined. Two of them have special interest, the particle displacement  $\mathbf{u}$  and the mesh (spatial) displacement  $\mathbf{u}_\Phi$ ,

$$\mathbf{u}(\mathbf{X}, t) = \mathbf{x}(\mathbf{X}, t) - \mathbf{X} \quad \text{and} \quad \mathbf{u}_\Phi(\chi, t) = \mathbf{x}(\chi, t) - \chi. \quad (5.2.1)$$

The particle velocity and the mesh velocity are respectively

$$\mathbf{v} = \frac{\partial \mathbf{x}}{\partial t} \Big|_{\mathbf{X}} \quad \text{and} \quad \mathbf{v}_{\text{mesh}} = \frac{\partial \mathbf{x}}{\partial t} \Big|_{\mathbf{x}}, \quad (5.2.2)$$

where, following standard notation,  $|_*$  means ‘‘holding \* fixed’’. The link between material and mesh motion is provided by the convective velocity,  $\mathbf{c} = \mathbf{v} - \mathbf{v}_{\text{mesh}}$ .

### 5.2.2 Constitutive model

Finite strain multiplicative plasticity is assumed. Thus, the particle deformation gradient,

$$\mathbf{F}(\mathbf{X}, t) = \frac{\partial \varphi}{\partial \mathbf{X}}(\mathbf{X}, t), \quad (5.2.3)$$

is locally decomposed into elastic and plastic parts as  $\mathbf{F} = \mathbf{F}^e \mathbf{F}^p$ . The local thermodynamic state is defined by means of the elastic left Cauchy–Green tensor  $\mathbf{b}^e = \mathbf{F}^e \mathbf{F}^{eT}$ , where the superscript  $T$  means transpose. No plastic internal variables are considered. The Kirchhoff stress tensor,  $\boldsymbol{\tau}$ , is given by the hyperelastic relationship

$$\boldsymbol{\tau} = 2 \frac{dW^e}{d\mathbf{b}^e} \mathbf{b}^e, \quad (5.2.4)$$

where  $W^e$  is the free–energy function per unit of undeformed volume (Bonet and Wood 1997). The Hencky’s hyperelastic law, which leads to a linear relationship between the principal Kirchhoff stresses and the logarithm of the principal stretches, is considered. The Cauchy stress tensor is given by

$$\boldsymbol{\sigma} = \frac{\boldsymbol{\tau}}{\det(\mathbf{F})}. \quad (5.2.5)$$

The plastic response of the material is assumed isotropic and density–dependent. The dependence on the density is incorporated through the relative density  $\eta(\mathbf{X}, t)$  of the particle  $\mathbf{X}$  at time  $t$  (Oliver et al. 1992, 1996, Brandt and Nilsson 1998, 1999). The relative density is equal to the real density of the material divided by a reference value, which usually is the solid density of the compacted material.

The elliptic yield function (Oliver et al. 1996)

$$f_{\text{ellip}}(\boldsymbol{\tau}, \eta) = 2J_2(\boldsymbol{\tau}) + a_1(\eta) \left( \frac{I_1(\boldsymbol{\tau})}{3} \right)^2 - \frac{2}{3} a_2(\eta) (\sigma_y)^2, \quad (5.2.6)$$

is considered, with the density dependent parameters

$$a_1(\eta) = \begin{cases} \left( \frac{1-\eta^2}{2+\eta^2} \right)^{n_1} & \eta < 1 \\ 0 & \eta \geq 1 \end{cases} \quad (5.2.7)$$

$$a_2(\eta) = \begin{cases} \left( \frac{0.02\eta_0}{1-0.98\eta_0} \right)^{n_2} & \eta \leq \eta_0 \\ \left( \frac{\eta-0.98\eta_0}{1-0.98\eta_0} \right)^{n_2} & \eta > \eta_0 \end{cases}$$

and  $I_1(\boldsymbol{\tau})$  equal to the first invariant of  $\boldsymbol{\tau}$  and  $J_2(\boldsymbol{\tau})$  to the second invariant of the deviatoric part of  $\boldsymbol{\tau}$ . The dependence of  $a_1$  and  $a_2$  on  $\eta$  for a particular set of material parameters is depicted on figure 5.1. The value of  $a_1(\eta)$  decreases from  $2^{-n_1}$  at  $\eta = 0$  to zero for  $\eta \geq 1$ . Parameter  $a_2(\eta)$  increases monotonically from a minimum value for  $\eta \leq \eta_0$  (Oliver, Oller and Cante 1992) and its value at  $\eta = 1$  is one. The trace of the yield function on the meridian plane  $p_{\boldsymbol{\tau}}-q_{\boldsymbol{\tau}}$ , with  $p_{\boldsymbol{\tau}} = -\frac{I_1(\boldsymbol{\tau})}{3}$  and  $q_{\boldsymbol{\tau}} = \sqrt{3J_2(\boldsymbol{\tau})}$ , and for different relative densities are depicted in figure 5.2. The intersection with the deviatoric axis is at  $q_{\boldsymbol{\tau}} = \sqrt{a_2(\eta)} \sigma_y$  and intersection with the hydrostatic axis is at  $p_{\boldsymbol{\tau}} = \pm \sqrt{\frac{2a_2(\eta)}{3a_1(\eta)}} \sigma_y$ . Thus,  $f_{\text{ellip}}$  becomes the von Mises yield function for  $\eta \geq 1$ .

The evolution of the elastic left Cauchy–Green tensor (i.e. flow rule) is defined in the ALE setting as

$$\frac{\partial \mathbf{b}^e}{\partial t} \Big|_{\mathbf{x}} + \mathbf{c} \nabla_{\mathbf{x}} \mathbf{b}^e - \mathbf{l} \mathbf{b}^e - \mathbf{b}^e \mathbf{l}^T = -2\dot{\gamma} \frac{\partial f_{\text{ellip}}}{\partial \boldsymbol{\tau}}(\boldsymbol{\tau}, \eta) \mathbf{b}^e, \quad (5.2.8)$$

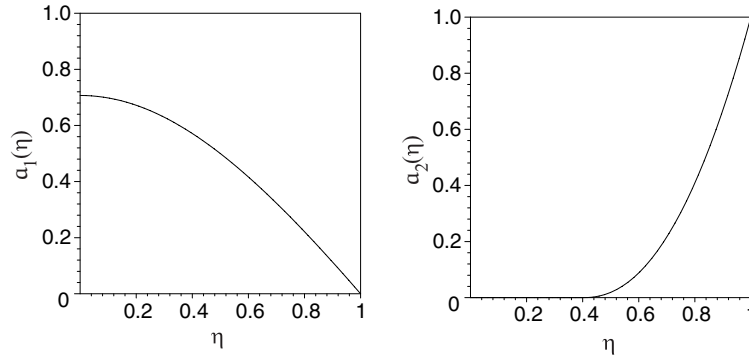


Figure 5.1: Dependence of parameters  $a_1(\eta)$  and  $a_2(\eta)$  on the relative density,  $\eta$ . Parameters of Powder-C material, see table 5.2.

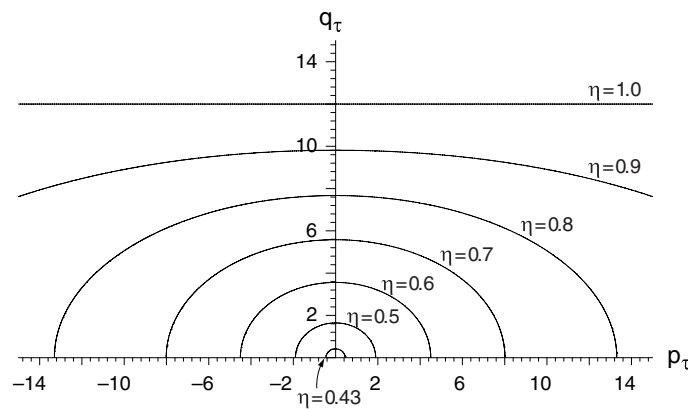


Figure 5.2: Trace of the elliptic yield function on the meridian plane  $q_\tau$ - $p_\tau$  for different relative densities,  $\eta$ . Parameters of Powder-C material, see table 5.2.

where  $\nabla_{\mathbf{x}}$  is the gradient operator with respect to spatial coordinates,  $\mathbf{l} = \nabla_{\mathbf{x}}\mathbf{v}$  is the velocity gradient tensor and  $\dot{\gamma}$  is the plastic multiplier, which is determined with the classical Kuhn-Tucker conditions:

$$\dot{\gamma} \geq 0 \quad , \quad f_{\text{ellip}}(\boldsymbol{\tau}, \eta) \leq 0 \quad \text{and} \quad \dot{\gamma} f_{\text{ellip}}(\boldsymbol{\tau}, \eta) = 0 . \quad (5.2.9)$$

The evolution of the relative density  $\eta$  is given by the mass conservation principle, which in ALE formulation reads

$$\frac{\partial \eta}{\partial t} \Big|_{\mathbf{X}} + \mathbf{c} \cdot \nabla_{\mathbf{x}} \eta + \eta \nabla_{\mathbf{x}} \cdot \mathbf{v} = 0 . \quad (5.2.10)$$

*Remark 5.2.1.* The Lagrangian evolution equations for  $\mathbf{b}^e$  and  $\eta$  can be found in a straightforward manner, just setting  $\mathbf{c} = \mathbf{0}$  in their ALE expressions, equations (5.2.8) and (5.2.10) respectively. In that situation, the referential time derivatives,  $\frac{\partial \mathbf{b}^e}{\partial t} \Big|_{\mathbf{X}}$  and  $\frac{\partial \eta}{\partial t} \Big|_{\mathbf{X}}$ , are equivalent to the material derivatives  $\frac{\partial \mathbf{b}^e}{\partial t} \Big|_{\mathbf{X}}$  and  $\frac{\partial \eta}{\partial t} \Big|_{\mathbf{X}}$ . The standard (spatial) expression of the flow rule

$$\mathcal{L}_{\mathbf{v}} \mathbf{b}^e = -2 \dot{\gamma} \frac{\partial f_{\text{ellip}}}{\partial \boldsymbol{\tau}}(\boldsymbol{\tau}, \eta) \mathbf{b}^e , \quad (5.2.11)$$

is obtained using that

$$\mathcal{L}_{\mathbf{v}} \mathbf{b}^e = \frac{\partial \mathbf{b}^e}{\partial t} \Big|_{\mathbf{X}} - \mathbf{l} \mathbf{b}^e - \mathbf{b}^e \mathbf{l}^T , \quad (5.2.12)$$

with  $\mathcal{L}_{\mathbf{v}}$  the Lie derivative with respect to the particle (spatial) velocity,  $\mathbf{v}$ . The standard (material) expression of the relative density evolution reads

$$\eta(\mathbf{X}, t) = \frac{\eta_0(\mathbf{X})}{\det(\mathbf{F})} , \quad (5.2.13)$$

with  $\eta(\mathbf{X}, t)$  equal to the relative density at time  $t = 0$ .  $\square$

---

FOR EVERY TIME-STEP  $[{}^n t, {}^{n+1} t]$ :

**Material phase**

- Neglect convective terms
- Advance the solution iteratively in an updated Lagrangian fashion: compute the increment of particle displacements  ${}^{n+1} \Delta \mathbf{u}$  and quantities  ${}^L \mathbf{b}^e$  and  ${}^L \eta$  (superscript L denotes Lagrangian)

**Remeshing**

- Compute the increment of mesh displacements  ${}^{n+1} \Delta \mathbf{u}_\Phi$  and the increment of convective displacements  ${}^{n+1} \Delta \mathbf{u}_{\text{conv}}$  by means of a remeshing algorithm that reduces element distortion
- Compute the convective velocity  $\mathbf{c} = {}^{n+1} \Delta \mathbf{u}_{\text{conv}} / \Delta t$

**Convection phase**

- Account for convective terms
  - Use the Godunov-type technique to convect quantities  ${}^L \mathbf{b}^e$  and  ${}^L \eta$  into  ${}^{n+1} \mathbf{b}^e$  and  ${}^{n+1} \eta$
  - Compute stresses  ${}^{n+1} \boldsymbol{\tau}$  and  ${}^{n+1} \boldsymbol{\sigma}$
- 

Table 5.1: The overall ALE scheme.

### 5.2.3 Numerical time–integration

The two fundamental unknowns in every time–step  $[{}^n t, {}^{n+1} t]$ , with  ${}^{n+1} t = {}^n t + \Delta t$ , are the increment of mesh displacements,

$${}^{n+1} \Delta \mathbf{u}_\Phi(\boldsymbol{\chi}) = {}^{n+1} \mathbf{x}(\boldsymbol{\chi}) - {}^n \mathbf{x}(\boldsymbol{\chi}) \quad (5.2.14)$$

and the increment of particle displacements,

$${}^{n+1} \Delta \mathbf{u}({}^n \mathbf{X}(\boldsymbol{\chi})) = {}^{n+1} \mathbf{x}({}^n \mathbf{X}(\boldsymbol{\chi})) - {}^n \mathbf{x}({}^n \mathbf{X}(\boldsymbol{\chi})) \quad (5.2.15)$$

which is referred to the particles  ${}^n \mathbf{X}$  associated to grid points  $\boldsymbol{\chi}$  at the beginning of the time–step,  ${}^n \mathbf{X} = \mathbf{X}(\boldsymbol{\chi}, {}^n t)$ . The difference between these two increments is the so–called increment of convective displacements,

$${}^{n+1} \Delta \mathbf{u}_{\text{conv}}(\boldsymbol{\chi}) = {}^{n+1} \Delta \mathbf{u}(\boldsymbol{\chi}) - {}^{n+1} \Delta \mathbf{u}_\Phi(\boldsymbol{\chi}), \quad (5.2.16)$$

which represents the relative motion between particles and grid points during the time–step. The convective velocity is assumed constant in the time–step and equal to  $\mathbf{c} = {}^{n+1} \Delta \mathbf{u}_{\text{conv}} / \Delta t$ .

The quantities to integrate are only  $\mathbf{b}^e$  and  $\eta$ , equations (5.2.8) and (5.2.10), see remark 5.2.2 below. The numerical time–integration is done by means of a fractional–step method, see section 2.2. Every time–step is divided into two phases: the Lagrangian phase and the convection phase. During the Lagrangian phase, convection is neglected and the increment of particle displacements  ${}^{n+1} \Delta \mathbf{u}$  is computed in the usual Lagrangian fashion, see section 4.4, using the evolution equations (5.2.11) and (5.2.13). After that, an ALE remeshing algorithm is employed to compute the increment of mesh displacements  ${}^{n+1} \Delta \mathbf{u}_\Phi$ . During the convection phase, the convective term is taken into account. A Godunov–like technique (Huerta et al. 1995, Rodríguez-Ferran et al. 1998) is used for that purpose. The overall scheme is summarized in table 5.1.

*Remark 5.2.2.* In a general setting, all quantities related with the particles should be convected. This includes the material parameters and the value of  $\det(\mathbf{F})$ , in addition to  $\mathbf{b}^e$  and  $\eta$  (and the plastic internal variables if they exist). A reduced increment of the computational cost due to the

	Powder-A	Powder-B	Powder-C
$E$	2 000. [MPa]	50 000. [MPa]	50 000. [MPa]
$\nu$	0.37	0.37	0.37
$\sigma_y$	90. [MPa]	170. [MPa]	12. [MPa]
$\eta_0$	0.489	0.4	0.41
$n_1$	1.	0.3	0.5
$n_2$	2.7	5.4	2.2

Table 5.2: Material parameters.

time-integration of additional quantities can be expected because the Godunov-like technique is explicit and the main computations of this scheme are already performed for the convection of  $\mathbf{b}^e$  and  $\eta$ . However, in the usual case that the material surfaces are tracked by the ALE remeshing algorithm and homogeneous materials are considered (as is the case in all the examples presented in this work), only the integration of  $\mathbf{b}^e$  and  $\eta$  is necessary. The value of  $\det(\mathbf{F})$  can be computed from the material mass conservation principle, equation (5.2.13).  $\square$

*Remark 5.2.3.* In the numerical simulations of section 5.3, only the Lagrangian phase is performed during iterations within each load increment. The remeshing and the convection are computed with the converged results at the end of each time-step. This results into a reduced computational cost overhead with respect to the standard pure Lagrangian approach. The equilibrium perturbation due to the remeshing and the convective time-integration of the converged results is taken into account in the subsequent load increment. Therefore, there are no accumulative errors in the results.  $\square$

### 5.3 Numerical simulations

Some representative powder compaction problems are simulated in this section. The elliptic material model and the ALE formulation presented in section 5.2 are used within a standard displacement based finite element formulation. The results of the present numerical simulations are compared with experimental data and other numerical results reported in the literature.

Four different examples are presented. First, two sets of homogenous tests (Dorémus et al. 1994, Ernst and Barnekow 1994, Oliver et al. 1996) are simulated. These examples are performed with the standard Lagrangian description and without friction effects. The material parameters of two different powders calibrated by Oliver et al. (1996) are used, powder-A and powder-B in table 5.2. The results obtained in this work are in agreement with those of references. Second, the simulation of the compaction of a plain bush component is presented (Gethin and Lewis 1994, Cante, Oliver and Oller 1998, Lewis and Khoei 1998, Khoei and Lewis 1999). The process is simulated with the Lagrangian formulation. Friction effects are included. The material parameters of a third powder material, powder-C in table 5.2, are used (Oliver et al. 1996). The results are compared with experimental data and those of previous simulations reported in the literature. Verification of the mass conservation principle is included.

The third and fourth examples are computed with the ALE formulation. They correspond to several compaction processes on two different multi-level components (Lewis and Tran 1994, Lewis and Khoei 1998, Khoei and Lewis 1999). A Lagrangian formulation on this type of problems usually leads to useless finite element meshes (i.e. highly distorted). Khoei and Lewis (1999) illustrate the application of an  $h$ -remeshing technique to powder compaction modelling with these examples. Here, they are used to illustrate that the ALE formulation can preclude any undesired mesh distortion. Relative density distributions without spurious oscillations are found. Examples with structured and unstructured meshes are included.

#### 5.3.1 Homogeneous tests

In this subsection, the results of the simulation of two sets of frictionless compaction tests with homogeneous cylindrical samples are briefly reviewed (see subsection 4.4.4 for a complete analysis of these simulations).



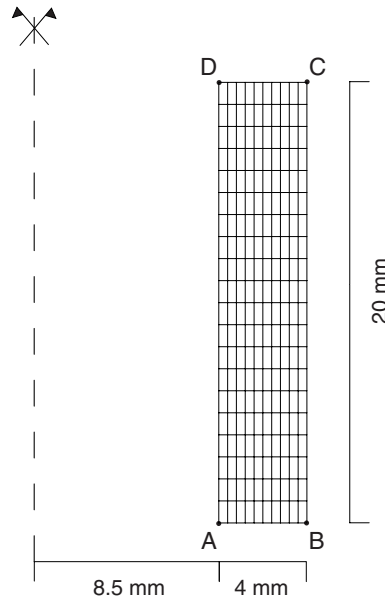


Figure 5.3: Plain bush component. Problem definition (after Lewis and Khoei 1998) and computational mesh.

All samples are modelled by a 2D structured mesh of 100 bilinear elements. Each set of tests is performed with a different material, powder-A and powder-B. The material parameters of both powders are summarized in table 5.2. The parameters are calibrated by Oliver et al. (1996) by comparing the results of numerical simulations with previous experiments reported in the literature (Dorémus et al. 1994, Ernst and Barnekow 1994). The same material parameters are used in this work. Recall that the plastic model is used in this work is very similar to that used by Oliver et al. (1996); the only difference between the two models is the treatment of the elastic deformations. As expected, the results obtained agree with those of Oliver et al. (1996) and the experiments.

The first set of compaction experiments (Dorémus et al. 1994) is modelled with powder-A parameters. A sample with an initial height of 24 mm and a diameter of 20 mm was used. Both isostatic compaction and triaxial tests were performed. The triaxial tests consisted of an initial isostatic compaction step up to a pressure of 50, 150 or 400 MPa, followed by an uniaxial compaction up to a vertical pressure of 1250 MPa (keeping the external radial pressure constant). The results of the numerical simulations and the experiments are compared in figure 4.29. The results of the present simulations agree with the experimental ones and with the results presented by Oliver et al. (1996), not shown in figure 4.29.

The second set of compaction experiments (Ernst and Barnekow 1994) is modelled with the powder-B parameters. A sample with an initial height of 80 mm and a diameter of 14.3 mm was used. Both isostatic and uniaxial compaction tests were performed. The results of the simulations and the experiments are compared in figure 4.32. In general, the simulation results agree with the experimental ones. Nevertheless, the density predicted in this work for a given value of the pressure is a little bit higher than the values shown by Oliver et al. (1996). These differences may be related with the large elastic strains, which in the present formulation are taken into account.

### 5.3.2 A plain bush component

The uniaxial compaction of a plain bush component is simulated next. Experimental data (Gethin and Lewis 1994) and numerical results (Gethin and Lewis 1994, Cante et al. 1998, Lewis and Khoei 1998, Khoei and Lewis 1999) are available for this example. Both are used here for comparative purposes.

The test is performed with the powder-C material parameters presented in table 5.2. These material parameters are calibrated by Cante et al. (1998) by comparing numerical results with those of Gethin and Lewis (1994). The results obtained in this work agree with the experiments and with

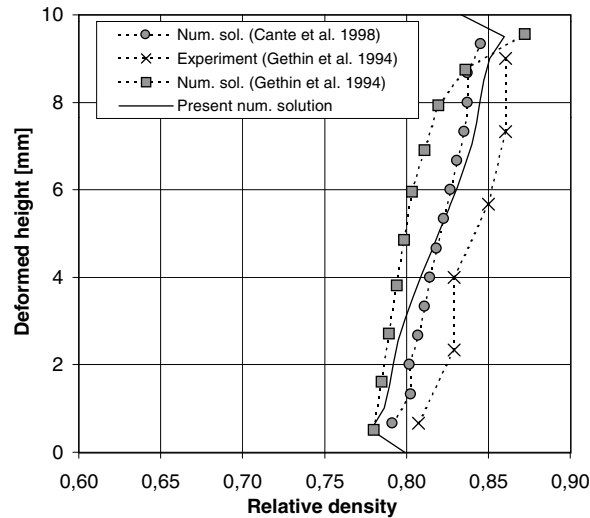


Figure 5.4: Plain bush component. Relative density profile at radius equal to 10.5 mm.

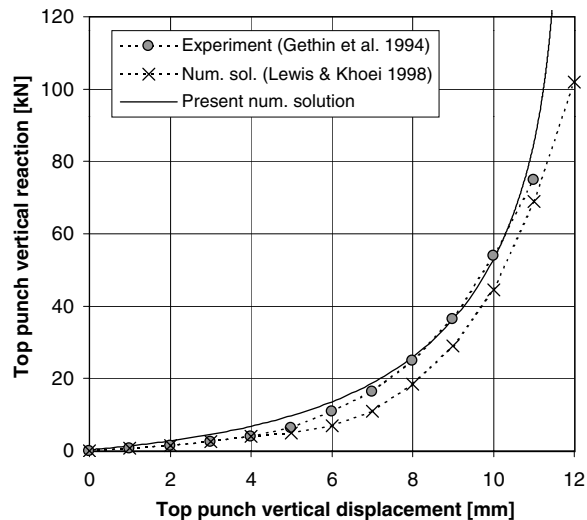


Figure 5.5: Plain bush component. Relationship between top punch vertical reaction and its vertical displacement.

those of Gethin and Lewis (1994) and Cante et al. (1998). They are also in general agreement with the results of Lewis and Khoei (1998), obtained with a completely different approach (dynamic analysis with a hypoelastic relationship and a cone-cap plastic model).

The component is modelled by an axisymmetric representation as illustrated in figure 5.3 (Lewis and Khoei 1998). A 2D structured mesh of 200 bilinear elements is used. The die wall friction is simulated with a Coulomb friction coefficient  $\mu = 0.15$  (Cante et al. 1998, Gethin and Lewis 1994) acting in the inner and outer walls of the sample, segments  $\overline{BC}$  and  $\overline{DA}$  of figure 5.3. In the numerical simulation of Cante et al. (1998) the relative radial movement of top and bottom surfaces with respect to the punches, segments  $\overline{AB}$  and  $\overline{CD}$ , is allowed, with a Coulomb friction coefficient equal to that of the lateral surfaces. Here, following Lewis and Khoei (1998), the radial displacement of the top and the bottom of the sample is restrained. The vertical displacement of segment  $\overline{AB}$  is also set equal to zero, and a vertical displacement of 11.5 mm is imposed to segment  $\overline{CD}$ , simulating the top punch movement.

The relative density profile at radius equal to 10.5 mm for a top punch displacement of 10 mm is shown in figure 5.4. The numerical results of Cante et al. (1998) and the experimental data and

the numerical results of Gethin and Lewis (1994) are included in the same figure. The results of the present numerical simulation are in agreement with all of them. However, as expected because of the similarities of the material model, the best agreement is found with the results of Cante et al. (1998). The lower relative density at the top part of the sample found by Cante et al. (1998), with respect to the present one, and the higher values in the lower part are directly related with the different simulation of the friction effects of top and bottom punches.

The evolution of the vertical reaction of the punch with respect to its vertical displacement is depicted in figure 5.5. The numerical results of Lewis and Khoei (1998) and the experimental data of Gethin and Lewis (1994) are also included. Lewis and Khoei (1998) present results for different formulations. Those presented in figure 5.5 are the most similar to the experimental data. The agreement between the results of the present simulation and the experimental ones is good.

Finally, the evolution of the relative density distribution over the sample is depicted in figure 5.6. Results for different vertical top punch displacements (from 4 to 11 mm) are shown. Two different relative density scales are used (one in each row) in order to show better the non-homogeneous distribution of the density. The shape of the relative density distributions are in general agreement with those presented by Lewis and Khoei (1998), although the quantitative values are a little bit higher. In order to check the present results, the evolution of the sample mass during the simulation has been computed. A constant value equal to the initial one has been found, up to six significant digits. Therefore, the mass conservation principle is verified. This implies, for instance, a mean value of the relative density equal to  $2\eta_0$  for a height reduction of 50% (i.e.  $\eta_{\text{mean}} = 0.82$  for a top displacement of 10 mm, see figures 5.5 and 5.6).

### 5.3.3 A rotational flanged component

The following compaction example is of a flanged component which is modelled by an axisymmetric representation, as illustrated in figure 2.32. The example is used by Lewis and Khoei (1998) to illustrate the applicability of a dynamic approach with a hypoelastoplastic model. The same example is used by Khoei and Lewis (1999) to show the utility of an adaptive remeshing technique to reduce mesh distortion. Here the hyperelastoplastic model and the ALE formulation presented in section 5.2 are used. Some experimental results (Lewis and Tran 1994) are available. The present results illustrate that the present approach allows to simulate high demanding powder compaction processes without mesh distortion and spurious oscillations in the results. Moreover, it is shown that the mass conservation principle is verified with a low relative error.

Three different compaction tests are simulated (Lewis and Khoei 1998): 1) a vertical movement of the top punch (6.06 mm); 2) a vertical movement of the bottom punch (5.10 mm); and 3) a simultaneous movement of both punches (6.06 mm the top punch and 7.70 mm the bottom punch). The same structured mesh of 170 eight-noded elements with reduced integration (four Gauss points per element) is used in the three tests. The die wall friction is simulated with a Coulomb friction coefficient  $\mu = 0.08$  acting in the segments  $\overline{BC}$ ,  $\overline{CD}$ ,  $\overline{DE}$  and  $\overline{FA}$ , see figure 2.32, and the radial displacement at the punches is restrained (Lewis and Khoei 1998).

The analysis is performed with powder-C material, see table 5.2, calibrated by Oliver et al. (1996) for the compaction of the plain bush component. The relationships between dimensionless vertical loads and punch displacements obtained in this work are compared with those of Lewis and Khoei (1998) in figure 5.7. The agreement between the two sets of curves is evident. However, the load reference for both simulations is different: 387 kN for the present results and 1550 kN for the results of Lewis and Khoei (1998) (in both cases the final reaction of the top punch in the double-punch compaction test). This difference can be related with the different modelling approach (dynamic versus static) and, specially, with the great difference between the elastic moduli used in both cases (40 MPa in Lewis and Khoei 1998, three orders of magnitude lower than that used here).

In the following, a detailed analysis of the relative density distribution obtained in each of the three tests is presented. The results are in general agreement with those presented by Lewis and Khoei (1998) and the experimental data of Lewis and Tran (1994).

In the first test, top punch compaction, the mesh region ABCG is Eulerian, and equal height elements are prescribed in the mesh region GDEF. The variation of the mass of the sample during the simulation is depicted in figure 5.8. A final reduction of 0.75% is found. This small

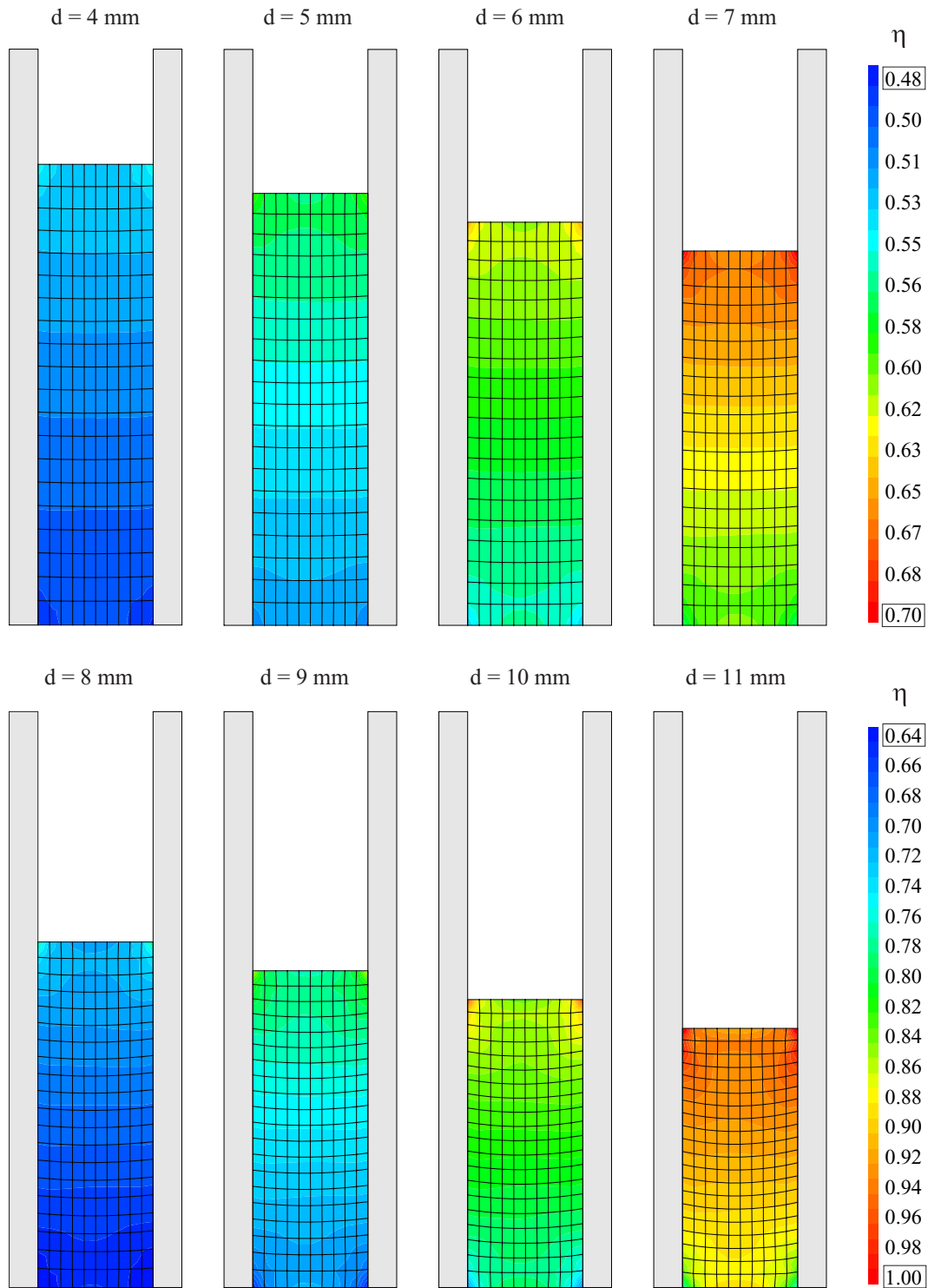


Figure 5.6: Plain bush component. Relative density distribution for different top punch movements. Note that two different scales are used.

variation corresponds to the truncation error in the discretization of the convective term of the ALE formulation (both temporal and spatial discretization).

The evolution of the relative density distribution is summarized in figures 5.9(a–d). The compaction process leads to a clearly non-homogenous density distribution. As expected, higher values are found in the outer region of the sample and lower ones close to the bottom surface. A smooth

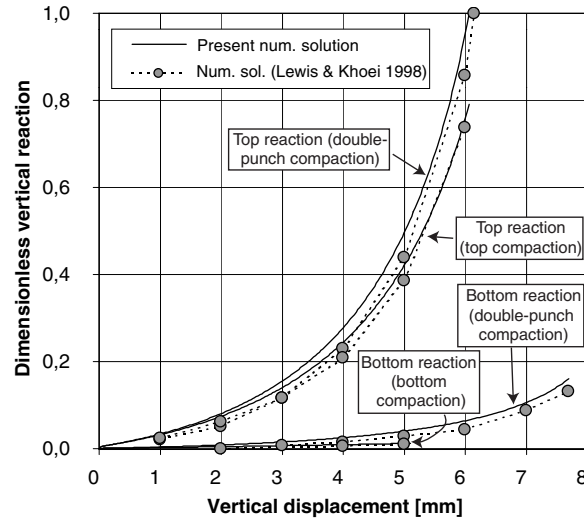


Figure 5.7: Flanged component. Relationships between the vertical reactions of the punches and their vertical movements: top reaction for top punch compaction, bottom reaction for bottom punch compaction, and top and bottom reactions for double-punch compaction.

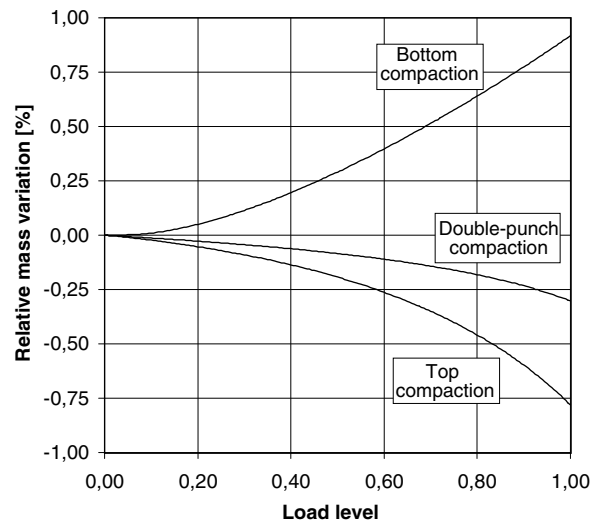


Figure 5.8: Relative mass variation during the three compaction processes of the flanged component. The load levels are referred to the punch displacements imposed at the end of each test.

transition from higher to lower densities is found. A dense zone is detected in the corner region, just over the point C, during all the process. Recall that there is not mesh distortion because, although the flux of mass is important, in the ALE formulation the mesh does not follow the material particles.

The final relative density profile at 1.88 mm from line  $\overline{GD}$  is depicted in figure 5.9(e). The present results are in general agreement with those presented by Lewis and Khoei (1998). Two zones with a quasi-uniform relative density are found in both cases. However, the density profile obtained by Lewis and Khoei (1998) presents a big oscillation between these two zones, and, on the contrary, the transition obtained in this work is smooth.

The second test consists in a bottom punch compaction. In this case the mesh region GDEF is Eulerian and equal height elements are prescribed in region ABCG. The variation of the mass of the sample during the simulation is depicted in figure 5.8. The mass gain is less than 1% at the end of the simulation. The error is a bit larger than for the top punch test. This indicates that the convective effects are more important in this case.

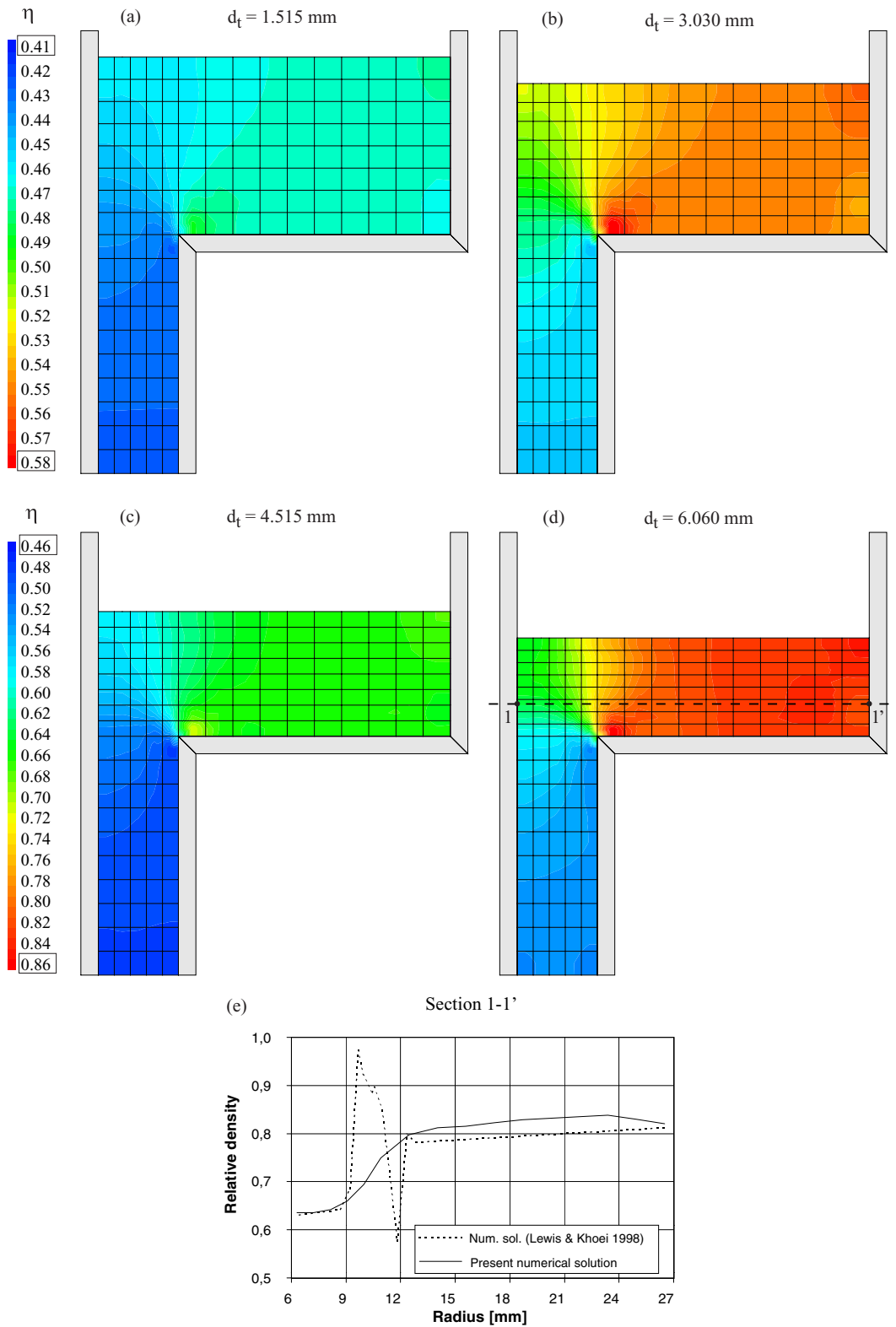


Figure 5.9: Top punch compaction. (a-d) Relative density distribution for different top punch movements and (e) relative density profile at 1.88 mm from line  $\overline{GD}$  (section 1-1').

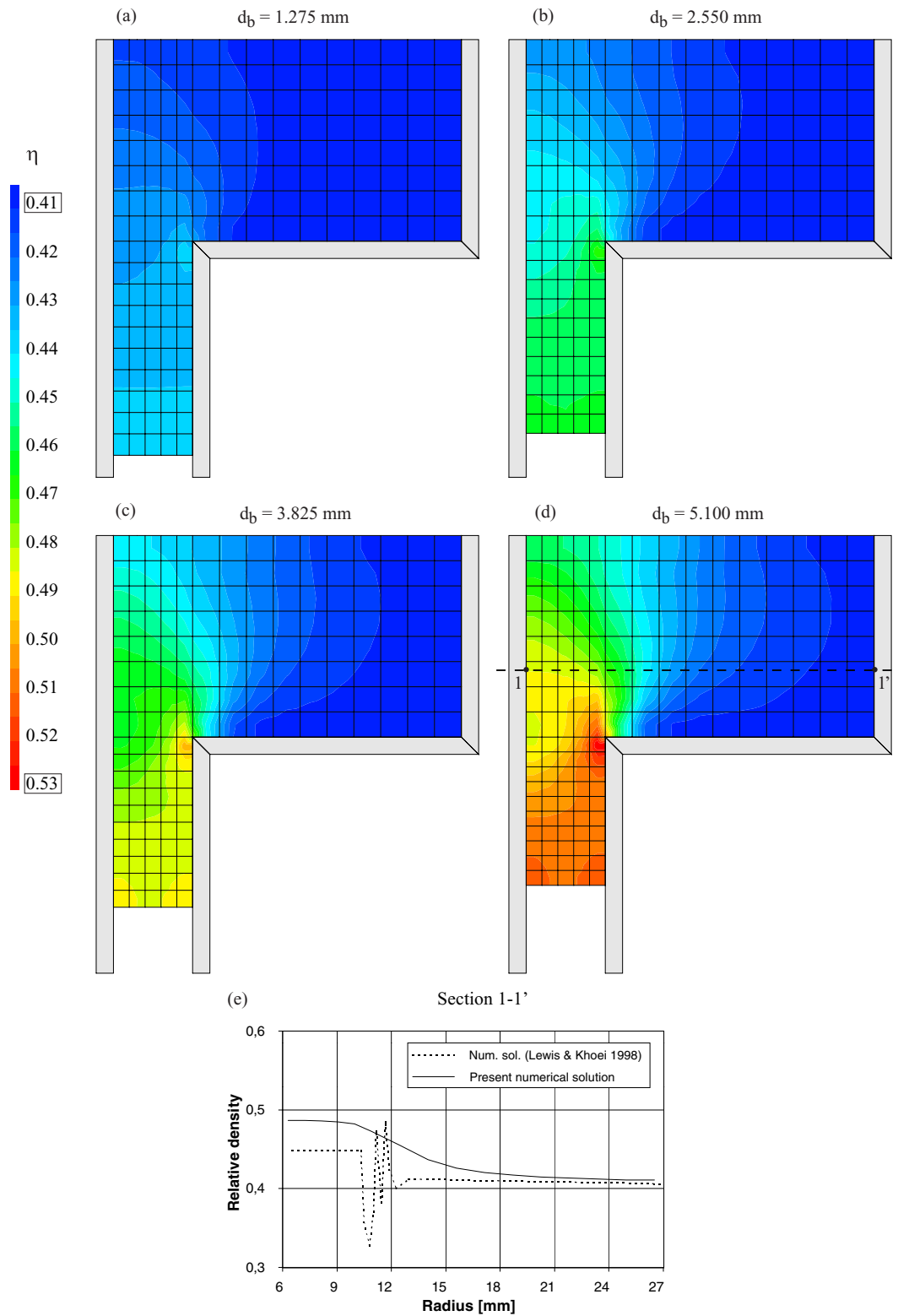


Figure 5.10: Bottom punch compaction. (a-d) Relative density distribution for different bottom punch movements and (e) relative density profile at 3.9 mm from line  $\overline{GD}$  (section 1-1').

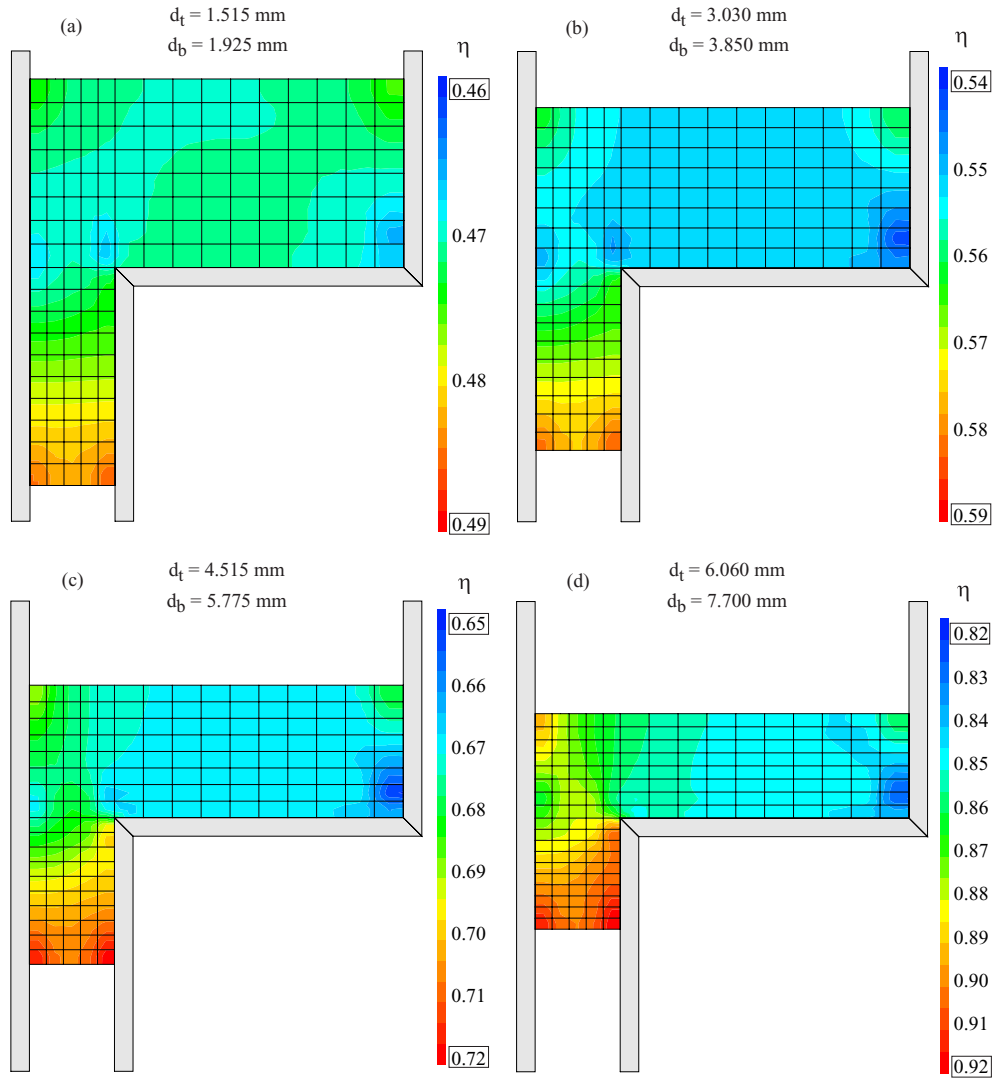


Figure 5.11: Double-punch compaction. Relative density distribution for different movements of the top and bottom punches.

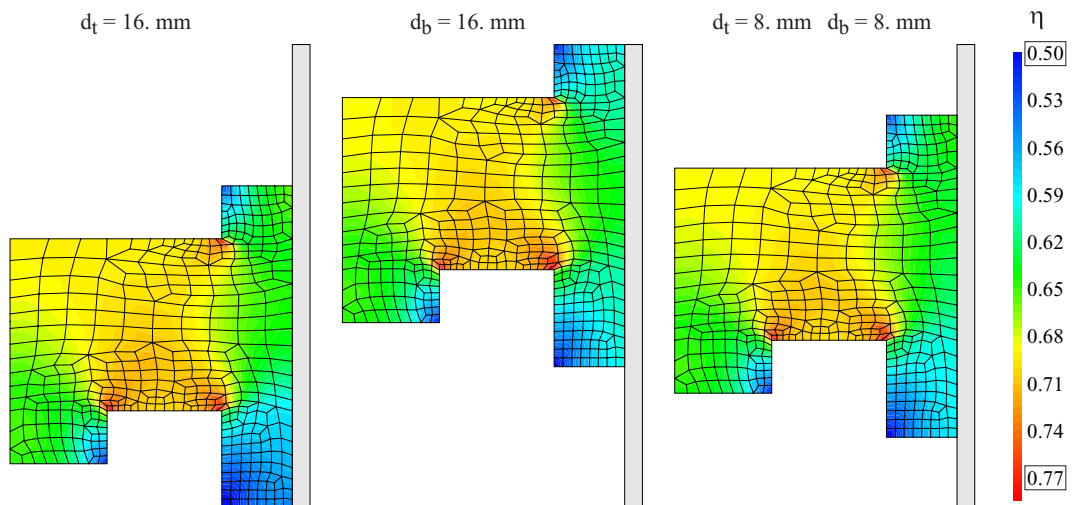


Figure 5.12: Multi-level component. Relative density distribution for three different compaction processes.



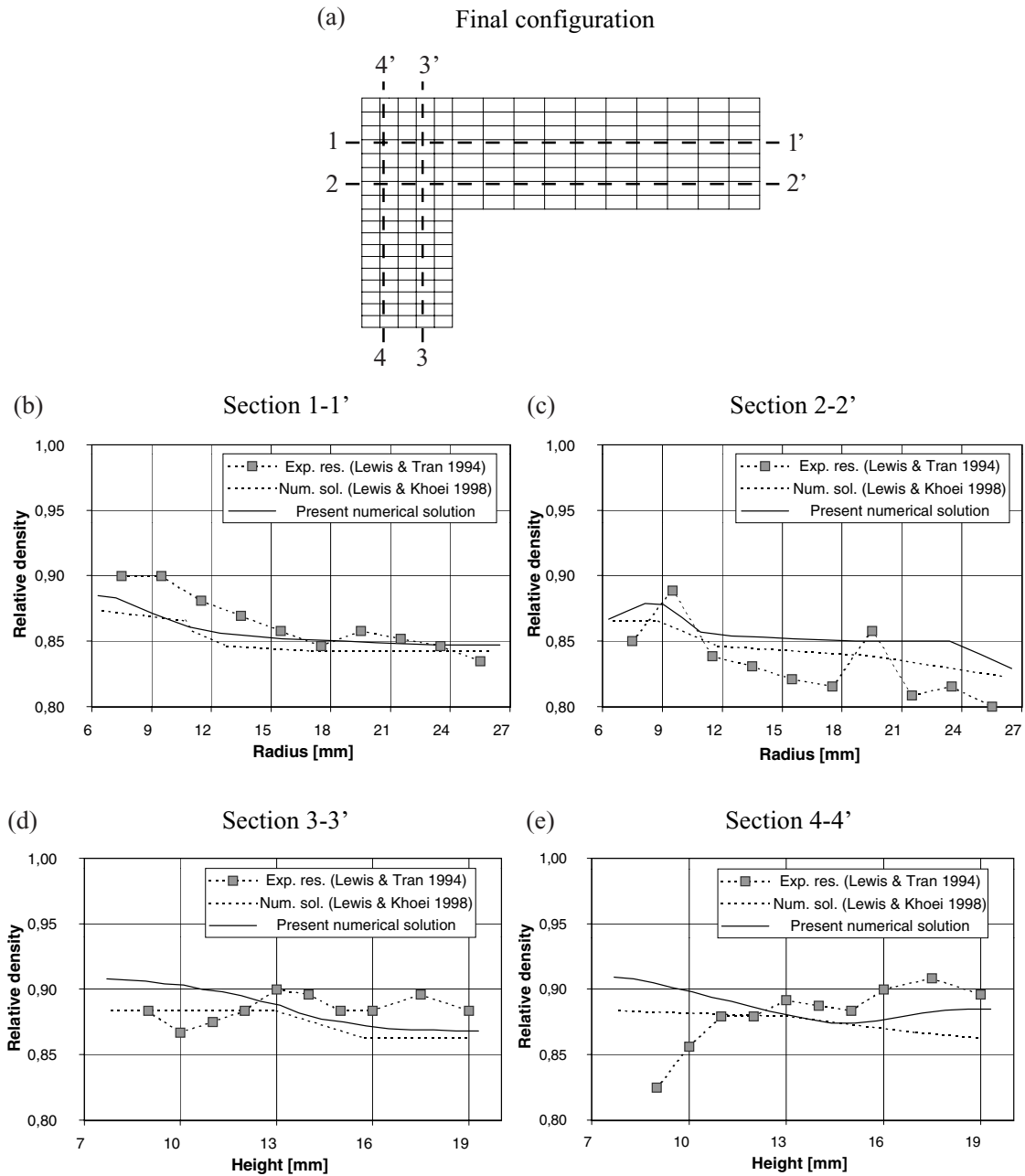


Figure 5.13: Double-punch compaction. Relative density profiles at 3.47 mm (section 1-1') and 1.3 mm (section 2-2') from the line  $\overline{GD}$ , and at radii equal to 9.37 mm (section 3-3') and 8.77 mm (section 4-4').

The evolution of the relative density distribution is summarized in figures 5.10(a-d). The expected values are obtained: higher densities in the lower part of the sample and lower densities in the outer part. A dense zone is detected in the corner region, just in the left side of point C, during all the process. This result agrees with the simulation of the top punch compaction (note that in this case the mass flux has the opposite direction). However, on the contrary of the top punch compaction, the dense zone extends in the mass flux direction. This can be related with the higher convective behaviour of the problem and the different mass flow pattern.

The final relative density profile at 3.9 mm from line  $\overline{GD}$  is depicted in figure 5.10(e). The numerical results presented by Lewis and Khoei (1998) are included in the same figure. Both simulations lead to similar values in outer and inner parts of the sample. The main difference between both is the presence of oscillations in the results of Lewis and Khoei (1998).

In the third test, the compaction of the flanged component is performed by a simultaneous top

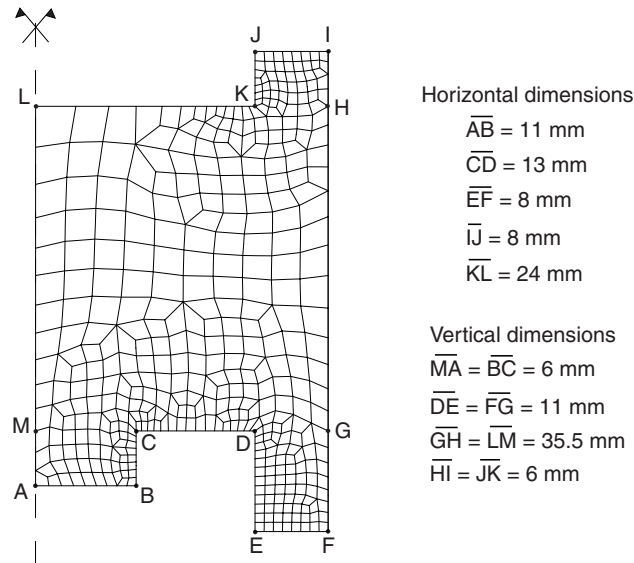


Figure 5.14: Multi-level component. Problem definition (after Khoei and Lewis 1999) and computational mesh.

and bottom punch movement. This process leads to a relatively uniform final density distribution (Lewis and Tran 1994, Lewis and Khoei 1998). Although in this case the Lagrangian formulation does not lead to excessive mesh distortion, the ALE approach has also been used. Equal height elements are prescribed in regions GDEF and ABCG. The variation of the mass of the sample during the simulation is depicted in figure 5.8. The relative error of the sample mass at the end of the test is approximately 0.3%. This is the lowest value of the three tests. This is directly related with the lower convective effects of the double-punch compaction process.

The evolution of the relative density distribution is summarized in figure 5.11. The distributions at four load levels (0.25, 0.5, 0.75 and 1) are depicted in figures 5.11(a–d). The compaction process leads to a quasi-homogeneous density distribution during all the test, with differences less than 10%. Higher values are found in the bottom of the sample and lower values close to point D. Four relative density profiles are depicted in figure 5.13. The numerical results presented by Lewis and Khoei (1998) and the experimental data of Lewis and Tran (1994) are included in the same figure. All these results are in good agreement.

*Remark 5.3.1.* As shown in the previous paragraphs, the ALE approach is essential in order to obtain accurate results. Moreover, if compared to Lagrangian formulations, the ALE approach significantly improves the convergence properties of the incremental-iterative scheme that is used to solve the boundary value problem. This additional feature of the ALE formulation is directly related with the uncoupling between particle and mesh movements, which reduces the degree of ill-conditioning of contact-friction problems.  $\square$

### 5.3.4 A multi-level component

The last example demonstrates the performance of the ALE formulation for the complicated die geometry of a multi-level component shown in figure 5.14. This geometry is used by Khoei and Lewis (1999) to show the applicability of an  $h$ -adaptive remeshing technique. It is included here to show that the ALE formulation also works with unstructured meshes. The material parameters of the two previous examples, powder-C, are used (see table 5.2).

An unstructured mesh of 410 eight-noded elements with reduced integration (four Gauss points per element) is used. The die wall friction is simulated with a Coulomb friction coefficient  $\mu = 0.08$  acting in the segment  $\overline{FI}$ . The radial displacement of top and bottom punches is set equal to zero. The symmetry conditions at the segment  $\overline{LA}$  imply a radial displacement equal to zero and free vertical movement.

Three different compaction tests are simulated: 1) a vertical movement of 16 mm of the top

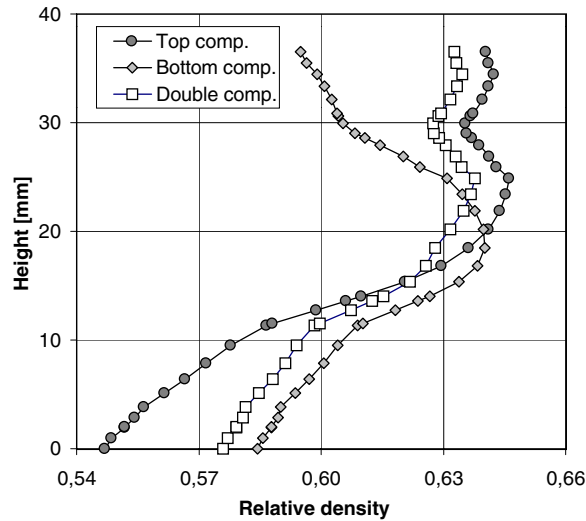


Figure 5.15: Multi-level component. Relative density profile at radius equal to 30 mm for the three different compaction processes.

punch (segments  $\overline{IJ}$ ,  $\overline{JK}$  and  $\overline{KL}$  of figure 5.14); 2) a vertical movement of 16 mm of the bottom punch (segments  $\overline{AB}$ ,  $\overline{BC}$ ,  $\overline{CD}$ ,  $\overline{DE}$  and  $\overline{EF}$ ); and 3) a simultaneous, and opposite, movement of 8 mm of both punches. The three compaction tests leads to the same final geometry.

The movement of the mesh is prescribed in the same way in the three tests. In the mesh regions ABCM and DEFG the mesh nodes are moved vertically the same as the bottom punch, and in the region HIJK the same as the top punch. In the central part of the sample, region MGHL, the vertical movement of the nodes is linearly interpolated between top and bottom movements. The radial movement of all nodes is restrained. Low relative errors of sample mass are found in the three tests. The maximum mass reductions have been found at the end of the tests. They are 0.20% for top compaction, 0.19% for bottom compaction and 0.17% for double-punch compaction.

The final relative density distributions of the three cases are depicted in figure 5.12. As expected, the results are similar and the influence of the compaction process is basically restricted to the top and bottom parts close to the die wall. The final relative density distributions are similar to those presented by Khoei and Lewis (1999). However, as in the previous examples, the present results do not present spurious oscillations. Moreover, the quantitative values of the relative density, which are lower than those presented by Khoei and Lewis (1999), are validated by the verification of the mass conservation principle.

The relative density profiles at 2 millimeters of the die wall (line  $\overline{FI}$ ) are depicted in figure 5.15. In the three tests, the influence of the non-uniform shape of the punches is clear. The difference between the shape of top and bottom punches is also reflected in these curves: in both tests involving top punch compaction the upper part has a quasi-uniform distribution, on the contrary of the lower part, where large density differences are found even in the bottom punch compaction test. This different behaviour is directly related with the different height of the indentations of both punches. On the other hand, note that the double-punch compaction curve gathers the main characteristics of top and bottom compaction curves, in its upper and lower halves respectively.

## 5.4 Concluding remarks

Several powder compaction problems have been simulated in this chapter. The powder material has been modelled with a isotropic finite strain density-dependent plastic model and the powder-die friction with the Coulomb dry friction model. An ALE formulation has been used to avoid the excessive mesh distortion characteristic of this type of problems.

The elastoplastic model consists in the hyperelastic Hecky's law and an elliptic yield function

expressed in terms of the relative density and the Kirchhoff stresses (Oliver et al. 1996). In contrast with previous applications of this plastic model, large elastic and plastic strains are considered here. Different simple tests (i.e. involving rectangular axisymmetric domains) have been simulated using a Lagrangian kinematic description. The results obtained agree with the numerical and experimental data available. Therefore, the proposed approach including large elastic strains is valid for powder compaction modelling. Moreover, it has been shown that the mass conservation principle is verified exactly in Lagrangian examples because of the complete kinematic description of the deformation process and the material version of the conservation principle (which does not need an approximation for time-integration).

The ALE formulation presented in section 2.2 (Rodríguez-Ferran et al. 2000) has been applied to several examples involving sharp boundaries and large mass fluxes between different parts of the sample. Time-integration of the ALE constitutive equations is performed in two phases: Lagrangian and convective. The Lagrangian phase is solved with the standard return mapping algorithm based on the exponential mapping and the convective one with an explicit Godunov-type scheme (Rodríguez-Ferran et al. 1998). A relative movement of the mesh with respect to the material particles is applied between the two phases with the goal of ensuring the good quality of the mesh during all the problem. Here, only the Lagrangian phase is computed during the iterative process for equilibrium. The remeshing and the convective phase are computed once per load increment, with the converged results. The use of simple remeshing techniques (as those used here with structured and unstructured meshes) and the explicit character of the Godunov-type scheme guarantee a low computational overhead of the proposed ALE approach with respect the standard Lagrangian formulation.

On the other hand, the efficiency of the proposed approach is complemented with the high accuracy of its results. In the ALE examples, the mass conservation principle has been verified with very low relative errors (less than 1% for all compaction processes). This represents a significant improvement with respect to previous results based on non-adaptive and  $h$ -adaptive Lagrangian approaches found in the literature. Because of the higher computational performance of the present approach, it has been possible to perform some detailed analysis in different tests, as the study of the location of high-density and low-density regions or the influence of sharp punches in the density distribution. Moreover, the present results agree with the experimental data available and the relative density distributions do not present spurious oscillations, even in compaction tests involving high convective effects.

## Chapter 6

# Summary and future developments

As stated in the introduction, the three main topics covered in this report are actual research fields. Different analyses and new developments related with these fields have been presented in the previous chapters. In the following, after a brief summary of the contributions, some directions for future research are outlined. Detailed presentations of the conclusions of each contribution are included in the corresponding sections and subsections.

The most relevant contributions of this report are the following.

1. With respect to the treatment of large boundary displacements:
  - ▷ Quasistatic and dynamic analyses of the vane test for soft materials using a fluid-based ALE formulation and different non-newtonian constitutive laws.
  - ▷ The development of a solid-based ALE formulation for finite strain hyperelastic-plastic models, with applications to isochoric and non-isochoric cases.
2. Referent to the solution of nonlinear systems of equations in solid mechanics:
  - ▷ The use of simple and robust numerical differentiation schemes for the computation of tangent operators, including examples with several non-trivial elastoplastic constitutive laws.
  - ▷ The development of consistent tangent operators for substepping time-integration rules, with the application to an adaptive time-integration scheme.
3. In the field of constitutive modelling of granular materials:
  - ▷ The efficient numerical modelling of different problems involving elastoplastic models, including work hardening-softening models for small-strain problems and density-dependent hyperelastic-plastic models in a large-strain context.
  - ▷ Robust and accurate simulations of several powder compaction processes, with detailed analysis of spatial density distributions and verification of the mass conservation principle.

Generally speaking and from a numerical modelling point of view, future lines of research related with complex geomechanical problems may go in the following three directions:

- ★ Apply specific adaptive schemes, both temporally and spatially, to problems involving regularized models for failure analysis of granular materials. These schemes should include the definition of proper error indicators and the application of goal-oriented accuracy analyses based on error estimation.

- ★ Develop efficient optimization algorithms for powder compaction problems. One of the main goals of powder compaction simulations is the definition of punch movements that lead to uniform final density distributions. An optimization scheme may help in the definition of real industrial processes.
- ★ And finally, in a more general context, devise robust, efficient and accurate algorithms for coupled thermo–hydro–geomechanical problems, including the definition of specific adaptive schemes to handle large scale problems.

# Bibliography

- Aas, G. (1965), ‘A study of the effect of vane shape and rate of strain on the measured values of in-situ shear strength of clays’, *Proc. 6th Int. Conf. Soil Mech. Found. Engrg.* **1**, 141–145.
- Abbo, A. J. and Sloan, S. W. (1995), ‘A smooth hyperbolic approximation to the Mohr–Coulomb yield criterion’, *Computers and Structures* **54**(3), 427–441.
- Abbo, A. J. and Sloan, S. W. (1996), ‘An automatic load stepping algorithm with error control’, *International Journal for Numerical Methods in Engineering* **39**, 1737–1759.
- Alawaji, H., Runesson, K. and Sture, S. (1992), ‘Implicit integration in soil plasticity under mixed control for drained and undrained response.’, *International Journal for Numerical and Analytical Methods in Geomechanics* **16**, 737–756.
- Alfano, G., Rosati, L. and Valoroso, N. (1999), ‘A tangent–secant approach to rate–independent elastoplasticity: formulations and computational issues’, *Computer Methods in Applied Mechanics and Engineering* **179**, 379–405.
- Armero, F. (1999), ‘Formulation and finite element implementation of a multiplicative model of couple poro–plasticity at finite strains under fully saturated conditions’, *Computer Methods in Applied Mechanics and Engineering* **171**, 205–241.
- Armero, F. and Love, E. (2000), An arbitrary Lagrangian-Eulerian (ALE) finite element method for finite strain elasto–plasticity, Technical Report No. UCB/SEMM-2000/04, Dept. of Civil and Environmental Engineering, University of California, Berkeley, California.
- Armero, F. and Pérez-Foguet, A. (2000), On the Formulation of Closest-Point Projection Algorithms in Elastoplasticity. Part I: The Variational Structure. Submitted for publication to *International Journal for Numerical Methods in Engineering*.
- Askes, H. (2000), Advanced spatial discretization strategies for localised failure. Mesh adaptivity and meshless methods., PhD thesis, Delft University of Technology.
- Askes, H., Rodríguez-Ferran, A. and Huerta, A. (1998), ‘Adaptive analysis of yield line patterns in plates with the arbitrary Lagrangian-Eulerian method’, *Computers and Structures* **70**, 257–271.
- ASTM-D2573-72 (1993), Standard Test Method for Field Vane Shear Test in Cohesive Soil, in ‘Annual book of ASTM standards’, Vol. 04.08, ASTM, Philadelphia, pp. 346–348.
- Aydin, I., Briscoe, B. J. and Sanliturk, K. Y. (1996), ‘The internal form of compacted ceramic components. A comparison of a Finite–Element modelling with experiment’, *Powder Technology* **89**(3), 239–254.
- Azzouz, A. S., Baligh, M. M. and Ladd, C. C. (1983), ‘Corrected field vane strength for embankment design’, *Journal of Geotechnical Engineering* **109**(5), 730–734.
- Baaijens, F. (1993), ‘An U-ALE formulation of 3-D unsteady viscoelastic flow’, *International Journal for Numerical Methods in Engineering* **36**, 1115–1143.
- Barnes, H. A. and Walters, K. (1985), ‘The yield stress myth ?’, *Rheologica Acta* **24**, 323–326.

- Belytschko, T., Liu, W. and Moran, B. (2000), *Nonlinear Finite Elements for Continua and Structures*, Wiley.
- Benson, D. J. (1986), 'An efficient, accurate, simple ALE method for nonlinear finite element programs', *Computer Methods in Applied Mechanics and Engineering* **72**, 305–350.
- Bentley, S. P. (1979), 'Viscometric assessment of remoulded sensitive clays', *Canadian Geotechnical Journal* **16**, 414–419.
- Berre, T. and Bjerrum, L. (1973), 'Shear strength of normally consolidated clays', *Proc. 8th Int. Conf. Soil Mech. Found. Engrg.* **1**, 39–49.
- Bićanić, N. and Pearce, C. J. (1996), 'Computational aspects of a softening plasticity model for plain concrete', *Mechanics of Cohesive-Frictional Materials* **1**, 75–94.
- Bjerrum, L. (1973), 'Problems of Soil Mechanics and Construction on Soft Clays', *Proc. 8th Int. Conf. Soil Mech. Found. Engrg.* **3**, 111–159.
- Bonet, J. and Wood, R. D. (1997), *Nonlinear continuum mechanics for finite element analysis*, Cambridge University Press.
- Borja, R. I. and Alarcón, E. (1995), 'A mathematical framework for finite strain elastoplastic consolidation. Part I: Balance laws, variational formulation, and linearization', *Computer Methods in Applied Mechanics and Engineering* **122**, 145–171.
- Borja, R. I. and Alarcón, E. (1998), 'Elastoplastic consolidation at finite strain. Part II: Finite element implementation and numerical examples', *Computer Methods in Applied Mechanics and Engineering* **159**, 103–122.
- Borja, R. I. and Tamagnini, C. (1998), 'Cam–Clay plasticity. Part III: Extension of the infinitesimal model to include finite strains', *Computer Methods in Applied Mechanics and Engineering* **155**, 73–95.
- Borja, R. I. and Wren, J. R. (1995), 'Micromechanics of granular media. Part I: Generation of overall constitutive equation for assemblies of circular disks', *Computer Methods in Applied Mechanics and Engineering* **127**(1-4), 13–36.
- Brandt, J. and Nilsson, L. (1998), 'FE–Simulation of compaction and solid–state sintering of cemented carbides', *Mechanics of Cohesive-Frictional Materials* **3**(2), 181–205.
- Brandt, J. and Nilsson, L. (1999), 'A constitutive model for compaction of granular media, with account for deformation induced anisotropy', *Mechanics of Cohesive-Frictional Materials* **4**(4), 391–418.
- Callari, C., Auricchio, F. and Sacco, E. (1998), 'A finite–strain Cam–Clay model in the framework of multiplicative elasto–plasticity', *International Journal of Plasticity* **14**(12), 1155–1187.
- Cante, J. C., Oliver, J. and Hernández, R. (1999), Simulación numérica de las etapas de transferencia y prensado del proceso de compactación de pulvimateriales, in 'IV Congreso de Métodos Numéricos en Ingeniería', Eds. R. Abascal, J. Domínguez and G. Bugada, SEMNI, Spain.
- Cante, J. C., Oliver, J. and Oller, S. (1998), 'Simulación numérica de procesos de compactación de pulvimateriales. Parte 2: Validación y Aplicaciones Industriales', *Revista Internacional de Métodos Numéricos para Cálculo y Diseño en Ingeniería* **14**(1), 101–116.
- Chaboche, J. L. and Cailletaud, G. (1996), 'Integration methods for complex plastic constitutive equations', *Computer Methods in Applied Mechanics and Engineering* **133**, 125–155.
- Chandler, R. J. (1988), The in-situ measurement of the undrained shear strength of clays using the field vane, in 'Vane shear strength testing in soils: field and laboratory studies, ASTM STP 1014', ASTM, Philadelphia, pp. 117–128.



- Cheng, R. Y. K. (1981), Effect of shearing strain–rate on the undrained strength of clay, in ‘Laboratory shear strength of soil, ASTM STP 740’, Eds. R. N. Yong and F. C. Townsend, ASTM, Philadelphia, pp. 243–245.
- Crisfield, M. A. (1991), *Non-linear finite element analysis of solids and structures. 1 Essentials*, John Wiley & Sons, Chichester.
- Crisfield, M. A. (1997), *Non-linear finite element analysis of solids and structures. 2 Advanced topics*, John Wiley & Sons, Chichester.
- Cuitiño, A. and Ortiz, M. (1992), ‘A material–independent method for extending stress update algorithms from small–strain plasticity to finite plasticity with multiplicative kinematics’, *Engineering Computations* **9**, 437–451.
- de Alencar, J. A., Chan, D. H. and Morgenstern, N. R. (1988), Progressive failure in the vane test, in ‘Vane shear strength testing in soils: field and laboratory studies, ASTM STP 1014’, ASTM, Philadelphia, pp. 117–128.
- de Souza Neto, E. A., Perić, D. and Owen, D. R. J. (1994), ‘A model for elastoplastic damage at finite strains: algorithmic issues and applications’, *Engineering Computations* **11**, 257–281.
- Dennis, J. E. and Moré, J. J. (1977), ‘Quasi-newton methods, motivations and theory’, *SIAM Review* **19**, 46–89.
- Dennis, J. E. and Schnabel, R. B. (1983), *Numerical methods for unconstrained optimization and nonlinear equations*, Prentice-Hall, New Jersey. (Reprinted by Siam, Classics in Applied Mathematics, 1996).
- di Prisco, C., Nova, R. and Lanier, J. (1993), A mixed isotropic-kinematic hardening constitutive law for sand, in D. Kolymbas, ed., ‘Modern approaches to plasticity’, Elsevier, pp. 83–124.
- Donald, I. B., Jordan, D. O., Parker, R. J. and Toh, C. T. (1977), ‘The vane test – A critical appraisal’, *Proc. 9th Int. Conf. Soil Mech. Found. Engrg.* **1**, 81–88.
- Donea, J. (1983), Arbitrary Lagrangian-Eulerian finite element methods, in T. Belytschko and T. Hughes, eds, ‘Computational Methods for Transient Analysis’, North-Holland, pp. 473–516.
- Donéa, J., Fasoli-Stella, P. and Giuliani, S. (1977), Lagrangian and Eulerian Finite Element Techniques for Transient Fluid Structure Interaction Problems, in ‘Transactions of the 4th Int. Conference on Structural Mechanics in Reactor Technology’, paper B1/2, San Francisco.
- Dorémus, P., Geindreau, C., Martin, A., Lécot, R. and Dao, M. (1994), High pressure triaxial apparatus for investigating the mechanical behaviour of metal powders, in ‘Powder Metallurgy 94, World Congress’, Paris, pp. 733–736.
- Dorémus, P. and Toussaint, F. (2000), Simple tests standard procedure for the characterisation of green compacted powder. Institut National Polytechnique de Grenoble, Laboratoire Sols Solides Structures.
- Eden, W. J. and Law, K. T. (1980), ‘Comparison of undrained shear strength results obtained by different tests methods in soft clays’, *Canadian Geotechnical Journal* **17**, 369–381.
- Ernst, E. and Barnekow, D. (1994), Pressure, friction and density during axial powder compaction, in ‘Powder Metallurgy 94, World Congress’, Paris, pp. 673–676.
- Etse, G. and Willam, K. (1994), ‘Fracture energy formulation for inelastic behavior of plain concrete’, *Journal of Engineering Mechanics* **120**(9), 1983–2011.
- Garga, V. K. and Khan, M. A. (1994), ‘Evaluation of  $k_0$  and its influence on the field vane strength of overconsolidated soils’, *Proc. 13th Int. Conf. Soil Mech. Found. Engrg.* **1**, 157–162.
- Gethin, D. T. and Lewis, R. W. (1994), Finite element modelling of powder compaction and its experimental validation, in ‘Powder Metallurgy 94, World Congress’, Paris, pp. 689–692.

- Ghosh, S. and Kikuchi, N. (1991), 'An Arbitrary Lagrangian-Eulerian finite element method for large deformation analysis of elastic-viscoplastic solids', *Computer Methods in Applied Mechanics and Engineering* **86**, 127–188.
- Gili, J. A., Huerta, A. and Corominas, J. (1993), Contribution to the study of mass movements: mudflow slides and block fall simulations, Technical report, Pierre Beghin Int. Workshop on rapid gravitational mass movements, CEMAGREF, Grenoble.
- Goicolea, J. (1985), Numerical Modelling in Large Strain Plasticity with Application to Tube Collapse Analysis, PhD thesis, University of London.
- Griffiths, D. V. and Lane, P. A. (1990), 'Finite element analysis of the shear vane test', *Computers and Structures* **37**(6), 1105–1116.
- Hight, D. W., Jardine, R. J. and Gens, A. (1987), The behaviour of soft clays. Embankments on soft clays., Technical Report 40007-1, Special Publication, Bulletin of the Public Works Research Center of Greece, Norway.
- Hoffman, J. D. (1982), *Numerical methods for engineers and scientists*, Prentice-Hall, New Jersey.
- Hofstetter, G., Simo, J. C. and Taylor, R. L. (1993), 'A modified cap model: closest point solution algorithms.', *Computers and Structures* **46**(2), 203–214.
- Huerta, A. and Casadei, F. (1994), 'New ALE applications in non-linear fast-transient solid dynamics', *Engineering Computations* **11**, 317–345.
- Huerta, A., Casadei, F. and Donea, J. (1995), ALE stress update in transient plasticity problems, in 'Proceedings of the Fourth International Conference on Computational Plasticity (COMPLAS IV)', Vol. 2, pp. 1865–1876.
- Huerta, A. and Liu, W. K. (1988), 'Viscous Flow with Large Free Surface Motion', *Computer Methods in Applied Mechanics and Engineering* **69**, 277–324.
- Huerta, A., Rodríguez-Ferran, A., Díez, P. and Sarrate, J. (1999), 'Adaptive finite element strategies based on error assessment', *International Journal for Numerical Methods in Engineering* **46**, 1803–1818.
- Huétink, J., Vreede, P. and van der Lugt, J. (1990), 'Progress in mixed Eulerian-Lagrangian finite element simulation of forming processes', *International Journal for Numerical Methods in Engineering* **30**, 1441–1457.
- Hughes, T. J. R., Liu, W. K. and Zimmermann, T. K. (1981), 'Lagrangian-Eulerian finite element formulation for incompressible viscous flows', *Computer Methods in Applied Mechanics and Engineering* **29**, 329–349.
- Isaacson, E. and Keller, H. B. (1966), *Analysis of numerical methods*, Constable and Company, London. (Reprinted by Dover Publications, 1994).
- Jeremić, B. and Sture, S. (1994), Implicit integrations rules in plasticity: Theory and implementation, Technical report, Report to NASA Marshall Space Flight Center, Contract: NAS8-38779, University of Colorado at Boulder.
- Jeremić, B. and Sture, S. (1997), 'Implicit integrations in elastoplastic geotechnics', *Mechanics of Cohesive-Frictional Materials* **2**, 165–183.
- Jinka, A. G. K., Bellet, M. and Fourment, L. (1997), 'A new three-dimensional finite element model for the simulation of powder forging processes: Application to hot forming of P/M connecting rod', *International Journal for Numerical Methods in Engineering* **40**, 3955–3978.
- Keentok, M., Milthorpe, J. F. and O'Donovan, E. (1985), 'On the shearing zone around rotating vanes in plastic liquids: theory and experiment', *Journal of Non-Newtonian Fluid Mechanics* **17**, 23–35.

- Khan, A. S. and Huang, S. (1995), *Continuum theory of plasticity*, John Wiley & Sons, New York.
- Khoei, A. R. and Lewis, R. W. (1999), 'Adaptive finite element remeshing in a large deformation analysis of metal powder forming', *International Journal for Numerical Methods in Engineering* **45**, 801–820.
- Kim, M. K. and Lade, P. V. (1988), 'Single hardening constitutive model for frictional materials. i plastic potential function', *Computers and Geotechnics* **5**, 307–324.
- Kimura, T. and Saitoh, K. (1983), 'Effect of disturbance due to insertion on vane shear strength of normally consolidated cohesive soils', *Soils and Foundations* **23**(2), 113–124.
- Kirkpatrick, W. M. and Khan, A. J. (1981), 'Interpretation of the vane test', *Proc. 10th Int. Conf. Soil Mech. Found. Engrg.* **2**, 501–506.
- Kirkpatrick, W. M. and Khan, A. J. (1984), 'The influence of stress relief on the vane strength of clays', *Géotechnique* **34**(3), 428–432.
- Komamura, F. and Huang, R. J. (1974), 'New rheological model for soil behaviour', *Journal of Geotechnical Engineering* **100**(7), 807–824.
- Lacasse, S. (1979), Effect of load duration on undrained behaviour of clay and sand — literature survey, Technical Report 40007-1, NGI Internal report, Norway.
- Ladd, C. C. and Foott, R. (1974), 'New design procedure for stability of soft clays', *Journal of Geotechnical Engineering* **100**(7), 763–786.
- Lade, P. V. (1989), 'Experimental observations of stability, and shear planes in granular materials.', *Ingenieur Archiv* **59**, 114–123.
- Lade, P. V. (1994), 'Instability and liquefaction of granular materials.', *Computers and Geotechnics* **16**, 123–151.
- Lade, P. V. and Duncam, J. M. (1975), 'Elastoplastic stress-strain theory for cohesionless soil.', *Journal of Geotechnical Engineering* **101**(10), 1037–1053.
- Lade, P. V. and Kim, M. K. (1988*a*), 'Single hardening constitutive model for frictional materials. II Yield criterion and plastic work contours', *Computers and Geotechnics* **6**, 13–29.
- Lade, P. V. and Kim, M. K. (1988*b*), 'Single hardening constitutive model for frictional materials. iii comparisons with experimental data', *Computers and Geotechnics* **6**, 31–47.
- Landva, A. O. (1980), 'Vane testing in peat', *Canadian Geotechnical Journal* **17**(1), 1–19.
- Larsson, R. and Runesson, K. (1996), 'Implicit integration and consistent linearization for yield criteria of the mohr-coulomb type.', *Mechanics of Cohesive-Frictional Materials* **1**, 367–383.
- Law, K. T. (1979), 'Triaxial-vane tests on a soft marine clay', *Canadian Geotechnical Journal* **16**, 11–18.
- Leroueil, S., Kabbaj, M., Tavenas, F. and Bouchard, R. (1985), 'Stress-strain-strain rate relation for the compressibility of sensitive natural clays', *Géotechnique* **35**(2), 159–180.
- Lewis, R. W. and Khoei, A. R. (1998), 'Numerical modelling of large deformation in metal powder forming', *Computer Methods in Applied Mechanics and Engineering* **159**, 291–328.
- Lewis, R. W. and Tran, D. V. (1994), 'Finite element approach to problems in particulate media with special reference to powder metal forming', *Bull. Tech. Univ. Istanbul* **47**, 295–310.
- Li, X. (1995), 'Large strain constitutive modelling and computation for isotropic, creep elastoplastic damage solids', *International Journal for Numerical Methods in Engineering* **38**, 841–860.
- Liu, W. K., Belytschko, T. and Chang, H. (1986), 'An Arbitrary Lagrangian-Eulerian finite element method for path-dependent materials', *Computer Methods in Applied Mechanics and Engineering* **58**, 227–245.

- Locat, J. and Demers, D. (1988), 'Viscosity, yield stress, remolded strength, and liquidity index relationships for sensitive clays', *Canadian Geotechnical Journal* **25**, 799–806.
- Lubliner, J. (1990), *Plasticity theory*, Macmillan Publishing Company, New York.
- Lyness, J. N. and Moler, C. B. (1967), 'Numerical differentiation of analytic functions', *SIAM Journal of Numerical Analysis* **4**, 202–210.
- Macari, E. J., Runesson, K. and Sture, S. (1994), 'Response prediction of granular materials at low effective stresses', *Journal of Geotechnical Engineering* **120**, 1252–1268.
- Macari, E. J., Weihe, S. and Arduino, P. (1997), 'Implicit integration of elastoplastic constitutive models for frictional materials with highly non-linear hardening functions', *Mechanics of Cohesive-Frictional Materials* **2**, 1–29.
- Matsui, T. and Abe, N. (1981), 'Shear mechanisms of vane test in soft clays', *Soils and Foundations* **21**, 69–80.
- Menschke, G. and Liu, W. N. (1999), 'A re-formulation of the exponential algorithm for finite strain plasticity in terms of cauchy stresses', *Computer Methods in Applied Mechanics and Engineering* **173**, 167–187.
- Menzies, B. K. and Merrifield, C. M. (1980), 'Measurements of shear stress distribution on the edges of a shear vane blade', *Géotechnique* **30**, 314–318.
- Meschke, G., Liu, C. and Mang, H. A. (1996), 'Large strain finite-element analysis of snow', *Journal of Engineering Mechanics* **122**(7), 591–602.
- Mesri, G., Febres-Cordero, E., Shields, D. R. and Castro, A. (1981), 'Shear stress-strain-time behaviour of clays', *Géotechnique* **31**(4), 537–552.
- Miehe, C. (1996), 'Numerical computation of algorithmic (consistent) tangent moduli in large-strain computational inelasticity', *Computer Methods in Applied Mechanics and Engineering* **134**, 223–240.
- Miehe, C. (1998), 'A formulation of finite elastoplasticity based on dual co- and contra-variant eigenvector triads normalized with respect to a plastic metric', *Computer Methods in Applied Mechanics and Engineering* **159**, 223–260.
- Morris, P. H. and Williams, D. J. (1993), 'A new model of vane shear strength testing in soils', *Géotechnique* **43**(3), 489–500.
- Morris, P. H. and Williams, D. J. (1994), 'Effective stress vane shear strength correction factor correlations', *Canadian Geotechnical Journal* **31**, 335–342.
- Nguyen, Q. D. and Boger, D. V. (1983), 'Yield stress measurement for concentrated suspensions', *Journal of Rheology* **27**, 321–349.
- Nguyen, Q. D. and Boger, D. V. (1985), 'Thixotropic behaviour of concentrated bauxite residue suspensions', *Rheologica Acta* **24**, 427–437.
- Nova, R. and Wood, D. M. (1979), 'A constitutive model for sand in triaxial compression.', *International Journal for Numerical and Analytical Methods in Geomechanics* **3**, 255–278.
- Oliver, J., Oller, S. and Cante, J. C. (1992), Numerical simulation of uniaxial compaction processes in powder materials, in 'Proceedings of the International Congress on Numerical Methods in Engineering and Applied Sciences', Chile, pp. 1277–1286.
- Oliver, J., Oller, S. and Cante, J. C. (1996), 'A plasticity model for simulation of industrial powder compaction processes', *International Journal of Solids and Structures* **33**(20–22), 3161–3178.
- Ortiz, M. and Martin, J. B. (1989), 'Symmetry-preserving return mapping algorithms and incrementally extremal paths: a unification of concepts', *International Journal for Numerical Methods in Engineering* **28**, 1839–1853.

- Ortiz, M. and Popov, E. P. (1985), ‘Accuracy and stability of integration algorithms for elastoplastic constitutive relations’, *International Journal for Numerical Methods in Engineering* **21**, 1561–1576.
- Osipov, V. I., Nikolaeva, S. K. and Sokolov, V. N. (1984), ‘Microstructural changes associated with thixotropic phenomena in clay soils’, *Géotechnique* **34**(2), 293–303.
- Owen, D. R. J., Perić, D., de Souza Neto, E. A., Yu, J. and Dutko, M. (1995), Advanced computational strategies for 3D large scale metal forming simulations, in ‘NUMIFORM. Simulation of Materials Processing: Theory, Methods and Applications.’, Enschede, Netherlands, pp. 7–22.
- Pérez-Foguet, A. and Armero, F. (2000), On the Formulation of Closest-Point Projection Algorithms in Elastoplasticity. Part II: Globally Convergent Schemes. Submitted for publication to *International Journal for Numerical Methods in Engineering*.
- Pérez-Foguet, A. and Huerta, A. (1999), ‘Plastic flow potential for the cone region of the MRS–Lade model’, *Journal of Engineering Mechanics* **125**(3), 364–367.
- Pérez-Foguet, A., Ledesma, A. and Huerta, A. (1999), ‘Analysis of the vane test considering size and time effects’, *International Journal for Numerical and Analytical Methods in Geomechanics* **23**, 383–412.
- Pérez-Foguet, A. and Rodríguez-Ferran, A. (1999), The MRS-Lade model for cohesive materials. Submitted for publication to *Mechanics of Cohesive-Frictional Materials*.
- Pérez-Foguet, A., Rodríguez-Ferran, A. and Huerta, A. (2000a), Arbitrary Lagrangian Eulerian simulation of powder compaction processes with density–dependent plastic models. Submitted for publication to *International Journal for Numerical Methods in Engineering*.
- Pérez-Foguet, A., Rodríguez-Ferran, A. and Huerta, A. (2000b), Consistent tangent matrices for density–dependent finite plasticity models. Submitted for publication to *Mechanics of Cohesive-Frictional Materials*.
- Pérez-Foguet, A., Rodríguez-Ferran, A. and Huerta, A. (2000c), Consistent tangent matrices for substepping schemes. To appear in *Computer Methods in Applied Mechanics and Engineering*.
- Pérez-Foguet, A., Rodríguez-Ferran, A. and Huerta, A. (2000d), ‘Numerical differentiation for local and global tangent operators in computational plasticity’, *Computer Methods in Applied Mechanics and Engineering* **189**, 277–296.
- Pérez-Foguet, A., Rodríguez-Ferran, A. and Huerta, A. (2000e), ‘Numerical differentiation for non-trivial consistent tangent matrices: an application to the MRS–Lade model’, *International Journal for Numerical Methods in Engineering* **48**, 159–184.
- Perić, D. and de Souza Neto, E. A. (1999), ‘A new computational model for Tresca plasticity at finite strains with an optimal parametrization in the principal space’, *Computer Methods in Applied Mechanics and Engineering* **171**, 463–489.
- Perić, D., Owen, D. R. J. and Honnor, M. E. A. (1992), ‘A model for finite strain elasto–plasticity based on logarithmic strains: computational issues’, *Computer Methods in Applied Mechanics and Engineering* **94**, 35–61.
- Perlow, M. and Richards, A. F. (1977), ‘Influence of shear velocity on vane shear strength’, *Journal of Geotechnical Engineering* **103**(1), 19–32.
- Pijaudier-Cabot, G., Bodé, L. and Huerta, A. (1995), ‘Arbitrary Lagrangian–Eulerian finite element analysis of strain localization in transient problems’, *International Journal for Numerical Methods in Engineering* **38**, 4171–4191.
- Potts, D. M. and Ganendra, D. (1994), ‘An evaluation of substepping and implicit stress point algorithms’, *Computer Methods in Applied Mechanics and Engineering* **119**, 341–354.

- Potts, D. M. and Gens, A. (1985), 'A critical assessment of methods of correcting for drift from the yield surface in elasto-plastic finite element analysis', *International Journal for Numerical and Analytical Methods in Geomechanics* **9**, 149–159.
- Pramono, E. and Willam, K. (1989a), 'Fracture energy-based plasticity formulation of plain concrete', *Journal of Engineering Mechanics* **115**(6), 1183–1204.
- Pramono, E. and Willam, K. (1989b), 'Implicit integration of composite yield surfaces with corners', *Engineering Computations* **6**, 186–197.
- Ragab, A. R. and Saleh, C. A. R. (1999), 'Evaluation of constitutive models for voided solids', *International Journal of Plasticity* **15**, 1041–1065.
- Ramm, E. and Matzenmiller, A. (1988), 'Consistent linearization in elasto-plastic shell analysis', *Engineering Computations* **5**, 289–299.
- Rickenmann, D. (1991), 'Hyperconcentrated flow and sediment transport at steep slopes', *Journal of Hydraulical Engineering* **117**(11), 1419–1439.
- Rochelle, P. L., Roy, M. and Tavenas, F. (1973), 'Field measurements of cohesion in Champlain clays', *Proc. 8th Int. Conf. Soil Mech. Found. Engrg.* **1**, 229–236.
- Rodríguez-Ferran, A., Casadei, F. and Huerta, A. (1998), 'ALE Stress Update for Transient and Quasistatic Processes', *International Journal for Numerical Methods in Engineering* **43**, 241–262.
- Rodríguez-Ferran, A., Pérez-Foguet, A. and Huerta, A. (2000), Arbitrary Lagrangian–Eulerian (ALE) formulation for hyperelastoplasticity. Submitted for publication to *International Journal for Numerical Methods in Engineering*.
- Roy, M. and Leblanc, A. (1988), Factors affecting the measurements and interpretation of the vane strength in soft sensitive clays, in 'Vane shear strength testing in soils: field and laboratory studies, ASTM STP 1014', ASTM, Philadelphia, pp. 117–128.
- Rudnicki, J. and Rice, J. (1975), 'Conditions for the localization of deformation in pressure-sensitive dilatant materials', *Journal of the Mechanics and Physics of Solids* **23**, 371–394.
- Runesson, K. (1987), 'Implicit integration fo elastoplastic relations with reference to soils.', *International Journal for Numerical and Analytical Methods in Geomechanics* **11**, 315–321.
- Runesson, K. and Larsson, R. (1993), 'Properties of incremental solutions for dissipative material', *Journal of Engineering Mechanics* **119**(4), 647–666.
- Runesson, K., Samuelsson, A. and Bernspang, L. (1986), 'Numerical technique in plasticity including solution advancement control', *International Journal for Numerical Methods in Engineering* **22**, 769–788.
- Runesson, K., Sture, S. and Willam, K. (1988), 'Integration in computational plasticity', *Computers and Structures* **30**(1/2), 119–130.
- Shinohara, K., Oida, M. and Golman, B. (2000), 'Effect of particle shape on angle of internal friction by triaxial compression test', *Powder Technology* **107**, 131–136.
- Silvestri, V., Aubertin, M. and Chapuis, R. (1993), 'A study of undrained shear strength using various vanes', *Geotechnical Testing Journal* **16**(2), 228–237.
- Simo, J. C. (1988), 'A framework for finite strain elastoplasticity based on maximum plastic dissipation and the multiplicative decomposition: Part II. Computational aspects', *Computer Methods in Applied Mechanics and Engineering* **68**, 1–31.
- Simo, J. C. (1992), 'Algorithms for static and dynamic multiplicative plasticity that preserve the classical return mapping schemes of the infinitesimal theory', *Computer Methods in Applied Mechanics and Engineering* **99**, 61–112.

- Simo, J. C. (1998), Numerical analysis and simulation of plasticity, in 'Handbook of Numerical Analysis', Vol. VI, Eds. P. G. Ciarlet and J. L. Lions, Elsevier, Amsterdam, pp. 179–499.
- Simo, J. C. and Hughes, T. J. R. (1998), *Computational inelasticity*, Springer-Verlag.
- Simo, J. C., Kennedy, J. G. and Govindjee, S. (1988), 'Non-smooth multisurface plasticity and viscoplasticity. Loading/unloading conditions and numerical algorithms', *International Journal for Numerical Methods in Engineering* **26**, 2161–2185.
- Simo, J. C. and Meschke, G. (1993), 'A new class of algorithms for classical plasticity extended to finite strains. Application to geomaterials', *Computational Mechanics* **11**, 253–278.
- Simo, J. C. and Miehe, C. (1992), 'Associative coupled thermoplasticity at finite strains: Formulation, numerical analysis and implementation', *Computer Methods in Applied Mechanics and Engineering* **98**, 41–104.
- Simo, J. C. and Taylor, R. L. (1985), 'Consistent tangent operators for rate-independent elastoplasticity', *Computer Methods in Applied Mechanics and Engineering* **48**, 101–118.
- Sloan, S. W. (1987), 'Substepping schemes for the numerical integration of elastoplastic stress-strain relations', *International Journal for Numerical Methods in Engineering* **24**, 893–911.
- Sloan, S. W. and Booker, J. R. (1986), 'Removal of singularities in Tresca and Mohr-Coulomb yield functions', *Communications in Applied Numerical Methods* **2**, 173–179.
- Sloan, S. W. and Booker, J. R. (1992), 'Integration of Tresca and Mohr-Coulomb constitutive relations in plane strain elastoplasticity', *International Journal for Numerical Methods in Engineering* **33**, 163–196.
- Sloan, S. W., Sheng, D. and Abbo, A. J. (2000), 'Accelerated initial stiffness schemes for elastoplasticity', *International Journal for Numerical and Analytical Methods in Geomechanics* **24**, 579–599.
- Squire, W. and Trapp, G. (1998), 'Using complex variables to estimate derivatives of real functions', *Siam Review* **40**(1), 110–112.
- Stempleman, R. S. and Winarsky, N. D. (1979), 'Adaptive numerical differentiation', *Mathematics of Computation* **33**(148), 1257–1264.
- Sture, S., Runesson, K. and Macari-Pasqualino, E. J. (1989), 'Analysis and calibration of a three-invariant plasticity model for granular materials', *Ingenieur Archiv* **59**, 253–266.
- Tanaka, H. (1994), 'Vane shear strength of a Japanese marine clay and applicability of Bjerrum's correction factor', *Soils and Foundations* **34**(3), 39–48.
- Tavenas, F. and Leroueil, S. (1980), 'The behaviour of embankments on clay foundations', *Canadian Geotechnical Journal* **17**, 236–260.
- Torrance, J. K. (1987), 'Shear resistance of remoulded soils by viscometric and fall-cone methods: a comparison for the Canadian sensitive marine clays', *Canadian Geotechnical Journal* **24**, 318–322.
- Torstensson, B. A. (1977), Time-dependent effects in the field vane test, in 'Int. Symp. on Soft Clay', Vol. 04.08, Eds. Brenner and Brand, Asian Inst. of Technology, Bangkok, pp. 387–397.
- van der Berg, P., Teunissen, J. A. M. and Huetink, J. (1994), Cone penetration in layered media, an ALE finite element formulation, in 'Computer Methods and Advances in Geomechanics', Eds. Siriwardane and Zaman, Balkema, Rotterdam, pp. 1957–1962.
- Vulliet, L. and Hutter, K. (1988), 'Continuum model for natural slopes in slow movement', *Géotechnique* **38**(2), 199–217.
- Weltman, A. J. and Head, J. M. (1983), Site investigation manual, Technical Report CIRIA special publication, 25, Property Services Agency, London.

- 
- Wiesel, C. E. (1973), 'Some factors influencing in-situ vane test results', *Proc. 8th Int. Conf. Soil Mech. Found. Engrg.* **1-2**, 475–479.
- Worth, C. P. (1984), 'The interpretation of in situ soil tests', *Géotechnique* **34**(4), 449–489.
- Wren, J. R. and Borja, R. I. (1997), 'Micromechanics of granular media. Part II: Overall tangential moduli and localization model for periodic assemblies of circular disks', *Computer Methods in Applied Mechanics and Engineering* **141**(3-4), 221–246.
- Yamada, T. and Kikuchi, F. (1993), 'An arbitrary Lagrangian-Eulerian finite element method for incompressible hyperelasticity', *Computer Methods in Applied Mechanics and Engineering* **102**, 149–177.
- Zienkiewicz, O. C. and Taylor, R. L. (1988), *The Finite Element Method. 1 Basic formulation and linear problems*, 4th edn, McGraw-Hill.



# Index

- adaptive time-integration rule, 65
- ALE
  - algorithm, 32, 139
  - density, 138
  - examples, 15, 33–43, 143–151
  - fluids, 14–16
  - friction, 150
  - hyperelasticity, 30
  - hyperelastoplasticity, 32
  - hypoelastoplasticity, 37
  - solids, 27–43
- algebraic manipulator, 46
- apex, 68, 108, 132
- associate plasticity, 47
- auxiliar predictor, 63
- boundary influence, 68
- Cauchy stress tensor, 29
- cohesion, 106–111, 127, 131, 132
- complex variable, 51, 55, 58, 98
- cone-cap model
  - density-dependent, 127–129, 132
  - work hardening-softening, 81–111
- consistent linearization
  - density-dependent, 116
  - density-independent, 115
  - large strains, 115–118
  - small strains, 48, 90
  - substepping, 66–67
- consolidation, 111
- convection phase, 33, 139
- corner problem, 81–85, 109, 132
- deformation gradient, 28, 112
  - incremental, 31
- density evolution
  - ALE formulation, 138
  - material formulation, 113, 138
- dimensionless
  - analysis, 15, 24–26
  - variable, 17, 113, 143
- displacements, 30
  - incremental, 31
- eigenvalues
  - Cauchy stress tensor, 130
  - Kirchhoff stress tensor, 114
  - left Cauchy–Green tensor, 114
- eigenvectors, 115
- elastic left Cauchy–Green tensor, 28, 113
- elastic predictor, 65, 114
- elastoplastic models
  - Cauchy-based, 111, 113, 130
  - density-dependent, 111–152
    - cone-cap, 127, 132
    - elliptic, 40, 122–127, 131, 137–152
  - Drucker–Prager, 119, 130
  - Kirchhoff-based, 29, 113, 130, 137
  - MRS–Lade, 71–76, 81–111
    - cohesion, 106–111
    - flow potential, 81–85
    - flow vector, 104
  - Rounded Hyperbolic Mohr–Coulomb, 52, 59, 68
  - von Mises, 52, 57
  - von Mises–Tresca, 33–40
- error analysis, 49
- examples
  - coining, 39
  - compaction, 40, 122–129, 140–151
  - necking, 33
  - perforated strip, 57
  - pile, 59, 97
  - rigid footing, 60, 68
  - triaxial test, 71, 98–103, 122
  - uniaxial compression, 119
  - vane test, 6–26
- failure mechanism, 69
- fluid models, 14, 17–24
- fractional-step, 33, 139
- free energy, 29
- friction
  - ALE, 150
  - angle, 72, 88, 119, 127, 132
  - coefficient, 142
  - Coulomb, 135
  - density, 127
  - effects, 39, 71, 126, 142, 143, 150
- geomaterials
  - powder, 40, 122–129, 140–152
  - red mud, 20
  - sand, 73, 91
  - soft clay, 22
- Godunov technique, 33, 139

- Hencky's law, 118, 137
- hyperelasticity, 30, 112
- hyperelastoplasticity, 47, 113, 137
- hypoelastoplasticity, 33, 37
- incompressible flow, 15
- invariants, 104, 130
- isochoric plasticity, 29
- Kirchhoff stress tensor, 29
- Kuhn-Tucker conditions, 64, 113
- Lagrangian phase, 33, 139
- Lie derivative, 29, 113, 138
- line-search, 63
- liquid limit, 13
- liquidity index, 13
- localization, 17, 73, 100
- Lode angle, 55, 92, 93, 104
- machine precision, 50, 91
- mass conservation, 14, 113, 138, 143, 151
- multiplicative plasticity, 27–43, 111–152
- Newton number, 15
- Newton-Raphson
  - full, 47, 48, 64, 66, 90, 115
  - modified, 100
- non-associate plasticity, 47
- non-convergence, 65, 68, 130
- non-isochoric plasticity, 29
- numerical differentiation
  - analysis, 45–51
  - finite-strains, 118
  - small strains, 51–62, 90–104
  - substepping, 64
- Picard iteration, 48
- plastic corrector, 114
- plastic work, 89, 109
- powder compaction
  - flanged component, 40, 123–129, 143–150
  - frictionless, 40, 122–129
  - isostatic, 123
  - multi-level component, 150
  - plain bush, 141
  - triaxial, 122
  - uniaxial, 122, 123, 141–143
- Prandtl collapse force, 69
- reduced integration, 33, 123, 143, 150
- regularized constitutive law, 3
- relative
  - density, 113, 138
  - stepsize, 49
- Reynolds number, 15
- rounding error, 49, 50, 91
- Sherman and Morrison's lemma, 79, 80
- stepsize, 48
- strain rate tensor, 13
- strains
  - finite, 27–43, 111–152
  - small, 45–111
- stress path, 92, 94
- substepping, 62–80
  - adaptive, 65
  - backward Euler, 65
  - forward Euler, 79
  - midpoint rule, 77
  - numerical differentiation, 64
- symmetrized moduli, 122
- tangent operator
  - large strains
    - density-dependent, 116
    - density-independent, 115
  - local problem, 47, 65, 90
  - numerical differentiation, 48
  - substepping, 66–67
  - work-hardening, 90
- transfer stage, 127
- trial state, 65, 114
- triaxial test
  - homogeneous, 98, 104, 122
  - non-homogeneous, 71, 100
  - rate effects, 22
- truncation error, 49
- undrained condition, 15
- viscoplastic limit, 13
- viscosimeter, 22–24
- viscosity, 13
- volumetric deformation
  - rate, 29
  - stress measure, 111